# Characterization of Detectors and Instrument Systematics for the SPIDER CMB Polarimeter

Thesis by

Rebecca Suzanne Tucker

In Partial Fulfillment of the Requirements

for the Degree of

Doctor of Philosophy

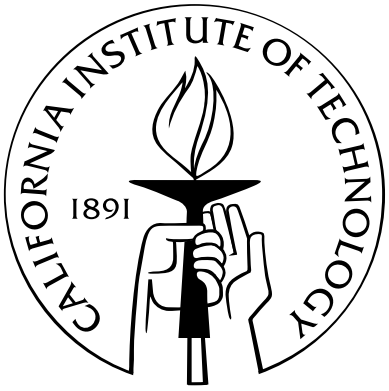


California Institute of Technology

Pasadena, California

2014

(Defended 19 May 2014)

To my family, for their unconditional love and support.

# Acknowledgements

Many people have helped me along my way, and it will be impossible for me to thank them all. Nonetheless, the following is my best effort to do just that.

It seems fitting to begin by thanking my parents, who taught me to love reading and learning when I was very young. It's a gift that has lasted a lifetime. They've cheered me on every step of the way, from building toothpick bridges and trebuchets through the mysterious process that is graduate school. I want to thank them for their support and for their enthusiasm, even when they didn't always know what I was talking about.

My early love for physics was fostered by an amazing high school teacher, Mrs. Jill McLean. Without her, I would never have gone into physics.

Dr. James Sowell was a pivotal mentor to me during my years as an undergraduate at Georgia Tech. He was one of the few faculty who would work with an undergraduate researcher. He encouraged me to apply to REUs and then to graduate school. Without the experience I gained while doing research with him, I would have been woefully underprepared for both.

Jenne Driggers, Kim Boddy, and Alicia Lanz kept me sane through several years of classes and qualifying exams. Their good humor and friendship have made Caltech a enjoyable place. My sister, Jennifer, has always been a useful sounding board and a constant source of encouragement.

My graduate career would not have been the same without the patience and knowledge of my advisor, Sunil Golwala. His support has been crucial to every milestone I passed as a graduate student, from teaching me statistical mechanics in order to pass my qualifying exams, to giving feedback on talks for candidacy and defense. I have benefitted enormously from his deep knowledge of experimental physics and his ability to quickly derive useful suggestions and advice.

SPIDER is a collaboration, and the SPIDER team has been delightful to work with over

the past five years. I have learned so much from the other SPIDER graduate students, post-docs, and professors. Though I never want to repeat it, I suspect our summer in Palestine, TX will be the standout memory of my time in graduate school.

I was extremely fortunate to have many mentors at Caltech over the past few years. Amy Trangsrud took me under her wing and taught me not only the basics of doing research, but also how to succeed as a graduate student. The SPIDER and Keck post-docs (Marc Runyan, Lorenzo Moncelsi, Roger O'Brient, and Zak Staniszewski) have been consistently helpful and willing to share their experience and knowledge.

Of all the post-docs I've worked with, I owe the deepest debt of gratitude to Jeff Filippini. For five years, on an almost daily basis, I have peppered him with questions ranging from cosmology to cryogens. He has patiently answered each and every one. It's not too much of an exaggeration to say that he taught me almost everything I know about being an experimental physicist. He also generously sat through countless practice talks and read endless drafts of talks, proposals and this very document. My graduate experience would have been considerably worse without his excellent advice and mentorship.

Finally, I need to thank Bradley for his encouragement and love. There were plenty of times when I felt I couldn't do this, that I wasn't smart enough to be at Caltech. His unwavering belief in me kept me going. He's tagged along to midnight helium fills and kept our life running while I left for months at a time to go integrate a telescope in the middle of Texas. He never lost his good humor about this process, even when I brought a kitten home from Palestine because I just couldn't leave him behind. He believes I can do anything, which is the most powerful statement of love I could possibly imagine.

# Abstract

We know from the CMB and observations of large-scale structure that the universe is extremely flat, homogenous, and isotropic. The current favored mechanism for generating these characteristics is inflation, a theorized period of exponential expansion of the universe that occurred shortly after the Big Bang. Most theories of inflation generically predict a background of stochastic gravitational waves. These gravitational waves should leave their unique imprint on the polarization of the CMB via Thompson scattering. Scalar perturbations of the metric will cause a pattern of polarization with no curl (E-mode). Tensor perturbations (gravitational waves) will cause a unique pattern of polarization on the CMB that includes a curl component (B-mode). A measurement of the ratio of the tensor to scalar perturbations ($r$) tells us the energy scale of inflation. Recent measurements by the BICEP2 team detect the B-mode spectrum with a tensor-to-scalar ratio of $r = 0.2^{+0.05}_{-0.07}$. An independent confirmation of this result is the next step towards understanding the inflationary universe.

This thesis describes my work on a balloon-borne polarimeter called SPIDER, which is designed to illuminate the physics of the early universe through measurements of the cosmic microwave background polarization. SPIDER consists of six single-frequency, on-axis refracting telescopes contained in a shared-vacuum liquid-helium cryostat. Its large format arrays of millimeter-wave detectors and tight control of systematics will give it unprecedented sensitivity. This thesis describes how the SPIDER detectors are characterized and calibrated for flight, as well as how the systematics requirements for the SPIDER system are simulated and measured.

# Contents

# List of Figures

# List of Tables

# Preface

As is the nature of most modern physics experiments, SPIDER is a collaboration involving seven institutions and almost 50 people. Much of the work described in this thesis is a product of this collaboration and is, therefore, not necessarily my own. This preface was written to clarify which portions of this thesis reflect my contributions to SPIDER.

Throughout this text, I have attempted to given credit for figures and pictures created by others and to acknowledge which institutions are responsible for major subsystems of the experiment. Please forgive any errors or omissions.

## Detector Testing

From the start of my graduate career with SPIDER, I have been involved in the testing and characterization of the SPIDER detectors. I worked extensively with the detector/insert team at Caltech, learning to integrate focal planes and telescopes, mastering the process of closing up the test cryostat, and becoming familiar with cryogenic procedures for cooling down the SPIDER detectors.

My work on focal plane integration included spending time at the Microfabrication Lab at JPL (where our detectors are fabricated), where I learned to wire bond and did the majority of the wire bonding for two of our focal planes. After the detectors are installed in the focal plane, the focal plane must be integrated into the telescope. During my time at Caltech, I took apart and rebuilt the SPIDER telescopes dozens of times.

Over the course of 22 runs of Caltech test cryostat (each of which take between three and five weeks), I became an expert at working with liquid nitrogen and helium. I wrote a set of standardized procedures for cooling and filling the test cryostat. During these runs I learned how to run the detectors through our Multichannel Electronics (MCE), and how to independently perform and analyze all of the standard SPIDER calibration measurements

(measuring device parameters, optical efficiencies, taking spectra with a Fourier transform spectrometer, taking both low- and high-bandwidth noise measurements, etc).

## Hardware

In addition to integrating the SPIDER telescopes for detector testing, I was responsible for building several components of the SPIDER experiment. I did all of the annealing and AR-coating of the SPIDER lenses and nylon filters. I built three of the original cooled optics sleeves and helped blacken all of the baffle rings that were installed in them afterwards. I also helped blacken most of the spittoons and repaired cracks after thermal cycling.

Many of our measurements require specialized calibration sources. I helped to build one of the original sources for Caltech (a large aperture, mechanically chopped thermal source) and designed and built two additional sources myself: a rotating polarized source and an additional thermal source. As I was also typically in charge of the measurements made with these sources, I spent a great deal of time in balconies and cherry pickers setting these sources up for far field measurements of our beams.

## Beam Measurements

One of my unique contributions to the SPIDER collaboration was my work on measuring and analyzing the beams (and particularly the systematic errors from beams) of the SPIDER telescopes. I set up and analyzed the earliest measurements of the SPIDER beams and used those beam maps to probe previously unknown characteristics of the system, such as the characteristics of ghost beams from internal reflections, the profile of the near sidelobes, the cross-polar response of the detectors, the power coupling to large angles, the properties of the HWP, and dark loading on the detectors.

I also did many analyses of the beams, measuring their individual properties and systematic errors (such as differential pointing, differential width, and differential ellipticity), as part of my work on updating and maintaining the SPIDER systematics table. I also wrote a simulation that measured the beam function from observations of the CMB, as part of an effort to see if any of our pre-flight calibration measurements could be removed from the campaign.

## Pre-flight integration at CSBF

I spent almost three months in Palestine, TX at the Columbia Scientific Ballooning Facility in summer 2013, where we integrated five telescopes into the flight cryostat along with the gondola and pointing systems for the first complete test of all the SPIDER subsystems. While there, I helped build the telescopes, close the cryostat, and run/test the detectors. Much of my time during the integration campaign was spent helping to run the detectors and take measurements as part of the detector team. I also set up and analyzed the first beam maps in the SPIDER flight cryostat, in addition to participating in many other measurements. I did the analysis for the optical efficiencies, polarization angle calibration, and beam maps.

## Conclusion

Building hardware and components for the SPIDER telescopes was a very tangible contribution to the collaboration. My work on detector testing substantially improved the quality and understanding of the SPIDER flight detectors. The detector testing team regularly fed information back to the detector fabrication team at JPL, who used it to improve the fabrication process. My measurements and analyses of the SPIDER beams are crucial for understanding the systematic errors of our instrument.

# Chapter 1

# Introduction

## 1.1 The Journey to Modern Cosmology

### 1.1.1 The Expanding Universe

Cosmology, the study of the history and evolution of the universe, has only in the last century become a rigorous scientific discipline. The earliest cosmologies were inextricably bound up in religion and myth — from the Babylonians, who believed that we lived on a flat earth surrounded by waters of chaos, to Galileo, who fought to have his scientific studies separated from the scripture of the Catholic church. In the scientific revolution of the late seventeenth and eighteenth centuries, Kepler's observations of the motions of the planets and Newton's theories about the nature of gravity revolutionized how science was practiced and gave birth to the modern fields of astronomy and physics.

Modern cosmology is generally considered to have begun with Einstein's publication of the theory of general relativity [31] in 1917. In the years that followed, Einstein and other cosmologists (e.g. de Sitter, Schwarzschild) proposed radically new ideas about cosmology and our universe as logical consequences of general relativity. The long-standing assumption that the universe was static and unchanging was finally overthrown by Edwin Hubble in 1929, when he published a paper describing a linear relationship between distance and radial velocity in extra-galactic nebulae (today known as galaxies) [48]. He found that objects are moving away from us with speeds proportional to their distances, a relationship now known as Hubble's Law.

$$v \simeq Hd. \tag{1.1}$$

Here, $H$ is a parameter known as the Hubble parameter and it describes the rate at which

the universe is expanding at a particular moment in time. This relationship was the first widely-known evidence that we live in an expanding, rather than a static, universe. This new model of the universe implied that, if we run the clock backward, the universe eventually becomes very small, hot and dense. When the clocks run forward again, the entire universe then springs forth in a "Big Bang."

The Big Bang theory of cosmology was first proposed by Georges Lemaître in 1927 [59], [60]. He proposed that "the radius of the universe increases without limit from an asymptotic value $R_0$ for $t = -\infty$" (i.e., that the radius of the universe is not fixed) and that "the receding velocities of extragalactic nebulae are a cosmic effect of the expansion of the universe." These two statements combined are the essence of the Big Bang theory. Note that the second statement is a version of what we now call "Hubble's Law," though Hubble did not propose it until two years later.

In the late 1920s and early 1930s, Alexander Friedmann, Georges Lemaître, Howard Robertson, and Arthur Walker all published results pertaining to an exact solution of Einstein's field equations of general relativity for homogenous, isotropic expanding (or contracting) universes [60], [37], [38], [77], [89]. Their results are now known as the FLRW metric.

The following discussion follows the arguments made in Trodden and Carroll's cosmology lectures [87]. The FLRW metric starts with the assumptions that the universe is isotropic (looks the same in all directions) and homogenous (looks the same at every point). The metric is

$$ds^2 = -dt^2 + a^2(t)\left[\frac{dr^2}{1-kr^2} + r^2(d\theta^2 + \sin^2\theta d\phi^2)\right], \tag{1.2}$$

where $k$ = -1, 0, or 1 depending on the spatial curvature of the universe (negative, flat, and positive, respectively). The time coordinate $t$ is the proper time as measured by a comoving observer and the function $a(t)$ is called the scale factor.

The scale factor of the universe, $a(t)$, is related to the Hubble parameter by

$$H \equiv \frac{\dot{a}(t)}{a(t)}. \tag{1.3}$$

The Hubble constant is a function of time, so $H_0 = H(t_0)$, where $t_0$ is the time at present day. The most recent measurements of the Hubble constant by the Planck satellite give a value for $H_0$ of $(67 \pm 1.2)$ km s$^{-1}$ Mpc$^{-1}$ [1]. This result strongly depends on the

underlying model assumed for the analysis. Other measurements of the Hubble parameter using type Ia supernovae or galaxy redshift surveys find somewhat larger values ($(72 \pm 3)$ km s$^{-1}$ Mpc$^{-1}$ [49]).

The FLRW metric can be derived purely from the consequences of requiring homogeneity and isotropy in a spatial metric. However, in order to understand the dynamics of the universe, we want to look at the differential equations that govern the evolution of the scale factor $a(t)$. For that, we apply Einstein's equation,

$$R_{\mu\nu} - \frac{1}{2}Rg_{\mu\nu} = 8\pi G T_{\mu\nu} + \Lambda \tag{1.4}$$

to the metric. In the above equation, $R_{\mu\nu}$ is the Ricci curvature tensor, $R$ is the Ricci scalar, $g_{\mu\nu}$ is the metric tensor, $G$ is Newton's gravitational constant, and $T_{\mu\nu}$ is the energy-momentum tensor. Here $\Lambda$ is a cosmological constant, originally introduced by Einstein to achieve a description of a static universe. Since the discovery of the accelerated, expanding universe [76], the cosmological constant is now considered the simplest possible form for the dark energy that causes the acceleration. Current observations indicate that dark energy constitutes roughly 68% of the total energy density of the universe, while cold dark matter constitutes 27%, and the remaining 5% of the energy density is due to ordinary matter. This model, part of the $\Lambda$CDM model of cosmology, is a good fit to most current cosmology observations.

The energy-momentum tensor is typically assumed to be of the form that describes a perfect fluid for cosmological calculations:

$$T_{\mu\nu} = (\rho + p)U_\mu U_\nu + p g_{\mu\nu}, \tag{1.5}$$

where $U^\mu$ is the fluid four-velocity, $\rho$ is the energy density in the rest frame of the fluid, and $p$ is the pressure in the rest frame. By applying Eqn. 1.4 to Eqn. 1.2, we get the Friedmann equation:

$$H^2 \equiv \left(\frac{\dot{a}}{a}\right)^2 = \frac{8\pi G}{3}\sum_i \rho_i - \frac{k}{2a^2}, \tag{1.6}$$

where $i$ indexes all the possible types of energy in the universe and $k$ takes on the values (-1,0,1) depending on the curvature of the universe. (We also get the Friedmann acceleration equation, which I do not discuss here.) The Friedmann equation relates the increase in

the scale factor to the total energy density of all matter in the universe. If the universe is precisely flat ($k = 0$), we can use this equation to get an expression for the critical energy density:

$$\rho_c \equiv \frac{3H^2}{8\pi G}. \tag{1.7}$$

The density parameter is then defined as

$$\Omega_{total} \equiv \frac{\rho}{\rho_c} = \sum_i \frac{\rho_i}{\rho_c}, \tag{1.8}$$

where $\rho_i$ is the density of a particular component of the universe. This parameter determines the overall spatial geometry of the universe.

Even prior to the high precision measurements of the density of the universe that can be made today, it was believed in the 1960s and 1970s that $0.01 \leq \Omega_{total} \leq 10$. Although these do not seem to be especially strict bounds, they tell us that the universe is nearly flat today, which has enormous implications for the flatness of the universe at earlier times (§1.2.1).

The Friedmann equation is often expressed in terms of density parameters:

$$\frac{H^2}{H_0^2} = \Omega_R a^{-4} + \Omega_M a^{-3} + \Omega_k a^{-2} + \Omega_\Lambda, \tag{1.9}$$

where $\Omega_R$ is the radiation energy density, $\Omega_M$ is the matter energy density, $\Omega_k = 1 - \Omega_{total}$ is the curvature energy density, $\Omega_\Lambda$ is the vacuum density (or cosmological constant), and $a(t_0) = 1$ ($t_0$ = present time).

The Friedmann equation will be important in the discussion of the motivations for an inflationary universe in §1.3.

### 1.1.2 The Homogenous, Isotropic Universe

After Lemaître and Hubble's observations of the expanding universe, the next major observational confirmation of the Big Bang occurred in 1965, when Penzias and Wilson observed an excess temperature in their microwave telescope of 3.5K [73]. A companion paper produced at the same time by Dicke et. al. gave an explanation for this isotropic radiation — the cosmic microwave background [30].

The cosmic microwave background (CMB) is one of the most fundamental tests of the

Big Bang model. As we extrapolate the expanding universe back to the beginning of time, the universe becomes hot and dense. The photons of that era were easily energetic enough to ionize neutral hydrogen and so the universe was filled with an opaque, charged plasma. This plasma is also called the photon-baryon fluid. This phase of the universe lasted until the universe had expanded and cooled sufficiently such that the photons redshifted enough to allow protons and electrons to stably combine. (This is known as recombination). Shortly after the formation of neutral hydrogen, the photons decoupled from the now-neutral plasma and began free-streaming through the universe.

During these early times the density of the universe was so high that matter was in approximately thermal equilibrium at every point in space. This predicts that the spectrum of radiation emitted from the plasma should be described by a blackbody. The energy flux of a blackbody is given by

$$P(\nu, T)d\nu = 8\pi h \left(\frac{\nu}{c}\right)^3 \frac{1}{e^{h\nu/kT} - 1} d\nu, \tag{1.10}$$

where $h$ is Planck's constant and $k$ is the Boltzmann constant. The wavelengths of a blackbody will stretch with cosmic expansion and the frequencies will scale inversely. The effect of cosmic expansion on a blackbody is just to lower its temperature, while keeping the spectral shape of a blackbody. If the predictions of the Big Bang model are correct, the universe should be filled with radiation from a cold blackbody, with a temperature that is inversely proportional to the scale factor $a$. Indeed, in 1994, the FIRAS instrument on the COBE satellite determined that the CMB fits a blackbody spectrum to extremely high precision (within 0.03%) [64]. After final calibration, the temperature of the CMB was determined to be $2.725 \pm 0.002$K [65]. These results were a stunning confirmation of the Big Bang model.

## 1.2 Problems with Standard Cosmology

The discovery of the CMB was a valuable source of confirmation of the Big Bang Theory and the modern picture of cosmology (i.e., that we live a flat, homogenous, and isotropic universe). However, there were known problems with the standard cosmology, including some that were motivated by the properties of the CMB. These issues mostly fall under the category of initial conditions problems and they are the motivation for a period of

accelerated expansion in the early universe, known as inflation.

### 1.2.1 The Flatness Problem

We can rewrite the Friedmann equation (Eqn. 1.6) as

$$(\Omega^{-1} - 1)\rho a^2 = \frac{-3k}{8\pi G}. \tag{1.11}$$

Here $\rho$ is the total density of the universe and $\Omega$ is the time-dependent ratio of the mean density to the critical density $\rho/\rho_c$. Since the right-hand side of the equation is composed entirely of constants, the left-hand side must also remain constant throughout the history of the universe. As the universe expands, the scale factor $a$ increases but the overall density $\rho$, which is either matter- or radiation-dominated, decreases as $a^3$ or $a^4$, and so the term $\rho a^2$ decreases over all. In fact, this term has decreased by a factor of approximately $10^{60}$ since the Planck era (when the age of the universe was less than the Planck time, $t_P \approx 5.4 \times 10^{-44}$ s). So $(\Omega^{-1} - 1)$ must have increased by the same amount:

$$|\Omega_{Planck} - 1| \approx 10^{-60}|\Omega_0 - 1|. \tag{1.12}$$

Here we have made the following approximation: $(\Omega^{-1} - 1) \approx (1 - \Omega) \Rightarrow |\Omega^{-1} - 1| \approx |\Omega - 1|$. $\Omega_0$ is the value of the density parameter today.

Observationally we know that $|\Omega_0 - 1| \leq 0.01$ [1], which implies that the value of the density parameter during the Planck era must have been extremely close to one:

$$|\Omega_{Planck} - 1| \leq 10^{-62}. \tag{1.13}$$

This is extremely fine-tuned. Why should the density of the universe right after the Big Bang be so close to the critical density? That is, why is our universe so flat? One can consider it a remarkable coincidence of initial conditions, but this is a sort of explanation that physicists abhor. Inflation solves this problem by letting the scale factor $a$ grow exponentially for a brief period of time. Then the length scales of any curvature of the universe are much larger than the size of the observable universe, and so the universe will appear almost perfectly flat.

### 1.2.2 The Horizon Problem

Cosmological horizons exist because a photon can only have traveled a finite distance in the period of time since the Big Bang. The horizon problem is that the CMB is highly isotropic, even though widely separated points on the last scattering surfaces are outside each other's horizons (i.e., they were causally disconnected at decoupling). How, then, do they have the same temperature?

More concretely, we can calculate the angle subtended by the horizon at recombination:

$$\theta_{hor} = \frac{d_{hor}}{d_A}, \tag{1.14}$$

where $d_{hor}$ is the comoving horizon distance at recombination and $d_A$ is the angular diameter distance from us to recombination.

To find the distance between two comoving redshifts, we use the following equation:

$$\tau_2 - \tau_1 = \int_{z_1}^{z_2} \frac{dz}{H(z)} \equiv \mathcal{I}(z_1, z_2), \tag{1.15}$$

where $z$ is the redshift (which is related to the scale factor via $a = 1/(1+z)$) and $H(z)$ is Friedmann equation (Eqn. 1.9).

Using this equation, we can calculate the value of the particle horizon at recombination:

$$d_{hor} \approx \mathcal{I}(z_{rec}, \infty), \tag{1.16}$$

where $z_{rec} = 1100$ is the redshift at recombination, which is determined by the observed CMB temperature.

In a flat universe, the angular diameter distance from us to recombination is

$$d_A = \mathcal{I}(0, z_{rec}). \tag{1.17}$$

Putting the previous equations together, we see that

$$\theta_{hor} = \frac{\mathcal{I}(z_{rec}, \infty)}{\mathcal{I}(0, z_{rec})}. \tag{1.18}$$

If we use the Friedmann equation (Eqn. 1.9) with sensible values for the density param-

eters, the above equation can be numerically evaluated to get

$$\theta_{hor} \approx 1.16^{\circ}. \tag{1.19}$$

This means that patches of the CMB that are separated by more than $\theta \approx 2.3^{\circ}$ will have had non-overlapping horizons and therefore could not have been in causal contact with each other. Yet, the CMB is isotropic over the entire sky to very high precision. Inflation solves the horizon problem because it implies that the entire observable universe was initially contained in a volume much smaller than the particle horizon at the time, where the photons had enough time to thermalize prior to the onset of inflation.

### 1.2.3 Magnetic Monopoles

Most Grand Unified Theories (GUTs) predict the existence of magnetic monopoles or other exotic relic particles. These particles are predicted as a result of symmetry breaking in the very early universe. By most calculations, there is expected to be at least one monopole per horizon volume at the time of the symmetry breaking. Since this is expected to have happened during the GUT era, when the horizon volume was extremely small, there should be an enormous density of monopoles today. However, we observe that the density of magnetic monopoles is essentially zero [92, 74]. Inflation, assuming that it occurred after the formation of the magnetic monopoles, would significantly dilute the density of these and other relic particles.

### 1.2.4 A Solution to the Problems

A solution to these problems was proposed by Alan Guth in 1980 — the inflationary universe [42]. He proposed a universe that supercools towards a metastable false vacuum. While in the false vacuum state, the universe will expand exponentially. Inflation blows up an extremely small spatial region in size, smoothing out perturbations (creating a smooth and isotropic universe) as well as diminishing spatial curvature (creating a flat, or almost flat, universe). It also solves the horizon problem by putting widely separated regions in the sky in casual contact with each other prior to this inflationary epoch.

Guth's model had two problems. The first was that there was no way to smoothly end the period of exponential expansion. The second problem was reheating, a period of time

after inflation in which the universe returns to its pre-inflationary temperature and the universe is filled with the particles of the Standard Model. In this model, the exponential expansion of the universe occurs while the universe is trapped in the false-vacuum state. In order to achieve a sufficiently large inflation, the tunneling rate from the false-vacuum state to bubbles of true vacuum had to be small. This indicated that the nucleation of the bubbles was rare. However, the reheating of the universe was proposed to come from bubble collisions. With the small bubble nucleation rate necessary for inflation, the universe would never reheat.

These problems were solved by later models of inflation proposed by Andrei Linde [61] and Steinhardt and Albrecht [10]. These models of inflation are known as "slow-roll" models. Instead of having the exponential expansion caused by a decaying false vacuum state, their models used a scalar field (the inflaton) rolling down a potential energy hill. After inflation ends, the inflaton decays into the particles of the Standard Model that we observe today.

There are many models of inflation, including chaotic inflation, eternal inflation, and hybrid inflation. Until very recently, the experimental evidence for inflation was largely circumstantial and there was no direct experimental information about the energy scales at which inflation might have occurred.

## 1.3 Inflation Theory

The basic idea of inflation is that very, very shortly ($t \approx 10^{-35}$ seconds) after the Big Bang, the universe underwent a period of accelerated expansion ($\ddot{a} > 0$). The universe increased in size by at least 60 e-folds in much less than a second. The effect of this expansion was to create an apparently flat, isotropic, and homogenous universe.

### 1.3.1 Basics

This section follows the arguments made in [15]. Another way to think about inflation is as a phase of decreasing Hubble radius ($1/aH$). The particle horizon $\Delta r_{max}$(the maximum distance a particle can travel between an initial time $t_i = 0$ and a later time $t > t_i$) depends on evolution of the comoving Hubble radius:

$$\Delta r_{max} = c \int_0^t \frac{\mathrm{d}t'}{a(t')} = \int (aH)^{-1} \, \mathrm{d} \ln a. \tag{1.20}$$

A decreasing Hubble radius means that large scales that enter the universe at the present time were inside the horizon prior to inflation, and so had time to become homogenous. We describe a decreasing Hubble radius as

$$\frac{d}{dt}(aH)^{-1} < 0. \tag{1.21}$$

We will see that this statement implies accelerated expansion. We begin by evaluating the expression on the left-hand side:

$$\frac{d}{dt}(aH)^{-1} = \frac{d}{dt}(\dot{a})^{-1} = -\frac{\ddot{a}}{\dot{a}^2}. \tag{1.22}$$

Then,

$$-\frac{\ddot{a}}{\dot{a}^2} < 0 \Rightarrow \ddot{a} > 0, \tag{1.23}$$

which is our expression for accelerated expansion.

Another way to evaluate Eqn. 1.21 is

$$\frac{d}{dt}(aH)^{-1} = -\frac{\dot{a}H + a\dot{H}}{(aH)^2} = -\frac{1}{a}(1-\epsilon), \tag{1.24}$$

where

$$\epsilon = -\frac{\dot{H}}{H^2}. \tag{1.25}$$

Using the same inequality relation as above (Eqn. 1.21), we find that the necessary condition for inflation also corresponds to

$$-\frac{1}{a}(1-\epsilon) < 0 \Rightarrow \epsilon < 1. \tag{1.26}$$

To solve the cosmological problems outlined in the previous section, we not only want the universe to exponentially expand, we also want it to expand for a sufficiently long period of time. That is, we want $\epsilon$ to remain small through a minimum of 50-60 e-fold expansions of the universe. To achieve this condition, we define another parameter:

$$\eta = \frac{\dot{\epsilon}}{H\epsilon}. \tag{1.27}$$

When $|\eta| < 1$, the fractional change in $\epsilon$ per Hubble time is small, and inflation persists for

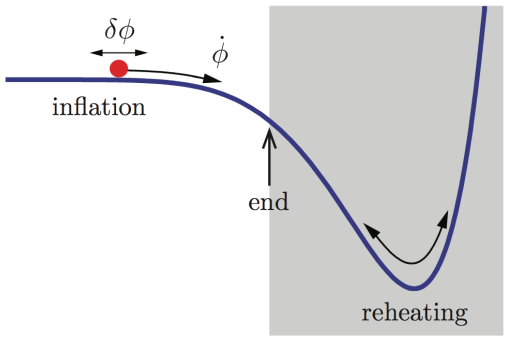


Figure 1.1: A slowly rolling inflaton potential. From [15].

many e-foldings.

As mentioned in §1.1.1, for cosmological calculations we typically assume the energy-momentum tensor is of the form that describes a perfect fluid. The Friedmann Equations can be recast to use the pressure $p$ and density $\rho$ of this fluid:

$$H^2 = \frac{1}{2M_{pl}^2}\rho \tag{1.28}$$

$$\dot{H} + H^2 = -\frac{1}{6M_{pl}^2}(\rho + 3p), \tag{1.29}$$

where $M_{pl}$ is the Planck mass and $H$ is the Hubble parameter.

If we use this form of the Hubble equations in the definition of $\epsilon$ (Eqn. 1.25), we find

$$\epsilon = -\frac{\dot{H}}{H^2} = \frac{3}{2}\left(1 + \frac{p}{\rho}\right) < 1 \Rightarrow \frac{p}{\rho} < -\frac{1}{3}, \tag{1.30}$$

which indicates that inflation requires a negative pressure.

### 1.3.2 Slow-roll Inflation

So far we have not discussed the physics that lead to the conditions ($\epsilon < 1$ and $|\eta| < 1$) that ensure inflation. The most common inflationary theories are those involving slowly rolling scalar fields (see Fig. 1.1). In these theories, we consider a scalar field $\phi$ (the "inflaton") with a potential $V(\phi)$. The following discussion relies on [87].

The energy momentum tensor for $\phi$ is

$$T_{\mu\nu} = (\nabla_\mu \phi)(\nabla_\nu \phi) - g_{\mu\nu}\left[\frac{1}{2} g^{\alpha\beta}(\nabla_\alpha \phi)(\nabla_\beta \phi) + V(\phi)\right]. \tag{1.31}$$

If we simplify to the homogenous case, all quantities depend only on the time, $t$. We can also set $k = 0$ by the following reasoning — even if the universe started out with a significant curvature, inflation will quickly drive it towards flatness and, hence, $k = 0$. A homogenous, real scalar field behaves as a perfect fluid with density and pressure given by

$$\rho_\phi = \frac{1}{2}\dot{\phi}^2 + V(\phi) \tag{1.32}$$

$$p_\phi = \frac{1}{2}\dot{\phi}^2 - V(\phi). \tag{1.33}$$

From these equations it is clear that if $\dot{\phi}^2 << V(\phi)$, then the potential of the scalar field will dominate both the pressure and density, with the result that $\rho_\phi \simeq -p_\phi$. This is the same situation as described at the end of §1.3.1, which, as we have already noted, results in an accelerated expansion of the universe.

The time evolution of the scalar field is described by the Klein-Gordon equation, which can be thought of as the equation of motion for a scalar field in Minkowski space, but with a friction term due to the expansion of the universe:

$$\ddot{\phi} + 3\frac{\dot{a}}{a}\dot{\phi} + \frac{dV}{d\phi} = 0. \tag{1.34}$$

To simplify the equation of motion, we make the *slow-roll approximation*. One of the assumptions made in the slow-roll approximation is that $\ddot{\phi} \approx 0$. So this equation can be rearranged as

$$\dot{\phi} \simeq -\frac{dV/d\phi}{3H}. \tag{1.35}$$

The Friedmann equation with such a field as the sole energy source is

$$H^2 = \frac{8\pi G}{3}\left[\frac{1}{2}\dot{\phi}^2 + V(\phi)\right]. \tag{1.36}$$

The other assumption made by using the slow-roll approximation is to neglect the kinetic

energy of $\phi$ compared to the potential energy (drop the $\dot{\phi}^2$ in the equation above). The Friedmann equation then becomes

$$H^2 \simeq \frac{8\pi G}{3} V(\phi). \tag{1.37}$$

Plugging Eqn. 1.37 and Eqn. 1.35 into the definitions of $\epsilon$ and $\eta$ gives

$$\epsilon = \frac{M_p^2}{2}\left(\frac{V'}{V}\right)^2 \tag{1.38}$$

and

$$\eta \equiv M_p^2 \frac{V''}{V}, \tag{1.39}$$

where $M_p$ is the Planck mass and the prime mark indicates a derivative with respect to $\phi$. The slow roll conditions are satisfied if $|\epsilon| << 1$ and $|\eta| << 1$.

### 1.3.3 Perturbations

During inflation, quantum fluctuations in the inflaton field are expanded to cosmological scales. The decay of the inflaton field results in a spectrum of remnant density and gravitational wave perturbations. Most inflationary models predict that this spectrum will be scale invariant (the same at all wavelengths).

Scale invariance implies that the inflaton field experiences fluctuations that are the same for every wavenumber, $\delta\phi_k$ = constant. Those fluctuations can be related to the ones in density by

$$\delta\rho = \frac{dV}{d\phi}\delta\phi. \tag{1.40}$$

From this we expect nearly scale-invariant density perturbations (the scale factor $\frac{dV}{d\phi}$ evolves with time, which is why we do not get exactly scale-invariant perturbations). The density perturbation (or "scalar") spectrum is related to the inflationary potential as follows:

$$A_S^2 \approx \left.\frac{V^3}{M_p^6 (V')^2}\right|_{k=aH}, \tag{1.41}$$

where $k = aH$ indicates that the values of $V'$ and $V$ are to be evaluated at the moment when the physical scale of the perturbation $\lambda = a/k$ is equal to the Hubble radius $H^{-1}$. These density fluctuations are also known as scalar fluctuations, since they are scalar fluc-

tuations of the metric. The density fluctuations produced by inflation are adiabatic (by which we mean that perturbations in the density of all components of the universe are correlated), Gaussian, and uncorrelated (i.e., the phases of the Fourier modes describing the fluctuations at different scales are uncorrelated). It should be noted that inflation does predict some small amount of nongaussianity, but the fluctuations should be nearly Gaussian. These predictions of inflation — an adiabatic, nearly scale-free spectrum of density perturbations with a Gaussian distribution, have been confirmed to new precision by the Planck instrument [3, 2]. The graviton is also excited during inflation, which creates tensor perturbations in the metric, or gravitational waves. Their spectrum is described by

$$A_T^2 \approx \left.\frac{V}{M_p^4}\right|_{k=aH}. \tag{1.42}$$

The existence of tensor perturbations is one of the most crucial predictions of the theory of inflation, since it can be observationally verified via measurements of the polarization of the cosmic microwave background (to be explained in the next section). Note that the tensor perturbation spectrum depends only on the potential $V$, and not its derivatives. So observations of the tensor modes are directly related to the energy scale of inflation:

$$V_{\text{inflation}}^{1/4} \sim \epsilon^{1/4} 10^{16} \text{ GeV}, \tag{1.43}$$

where the calibration factor comes from the measurements of $A_S$ from the COBE experiment.

The ratio of the tensor and scalar perturbation spectra, known as the tensor-to-scalar ratio $r$ can be related back to the slow roll parameters:

$$r = \frac{A_T^2}{A_S^2} = \text{constant} \times \epsilon, \tag{1.44}$$

where the constant depends on the exact approximations used to calculate the tensor and scalar spectra and typically takes a value between 12 and 16. By combining Eqn. 1.43 and Eqn. 1.44, we can get an equation that directly relates the tensor-to-scalar ratio, $r$ to the inflationary potential:

$$V_{\text{inflation}}^{1/4} \sim \left(\frac{r}{10}\right)^{1/4} 10^{16} \text{ GeV}. \tag{1.45}$$

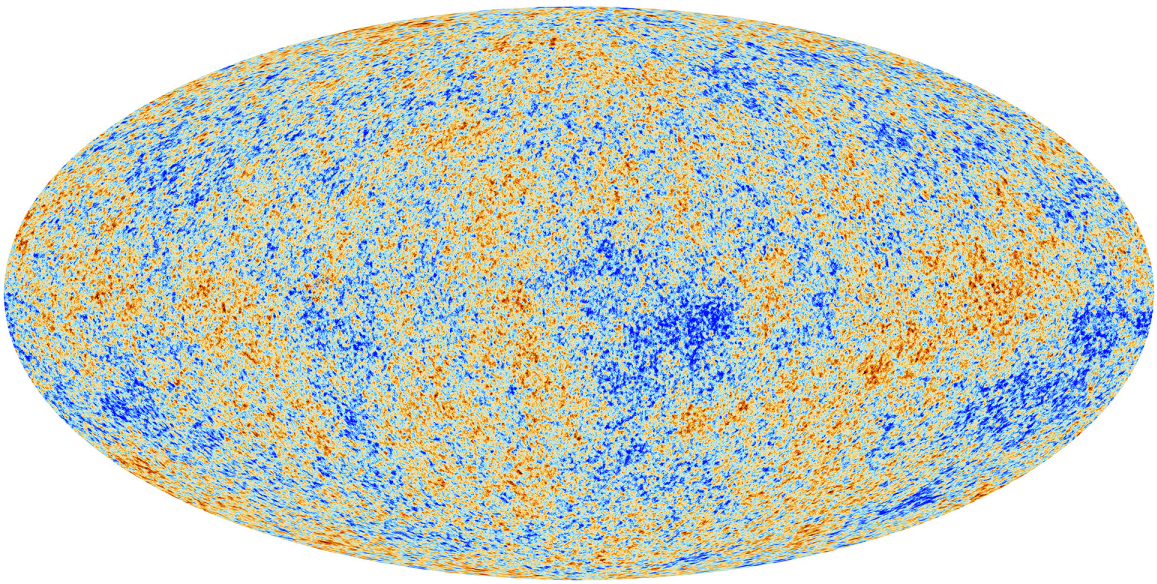

Figure 1.2: The anisotropies of the CMB as observed by Planck. Image courtesy of ESA and Planck Collaboration.

## 1.4 How to Detect Inflation

We now know what the standard model of the universe looks like and why inflation seems like a necessary component of that model. Our next question is, how do we definitely determine whether this period of accelerated expansion actually happened? The answer lies in the measurements of the cosmic microwave background.

### 1.4.1 CMB Temperature Anisotropies

In the mid-1990s, the FIRAS instrument on the COBE satellite determined that the CMB fits a blackbody spectrum with temperature 2.725K with extremely high precision. Another instrument on the COBE satellite, DMR, was also able to detect very faint fluctuations in the CMB [90]. These deviations from isotropy are measured to be one part in $10^5$. More sensitive experiments, such as BOOMERanG [28] and WMAP [17], made high fidelity measurements of the temperature anisotropies and the temperature anisotropy power spectrum. A successor experiment to WMAP, the Planck satellite, provides the current best measurement of the CMB temperature anisotropies (Fig. 1.2) and power spectrum [1] at scales greater than 7 arcminutes and over the full sky. The South Pole Telescope (SPT) [82] and Atacama Cosmology Telescope (ACT) [25] provide the best measurements at small angular scales (Fig. 1.3).

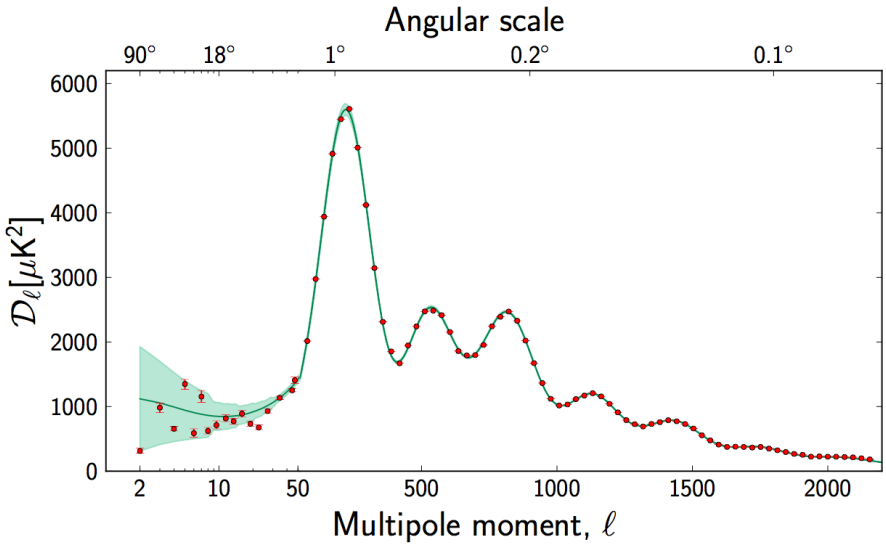


(a) The temperature angular power spectrum of the CMB. The red points and error bars represent measurements, while the green shaded area represents cosmic variance. The vertical axis is $\ell(\ell+1)C_\ell/2\pi$. Figure is from the 2013 release of Planck science results [1].

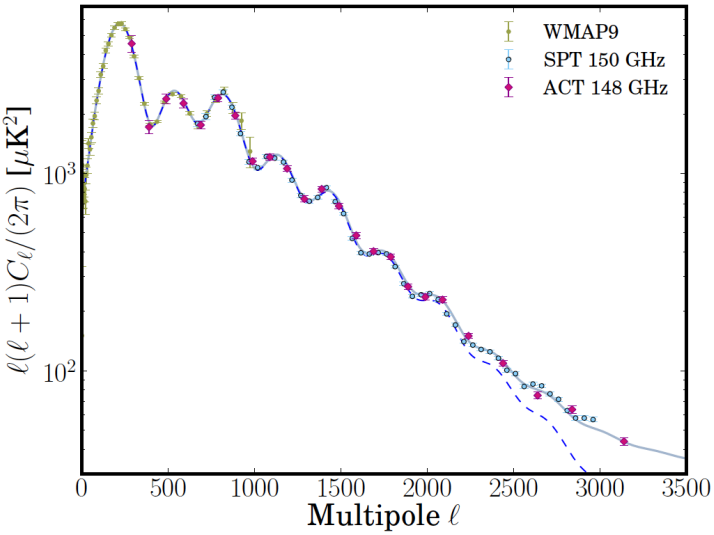


(b) The temperature angular power spectrum of the CMB with combined data from WMAP9 [17], ACT [25], and SPT [82]. The solid line shows a best fit model to the data. The dashed line shows the CMB-only component of that model. Figure from [25].

Figure 1.3: Current best measurements of the CMB power spectrum from Planck, SPT, and ACT.

The CMB temperature anisotropies have become one of the most important tools of modern experimental cosmology. To analyze these small temperature anisotropies, we decompose them into spherical harmonics on the sky:

$$\frac{\Delta T}{T} = \sum_{\ell m} a_{\ell m} Y_{\ell m}(\theta, \phi), \tag{1.46}$$

where $a_{\ell m}$ are expansion coefficients and $\theta$ and $\phi$ are spherical polar angles on the sky. From here, we take a power spectrum:

$$C_\ell = \langle |a_{\ell m}|^2 \rangle. \tag{1.47}$$

We typically multiply this quantity by $\ell(\ell + 1)$ for plots of the CMB power spectrum (see Fig. 1.3).

The CMB temperature anisotropy power spectrum is extremely valuable for understanding the early universe. From it, we can construct a model of what the universe looked like just prior to recombination and place valuable constraints on many of the fundamental parameters of the universe. In order to understand the power spectrum, it is helpful to think about how the temperature anisotropies formed.

Small, random quantum mechanical fluctuations in the density of the universe were blown up to cosmological scales by the process of inflation. These density perturbations source gravitational potential wells that are the seeds of large-scale structure in the universe. Over time, the density fluctuations grow, through gravitational instability, to become the first stars, galaxies, and clusters. A competition between the overdensity of the fluid in the gravitational potential wells and the gravitational redshifting of the photons as they climb out of the potential wells determines the observed CMB temperature fluctuations. The temperature fluctuation due to redshifting is larger than that from the overdensities and thus, the overdense regions actually correspond to cold spots on the sky. These density fluctuations also cause the photons of CMB to have small variations in temperature. Since the photons of the CMB have propagated freely through the universe since decoupling, affected by little except cosmic expansion and reionization (which rescatters approximately 10% of the photon of the CMB), we still see the anisotropies today.

One of the most remarkable features of the CMB power spectrum is the series of peaks

known as the "acoustic peaks." These peaks come from the physics of the photon-baryon fluid in gravitational potential wells prior to decoupling. The photon-baryon fluid compresses in gravitational wells. As the fluid compresses, the radiation pressure of the fluid increases and provides a restoring force. The interplay of these two forces results in acoustic oscillations of the fluid. The compression of the fluid in the gravitational well causes it to heat up. The rarefaction of the fluid in corresponding gravitational "hills" (underdense regions) causes the fluid to cool. When the photons are released at recombination, the acoustic oscillations will be "frozen in" and we see the oscillations of the fluid as changes in the temperature of the CMB photons.

As mentioned in §1.3, inflation causes these random fluctuations to occur at all scales. However, wave modes that have reached either the crest or trough of their oscillations at the time of recombination will have enhanced temperature fluctuations. The largest of these will be the mode that had time to compress exactly once before recombination, but not enough time to rebound. This wavenumber of this mode will correspond to $\pi$ divided by the amount of distance that sound could travel prior to recombination — the sound horizon. Harmonics of this mode will also have enhanced temperature fluctuations for the same reason. These are the modes that were frozen in at exactly one of the extrema of their oscillations. We see the spatial variations in the temperature as angular scales on the sky today. The enhanced modes become the acoustic peaks of the CMB spectrum. Thus, the first peak in the CMB power spectrum corresponds to the angular size of the sound horizon at recombination, and all the subsequent peaks are the result of the harmonics of that mode. We can use estimates of the density of matter just prior to recombination to calculate the speed of sound in the photon-baryon fluid, which allows to evaluate the size of the particle horizon at the time of recombination.

This first peak in the CMB temperature power spectrum occurs around $\ell \simeq 220$, or an angular scale of approximately one degree, which is in excellent agreement with the prediction for a flat universe ($k = 0$, $\rho = \rho_c$). BOOMERanG, in particular, is noted for being the first experiment to map the first acoustic peak of the CMB power spectrum [28]. (Their result was quickly followed by one from the MAXIMA experiment [44].) The flatness of the universe, as shown by the location of the first peak, indicates that the total density of the universe is very near the critical density.

The odd-numbered peaks in the CMB power spectrum are associated with modes that

were at their maximum compression at the time of recombination. Similarly, the even-numbered peaks are associated with modes at their maximum rarefaction. The baryons in the photon-baryon fluid add inertial and gravitational mass to the system, so a very high baryon density will enhance the compression of the fluid, and therefore the heights of the odd numbered peaks. We see from the power spectra that the height of the second peak is suppressed relative to the first and third peaks, and from this we can constrain the baryon density. The relative amplitudes of the higher acoustic peaks also allow us to constrain the dark matter density.

The oscillations at very high multipoles (small angular scales) are damped out due to the random walk that CMB photons make at the time of recombination. Photons within the distance traveled by a random walk will thermalize, and the temperature anisotropies on those scales will be averaged away. The damping scale provides another check on the curvature of the universe, as well as the baryon density. A higher baryon density will decrease the mean free path of the photon's random walk, thereby decreasing the damping scale and shifting the damping tail of the CMB power spectrum to higher multipoles.

Our ability to measure the power spectrum at very low multipoles is fundamentally limited by sample variance, by which we mean that there are only $2\ell+1$ $m$ samples at each multipole. This leads to an error of

$$\Delta C_\ell = \sqrt{\frac{2}{2\ell+1}} C_\ell. \tag{1.48}$$

This "cosmic variance" becomes the limiting error on the power spectrum at very low multipoles.

There are additional, practical limits on how well the power spectrum can be measured due to the realities of experimental science [47]. Most instruments will observe only some fraction of the sky. This will increase the errors by a factor of $f_{sky}^{-1/2}$:

$$\Delta C_\ell = \sqrt{\frac{2}{(2\ell+1)f_{sky}}} C_\ell. \tag{1.49}$$

The noise of the experiment will also increase the error on the power spectrum:

$$\Delta C_\ell = \sqrt{\frac{2}{(2\ell+1)f_{sky}}} (C_\ell + N_\ell), \tag{1.50}$$

where $N_\ell$ is the power spectrum of the noise projected onto the sky. The error due to the noise will dominate at small angular scales (large multipoles) since the signal-to-noise of the instrument will be poor on scales smaller than the size of the instrument beam.

Lastly, averaging over bins in multipole space, $\Delta\ell \approx \ell$, will add an additional factor of $\Delta\ell^{-1/2}$ to the error:

$$\Delta C_\ell = \sqrt{\frac{2}{(2\ell+1)f_{sky}\Delta\ell}}(C_\ell + N_\ell). \tag{1.51}$$

The measurement of the CMB temperature power spectrum was the start of a new era in precision cosmology. Although many of the parameters estimated from it were supportive of the theory of inflation, definitive proof would have to come from an even more subtle measurement.

### 1.4.2 CMB Polarization

Most theories of inflation generically predict a background of scale-invariant gravitational waves, which are then "imprinted" on the polarization of the CMB. The following section gives an overview of how polarized light is typically described for CMB polarimetry and a discussion of CMB polarizing mechanisms, including polarization from gravitational waves. References for this section include [80] and [54].

#### 1.4.2.1 Stokes Parameters

The Stokes parameters are a common way to describe the polarization state of electromagnetic radiation. We start with the following form for a linearly polarized electromagnetic wave propagating along the $\hat{z}$ direction with frequency $\omega$:

$$\vec{E} = E_x \cos(\omega t - \theta_x)\hat{x} + E_y \cos(\omega t - \theta_y). \tag{1.52}$$

The Stokes parameters (I, Q, U, and V) are then given by

$$I = \langle |E_x|^2 + |E_y|^2 \rangle \tag{1.53}$$

$$Q = \langle |E_x|^2 - |E_y|^2 \rangle \tag{1.54}$$

$$U = 2\langle |E_x||E_y| \cos(\theta_x - \theta_y) \rangle \tag{1.55}$$

$$V = 2\langle |E_x||E_y| \sin(\theta_x - \theta_y)\rangle, \tag{1.56}$$

where $\langle\rangle$ denotes a time average. The total intensity of the light is given by $I$, and for purely monochromatic, coherent radiation $I^2 = Q^2 + U^2 + V^2$. Unpolarized light is described by $Q = U = V = 0$. Thomson scattering, the process that polarizes the CMB, does not produce net circular polarization. Since $|V|$ describes the intensity of circular polarization, it is typically equal to zero for CMB polarimetry. The Stokes parameters have units of power and are experimentally convenient because each parameter is a sum or difference of a measurable intensity.

Polarization has an orientation and a magnitude (though it is not strictly a vector, since the orientation does not have a direction). Its orientation angle is given by

$$\alpha = \frac{1}{2} \tan^{-1} \frac{U}{Q}, \tag{1.57}$$

and the magnitude is given by

$$P = \sqrt{U^2 + Q^2}. \tag{1.58}$$

Polarization transforms as a rank-2, symmetric, trace-free tensor. It can be described in spherical polar coordinates:

$$\mathcal{P}_{ab}(\theta, \phi) = \frac{1}{2} \begin{pmatrix} Q(\theta, \phi) & -U(\theta, \phi, ) \sin\theta \\ -U(\theta, \phi) \sin\theta & -Q(\theta, \phi) \sin^2\theta \end{pmatrix}. \tag{1.59}$$

In the same way that the temperature anisotropies of the CMB can be decomposed into scalar spherical harmonics, any polarization on the sky can be decomposed into two modes using an orthonormal set of tensor spherical harmonics:

$$\frac{\mathcal{P}_{ab}(\theta, \phi)}{T_0} = \sum_{\ell=2}^{\infty} \sum_{m=-\ell}^{\ell} [a^E_{\ell m} Y^{E\ ab}_{\ell m}(\theta, \phi) + a^B_{\ell m} Y^{B\ ab}_{\ell m}(\theta, \phi)], \tag{1.60}$$

where

$$a^E_{\ell m} = \frac{1}{T_0} \int d\theta d\phi\ \mathcal{P}_{ab}(\theta, \phi) Y^{E\ ab}_{lm}(\theta, \phi), \tag{1.61}$$

and

$$a^B_{\ell m} = \frac{1}{T_0} \int d\theta d\phi\ \mathcal{P}_{ab}(\theta, \phi) Y^{B\ ab}_{lm}(\theta, \phi). \tag{1.62}$$

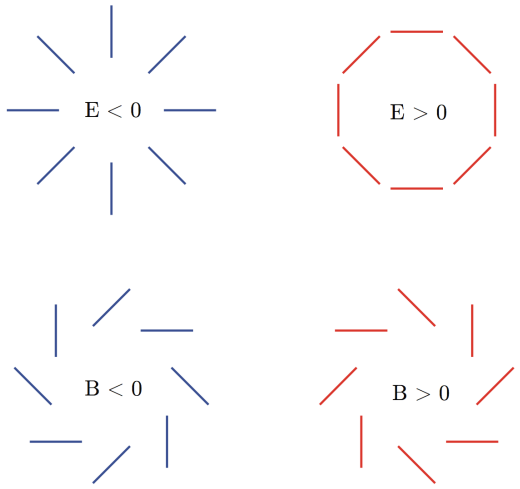


Figure 1.4: Examples of E- and B-mode polarization patterns. Note that E-mode patterns are identical upon reflection, while the positive and negative B-mode patterns are interchanged. From [15].

The $Y^E_{lm}(\theta,\phi)$ harmonics are known as "E-modes" and the $Y^B_{lm}(\theta,\phi)$ harmonics are known as "B-modes." The E-modes, like electric fields, are curl-free and have an even parity. The B-modes, like magnetic fields, contain a curl and have an odd parity.

Explicit forms of the tensor spherical harmonics are

$$Y^E_{(\ell m)ab}(\theta,\phi) = \frac{M_\ell}{2}\begin{bmatrix} W_{\ell m}(\theta,\phi) & X_{\ell m}(\theta,\phi)\sin\theta \\ X_{\ell m}(\theta,\phi)\sin\theta & -W_{\ell m}(\theta,\phi)\sin^2\theta \end{bmatrix} \tag{1.63}$$

and

$$Y^B_{(\ell m)ab}(\theta,\phi) = \frac{M_\ell}{2}\begin{bmatrix} -X_{\ell m}(\theta,\phi) & W_{\ell m}(\theta,\phi)\sin\theta \\ W_{\ell m}(\theta,\phi)\sin\theta & X_{\ell m}(\theta,\phi)\sin^2\theta \end{bmatrix}, \tag{1.64}$$

where

$$M_\ell \equiv \sqrt{\frac{2(\ell-2)!}{(\ell+2)!}}, \tag{1.65}$$

$$W_{\ell m}(\theta,\phi) = 2\left(\frac{\partial^2}{\partial\theta^2} - \ell(\ell+1)\right)Y_{\ell m}(\theta,\phi), \tag{1.66}$$

and

$$X_{\ell m}(\theta,\phi) = \frac{2im}{\sin\theta}\left(\frac{\partial}{\partial\theta} - \cot\theta\right)Y_{\ell m}(\theta,\phi). \tag{1.67}$$

The multipole moments $a^T_{\ell m}$, $a^E_{\ell m}$, and $a^B_{\ell m}$ that have been described in this section and

in §1.4.1 can be used to create power spectra and cross-spectra for the temperature and polarization of the CMB sky:

$$\langle a^{T*}_{\ell m} a^{T}_{\ell' m'} \rangle = C_\ell^{TT} \delta_{\ell\ell'} \delta_{mm'} \qquad \langle a^{E*}_{\ell m} a^{E}_{\ell' m'} \rangle = C_\ell^{EE} \delta_{\ell\ell'} \delta_{mm'} \tag{1.68}$$

$$\langle a^{B*}_{\ell m} a^{B}_{\ell' m'} \rangle = C_\ell^{BB} \delta_{\ell\ell'} \delta_{mm'} \qquad \langle a^{T*}_{\ell m} a^{E}_{\ell' m'} \rangle = C_\ell^{TE} \delta_{\ell\ell'} \delta_{mm'} \tag{1.69}$$

$$\langle a^{T*}_{\ell m} a^{B}_{\ell' m'} \rangle = C_\ell^{TB} \delta_{\ell\ell'} \delta_{mm'} \qquad \langle a^{E*}_{\ell m} a^{B}_{\ell' m'} \rangle = C_\ell^{EB} \delta_{\ell\ell'} \delta_{mm'}. \tag{1.70}$$

$$\tag{1.71}$$

Since scalar spherical harmonics and the E-mode tensor harmonics have parity $(-1)^\ell$, while the B-mode tensor harmonics have parity $(-1)^{\ell+1}$, symmetry under parity transitions will require that $C_\ell^{TB} = C_\ell^{EB} = 0$. These moments are typically used to monitor foreground emission, though a non-zero detection of the $C_\ell^{TB}$ or $C_\ell^{EB}$ spectra would be a remarkable finding.

A non-zero detection of the $C_\ell^{BB}$ spectrum is frequently called the "smoking gun" of inflation, since tensor modes are one of the unique predictions of inflation. The $C_\ell^{BB}$ spectrum can be related back to the primordial tensor power spectrum as follows [15]:

$$C_\ell^{BB} = (4\pi)^2 \int k^2 \, dk \; A_T(k) \; \Delta_{B\ell}(k), \tag{1.72}$$

where $A_T(k)$ is the primordial tensor power spectrum and $\Delta_{B\ell}(k)$ is the transfer function for B-modes. A similar, though more complicated, equation can be written to relate the E-mode power spectrum to the primordial scalar and tensor modes. Both the tensor ($A_T(k)$) and scalar ($A_S(k)$) spectra will be necessary, since gravitational waves contribute to both E- and B-mode polarization. The transfer function is how the primordial spectrum is "processed" by the plasma physics of the early universe into the CMB polarization spectra we see today.

As mentioned in §1.3, the amplitude of the gravitational wave spectrum is typically parameterized by the tensor-to-scalar ratio, $r$ (Eqn 1.44). A measurement of the polarization power spectra allows us to get an estimate for $r$, and therefore the energy scale of inflation.

#### 1.4.2.2 Thomson Scattering

The physical mechanism that causes the polarization of the CMB is Thomson scattering of photons off of electrons in the presence of a local quadrupole temperature anisotropy.

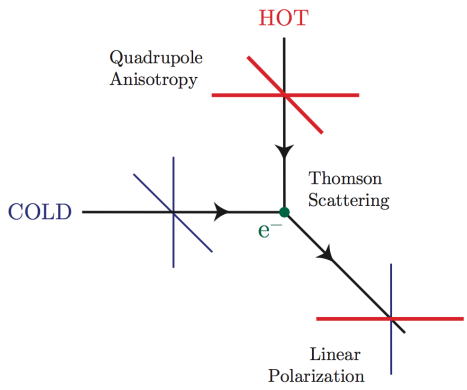


Figure 1.5: Thomson scattering of a quadrupole anisotropy. Figure from [15].

These anisotropies can be caused by either density anisotropies or by gravitational waves. Density anisotropies (scalar perturbations of the metric) result in E-mode only polarization. Gravitational waves (tensor perturbations of the metric) result in both E and B-mode polarization.

The Thomson scattering cross-section depends on polarization. The energy flux radiated into polarization state $\boldsymbol{\epsilon}$ by an incident plane wave with propagation vector $\boldsymbol{k_0}$ and polarization vector $\boldsymbol{\epsilon_0}$ is

$$\frac{d\sigma}{d\Omega} = \frac{3\sigma_T}{8\pi}|\boldsymbol{\epsilon}^* \cdot \boldsymbol{\epsilon_0}|^2, \tag{1.73}$$

where $\sigma_T$ is the total Thomson cross-section. The incoming light causes the electron to vibrate in the direction of its electric field vector with the same frequency as its own. This vibration reradiates the light with a polarization direction parallel to the direction of the shaking. If radiation is incident upon the electron equally in all directions, no net polarization will occur. However, if the intensity of the radiation varies at 90° (i.e., a quadrupole pattern), then the resulting radiation will have a net polarization (see Fig. 1.5).

Let us assume that radiation is incident upon the scattering electron from all directions with intensity $I(\phi, \theta)$ (Fig. 1.6). We can model an unpolarized incident beam as the linear superposition of two linearly polarized beams of equal intensity:

$$\vec{E}_{incident} = \vec{E}_{i,1} + \vec{E}_{i,2}. \tag{1.74}$$

The polarization of $\vec{E}_{i,1}$ will point along the direction $\boldsymbol{\epsilon_{i,1}}$ and the polarization of $\vec{E}_{i,2}$ will

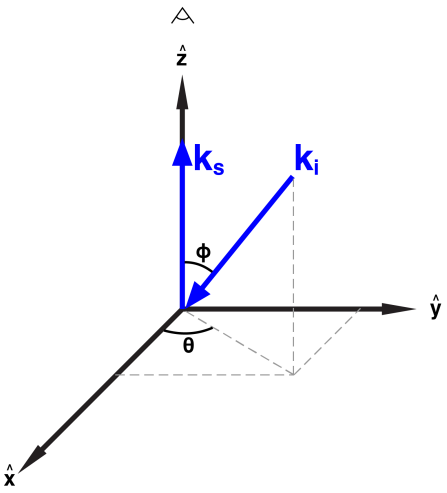


Figure 1.6: Scattering diagram for an incoming wave $k_i$ scattering off an electron at the origin, producing a scattered wave $k_s$.

point along $\boldsymbol{\epsilon_{i,2}}$:

$$\boldsymbol{\epsilon_{i,1}} = \sin\theta\ \hat{x} + \cos\theta\ \hat{y} \tag{1.75}$$

$$\boldsymbol{\epsilon_{i,2}} = \cos\theta\cos\phi\ \hat{x} + \sin\theta\cos\phi\ \hat{y} + \sin\phi\ \hat{z}. \tag{1.76}$$

Note that $\boldsymbol{\epsilon_{i,1}}$ and $\boldsymbol{\epsilon_{i,2}}$ are not unit vectors.

We are viewing the scattered radiation from the axis $\hat{z}$. The polarization we will see from the scattered waves will be perpendicular to the scattering direction. The scattered waves will be polarized along $\boldsymbol{\epsilon_{s,1}}$ and $\boldsymbol{\epsilon_{s,2}}$:

$$\boldsymbol{\epsilon_{s,1}} = \sin\theta\ \hat{x} + \cos\theta\ \hat{y} \tag{1.77}$$

$$\boldsymbol{\epsilon_{s,2}} = \cos\theta\cos\phi\ \hat{x} + \sin\theta\cos\phi\ \hat{y}. \tag{1.78}$$

From here, we can calculate the polarization fraction along the x-axis. Here I am stating the result found in [86]:

$$\Pi_x = \frac{\int_0^{2\pi} d\theta \int_0^{\pi} \sin\phi\ d\phi\ I(\phi,\theta)(\sin^2\theta - \cos^2\theta)\sin^2\phi}{\int_0^{2\pi} d\theta \int_0^{\pi} \sin\phi\ d\phi\ I(\phi,\theta)(1+\cos^2\phi)}. \tag{1.79}$$

An examination of this equation will provide some useful intuition. If there is azimuthal symmetry with respect to $k_i$ (i.e., if $I(\phi,\theta) = I(\phi)$), the polarization fraction will be zero.

In fact, if we assume $I(\phi, \theta)$ is of the form

$$I(\phi, \theta) = I_0 Y_{\ell m}(\phi, \theta), \tag{1.80}$$

then the polarization fraction will be zero for all spherical harmonics except for $\ell = 2$. Therefore, only scalar ($Y_{20}$), vector ($Y_{2\pm1}$), and tensor quadrupoles ($Y_{2\pm2}$) will result in a net polarization in the scattered light.

As mentioned above, the scalar quadrupoles are the result of density perturbations in the early universe and are the dominant polarization mechanism of the CMB at angular scales less than 10°. Due to the axial symmetry of $Y_{20}$ spherical harmonics, scalar perturbations result only in E-mode polarization (no B-modes).

The vector modes ($Y_{2\pm1}$) are not typically generated by inflationary theories (although some theories based on topological defects do predict them). The vector modes arise due to vorticity in the photon-baryon fluid. However, as the universe expands, the rotation rate will decrease (due to conservation of angular momentum) and the vector modes will quickly decay. We typically ignore vector perturbations in cosmological calculations for these reasons.

The tensor quadrupoles are the result of inflationary gravitational waves, which are predicted by most inflationary models. The quadrupoles are created by the gravitational wave stretching and compressing the light around the scattering electron (see Fig. 1.7b). The Thomson scattering of this quadrupole ($Y_{2\pm2}$) will generate both E- and B-mode polarization in equal amounts. As mentioned before, B-mode polarization is uniquely generated by gravitational waves and is considered to be the "smoking gun" of inflation.

It should be noted here that B-mode polarization at small angular scales can also be caused by the gravitational lensing of the E-mode spectrum [4]. These lensing B-modes come from gravitational lensing of the E-mode spectrum by all the matter between us and the CMB. This lensing distorts the E-mode signal and creates both E and B modes. The lensing B-mode spectrum can be used to probe things like the matter distribution, neutrino masses, and dark energy. Since these angular scales ($\sim$ 1 arcminute) are out of reach of the SPIDER instrument due to our large-aperture telescopes, I do not discuss them further here.

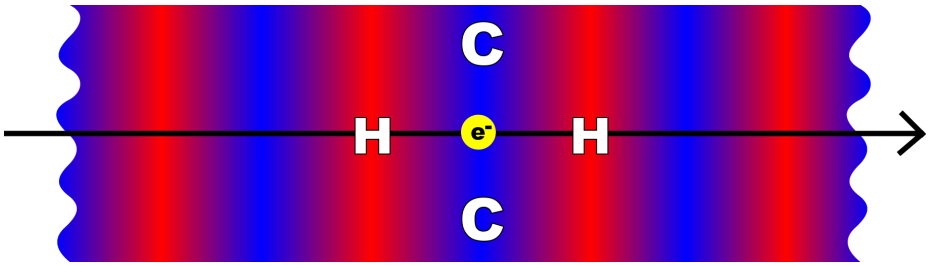


(a) Quadrupole temperature anisotropies created by density waves.

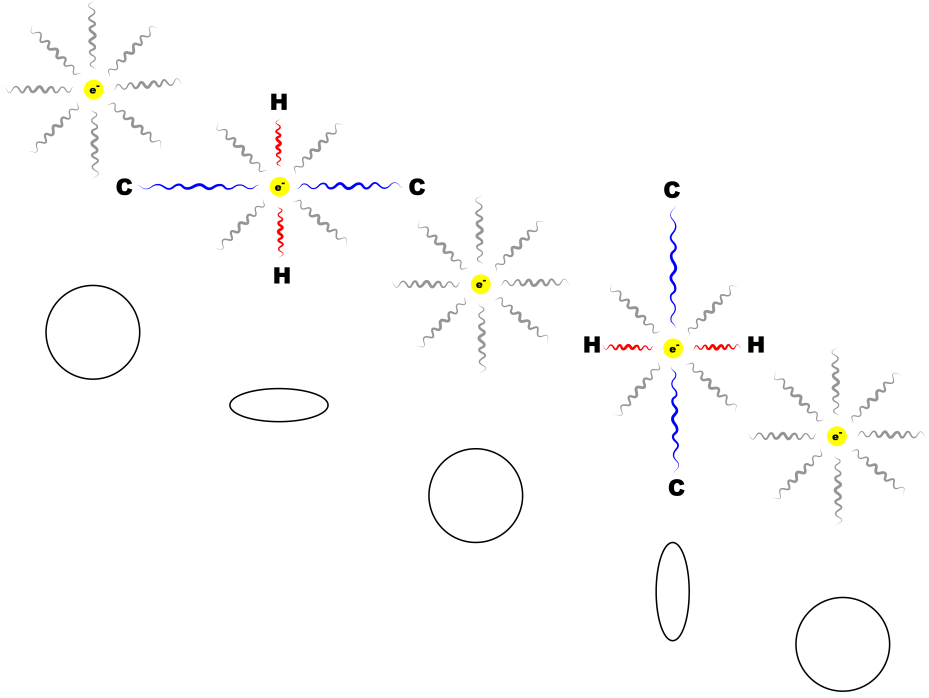


(b) Quadrupole temperature anisotropies created by gravitational waves.

Figure 1.7: Temperature anisotropies created by scalar and tensor perturbations.

### 1.4.3 Predicted Polarization Spectra

So far this section has explained how we describe polarization on the sky and how the CMB becomes polarized from Thomson scattering. Here we describe the predicted CMB polarization spectra. The temperature anisotropies are very small — one part in $10^5$, which translates to a signal of a few hundred $\mu$K. Prior to the recent measurements by BICEP2, the amplitude of the B-mode power spectrum was unknown, but estimated to be several orders of magnitude fainter than that of the temperature anisotropy spectrum — a signal of less than a $\mu$K. A plot of the temperature anisotropy spectrum, E-mode power spectrum, and B-mode power spectrum (for $r = 0.1$) is shown in Fig. 1.8.

The shape of the TT spectrum is described in §1.4.1. The E-mode spectrum peaks near the diffusion scale. There is a second peak on large angular scales representing the same scattering process but arising from more recent times when the hydrogen in the universe was ionized by the first stars (known as reionization). The E-mode spectrum also exhibits acoustic oscillations, since the quadrupole anisotropies that generate it are themselves formed from the acoustic motions of the fluid. The peaks track the acoustic velocity and are out of phase with the temperature peaks. Scales larger than the sound horizon have not had time to drive the velocities that create E-modes, so there is a sharp decline in the power spectrum at low multipoles.

The tensor modes act like a damped harmonic oscillator, and the damping is proportional to expansion, but only if the modes are inside the horizon. By the time the longer modes have entered the horizon, recombination has already occurred and there are no longer any free electrons to scatter photons. Shorter modes that enter the horizon before recombination have time to redshift away. Thus, the modes entering the particle horizon just at recombination produce the strongest B-modes (i.e. the peak of the B-mode spectrum corresponds to the size of the particle horizon at recombination).

Note that the amplitudes of the E- and B-mode spectra are many orders of magnitude smaller than the amplitude of the TT spectrum. Even in the absence of complicating factors, such as experiment systematics and polarized foregrounds, detecting these very faint signals is an experimental challenge.

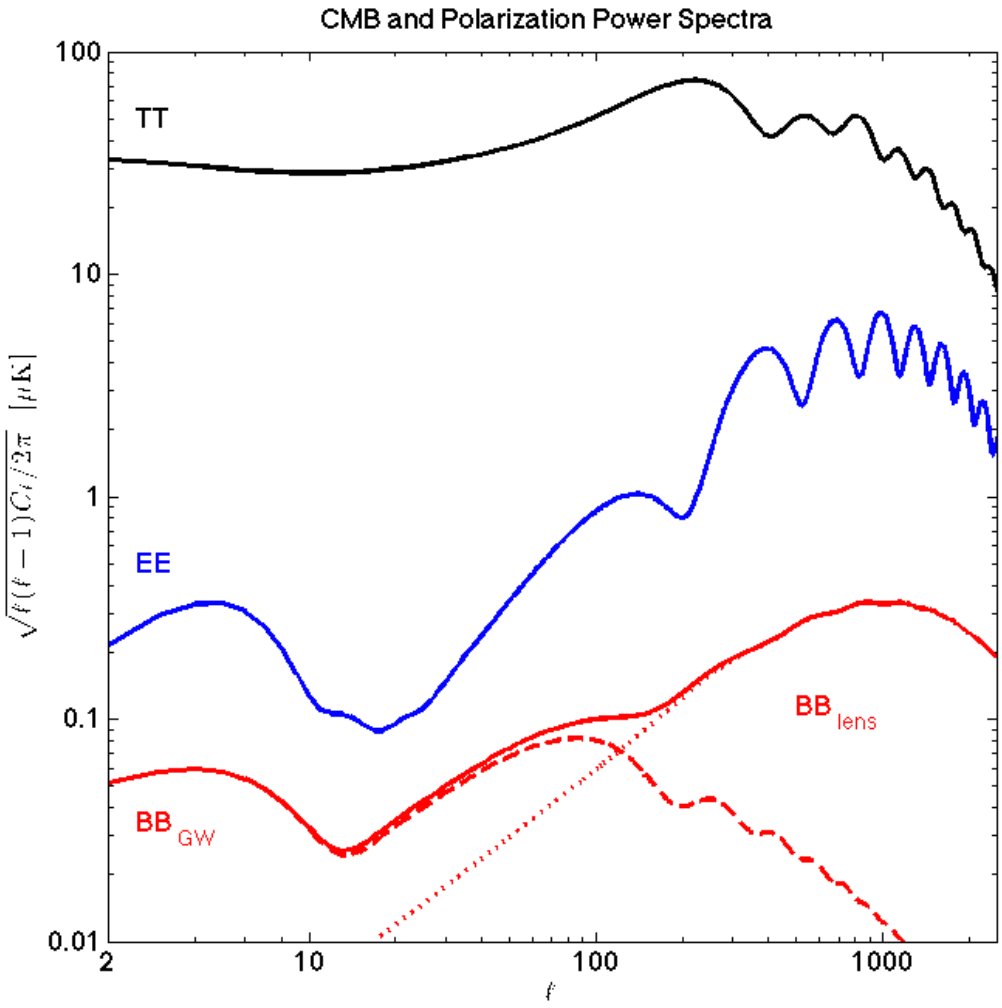


Figure 1.8: Temperature, E-mode, and B-mode power spectra. Data is from CAMB for $r = 0.1$. The contribution from inflationary gravitational waves to the B-mode spectrum peaks at angular scales of approximately two degrees, while gravitational lensing of the CMB causes B-modes at smaller angular scales.

## 1.5 Polarized Foregrounds

One of the main challenges in detecting the CMB polarization power spectra is the presence of confounding signals from polarized foregrounds. It is necessary to understand these foregrounds in order to separate them from the primordial signal. Polarized foregrounds are not under the same symmetry constraints as the primordial perturbations, and so there is no reason they cannot generate both E- and B-modes. We expect the main sources of SPIDER's polarized foregrounds to be from dust and synchrotron radiation.

Both of these foregrounds are the result of galactic magnetic fields. The galactic magnetic field, which was originally proposed by Enrico Fermi, is not well understood. Our current knowledge of the galactic magnetic field is that it is aligned with the disk and arms of our spiral galaxy on large scales and is turbulent on small scales. It is sustained by an unknown dynamo mechanism, and magnetic fields can vary widely from galaxy to galaxy. Models of the galactic magnetic field feed directly into SPIDER simulations of synchrotron and thermal dust emission.

### 1.5.1 Synchrotron Radiation

Synchrotron radiation is generated by electrons forced to travel on a curved path by a magnetic field. It can be highly polarized at microwave frequencies in the direction orthogonal to the magnetic field. We use the WMAP 23 GHz data to estimate the amplitude of polarized synchrotron radiation at frequencies in SPIDER's bands. We extrapolate using a power law and find that it should be negligible at 150GHz in SPIDER's sky region (synchrotron radiation is quite bright in the galactic plane). At 90GHz it is estimated to be a factor of two higher than a B-mode signal equivalent to $r = 0.03$ at large scales ($10 < \ell < 30$), but still a factor of five smaller than the foreground contribution from polarized dust. We find that the multipole dependence of the polarized synchrotron emission to be well-described by a power law , $C_\ell \propto \ell^{-2.5}$, which brings the signal to less than the $r = 0.03$ B-mode spectrum by $\ell \sim 30$. At the peak of BB spectrum, $\ell \sim 80$, the polarized emission from synchrotron radiation is estimated to be an order of magnitude fainter than the signal at $r = 0.03$ [36].

### 1.5.2 Dust

Polarized emission from galactic dust is expected to be the dominant foreground for SPIDER. Although we still do not have a complete theoretical understanding of the physical process by which dust grains radiate polarized emission, it was first proposed as a way to explain the polarization of starlight by Albert Hiltner and independently by John Hall in 1949 [46, 43]. The essential idea is that radiation from galactic and intergalactic objects is absorbed by dust grains in the interstellar medium and then reradiated in the infrared. To get polarized emission, Hiltner and Hall proposed that non-spherical dust grains aligned with the galactic magnetic field. With the long axis of the dust grain aligned perpendicular to the field, a grain of dust will absorb more incident radiation in the direction perpendicular to the local magnetic field than the direction parallel to it. This differential absorption results in a net polarization of the incident radiation in a direction parallel to the magnetic field and, therefore, a net polarization of the emission of radiation from the dust grain. So the polarization of thermal dust emission is expected to be perpendicular to the sky-projected direction of the magnetic field. There are several proposed alignment mechanisms, including the Davis-Greenstein mechanism [26] (paramagnetic alignment of thermally rotating grains) and radiative torques (which models dust grains as helical and then assumes that geometric optics apply).

Dust is typically composed of both carbonaceous material and silicate minerals. There is no single power law emissivity model that fits the known dust spectrum, likely because of the multiple components. The most frequently used thermal (non-polarized) emission model (FDS model 8) assumes there are two dust components and fits four parameters [34]. Polarized dust models include randomly oriented polycyclic aromatic hydrocarbons (PAHs), oblate spheroidal silicate grains, and graphite grains assumed to be spheres or oblate spheroids.

SPIDER simulations of polarized thermal dust emission use a 3-dimensional model of the galactic magnetic field and dust distribution. Since the overall normalization of the polarized emission in SPIDER dust model is a free parameter, we set this parameter to 3.6% to match the average value derived by WMAP [70] for areas outside the Galactic plane. We extrapolate polarized intensity maps to the SPIDER bands by using FDS model 8 to account for the frequency dependence [34].

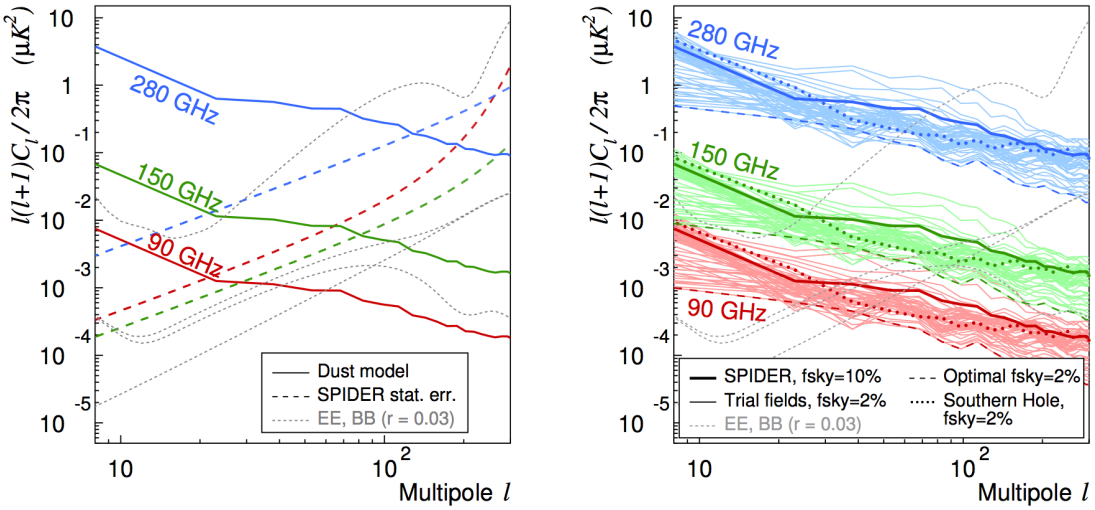


Figure 1.9: *Left*: A comparison of statistical noise, astrophysical and cosmological signals in each SPIDER band, assuming two SPIDER flights. *Right*: Galactic foreground emission for the nominal SPIDER field ($f_{sky} = 10\%$) and constituent trial fields with $f_{sky} = 2\%$. The optimal 2% of the sky has polarized dust emission that it an order of magnitude smaller than that of the nominal field. Figure from [36].

Large-scale ($\ell \leq 10$) polarized dust emission is expected to be at least an order of magnitude brighter than the $r = 0.03$ primordial B-mode spectrum at 90GHz. However, at the scales of most interest to SPIDER, the power spectrum of the dust is compatible with a power-law $C_\ell \propto \ell^{-2.6}$, which results in the amplitude being comparable to the B-mode signal at $r = 0.03$ at $\ell = 40$ [24]. The dust signal at 150GHz is an order of magnitude higher than at 90GHz.

One of the ways SPIDER will deal with this foreground is to select fields of view that are exceptionally clean of galactic emission. Our field of view will include the cleanest 2% of the sky accessible from a McMurdo flight, where the polarized dust emission is expected to be an order of magnitude less than the levels shown in the left panel of Fig. 1.9. Additionally, we expect that the next release of results from the Planck satellite will include maps of polarized dust emission, which we can then use in our data analyses to subtract this foreground.

### 1.5.3 Honorable Mentions

Spinning and magnetic dust have also been proposed as possible sources of polarized dust emission. The theoretical expectation for spinning dust is that its emission will be unpolarized [58]. However, the polarization of magneto-dipole emission from magnetic dust can be

quite high, even if the intensity of the magnetic dust is subdominant to that from rotating grains. One of the characteristics of magnetic dust is that its polarization direction will vary with frequency, and so should be able to be separated from the CMB signal [58]. We have not included spinning or magnetic dust in the SPIDER foregrounds model.

Other possible sources of polarized radiation are free-free emission and galactic carbon monoxide (CO). Free-free emission (caused by free electrons scattering off charged particles without being captured) is intrinsically unpolarized. It may become polarized by Thomson scattering at the edge of HII clouds. As the Galactic plane will be masked during the analysis of SPIDER data, we do not include polarized emission from free-free emission in our models. Galactic CO has an emission line at 230GHz from the J 2-1 transition. Although we don't know much about CO at high galactic latitudes, this line is well above the current SPIDER bands.

## 1.6 CMB Polarization Measurements

The detection of the CMB polarization power spectra is difficult due to the small signals and the presence of polarized foregrounds. This measurement has been the focus of several experiments over the past decade, with ever increasing levels of success.

The earliest detections of the E-mode polarization power spectrum were made by the DASI experiment in 2002 [56]. In the following decade, measurements of the E-mode spectrum were made by many other experiments (see Fig. 1.10).

Detections of the B-mode lensing signal were made in early 2013 by SPT [45] and Polarbear [4]. However, a detection of the B-mode signal from primordial gravitational waves was elusive until very recently. BICEP2 announced their detection of the primordial B-mode signal on March 17th, 2014 [5]. Their observed B-mode spectrum is well-fit by a $\Lambda$CDM model with $r = 0.2^{+0.05}_{-0.07}$, with no foreground subtraction. Using a likelihood ratio test to compare the best fit $r$ to the null hypothesis ($r = 0$) and assuming the expected shape of the B-mode spectrum from gravitational waves without subtracting foregrounds, BICEP2 rejects the null hypothesis at $7\sigma$. This result (see Fig. 1.11) and its confirmation of inflation has enormous implications for cosmology.

A confirmation of the BICEP2 result by an independent experiment is the most important next step for cosmology. SPIDER, a balloon-borne polarimeter designed to detect

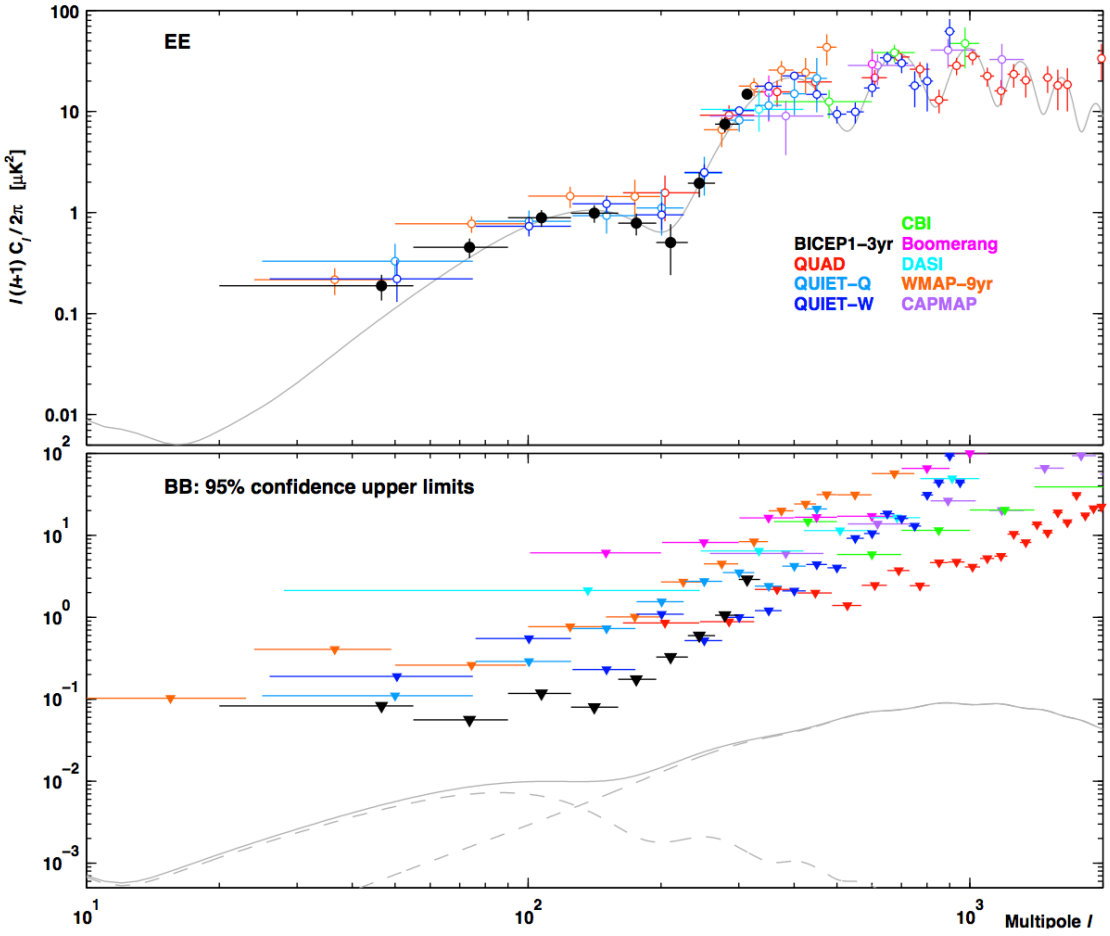


Figure 1.10: State-of-the-art measurements of the EE and BB spectra as of 2013. Theoretical spectra from an $r = 0.1$ $\Lambda$CDM model are shown for comparison. The BB curve shows both the inflationary gravitational wave and lensing components. Figure from [13].

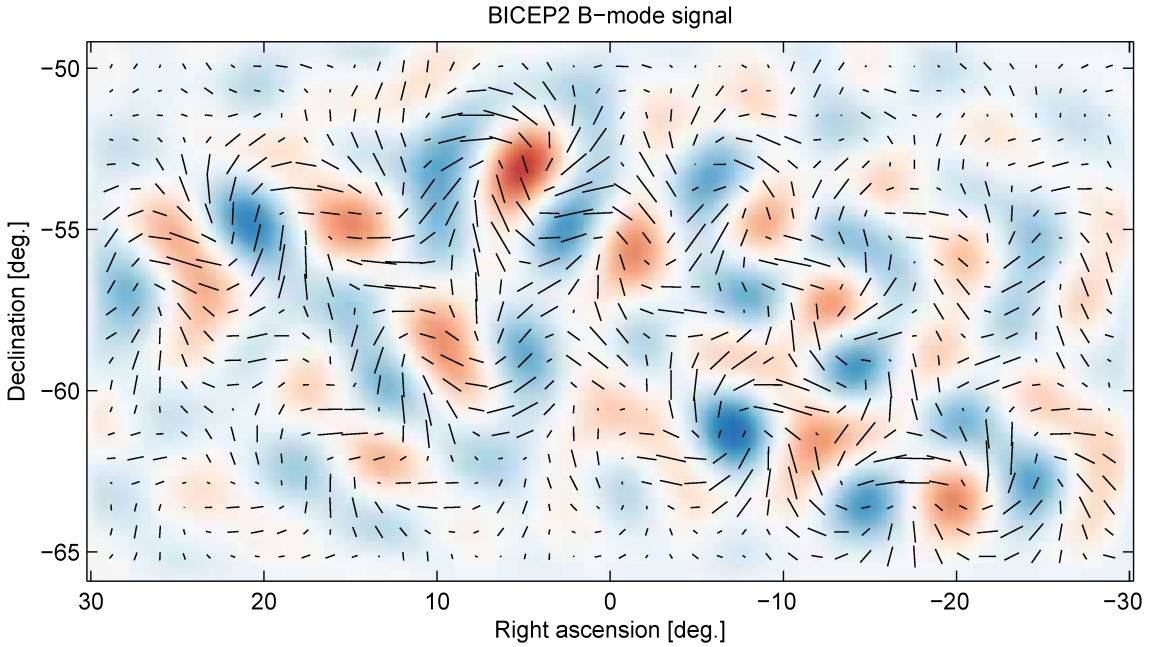


(a) The B-mode map observed by the BICEP2 telescope. The line segments represent the angle of the polarization on the sky. The faint "twisting" pattern seen here is the signature of B-mode polarization.

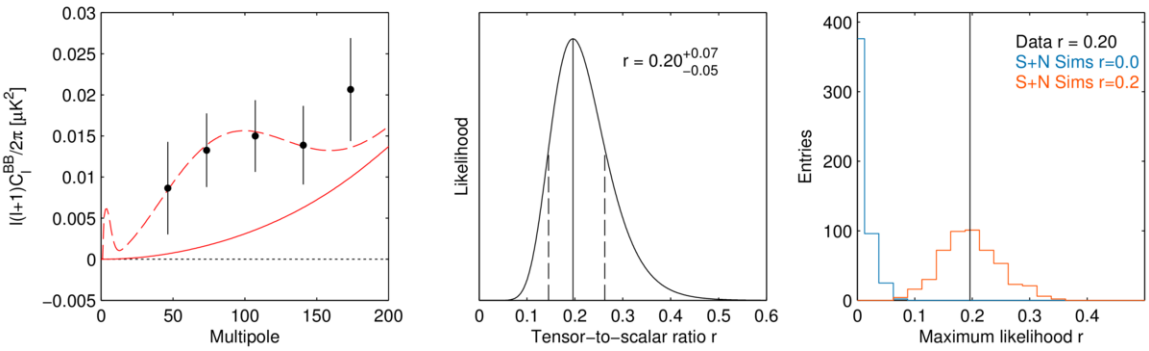


(b) *Left*: The BICEP2 bandpowers plotted with the maximum likelihood lensed-ΛCDM + $r$ = 0.20 model. The uncertainties are taken from that model and include sample variance on the r contribution. *Middle*: The constraint on the tensor-to-scalar ratio $r$. The maximum likelihood is indicated by the solid line and the ± 1 $\sigma$ interval is indicated by the dashed lines. Foregrounds have not been subtracted. *Right*: Histograms of the maximum likelihood values of r derived from simulations with $r = 0$ (blue) and $r = 0.2$ (red). The maximum likelihood value of $r$ for the real data is shown by the vertical line.

Figure 1.11: B-mode results from the BICEP2 experiment [5].

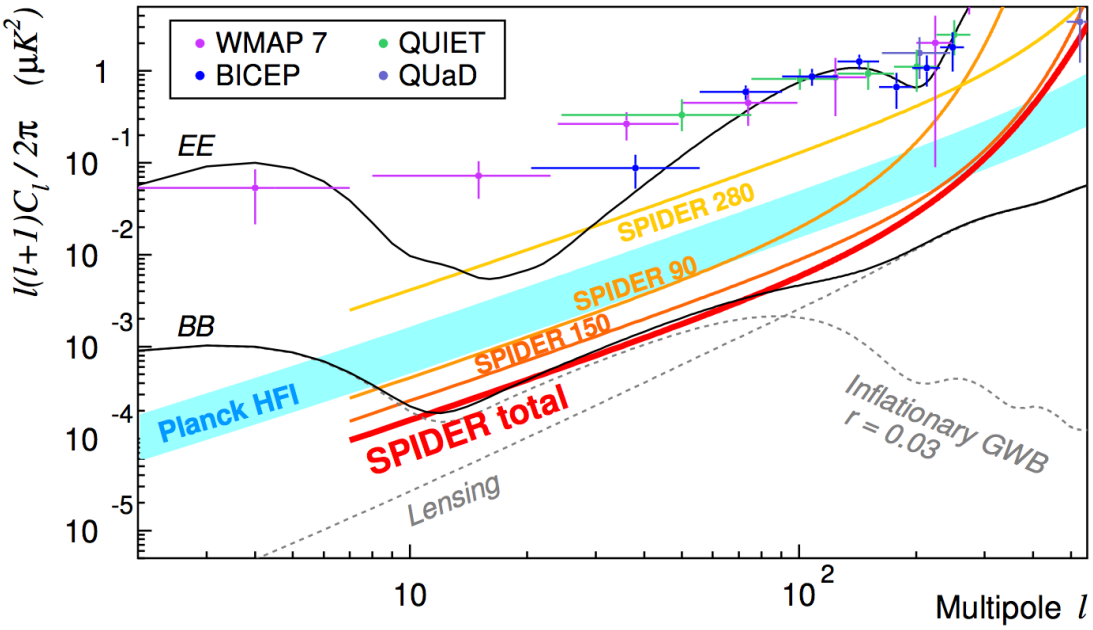


Figure 1.12: Projected statistical errors for SPIDER after two flights and Planck HFI. Theoretical spectra from an $r = 0.03$ ΛCDM model are shown for comparison. The BB curve shows both the inflationary gravitational wave and lensing components. The noise curves are derived from a simple Fisher model and assume that there is no foreground contamination. SPIDER is optimized to cover the $\ell \sim 80$ peak in the primordial B-mode spectrum. Figure from [36].

the primordial BB spectrum at the $r = 0.03$ level, is well-suited for this task. SPIDER uses similar detectors to the BICEP2 experiment, but will have 6 BICEP2-style telescopes on the sky. We expect the sub-orbital environment to result in improved sensitivity, and we will have an additional frequency band (90GHz) to help with foreground rejection. The SPIDER observing region is also largely non-overlapping with the BICEP2 observing region. In addition, we will observe a larger fraction of the sky, which allows us measure larger angular scales and will give us reduced sample variance, in comparison to BICEP2. Lastly, SPIDER's half-wave plate will allow for tight control of polarized systematics. A plot of how well SPIDER is expected to do in comparison to a $r = 0.03$ B-mode spectrum is shown in Fig. 1.12. SPIDER was designed to be a "B-mode machine" and so its data will the best and logical next step towards confirming BICEP2's revolutionary results.

# Chapter 2

# The SPIDER Instrument

## 2.1 Overview

SPIDER is a balloon-borne polarimeter that has been designed to measure the polarization of the CMB on degree scales in order to characterize the primordial B-mode power spectrum at a sensitivity of $r = 0.03$. It consists of six monochromatic, on-axis refracting telescopes contained in a shared-vacuum liquid helium cryostat (§2.2). Each SPIDER insert is a cryogenically cooled, azimuthally symmetric, two-lens refracting telescope (§2.3). Each of the telescopes will include a stepped rotation half-wave plate, which has been shown through simulation to reduce the contributions of many instrument systematics to negligible levels [62, 68] (§2.4). The whole system is cryogenically cooled to 4K, with $^3$He sorption fridges that further cool the detectors (§2.6) to approximately 300mK. SPIDER will scan the sky from a long-duration balloon launched from McMurdo Station, Antarctica(§2.9). The flight is expected to last 20-30 days. SPIDER will observe in two frequency bands to help discriminate between signals from the CMB and polarized foregrounds (§2.10).

Much of SPIDER's design is based on proven technologies that have been used in other experiments. The gondola and pointing are based on the successful BOOMERanG [27] and BLAST [72] balloon experiments. Much of the optical and telescope design is based on the highly successful BICEP1 [91] and BICEP2 [69] experiments. Our detectors are of the same style (photolithographed arrays of antenna-coupled TESs) as BICEP2. Unique challenges for SPIDER include the addition of monochromatic HWPs and the integration of an extremely large and complex cryostat. This chapter will describe each component of the SPIDER instrument.

## 2.2 The Cryostat

The SPIDER flight cryostat is one of the largest and most complex cryostats to have ever been built for a long-duration ballooning flight. The design of the flight cryostat was driven by the need to cool the six SPIDER telescopes to 4K for 20-30 days. Each telescope has an aperture of 30cm and is 1.3m long. These dimensions drove the size and scale of the cryostat, which weighs approximately 850 kg and is roughly 2.43m high and 2.04m in diameter. These numbers, as well as a detailed thermal analysis of the flight cryostat can be found in [41]. The SPIDER flight cryostat was built by Redstone Aerospace. Subsequent testing, characterization, and repair of the SPIDER flight cryostat have largely been the domain of the Princeton University arm of the SPIDER collaboration.

The roughly cylindrically shaped cryostat has five main components: a main tank, a superfluid tank, two vapor-cooled shields, and the vacuum vessel. These are illustrated in Fig. 2.1a. The main tank holds over 1200L of liquid helium. It is connected through a capillary system to the superfluid tank (SFT), which holds approximately 16L of superfluid liquid helium. The SFT will be pumped down and capped off prior to launch. At float, a valve will open to vent the SFT to ambient atmospheric pressure ($\sim$1 torr), which will maintain the pumping of the SFT. The SFT reaches temperatures of approximately 1.5K, which allows the closed-cycle $^3$He adsorption fridges to further cool the focal planes to 300mK.

As helium boils off in the main tank, it flows through two vapor cooled shields (VCS1 and VCS2). The enthalpy of this helium vapor provides additional cooling power. These shields surround the tanks and serve as radiation shields, protecting the main tank and the telescopes from warmer stages. By serving as baffles, the VCSs greatly reduce the liquid He consumption of the cryostat. The innermost vapor cooled shield (VCS1) sits at 30K during science operations; the outermost vapor cooled shield (VCS2) sits at 150K. These shields eliminate the need for a separate liquid nitrogen bath, as well as serving as thermal sinks for multi-layer insulation, filter blocks and heat exchangers.

Multi-layer insulation (MLI) is composed of alternating sheets of mylar and a thin insulating material (typically a white mesh or netting). It serves as a radiation shield and helps to reduce optical loading on the cryostat. The MLI is carefully installed in the flight cryostat such that it reduces compression of the MLI (which tends to thermally short the

mylar layers to each other) and also reduces the amount of gas that gets caught in the layers. If the pressure is sufficiently low, the heat conduction through the layers due to gas is negligible. The MLI "blankets" that must be installed on the front of the cryostat prior to cooling down must be carefully cut to fit around the telescope apertures. The installation of these blankets is painstaking and slow due to their proximity to many delicate parts (e.g., the shaders).

The thermal design of the SPIDER cryostat results in heat loads of 12mW, 550mW, 4W, and 9W on the superfluid tank, the main tank, VCS1 and VCS2, respectively [41]. The load on the superfluid tank is due to the closed-cycle $^3$He adsorption fridges that cool the focal planes. The heat loads on the other components are largely due to optical loading.

SPIDER is a balloon experiment, which imposes strict mass and mechanical requirements on the flight cryostat. In order to stay within the payload mass, most of the cryostat is made from aluminum 1100 and aluminum 5083. These alloys were chosen for their thermal and strength properties. The flight cryostat needs to have its lowest vibrational resonance frequency above 15Hz to avoid producing noise in the science band of the detectors. It also must be able to withstand 10g of parachute shock, since that is what we estimate it will sustain during the flight and termination. Additionally, there are requirements on the torsional and radial spring constants that are set by constraints on pointing and static deflections. A finite-element analysis of the SPIDER flight cryostat shows that the flight cryostat meets all of these requirements [41].

In addition to housing the SPIDER inserts, optics, and cryogens, the flight cryostat also provides the mounting surfaces for the multi-channel electronics (MCEs), MCE power supplies, housekeeping electronics crates, BLASTbus (which provides general-purpose analog and digital input/output), and HWP motor controller box. The bore-sight star camera and a set of batteries are also mounted on the top of the cryostat.

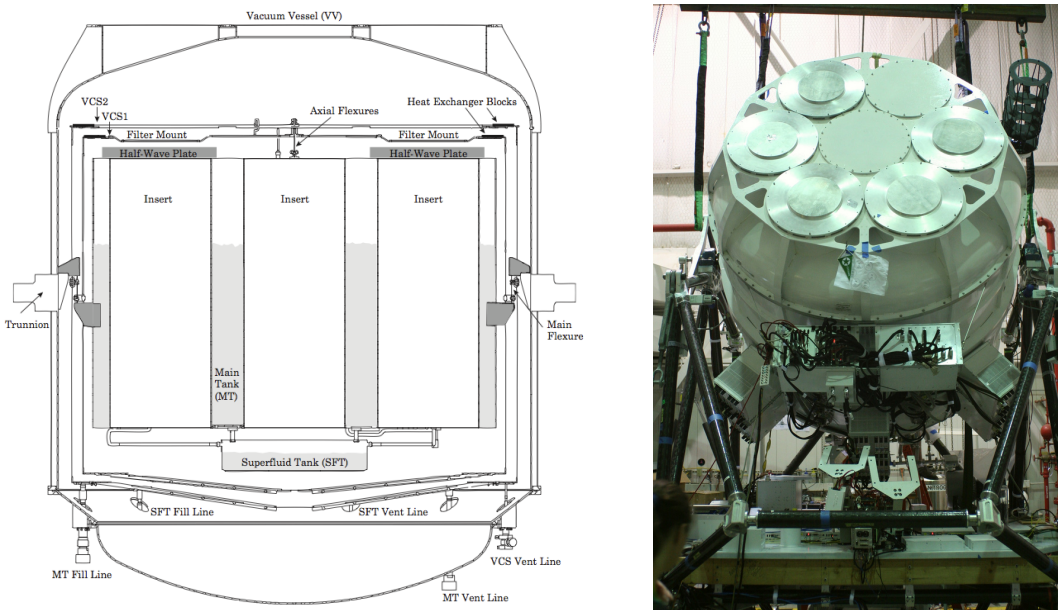


(a) Cross-section through the SPIDER flight cryostat (b) The SPIDER flight cryostat.

Figure 2.1: *Left*: Cross-section through the SPIDER flight cryostat. Shown are the five different stages of the flight cryostat: the vacuum vessel, the vapor-cooled shields (VCS1 and VCS2), the main tank, and the superfluid tank. All cryogenic ports are shown as they exit the cryostat at the bottom of the vacuum-vessel. The cryostat is attached to the gondola via the trunnions and an elevation drive (not shown). Figure from [41]. *Right*: The SPIDER flight cryostat mounted on the gondola in Palestine, TX at the Columbia Scientific Ballooning Facility. The center port is not meant for a telescope; it was created for mechanical convenience. During observation the flight cryostat will be nominally tilted at 40° elevation.

## 2.3 Inserts

Each SPIDER insert is a two-lens, on-axis refracting telescope, weighing approximately 100 lbs. The design of the SPIDER telescopes is extremely modular, allowing us to easily switch the telescope frequencies or repair the telescopes, should that be necessary after the first flight. The telescopes have been designed and built with the weight considerations of a balloon experiment in mind, so many of the components have been deliberately light-weighted or built from light-weight materials. Lastly, the entire telescope is cooled to 4K, so the choice of materials had to be balanced between the desire for a light-weight instrument and the need for appropriate values of the thermal conductivity such that the components cooled quickly.

The SPIDER telescopes have relatively small apertures (27 cm). This is motivated by our science goal of measuring the peak of the primordial B-mode spectrum, which peaks at angular scales of approximately two degrees. Our beam size is 30 arcminutes, which is small enough to detect this peak, although it is too large to capture some of the small-scale lensing features. One of the advantages of having small aperture telescopes is that they are easier to build and handle. This also allows us to build symmetric, on-axis telescopes rather than off-axis refracting telescopes, which is typically required for large apertures. This symmetric design makes us more robust to polarized systematics that can be caused by asymmetries in the optical chain. Small apertures also allow us to have simplified baffle designs. Lastly, they allow us to test the far-field of the optics in the laboratory, since $D^2/\lambda \approx 30$m (where $D$ is the diameter of the telescope and $\lambda$ is the central observing frequency of the telescope).

The number of inserts in the SPIDER system (6) is limited by the maximum weight and size of a ballooning payload. The telescopes are co-aligned, which increases the map depth by having more detectors observing the same patch of sky and helps to control systematics within the telescope.

A schematic of the SPIDER insert is shown in Fig. 2.2a. A photo of a completed insert is shown in Fig. 2.2b. The construction and testing of the six SPIDER inserts was the major responsibility of the Caltech portion of the SPIDER collaboration. More details about the design of the SPIDER inserts can be found in Runyan et. al. [78].

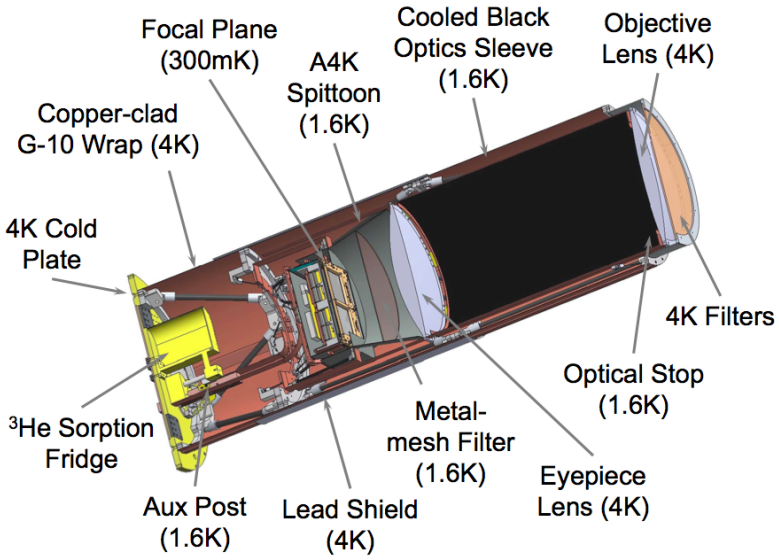


(a) A cross-section of the SPIDER insert Solidworks model, including the temperature at equilibrium. Figure courtesy of Marc Runyan.

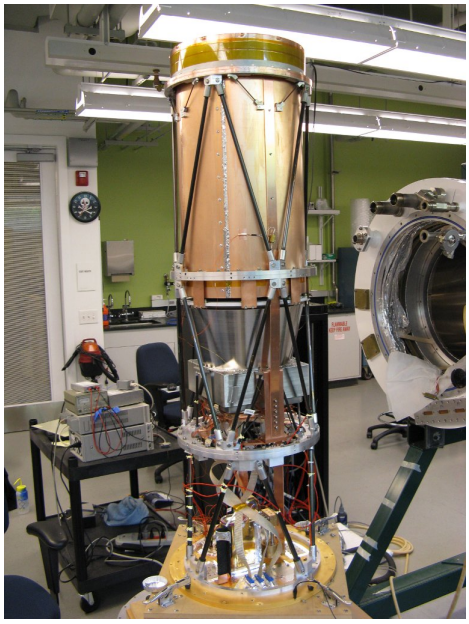

(b) A completed SPIDER insert, minus the copper-clad G10 wraps that cover the entire telescope. The black carbon fiber legs are visible around the outside of the telescope.

Figure 2.2: The SPIDER insert.

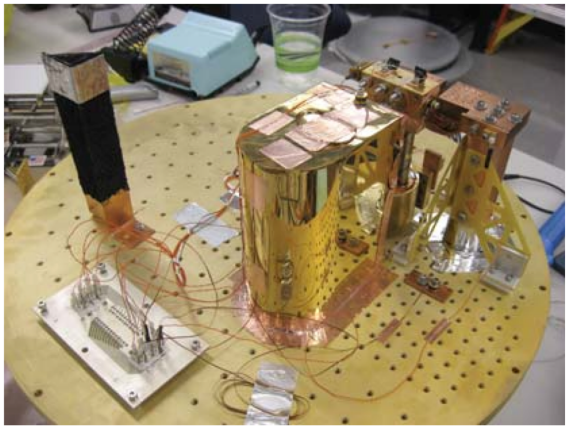

Figure 2.3: The SPIDER cold plate and mounted $^3$He sorption fridge. The aux post can be seen on the right side of the fridge. A charcoal covered post (a "getter") is the on the left side of the fridge.

### 2.3.1 Cold Plate

The base of each SPIDER insert is a gold-plated aluminum plate with thickness 0.5" and diameter 17.35". This plate also forms the interface to the cryostat helium tank, and so is known as the "cold plate." The $^3$He sorption fridge that cools the detectors to approximately 300mK is mounted directly to this plate, as is the truss structure that holds the focal plane and optical elements. The cold plate also includes a post that connects thermally to the superfluid helium tank, which is pumped down to achieve temperatures of 1.6K. This post (also called the "aux" post, since it connects to the auxiliary/superfluid helium tank) is thermally isolated from the 4K plate by G-10 standoffs and provides the condensation point for the fridge.

### 2.3.2 Truss

The truss supports the focal plane and optical elements above the cold plate. It is made from carbon fiber legs with aluminum end caps that attach each section of the truss to an aluminum ring. The aluminum rings provide the attachment points for most of the other telescope components. The bottommost part of the truss is called the camera truss. The camera truss used in the test cryostat is about four inches longer than the camera truss used in the flight cryostat. However, due to the interchangeable leg design of the truss, it is easy to swap out the carbon fiber legs for ones of a different length.

The decision to use carbon fiber was made early on in the development of SPIDER.

Carbon fiber has the advantages of being incredibly light and strong, as well as thermally isolating. It is also much cheaper than other materials that had been used for cryogenic structures in previous experiments (e.g., Vespel) [79].

### 2.3.3 Lenses

SPIDER's telecentric lens design is identical to that of the BICEP2 experiment [8]. The refracting design of the SPIDER telescopes requires an objective lens and eyepiece lens, whose surfaces are described by simple conics. The lenses are separated by 550mm, with an effective focal length of 583.5mm. This yields a plate scale of 0.98 deg/cm on the focal plane and a field of view of 20° [78].

The lenses were machined from thick slabs of high-density polyethylene (HDPE). These slabs were annealed in a programmable oven prior to machining to relieve any internal stress in the material. This annealing step was found to be necessary by the BICEP2 team, who found that the internal stress of the lenses caused deformities during the anti-reflection (AR) coating process. The rough cutting of the lenses was done by an outside shop. The rough cut lenses were shipped back to us for another annealing cycle prior to the final machining of the lens.

The final lenses are measured on a CMM machine to ensure that final shape and surface finish are within the allowable tolerances. The final shape of each lens is described by the conic lens equation, where the surface height $Z$ of the lens, in terms of the radius of curvature $R$, is

$$Z(R) = \frac{cR^2}{1 + \sqrt{1 - (1+k)c^2R^2}}, \tag{2.1}$$

where $c$ and $k$ are constants that determine the curvature.

The lenses are then AR coated with porous PTFE sheets made by Porex. These sheets

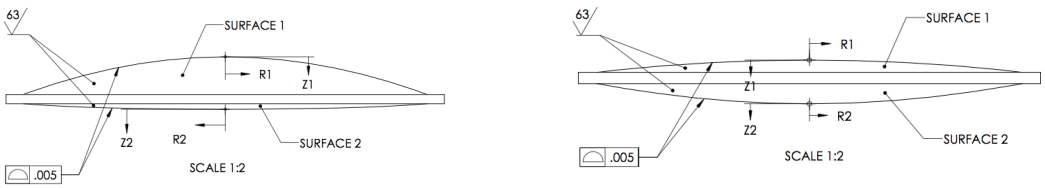


(a) Eyepiece (b) Objective

Figure 2.4: Diagrams of the SPIDER lenses.

Table 2.1: Material Properties for SPIDER optics.

Thickness and indices of refraction for lenses and AR coating materials.

| | $n$ | $d$ |
|---|---|---|
| HDPE | 1.52 | - |
| Nylon 6/6 | 1.75 | - |
| PM23DR (90GHz lenses) | 1.2 | 0.025” |
| PM23DR (150GHz lenses) | 1.2 | 0.016” |
| PM23JR (90GHz nylon filters) | 1.4 | 0.023” |
| PM23JR (150GHz nylon filters) | 1.4 | 0.015” |

are chosen to have an index of refraction close to the ideal of $n_{AR} = \sqrt{n_{lens}}$. The thicknesses are chosen such that they are nearly $\lambda/4n_{AR}$, to within the tolerances given by the manufacturer. Table 2.1 shows the indices of refraction and the thicknesses of the PTFE sheets used for AR coating.

Adhering the PTFE sheets to the curved surfaces of the lenses requires a specialized jig. After the surface preparation of the lenses, a thin sheet of low-density polyethylene (LDPE) and a thicker sheet of Porex are lightly taped to both sides of the lens. The lens is then set in a concave Teflon mold that has the exact shape of the lens. A silicone sheet is vacuum-drawn over the top surface of the lens to press the sheets smoothly across the surface and help the lens keep its shape while in the oven. The entire jig and lens is then put into a programmable oven (still under vacuum) for approximately 10 hours at 124° Celsius to melt the LDPE layer while remaining below the melting point of the HDPE lenses (130° Celsius). The AR coating process must be must be done carefully to avoid wrinkling the Porex or the LDPE underneath. The LDPE is typically pre-stretched with a separate jig prior to being taped to the lens. Additionally, the PTFE sheets pick up dust and dirt extremely quickly, so the whole AR coating process is best done with gloves and extremely clean working surfaces.

Early on in the creation of the SPIDER lenses, we found that the AR coating process was significantly changing the shape of the lenses (see Fig. 2.5). We eventually found that this was due to the fact that the AR coating mold was made from aluminum, which had a different coefficient of thermal expansion than the lenses and thus was actually a slightly different shape than the lenses at the temperatures necessary to bond the AR coating. A new jig made from Teflon was found to alleviate this problem.

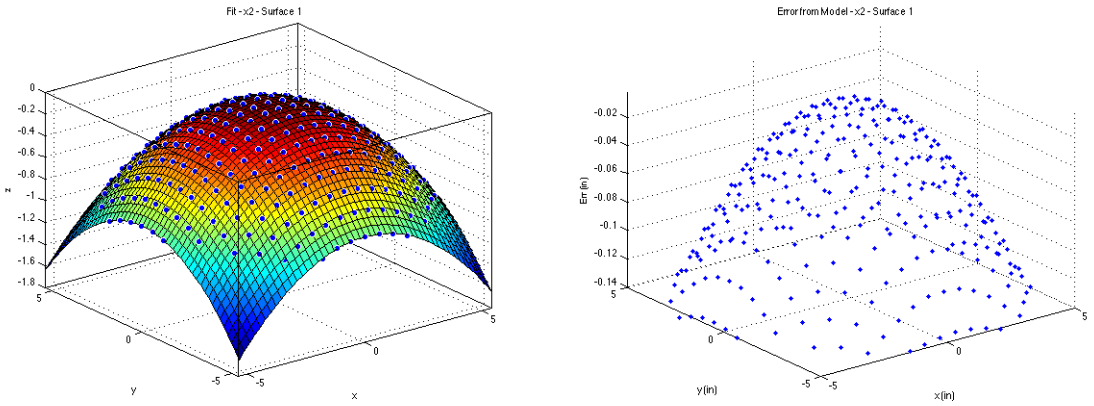


(a) (b)

Figure 2.5: *Left*: The results of fitting the CMM data from the X2 eyepiece to Eqn. 2.1. Units are in inches. *Right*: The error between the shape of the X2 eyepiece lens as measured and the ideal shape of the eyepiece lens. The distinctive "cup-like" shape of the error indicates that the lens is being warped (too convex) by the shape of the AR coating jig.

The AR coating for all of the flight lenses for SPIDER and many of the nylon filters was my responsibility. The process seems to be working well thus far. Many of the lenses have been through multiple cool downs and have so far shown no signs of delamination.

The HDPE lenses contract much more than their aluminum mounts when they are cooled. The HDPE contracts by approximately 2%, while the aluminum contracts by only 0.4%. This works out to a radial differential contraction between the lens and its aluminum support ring of approximately 0.1". In order to allow this contraction to happen while keeping the lens well centered (and not deforming the relatively soft plastic), we use copper flexures to attach the lens to the ring. There are eight of these flexures spaced evenly around the ring, as shown in Fig. 2.6.

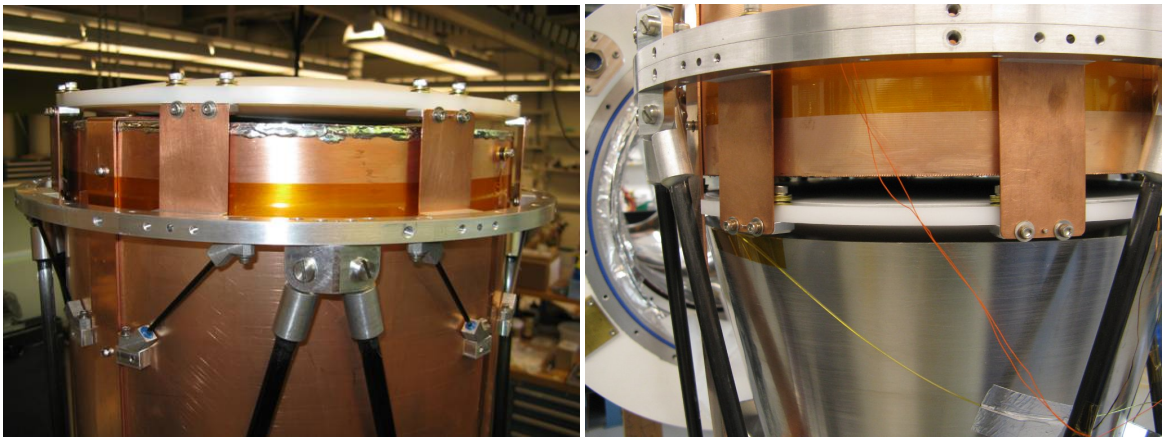

(a) (b)

Figure 2.6: Copper flexures holding the objective lens (left) and eye lens (right).

### 2.3.4 Cooled Optics Sleeve

The cooled optics sleeve is a blackened tube of aluminum that is capped with a stop-defining annulus just below the objective lens. It is suspended from the optics truss via a carbon fiber truss and is cooled to 1.6K via large copper thermal straps that connect to the superfluid helium tank. A sizable fraction of the power from the SPIDER beam terminates on this cold stop (approximately 25%). The cooled optics sleeve absorbs this sidelobe power and prevents it from escaping the cryostat. Cooling the sleeve allows us to reduce internal loading by approximately 0.3pW, which is on the order of the loading from the CMB and atmosphere at float, which we estimate to be $\sim$ 0.28pW per polarization at 150GHz.

The original design for the cooled optics sleeves used a riveted and soldered tube of copper-clad G10 as the base structure (Fig. 2.7b). To reduce reflections off the metal, these sleeves were lined with "steelcast," which is a combination of Stycast 2850, carbon lampblack, and 315 stainless steel powder. We added grooves in the steelcast while it was still soft in order to add surface roughness to the interior of the sleeves, so as to further reduce the effective reflection. The rough surface finish is desirable since any light that hits it and is not absorbed by the steelcast will be scattered inside the sleeve (where it may be absorbed by the steelcast on its second or third "bounce") rather than being reflected out of the stop. Measurements of the reflectivity of the steelcast, as applied to the sleeves, found that they were much more reflective than their design benchmark. This prompted the decision to add additional internal baffle rings to all the cooled optics sleeves. During the blackening of these baffles, some of the steelcast was made with charcoal, rather than

carbon lampblack. There was a concern that the charcoal would act as a helium getter while cold and then release the helium during fridge cycles or at low liquid levels. This prompted us to remake the optics sleeves.

The new iteration of the sleeve is made with an aluminum tube and internal baffle rings (Fig. 2.7a). The decision to switch to aluminum was made to ease the manufacturing process. The previous thickness of steelcast added to the tubes was found to be insufficient to reduce the internal reflections (power bouncing into the sidelobes) to less than 1%. This value has been calculated to unequivocally meet the sidelobe requirements in Fraisse et. al. [36]. Unfortunately, an enormous amount of steelcast is necessary to reduce the internal reflections to $\sim$1%, which poses several problems. The application of such a thick layer of steelcast is difficult to achieve and prone to cracking upon thermal cycling. Additionally, steelcast is quite heavy (which is always problematic for a mass-sensitive balloon experiment). Blackening each tube with the amount of steelcast required to meet our sidelobe benchmark would add an additional 8 kg per insert to the instrument. Alternative blackening methods, including the idea of blackening the interior of the cooled optics sleeve with HR-10, are still in development at the time of this writing.

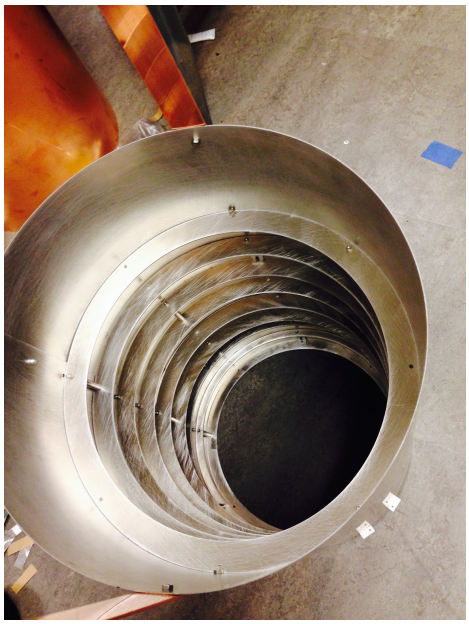

(a)

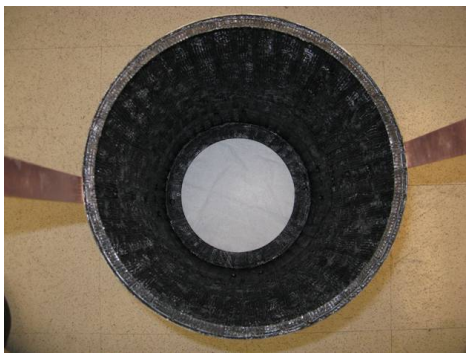

(b)

Figure 2.7: *Left*: The inside of the cooled optics sleeve prior to the application of the blackening material. The internal baffle rings are visible inside the tubes. The small blocks on the outside of the tube will connect to carbon fiber legs that suspend the cooled optics sleeve from the truss. *Right*: The inside of the blackened cooled optics sleeve. The sleeve is a previous design that did not include the internal baffle rings.

### 2.3.5 Magnetic Shielding

SPIDER is quite sensitive to magnetic fields, so magnetic shielding was an early focus of the Caltech group. The SPIDER detectors are susceptible to magnetic pickup due to the dependence of TES transition temperature on magnetic field strength [12], though we have never seen TES magnetic response in the lab. The dominant concern for magnetic pickup is the sensitivity of the SQUID readout system to changing magnetic fields. The SPIDER payload will move in the Earth's magnetic field in three axes (pitch, roll, and yaw) and in position during the flight, which makes it difficult to regress out a ground-fixed signal without filtering out large angular scales. One of the main advantages of a balloon-borne telescope is the relatively large sky fraction it will observe, which allows us to see larger angular scales than ground-based instruments. Clearly we would prefer not to filter them out. Ground-based instruments, in comparison, can accurately measure and subtract ground-synchronous modes from their data. Additionally, atmospheric fluctuations typically require ground-based instruments to filter out larger angular scales anyway, and so they will naturally filter out magnetic pickup.

The goal, then, is to shield the SPIDER detectors well enough that the pickup from the the Earth's magnetic field is well below the expected signal from the CMB. SPIDER's magnetic shielding scheme includes a superconducting niobium box that surrounds the detectors/read-out, secondary high-permeability and superconducting shields within the box (see Fig. 2.8b), the spittoon (see below and Fig. 2.8a), a superconducting lead sleeve centered on the focal plane structure, and Cryoperm shields that run the length of the helium tank.

The spittoon is one of the most visible elements of SPIDER's magnetic shielding scheme. It is made of Amuneal A4K, which is a high-permeability material. It is mechanically supported by carbon fiber rods that connect mechanically to the 4K plate. Its thermal connection is made through copper straps to the 1.6K ring. A picture of the spittoon can be seen in Fig. 2.8a.

A COMSOL model indicates that the magnetic shielding scheme is capable of providing shielding factors of greater than $10^8$ [78]. Additional shielding that is not in the model is estimated to provide an additional shielding factor of $\sim 50$. We have also measured the magnetic pickup in the lab and find that the shielding is at least this good. Since the

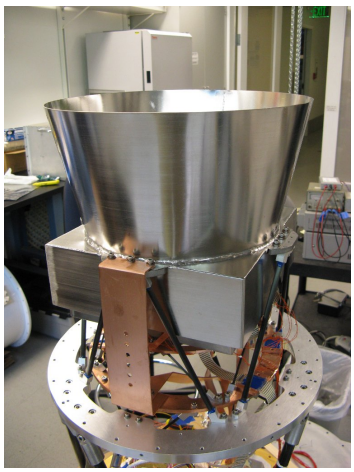

(a)

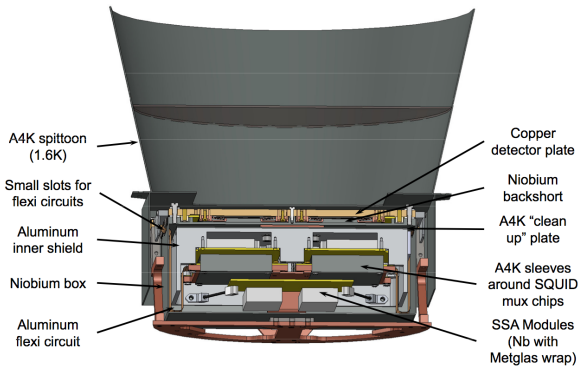


(b)

Figure 2.8: *Left*: A photo of the spittoon, as installed on the FPU. *Right*: A diagram of the cross-section of the SPIDER spittoon and FPU, with relevant magnetic shielding components labeled. The SSA modules are no longer installed inside the niobium box. They are now installed on the 2K ring outside the focal plane. Figure from [78].

shielding factor necessary for our flight is estimated to be $\sim 10^7$, the magnetic shielding factor is at least two orders of magnitude better than what is strictly necessary for our science goal (sensitivity at the $r = 0.03$ level). For more information about simulations involving the Earth's magnetic field, see [68].

### 2.3.6 Filters, Shaders, and Windows

Filtering is of special concern for a balloon payload, which needs to keep the optical loading on the detectors low in order to maximize the cryostat hold time. SPIDER utilizes a variety of filters and shaders [7] to reduce IR loading on the cryostat while maximizing the transmission of the frequencies of interest.

The spittoon contains a reflective hot-pressed metal-mesh filter (6 $\text{cm}^{-1}$ cutoff for the 150GHz band, 4 $\text{cm}^{-1}$ cutoff for the 90GHz band) [7]. This filter removes IR radiation above the SPIDER band that might otherwise couple to the antennas or TES islands. The aluminum cap (snout) at the top of each telescope contains an AR coated nylon filter (width 3/32") to help absorb IR radiation as well as an AR coated reflective hot-pressed metal-mesh filter (10 $\text{cm}^{-1}$ for both bands).

In addition to the filters in each SPIDER insert, we use a stack of reflective metal-

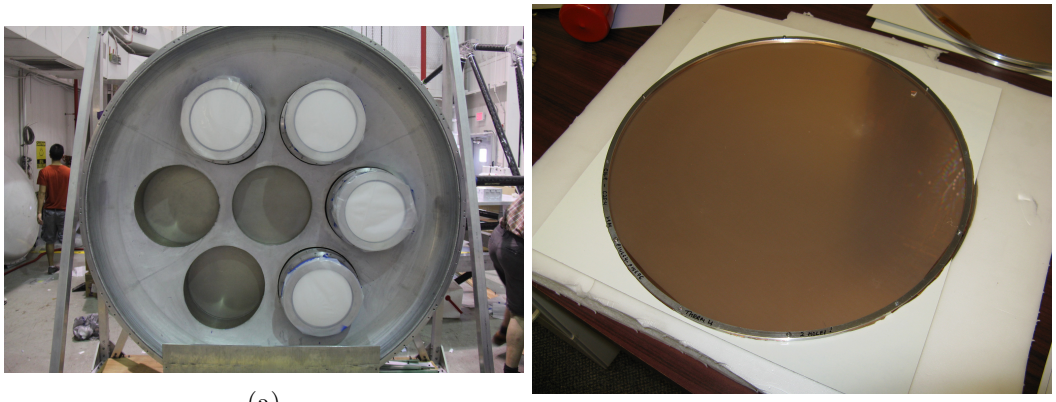

(a) (b)

Figure 2.9: *Left*: Flight windows installed in the top dome of the flight cryostat. Photo courtesy of Steve Benton. *Right*: A close-up of one of the IR shaders.

patterned mylar "shaders" on the VCSs to reduce the IR loading inside the cryostat [88]. An AR-coated nylon filter, a hot pressed filter (12 $cm^{-1}$ cutoff) and three IR shaders are installed at VCS1 (10K). Four IR shaders are installed on VCS2 (100K). One of the SPIDER shaders is shown in Fig. 2.9b.

The SPIDER windows are 1/8" thick slabs of AR coated ultra-high molecular weight polyethylene (UHMWPE). These thin slabs deflect by approximately 2.5" when they are pumped down and have been measured to have transmissions greater than 98%. A picture of four installed SPIDER windows can be seen in Fig. 2.9a.

## 2.4 Half-wave Plates

SPIDER's precise control of systematics will make it a very powerful B-mode instrument. The half-wave plate (HWP) is an important part of this control [22]. Our HWPs are cryogenic (mounted inside the cryostat) and mounted on a worm-gear-driven motorized ring that allows them to be stepped periodically. In flight the HWPs will be rotated by 22.5° daily. The rotation will allow each detector to independently measure the Stokes Q and U parameters, which will improve the fidelity of the reconstruction of the polarized signal. Since the HWP rotates the instrument polarization without rotating the beam, it will also reduce systematic effects due to beam asymmetry or differences between the beams in an A/B pair.

SPIDER's half-wave plates are constructed from single plates of birefringent single-

crystal sapphire, cut to a thickness such that the optical path length difference between waves polarized along its ordinary axis and extraordinary axes is exactly a half wavelength. This phase delay will cause linearly polarized light to rotate by exactly 90° as it passes through the plate. A perfect HWP will do this at any frequency. However, real HWPs are only perfect rotators of polarization at one frequency. (For a complete discussion of HWP non-idealities, see [23].) The thickness of the SPIDER HWPs has been chosen to correspond to the frequency at the center of the detector band.

Additionally, since real HWPs are made of materials that are at least partially reflective, our HWP design also includes a quarter-wave anti-reflection coating. A quarter-wave AR coating reduces the total reflectivity because the waves reflected from the front of the AR coating layer have a relative path difference of a half-wavelength from the waves reflected from the back of the AR coating layer. Thus the two waves will destructively interfere. These coatings are made of quartz for the 90GHz receivers and of Cirlex for the 150GHz receivers. The AR coating process for the 150GHz waveplates is a hot-pressed bonding similar to that used for the lenses in §2.3.3. The quartz coatings used for the 90GHz waveplates, on the other hand, cannot be bonded to the sapphire across the entire surface, as they are too fragile to survive the differential contraction that occurs upon cooling. Rather than a hot-pressed bonding, the AR coating process for the 90GHz waveplates uses a small drop of adhesive (Eccobond 24) in the center of the quartz to attach it to the sapphire.

The HWP optical stack is mounted to an Invar ring with bronze clips. This ring is attached to the aluminum main gear and bearing with flexible phosphor-bronze mounting tabs. The rotation mechanism consists of a rotor mounted in a three-point mechanical bearing rotated by a worm gear connected to a stepper-motor. (See Fig. 2.10). This mechanism was built with the design goal of being able to rotate the HWP with an absolute accuracy of $\pm 0.1$ degrees. The rotation is measured via optical encoders.

The initial characterization of the SPIDER HWPs was primarily done by our collaborators at Case Western Reserve University. They measured the millimeter-wave transmission spectra of the HWPs, both at room temperature and at cryogenic temperatures, and found that the HWPs were in excellent agreement with physical optics models. Additionally, their results indicated that the HWP non-idealities would not limit the SPIDER constraints on inflation [23]. Later tests of the HWPs were done in the SPIDER test cryostat and the flight cryostat.

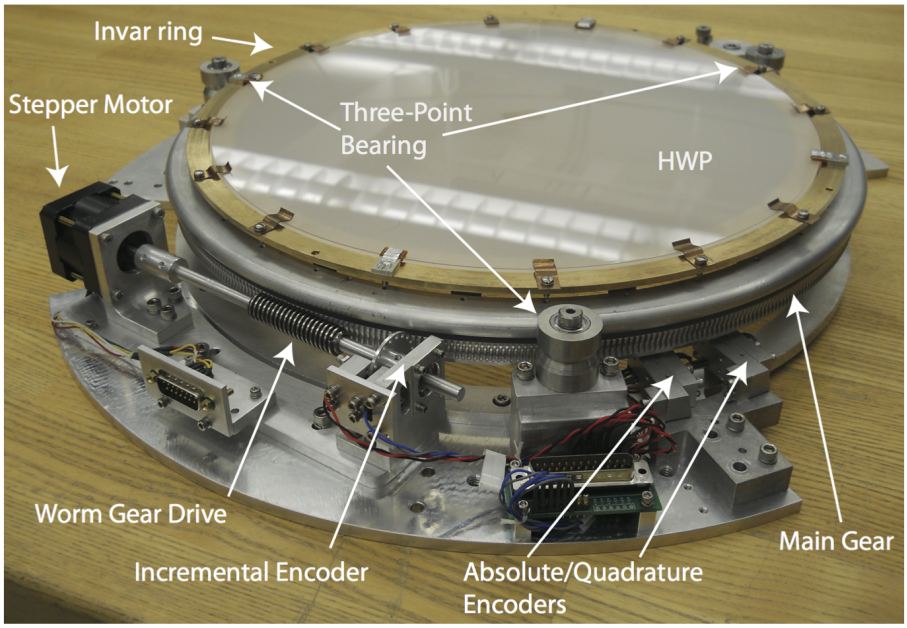


Figure 2.10: One of the SPIDER HWP rotation mechanisms with a 90GHz HWP installed. The HWP and AR coating are held onto the Invar ring with bronze clips. The Invar ring is attached to the aluminum main gear, which is turned on a three-point bearing. A cryogenic stepper motor turns the worm gear. Optical encoders monitor the rotation and verify that the HWP is at the desired angle. Figure courtesy of Sean Bryan [22].

## 2.5 Focal Plane

Early in SPIDER's development, the focal plane was extremely similar to the design used for the BICEP2 experiment. However, it was found that this architecture was not able to be adequately shielded from the Earth's magnetic field, due to the fact the magnetically sensitive SQUID multiplexer chips were placed on the same plate as the detector tiles and were insufficiently shielded. This finding prompted a redesign of the SPIDER focal plane, such that all of the SQUIDs could be placed inside a superconducting niobium box. More details about the redesign of the SPIDER focal plane design can be found in [78].

In the "RevX" design, the detector tiles are mounted onto a square gold-plated copper plate approximately 8.5" across. The tiles are registered to the plate with small pins and are held down by small beryllium copper clips. Hundreds of gold wire bonds connect the "gold picture frame" of the detector tiles to the gold-plated plate in order to thermally sink the detector tiles to the plate. The silicon detector tiles are covered (skyward) by quartz anti-reflection tiles to minimize reflections. Behind the detector tiles is a niobium backshort plate, spaced at $\lambda/4$ from the detectors by custom Macor space washers. The signal from

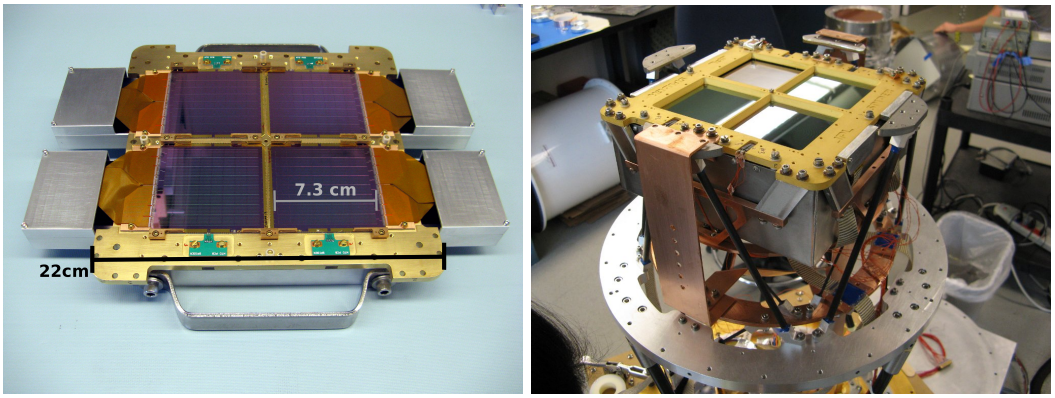


(a) (b)

Figure 2.11: *Left*: The SPIDER RevX focal plane, prior to installation. Here it is "anti-skyward" (it will be flipped over for installation). You can see four 150GHz tiles and the green circuit boards that read out the heaters and thermometry on the tiles. This FPU is only partially assembled; the SQUID chips are encased in boxes behind the FPU. *Right*: The SPIDER RevX focal plane, after installation. Note that the detector pixels are no longer visible, due to the AR tiles.

the detectors is fed into the niobium box that encloses all of the SQUIDs via extremely thin aluminum flexi circuits. Fig. 2.11a shows a picture of a Rev. X focal plane. The SQUIDs themselves are in their own shielded boxes at the end of the aluminum flexi circuits, inside the larger niobium box.

The FPU is supported by eight stainless steel heat capacity blocks, which provide the cooling path from the FPU to the 10 stp-liter $^3$He fridge (made by Simon Chase Research). This cooling path is purposefully designed to be slow, to thermally decouple the FPU from the fridge still. The fridges can hold the focal planes at approximately 300 mK for about two days before they need to be recycled. The heat capacity blocks connect the sides of the FPU to a copper ring. This FPU, blocks, and ring are all cooled to 300mK. They are supported by another copper ring cooled to 1.6K by the superfluid tank. This cooled ring is supported from a 4.2K aluminum ring with carbon fiber rods. This structure is visible in Fig. 2.11b.

There are four detector tiles on each SPIDER FPU. Each tile contains either an 8x8 (150GHz) or 6x6 (90GHz) array of dual-polarization pixels. Each pixel contains two antenna-coupled TESs - one for each polarization of light. To differentiate between the two polarizations in a pixel, they are frequently called the "A" and "B" polarizations (with "A" and "B" detectors), respectively. The tiles, TESs, and the readout system are described further

in §2.6 and §2.7.

## 2.6 TES Bolometers

The heart of the SPIDER system is the Transition Edge Sensor (TES) bolometer. Bolometers were invented in 1878 by the American astronomer Samuel Pierpont Langley [75]. They consist of a radiation absorber connected to a thermal reservoir (bath) via a weak thermal link. Any radiation that impinges on the absorber will heat it above the temperature of the reservoir. The more power absorbed, the higher the temperature will be. An attached temperature-sensitive resistor can read out the temperature of the absorptive element, and therefore how much power was incident upon it. The key advantages of bolometers are that they can be used to detect any frequency of radiation through an appropriate choice of absorber and that their sensitivity is ultimately set by the thermodynamic noise in the thermal link. A drawback of bolometers is that they are phase-insensitive (incoherent).

For the SPIDER system, polarized slot antennas receive radiation that is then summed in phase on a superconducting microstrip. The signal from the antennas passes through a band-defining LC filter and then is fed into a resistive gold meander (which dissipates the absorbed power as heat) on the bolometer island. The temperature-sensitive resistor is a Transition Edge Sensor (TES) [51]. The island on which the meander and the TES are located is suspended from the silicon tile via silicon nitride legs. These legs provide the weak thermal link between the TES island and the bath. The geometry and thickness of the legs can be tuned to provide a thermal conductance that meets the needs of the SPIDER experiment.

There are actually two transition-edge sensors (aluminum and titanium) in series on the island. This is because the the titanium TES saturates at room loading, so the aluminum TES is used for lab work while the titanium TES will be used in flight. All of their other optical properties are identical. Additionally, there are four TES detectors on each tile that are not bonded to antennas. These TESs are used a tracers of tile temperature changes and direct coupling to the TES island. The unbonded ("dark") TESs are typically located in outermost corners of the tiles.

The TESs are voltage biased by a small shunt resistor. When additional power on the island changes the TES resistance, there is a measurable change in current ($\Delta I_{TES} \approx$-

$\Delta P/V_{TES} \approx \Delta P/(I_b * R_{sh})$, see §2.6.2 for a more complete explanation), which is read out with the SQUID system (§2.7).

### 2.6.1 Microfabrication

The SPIDER detectors are fabricated at the Microdevices Lab at JPL. Each detector tile consists of an 8x8 or 6x6 array of dual-polarization pixels. Each pixel contains two TESs, which are coupled to slot-array, on-chip antennas. The TES sits on a suspended, thermally isolated nitride island. There are additional heater elements and NTD thermometry mounted on each tile. Fig. 2.12a shows a SPIDER pixel, including the antenna arrays, summing trees, and island. A close-up of the island can be seen in Fig. 2.12b.

The detectors are created photolithographically on silicon wafers that already have a thin layer of silicon nitride deposited on them. The components are built up in the following order:

- Aluminum TES - deposited by electron beam evaporation and patterned by liftoff.
- Protection layer ($SiO_2$) - deposited by RF sputtering.
- Titanium TES - deposited by sputtering and patterned by etching.
- Niobium ground plane - deposited by RF sputtering and patterned by liftoff.
- Interlayer dielectric ($SiO_2$) - deposited by RF sputtering.
- Gold meander - deposited by electron beam evaporation and patterned by liftoff.
- Niobium wiring and antenna pattern - deposited by RF sputtering and patterned by liftoff.
- Island and leg geometries - released through etching.
- Gold picture frame for heat sinking and gold layer on island - deposited by electron beam evaporation and patterned by liftoff.

A schematic of this process can be seen in Fig. 2.14. This process is as much an art as a science and many iterations were required to produce the flight-quality SPIDER detectors. This is, nonetheless, a vast improvement over the hand-assembly required for previous versions of polarized bolometers (e.g., feedhorn-coupled NTDs [39]).

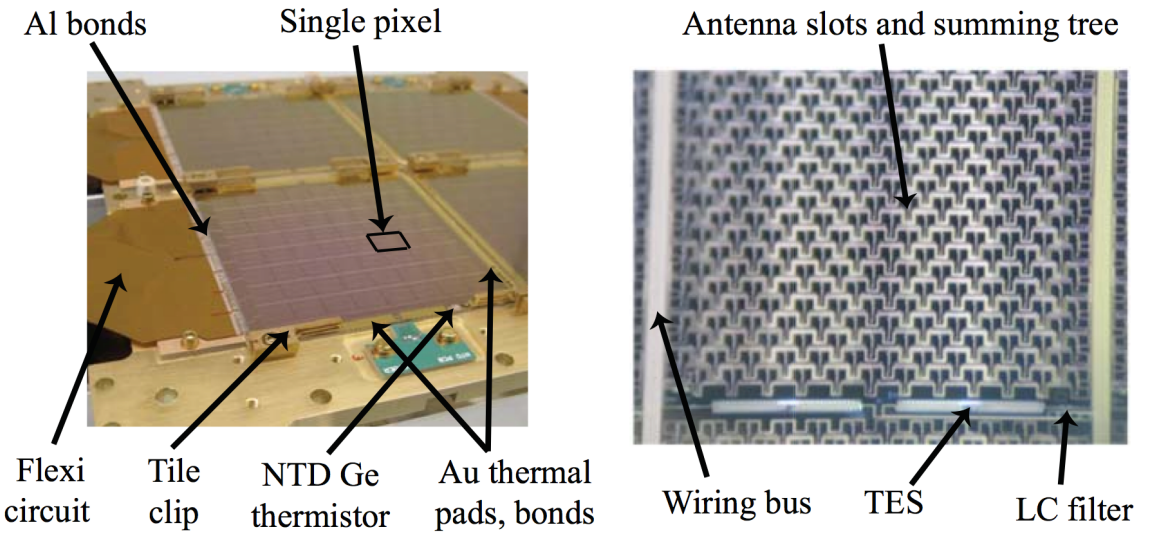


(a) *Left*: Four detector tiles installed in a SPIDER focal plane. The tiles are held mechanically by tile clips. The Au wire bonds thermally connect the tiles to the focal plane. The Al wire bonds electrically connect the detectors to the SQUID readout system via the aluminum Flexi circuits. Each tile has a NTD Ge thermistor to monitor its temperature. *Right*: A single detector pixel. A 150GHz pixel measures 7.8mm on a side; a 90GHz pixel measured 8.8mm on a side. Two interleaved phased array slot antennas cover most of the pixel. The signals from the antennas are summed in phase via a niobium microstrip summing tree. The signal passes through an LC filter before terminating on the TES island. Figure from [86].

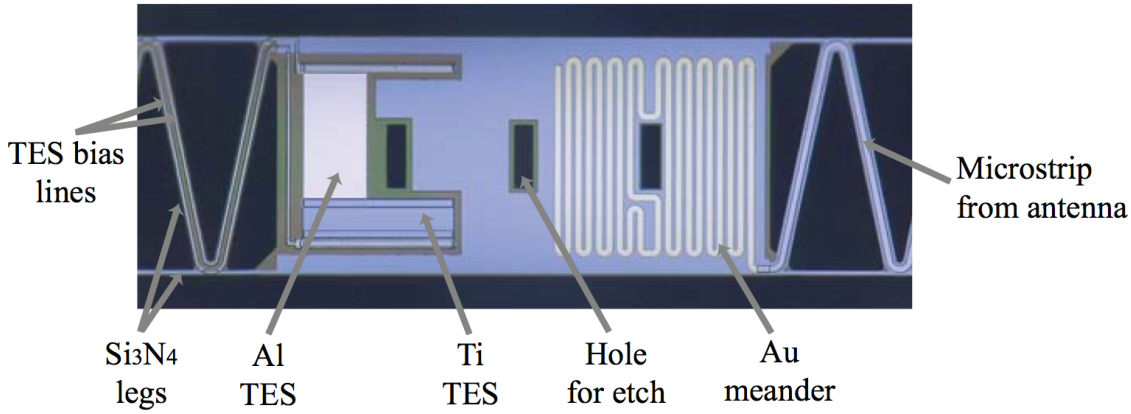


(b) An optical micrograph of the TES island, which measures 375$\mu$m by 150$\mu$m. The signal comes in through the microstrip on the right and terminate on the resistive gold meander. The TESs (Aluminum and Titanium, wired in series) measure the change in heat. The entire island is suspended by silicon nitride legs, which thermally isolate the island from the tile. Figure from [86].

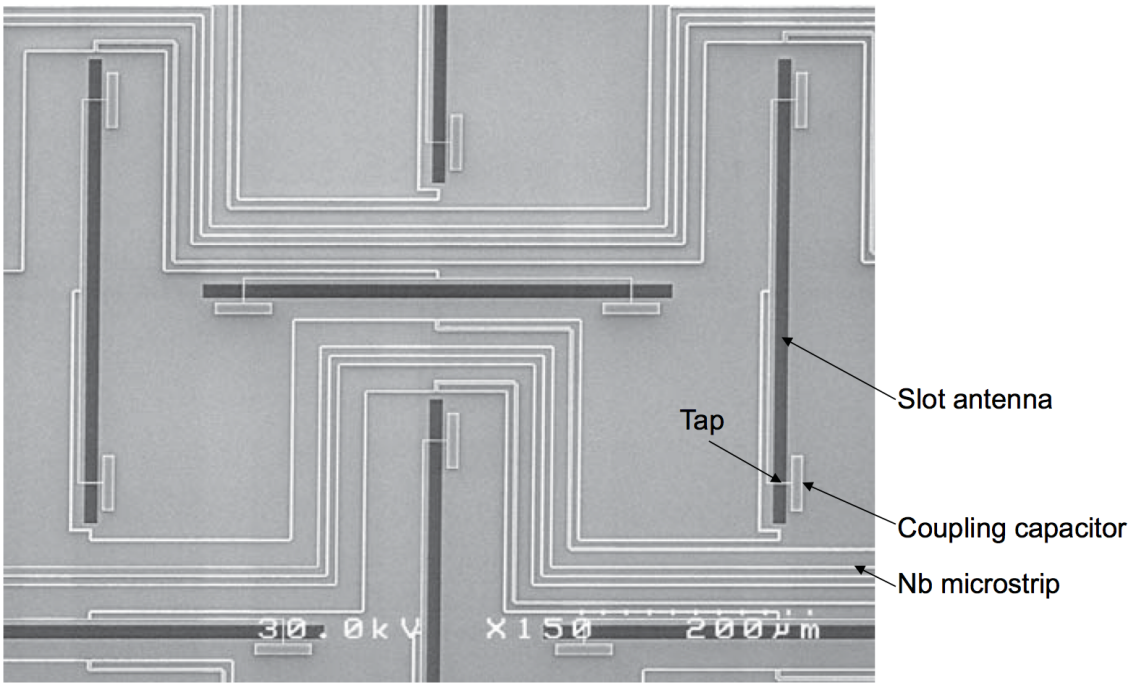


Figure 2.13: An SEM micrograph of the slot antennas and summing tree. Incoming radiation excited electric fields horizontally across the slots cut out of the niobium ground plane. Taps couple to this radiation and the tapped signal is added together in the niobium microstrip summing tree. Figure from [86].

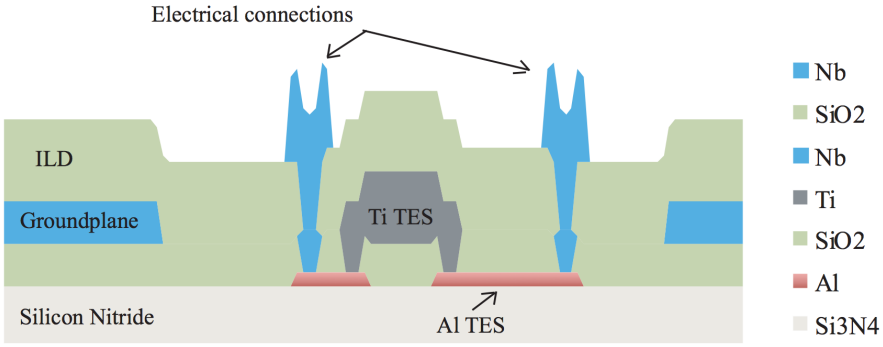


Figure 2.14: A diagram of a localized cross-section showing how the detector is built up in layers. The device shown here has not been released (thermally isolated). Figure from[86].

### 2.6.2 Bolometer Theory

#### 2.6.2.1 Thermal Model

At equilibrium, a bolometer can be described by

$$P_{Joule} + Q = \int_{T_{bath}}^{T} G(T)dT, \tag{2.2}$$

where $Q$ is the power incident on the detector, $P_{Joule}$ is the electrical power dissipated in the detector, and $G(T)$ is the thermal conductance to the thermal bath. The term on the right hand side of the equation represents the power dissipated through the legs of the island.

By using the following equation for the thermal conductance,

$$G(T) = G_0 \left(\frac{T}{T_0}\right)^{\beta}, \tag{2.3}$$

and integrating the right hand side of Eqn. 2.2 we get the following equation for the power flowing through the island legs:

$$P_{legs} = \frac{G_0 T_0}{1+\beta}\left[\left(\frac{T_{TES}}{T_0}\right)^{1+\beta} - \left(\frac{T_{substrate}}{T_0}\right)^{1+\beta}\right]. \tag{2.4}$$

Here the value of the thermal conductance $G_0$ depends on the reference temperature $T_0$. Common choices for $T_0$ are $T_0 = T_c$, the transition temperature of the TES (∼500mK) and $T_0 = 450$mK, which is a temperature at the scale of interest. The thermal conductance is fundamentally a function of the geometry and materials used to make the legs. Typical

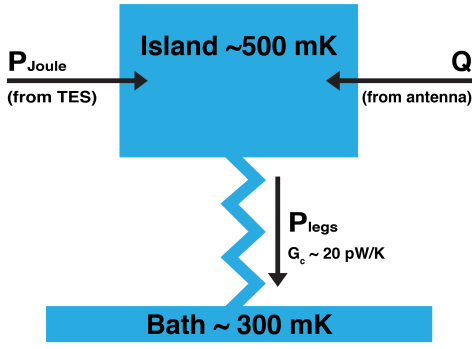


Figure 2.15: Thermal diagram for TES circuit.

values for $\beta$, which describes the strength of the power law of the thermal conductance, are 2.0-2.5. The derivatives of Eqn. 2.4 are quantities that are can be measured in the SPIDER system:

$$\frac{dP_{legs}}{dT_{TES}} = G\left(\frac{T_{TES}}{T_0}\right)^{\beta}. \tag{2.5}$$

When the TES is on transition, by definition the temperature of the TES is the same as its transition temperature, $T_{TES} = T_c$. If we choose $T_0 = T_c$, then the above equation simplifies to

$$G_c = \frac{dP_{legs}}{dT_{TES}}. \tag{2.6}$$

The quantity $dP_{legs}/dT_{TES}$ is can be measured in the SPIDER system by varying the temperature of the focal plane and using Eqn. 2.2 to calculate the corresponding power through the legs. This measurement then lets us determine the thermal conductance of the island legs. Note that the transition temperature of the TESs is a property of the thin films used to make the detectors, not of the thermal conductance of the legs. Because of this, we instead generally choose $T_0 = 450$mK, which allows us to quote a value of the island thermal conductance that is independent of the TES.

#### 2.6.2.2 Electrical Model

None of the discussion in §2.6.2.1 is specific to the TES detector. A transition edge sensor is a type of detector that exploits the strongly temperature-dependent resistance of superconducting materials. The TES detector operates in the very narrow transition region where the metal goes from its normal resistance to zero, which is an extremely steep function of the temperature. The sharp phase transition makes the TES an extremely sensitive thermometer.

Although the TES detector was invented in the 1940s [11], it did not become widely used until techniques to achieve stable operation in the transition region were developed in the 1990s. (An additional problem was matching the noise of the TES to the noise of readout amplifiers. This was largely eliminated through the use of SQUIDs, which are covered in the next section.) The SPIDER TESs are maintained at their transition temperature via voltage biasing, which takes advantage of negative electrothermal feedback. This technique was proposed by Kent Irwin [50] and the following discussion follows the seminal Irwin and Hilton review paper [51].

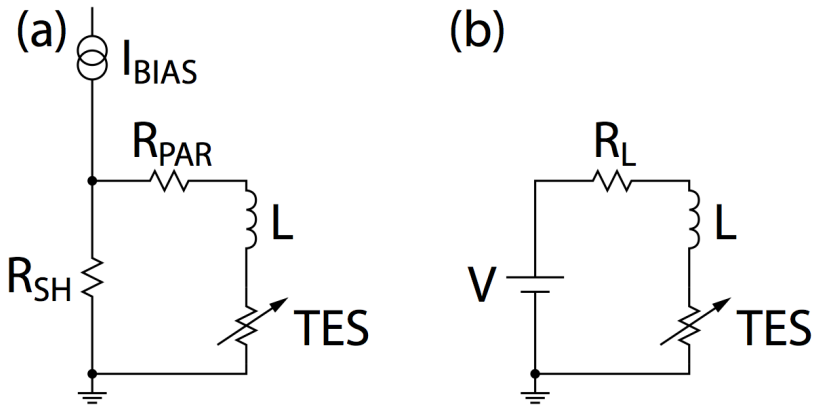


Figure 2.16: *(a)* A schematic of a simplified TES circuit. The shunt resistor $R_{SH}$ voltage biases the TES resistor $R_{TES}$, which is in series with the inductor $L$, which includes the SQUID and any stray inductance, and a parasitic resistance $R_{PAR}$. In the SPIDER system, the shunt resistor is located on a separate Nyquist chip, along with an additional inductor. *(b)* The Thevenin-equivalent circuit model used for the equations in this section. A bias voltage $V$ is applied to the load resistor $R_L = R_{SH} + R_{PAR}$, the inductance L, and the TES resistance $R$. Figure from [51].

The response of the TES is governed by two coupled differential equations that describe the electrical and thermal response of the circuit. The electrical differential equation that characterizes the TES circuit is

$$L\frac{dI}{dt} = V - IR_L - IR(T, I). \tag{2.7}$$

Here, $L$ is the electrical inductance, $I$ is the current, $V$ represents the bias voltage $I_{bias}R_{SH}$, $R_L$ is the resistance of the inductor, and $R(T, I)$ is the resistance of the TES, which generally depends on both the temperature and current. A schematic of the TES circuit is shown in Fig. 2.16.

The corresponding thermal differential equation is

$$C\frac{dT}{dt} = -P_{bath} + P_{Joule} + Q, \tag{2.8}$$

where $C$ is the heat capacity, $P_{bath}$ is the power lost to the bath, $P_{Joule}$ is the joule power dissipated in the TES, and $Q$ is the optical power incident on the detector.

The coupling between these two equations comes from the term for joule power:

$$P_{Joule} = I^2 R(T, I). \tag{2.9}$$

For small signals, the resistance of the TES can be expanded to first order as

$$R(T, I) \approx R_0 + \left.\frac{\partial R}{\partial T}\right|_{I_0} \delta T + \left.\frac{\partial R}{\partial I}\right|_{T_0} \delta I, \tag{2.10}$$

where $\delta I = I - I_0$.

Using the expression for the unitless logarithmic temperature sensitivity,

$$\alpha_I = \left.\frac{\partial \log R}{\partial \log T}\right|_{I_0} = \frac{T_0}{R_0}\left.\frac{\partial R}{\partial T}\right|_{I_0} \tag{2.11}$$

and current sensitivity

$$\beta_I = \left.\frac{\partial \log R}{\partial \log I}\right|_{T_0} = \frac{I_0}{R_0}\left.\frac{\partial R}{\partial I}\right|_{T_0}, \tag{2.12}$$

we can rewrite Eqn. 2.10 as

$$R(T, I) \approx R_0 + \alpha_I \frac{R_0}{T_0}\delta T + \beta_I \frac{R_0}{I_0}\delta I. \tag{2.13}$$

This equation shows the dependence of the TES resistance on both the temperature and the electrical current. A change in temperature on the TES island is transformed into an electrical current via the change in the resistance of the TES. The electric current in the TES is transformed into a temperature signal via Joule power dissipation in the TES. This process is known as electrothermal feedback (ETF) and it arises from the cross-terms in Eqn. 2.7 and Eqn. 2.8.

Electrothermal feedback (ETF) can be either positive or negative. When the circuit is voltage biased ($R_0 >> R_L$), the joule power $P_{Joule} = V^2/R$ decreases with increasing resistance and so the feedback is negative. There are several advantages to being in this regime. Negative ETF linearizes the detector response and increases the dynamic range. The TES is stable against thermal runaway even when the loop gain is high. The TES self-biases in temperature within its transition (over a certain range of signal powers and biases). Negative ETF also makes the bolometers much faster than the natural thermal time constant, which allows the detectors to recover quickly from cosmic ray hits and electronic

glitches.

The natural thermal time constant is given by

$$\tau = \frac{C}{G}, \tag{2.14}$$

while the electrical time constant (in the limit of low loop gain) is given by

$$\tau_{el} = \frac{L}{R_L + R_{dyn}}, \tag{2.15}$$

where $R_{dyn}$ is the constant-temperature dynamic resistance of the TES:

$$R_{dyn} \equiv \left.\frac{\partial V}{\partial I}\right|_{T_0} = R_0(1 + \beta_I). \tag{2.16}$$

Approximate values for the thermal, electrical, and ETF time constants are $\tau \sim 50$ ms, $\tau_{el} \sim 0.5$ ms, and $\tau_{ETF} \sim 3$ ms.

## 2.7 SQUIDS

SPIDER is read out with a three-stage SQUID time-domain multiplexer made by NIST [29]. Superconducting QUantum Interference Devices (SQUIDs) are superconducting magnetometers. They can be made to measure current by coupling them to the inductor in the TES circuit shown in Fig. 2.16. SQUIDs rely on the quantum mechanical effect of flux quantization and Josephson tunneling. A DC SQUID has two Josephson junctions in parallel in a superconducting loop. In the absence of any external magnetic field, the current splits down the two branches equally. When an external magnetic field is applied, a small screening current begins circulating in the loop, in the direction that will apply an opposite flux to cancel out the one from the external field. This screening current is in the same direction as $I$ in one half of the loop ($I_{upper} = I + I_s$) and the opposite direction in the other half of the loop ($I_{lower} = I - I_s$).

The flux enclosed by the superconducting loop must be an integral number of magnetic flux quanta $\phi_0$. If the external magnetic field is increased until it is half of the magnetic flux quantum, $\phi_0/2$, the SQUID will energetically prefer to increase it to $\phi_0$ rather than screening the external field. The screening current will therefore switch direction to make

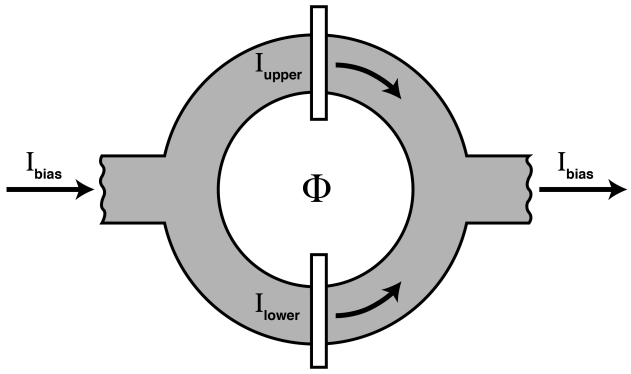


Figure 2.17: SQUID loop.

that happen. The screening current will continue to switch directions every time the external field is increased by $\phi_0/2$, and the critical current will oscillate as a function of the applied flux.

Typically the SQUID is biased by a current $I_b$ such that the critical current of the Josephson junction is exceeded and a voltage develops across the SQUID. This voltage will be a function of the applied magnetic field with a period equal to $\phi_0$. This voltage can be used to monitor the applied magnetic field. In practice, the current from the TES is fed into an input coil, which creates a magnetic field that is coupled to a SQUID loop. A feedback loop cancels the change in SQUID flux, which linearizes the readout. An additional inductor on a separate chip (the Nyquist chip) has an inductance of $2\mu$H. This inductor also serves as a low-pass L/R filter for SQUID and detector noise. The Nyquist chip is in series with the TES detector and also contains the shunt resistor.

The SPIDER system (like other experiments which utilize large arrays of bolometers) is a challenge to read out due to the fact that there are 512 TESs per insert, which means there are thousands of TES and SQUID wires. Each wire generates heat (through Joule heating) and also conducts heat from higher temperature stages within the system, which is problematic when trying to keep the focal plane at sub-Kelvin temperatures, so we multiplex the SQUIDs in the time domain to reduce the number of wires. Other similar systems use frequency domain multiplexing, in which each channel is impressed on its distinct carrier frequency and then demodulated at room temperature.

A single SQUID has a low source impedance ($\sim 1\Omega$), so there is a poor match between

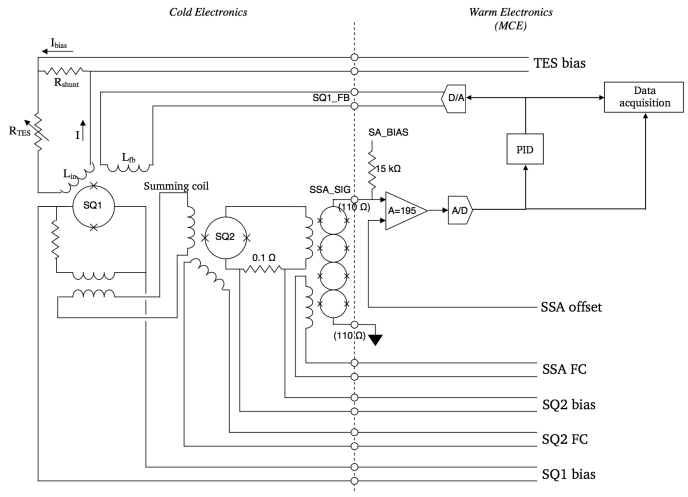


Figure 2.18: Circuit diagram for the SQUID read-out system. All of the components on the left side of the diagram are located inside the cryostat and so are cryogenically cooled. All the components on the right side of the diagram are outside the cryostat, at room temperature. Time domain multiplexing is achieved by switching the SQ1 bias lines at kHz frequencies. Adapted figure courtesy of Randol Aikin. Original figure can be found at `http://www.phas.ubc.ca/ mce/mcedocs/system/`.

a single SQUID and a room temperature (300K) amplifier, resulting in poor signal to noise. This is resolved by having three stages of SQUIDs (see Fig. 2.18 for an overview of the system). The final stage of the SQUID chain, the SQUID Series Array (SSA), has 100 SQUIDS in series per channel, which increases the source impedance to $100 - 200\Omega$.

The SQUIDs are contained on MUX chips provided by NIST. The signal from a bolometer is low-pass filtered and then fed into the input coil of the first stage of SQUIDS (SQ1). The 33 SQ1s on the chip read out 32 TESs that are biased in series - the additional SQUID is left "dark" to monitor drifts and common-mode magnetic pickup. The first stage SQUIDs feed into one summing coil. Time domain multiplexing requires that we bias only one row of the SQ1s at a time and read out all of the columns. The wire count is further reduced by biasing the SQ1s in different columns in series. The common SQ1 feedback for each row means that 33 readout cycles are needed to capture the full array. The SQ1 summing coil feeds flux to a second stage SQUID (SQ2) for each of the 16 columns in a FPU. Each SQ2 feeds out a final SQUID Series Array amplifier (SSA).

All of the biasing and timing of the SQUID circuits ("tuning") is handled by the Multi-Channel Electronics (MCE) crate made by the University of British Columbia. A process we call SQUID tuning sets the biases for each SSA, SQ2 and each row of SQ1s, and also

measures SQUID periodicities. In addition to handling the SQUID system, the MCE also handles TES biasing. Part of the tuning process for the SPIDER system includes choosing a single TES bias for all TESs in a column that gets as many detectors as possible on transition. A more complete description of the SQUID tuning process can be found in [21].

## 2.8 Multi-Channel Electronics

The TES detectors and SQUIDs are read out via a warm multi-channel electronics box (MCE) developed by the University of British Columbia. The MCE was originally designed for the SCUBA2 experiment and has since been used by BICEP2, the Keck Array, and SPIDER [14]. The MCE provides time-domain multiplexing of the SQUIDs and can read out over 500 channels at up to 20kHz. It uses FPGA-based processing with upgradeable firmware.

The MCE crate contains a number of individual cards that each provide a specific function. The address card switches SQ1 biases on and off for each row every $\sim 2\mu$s. There are two bias cards that provide low-noise DC biases to the SQ2s, SSAs, and TES feedbacks and biases. There are two readout cards that provide the SSA bias and readout across the SQUID rows. These values are then passed to a clock card which assembles the data frames and communicates with the outside world.

The data read out by the MCE is a 14-bit readout of the SSA voltage (the error signal). A digital PID loop calculates the feedback voltage to apply to the detector bias at a $\sim$15kHz revisit rate. The data is recorded at several hundred Hertz after downsampling and filtering. There is one MCE crate per insert; a crystal clock ("sync box") synchronizes the MCEs for all of the SPIDER inserts. The sync box also synchronizes the data acquisition on the gondola with the MCEs by providing regular synchronizing pulses and frame number time stamps.

Digital control and readout of the MCE is done through a fiber link to a dedicated Linux computer on board the payload. A library of scripts run by the flight computer implement the SQUID tuning algorithm and control the various biases and flux feedbacks.

## 2.9 Ballooning

One of SPIDER's strengths is its sub-orbital platform - a long-duration balloon. Ground-based instruments are limited by atmospheric fluctuations that generally require filtering out large angular scales. Additionally, the water vapor in the atmosphere emits in the microwave bands that are of interest to CMB experiments. While occasionally risky, ballooning allows SPIDER to get above the vast majority of Earth's atmosphere. At float, SPIDER will fly at approximately 32km above the ground. This is above 99% of the water vapor that is in the Earth's atmosphere (mostly in the troposphere). Moreover, the lack of atmosphere will greatly reduce the photon loading on the detectors. Photon noise (§3.9) is expected to be our dominant source of noise on the detectors and therefore the limiting factor on detector sensitivity. Reduced photon noise will vastly improve our mapping speed.

Sub-orbital balloons also have a rich heritage as prototypes for satellite missions. Many of the demands of a sub-orbital balloon flight, such as constraints on the mass and power of the payload, the need for autonomous operation, and the need for tight control of systematics, are directly comparable to the demands of a satellite mission. Operation under space-like loading and environmental conditions is also important for satellite prototyping. SPIDER-like detectors have been proposed for a number of CMB satellites, and SPIDER will serve as a pathfinder for those missions.

The ballooning program is run by NASA's Columbia Scientific Ballooning Facility. SPIDER will launch from McMurdo, Antarctica and will fly for 20-30 days. In flight, our ability to command the pointing systems or detectors will be minimal due to the limited bandwidth of the telemetry available. SPIDER's ability to receive and send information after "line-of-sight" (the initial 12 hours of the flight when the bandwidth is highest) will be especially limited, since it was determined during integration that SPIDER is especially sensitive to RF pickup from the telemetry. It is likely that during much of the flight we will be able only to read out the pointing and thermometry information, as well as a single detector. Therefore, SPIDER has been designed to be run autonomously with minimal commanding from the ground.

The seasonal circumpolar winds in the Antarctic continent will allow the balloon to fly in a large loop over the continent. This weather pattern allows us to have a fairly long flight without flying over the ocean and to terminate the balloon flight in a convenient place on

the continent. When the flight is over, SPIDER will separate from the balloon and parachute back to Earth. It is imperative that we recover the payload since the data is stored locally on the balloon and the bandwidth is too limited to transmit more than $\sim$1% of it back during flight.

### 2.9.1 The Gondola

The SPIDER flight cryostat is suspended beneath the balloon on a lightweight carbon fiber gondola, based on a similar design for the BLAST experiment and built by the University of Toronto. Traditionally, gondolas for balloon experiments have been made from welded aluminum. SPIDER is a very heavy payload for long-duration ballooning, and so the choice to use carbon fiber for the SPIDER gondola was made for the purposes of reducing mass. The entire gondola weighs approximately 1200 lbs, including the electronics, solar panels, sunshields, and pointing sensors.

The gondola consists of two parts: the inner frame and the outer frame. The inner frame attaches directly to the platform on which the cryostat rests. The outer frame attaches to the inner frame and to the flight train that attaches the entire payload to the balloon. A motorized reaction wheel allows the gondola to scan in azimuth, while simple linear actuators allow the inner frame to scan in elevation. An active pivot between the gondola and the balloon allows the entire instrument to rotate underneath the balloon and aids the azimuthal motions provided by the reaction wheel.

A set of asymmetrical sunshields that define the regions the telescope can observe while avoiding exposure to direct sunlight will mount to the outer frame of the gondola. The sunshields are made of an aluminum skeleton and carbon fiber tubing which is covered in aluminized Mylar. The main frame of the sunshields is a semi-cylindrical structure. There is a wing mounted on the port side of the main frame extending at 70° from the bore-sight.

During the flight, the gondola will make sinusoidal scans of 110° in azimuth that will come no closer to the sun than 70° on the port side and no closer than 90° on the starboard side. (The scan is asymmetric because the sunshields are asymmetric.) The telescope will scan at $6^\circ/s$ with a maximum acceleration of $0.8^\circ/s/s$. The telescope will step in elevation by .1° every sidereal hour between $28^\circ - 40^\circ$. A rendering of the flight cryostat with the sunshields attached is shown in Fig. 2.19.

The gondola has specific requirements for stiffness and strength. We have verified that

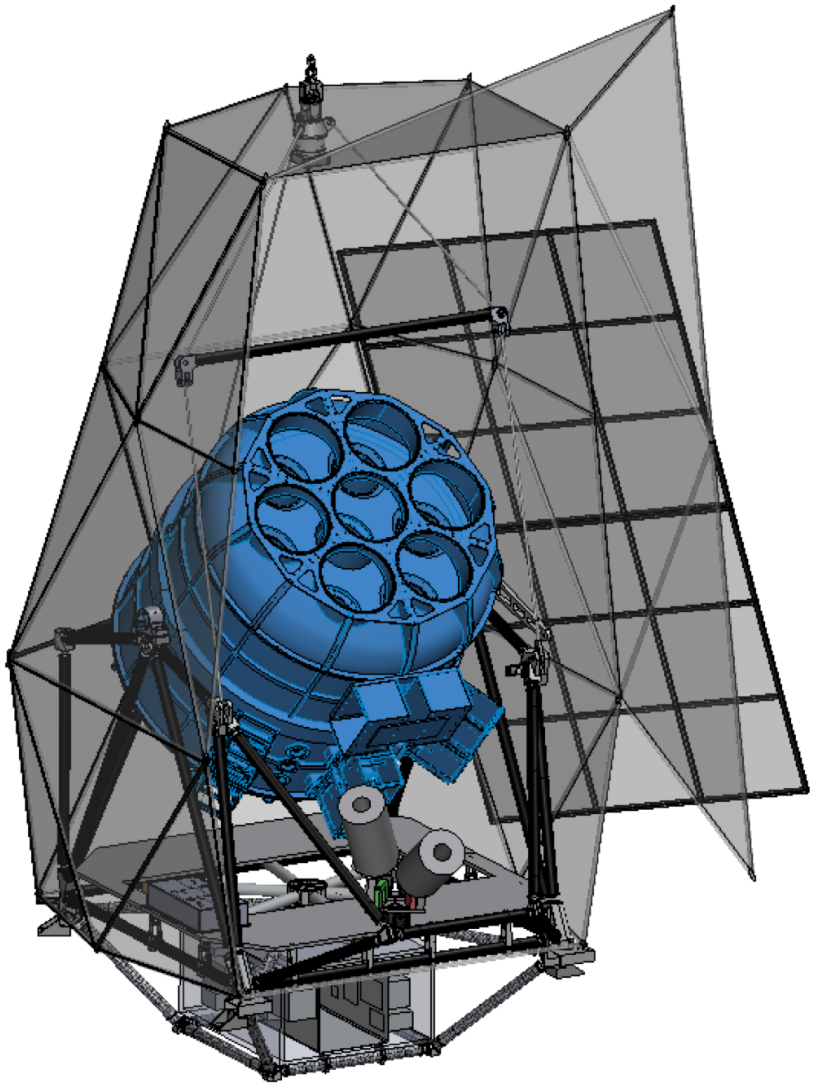

Figure 2.19: Rendering of the SPIDER gondola with flight cryostat mounted on the inner frame. In addition to the gondola frames, this diagram also shows the sun shields and two star cameras at the base of the cryostat. Figure courtesy of Juan Soler.

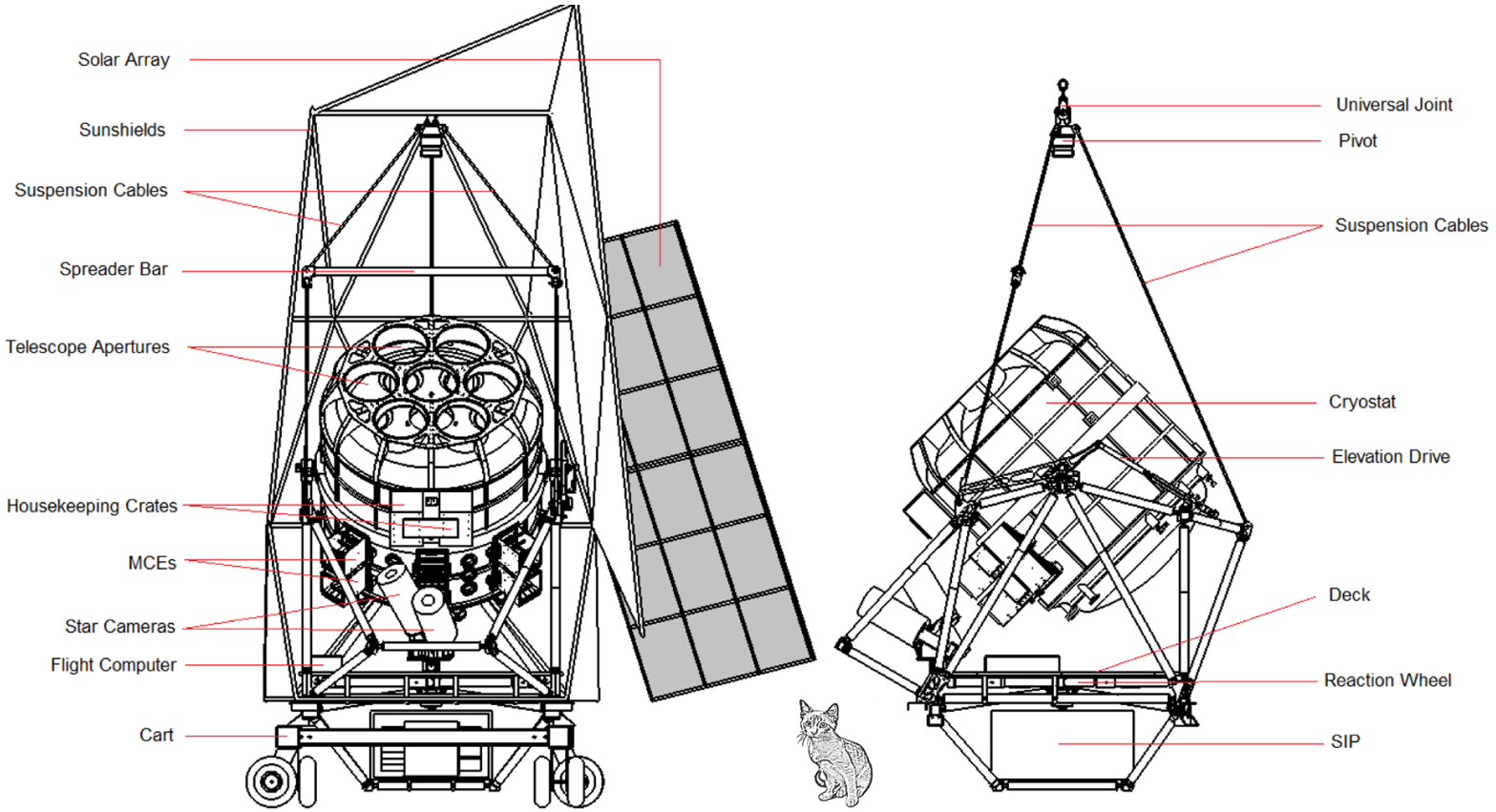


Figure 2.20: Diagram of the SPIDER experiment, including the gondola, cryostat, sunshields, electronics, and pointing systems. A 1m cat is shown for scale. Figure courtesy of Juan Soler. Cat is courtesy of the Columbia Scientific Ballooning Center.

the gondola meets these requirements through finite element analysis, as well as pull tests. These requirements are driven by the need to maintain pointing accuracy as the weight (and center of mass) of the payload changes during the course of the flight (either due to dropping ballast or the helium boil-off). The gondola design is also driven by the need for the cryostat to survive the impact shock when the payload separates from the balloon at the end of the flight. CSBF provides an impact attenuation system that will attach to the bottom of the payload to control some of the forces on landing. The gondola is designed to protect the cryostat in case of a roll-over after landing.

### 2.9.2 Pointing Systems

SPIDER is a balloon-borne experiment, which means that it must be able to point and to know where it is pointing during the flight. Our pointing systems have a long heritage, and have been well-tested in other balloon experiments, most notably BLAST-Pol [35]. The coarse sensors on the instrument include magnetometers (resolution $\sim 1^\circ$), pinhole sun sensors ($\sim 1^\circ$), and an elevation encoder ($\sim 20''$). Additionally, the instrument will carry a differential GPS ($\sim 0.5^\circ$), two 3-axis gyroscopes, and three star cameras. Two of the star cameras are mounted on a platform in front of the cryostat, while the third is mounted along the side. These star cameras will provide absolute pointing measurements. The data from the other pointing sensors allow us to reconstruct the pointing in between the star camera measurements. In flight, we will be able to determine the pointing to within 0.5 degrees. After the flight, the pointing reconstruction will allow us to know where we were pointed to approximately 6 arcseconds. As mentioned above, all of this will have to be done autonomously, since the ability to control the payload from the ground will be extremely limited after the first 12 hours of the flight.

## 2.10 Observing Strategy

### 2.10.1 Frequency Coverage

As mentioned in §1.5, polarized foregrounds can easily confound the faint CMB polarization signals. Synchrotron radiation is a concern at lower frequencies, although it is expected to be subdominant to emission from dust even at 90GHz. The polarized thermal emission from dust is expected to be the most important foreground.

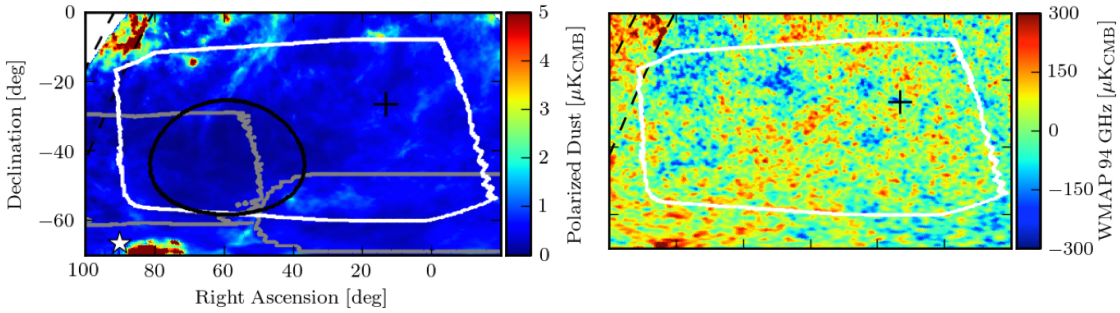


Figure 2.21: The SPIDER observing region is shown by the white outline. Both panels show the same portion of the sky, in equatorial coordinates, smoothed with a 30-arcminute beam. The southern galactic pole (black +) is overplotted, along with the 10- and 20-degree galactic latitude lines (dashed). Also shown are the BOOMERanG and BICEP2 fields (left and right gray outlines, respectively), and the region of minimum foreground contamination in the SPIDER field (black outline). It should be noted that this map projection is not area preserving. *Left*: Polarized dust emission amplitude at 150 GHz, according to the model in [68]. *Right*: WMAP 94 GHz TT data in the same area, showing relative absence of foreground contamination in the SPIDER observation region. Figure from [36].

In order to help discriminate between these foregrounds and the CMB, SPIDER will deploy telescopes at two frequencies. For its first flight in 2014, SPIDER will deploy three telescopes at 150GHz and three telescopes at 90GHz. These frequencies were chosen for maximum sensitivity to the CMB and for minimum foreground contamination. A future flight of SPIDER will also include detectors at 280GHz, which will further aid foreground rejection, especially the emission from polarized dust.

### 2.10.2 Sky Coverage

During each flight SPIDER will scan approximately 10% of the sky in a region near the galactic south pole that is exceptionally clear of galactic emission (see Fig. 2.21). The size of SPIDER's observing region (which is approximately five times the area covered by ground based instruments) allows us to study polarization anisotropies at low multipoles, where the contribution to the B-mode power spectrum from lensing is sub-dominant. The larger sky fraction also allows us to reduce sample variance.

# Chapter 3

# Instrument Systematics

## 3.1 Introduction

To achieve the sensitivity necessary to reach SPIDER's science goal, we will need an accurate and precise characterization of the detectors, optical components, and the resultant beams. Non-idealities in any of these can result in systematic errors that have the potential to either leak temperature anisotropies into polarization or leak E-mode polarization into B-mode polarization. These systematic errors also include calibration uncertainties that can cause map distortions without necessarily causing false polarization signals.

A full description of SPIDER's systematic errors requires both simulation and calibration efforts. We simulated many of the possible systematic errors to describe their effects on the final science result and set benchmark values for all of the simulated systematics. The benchmark values establish how precisely each source of systematic error must be measured or removed to achieve the design goal of measuring CMB polarization at a sensitivity equivalent to $r = 0.03$. It was our calibration goal during testing, both at Caltech in the test cryostat and in the flight cryostat during the integration of SPIDER at CSBF in Palestine, TX, to measure these systematics to the accuracy specified by the simulations. The actual measurements of these systematics will be covered in Chapters 4 and 5.

Ideally, the simulations described in this chapter would be done with variations in the instrument setup (e.g., with and without a half-wave plate, changing the flight parameters or sky coverage, different scan strategies, etc.), which would be helpful for building an intuitive understanding of the results. In practice, these simulations are too computationally intensive to allow this. It should be noted that these simulations often depend on the specifics of the observing and flight strategy, so many of the values in Table 3.1 are from

simulations that do not describe our current plan for an Antarctic flight from McMurdo Station. Most of the values listed in Table 3.1 are based on the residual of false B-mode signal in the $r = 0.03$ polarization spectrum for a four-day flight from Alice Springs, Australia. Simulations that use a 20-30 day Antarctic flight will have reduced map noise, reduced sky rotation, and more time for rotation of the half-wave plate (HWP) to modulate polarization on the sky in comparison to an Alice Springs flight. These competing factors make it hard to predict how these benchmarks would change for an Antarctic simulation. As the use of the HWP ameliorates many systematic errors, we do not expect that the benchmarks would change significantly.

Our primary simulation pipeline is largely derived from the analysis pipeline used for the 2003 Antarctic flight of the BOOMERanG experiment [53]. The pipeline has several key components. The first step in the pipeline is to simulate flight pointing data for each detector (right ascension, declination, and polarization angle). Full-sky temperature and polarization maps are then simulated using the `synfast` program, which is part of the HEALPix software package. These maps are then smoothed by a Gaussian beam of the same width as the SPIDER beam (which has been measured to be approximately Gaussian). The full-sky maps are pixelized at a resolution which corresponds to $\sim 3.4'$ to ensure that the signal variation within a pixel is small. These full sky maps are then converted into timestreams using the pointing data from the flight simulator. The timestreams are high-pass filtered at 10mHz to approximate the filtering that will be done with real data in order to remove long timescale drifts (e.g., in gains or noise).

The timestream generation step includes the rotation of the half-wave plate, which is added to the polarization angle of each detector, and pointing effects such as pendulation and pointing jitter. The set of systematics we are simulating is also applied during this step.

Finally, a Jacobi-method-based iterative map-maker transforms the simulated time streams into maps of the observed Stokes parameters, $I^{obs}$, $Q^{obs}$, and $U^{obs}$. The simulations were done with signal-only inputs, though the map-maker algorithm includes an inverse noise filtering of the timestreams. This is included because we would do this to real data in order to reduce 1/f noise, which can reduce map-making efficiency.

The simulations in this pipeline used 16 detectors, arranged in evenly-spaced pairs in a single column that extends the full height of the focal plane. The detectors in a pair have

orthogonal polarization sensitivities. These simulations assumed four days of operation during an Alice Springs flight in mid-November with a stepped half-wave plate operating mode.

There were two main simulation efforts, resulting in two papers which will be referred to from here forward by the first authors of the papers. The MacTavish [62] simulations explored the effects of polarization angle systematics, beam offsets, and gain drifts. The O'Dea simulations [68] investigated the impact of a non-ideal spectral response of half-wave plates, detector coupling to Earth's magnetic field, beam mismatches and asymmetries, and the interaction of a foreground model with observing and flight strategies. The O'Dea simulations were done using the same simulation pipeline, but with the addition of a sky model that included a detailed model of foreground emission. This model includes polarized galactic dust emission (which requires a model of the galactic magnetic field), which is expected to be the dominant foreground for SPIDER. Synchrotron emission is expected to be sub-dominant at the SPIDER detector frequencies, and so it was not included in this model. As with the MacTavish simulations, the O'Dea simulations were done for a four-day Alice Springs flight. This is noticeably different from an Antarctic flight in that the observing time is much shorter and the fraction of the sky observed is much larger.

The simulations are evaluated by looking at the residuals (the difference between the input and output maps). However, to truly understand how the systematics will affect the science result, the maps must be transformed into power spectra. This is done using `anafast` (also part of HEALPix) to do the spherical harmonic transforms. However, due to the fact that we are observing only a portion of the sky and not the full sky, the decomposition of the maps into E-modes and B-modes is not unique. The recovered B-mode spectrum is heavily biased by the input E-mode spectrum. This bias is removed by estimating the pseudo-spectra of the residual maps, which eliminates the true sky and leaves behind the systematic errors.

Table 3.1 summarizes the systematic errors and their $r = 0.03$ calibration goals, as well as their measured values. The following section describes each source of systematic error and how its benchmark value is derived, as well as the current scheme for measurement.

Table 3.1: SPIDER Systematics Table.

| **Systematic** | **Target** | **Fake BB Signal (% of r=0.03)** | **Current status 90GHz** | **Current Status 150GHz** | **Notes** |
|---|---|---|---|---|---|
| Relative gain uncertainty | 0.50% | 17% | 0.10% | 0.10% | Achieved by Boomerang |
| Differential Pointing | 10% | 20% | 2.40% | 2.30% | (X2, R6.1) and (X3, R8.0) measured by SPIDER |
| Differential Beam Size | 0.50% | | 0.30% | 0.40% | (X2, R6.1) and (X3, R8.0) measured by SPIDER |
| Differential Ellipticity | 0.60% | | 0.20% | 0.60% | (X2, R6.1) and (X3, R8.0) measured by SPIDER |
| Absolute polar angle calibration | 1 degree | 17% | 0.7 degree | | Achieved by BICEP |
| Relative polar angle calibration | 1 degree | 6% | 0.1 degree | | Achieved by BICEP |
| Telescope pointing uncertainty | 10' | 6% | 5" | | Achieved by BLAST |
| Beam centroid uncertainty | 1.2' | 12% | 1.2' | | Achieved by BICEP |
| Polarized sidelobes | -67dB | 8% | -72dB | -67dB | Achieved by BICEP |
| Optical ghosting | <2% | 6% | 1.5%-3.5% | | Measured by SPIDER |
| HWP differential transmission | 0.70% | 10% | TBD | | Modeled by SPIDER |
| Magnetic shielding at focal plane | 10 uKcmb/B_earth | 3% | <5 uKcmb/B_earth | | (X0, R4.0) measured by SPIDER |
| Cross-polarization response | 0.80% | TBD | 0.50% | | (X3, R8.0) measured by SPIDER |

## 3.2 Relative Gain Uncertainty

In flight, we will need to have an accurate monitor of each detector's optical responsivity. Relative gain refers to the fact that the two detectors in an orthogonal pair may not have the same sensitivity. That is, if you were to observe the temperature anisotropies of the CMB with both detectors, and then take the difference of the spectra resulting from each detector, the TT spectrum would not cancel. If the relative gain between the two detectors is well-measured, the effects of the mismatch can be removed in the data analysis. If the relative gain is unknown or not corrected prior to analysis, the mismatch will leak the much larger temperature anisotropies into the polarization spectra. The detector with the higher gain will measure a larger intensity than its orthogonal mate, which can cause a completely unpolarized signal to appear polarized.

In previous CMB polarimeters, differencing the time streams of the two orthogonal detectors was necessary to remove common mode noise. This is especially true for ground-based experiments, which have to filter out large-scale atmospheric fluctuations. SPIDER will not need to depend as heavily on pair differencing, but it is still important that the gains of the detectors in a pixel pair are well matched and that any mismatch between them is well measured. A difference plot of two ideal Gaussian beams with uncorrected relative gain mismatches is shown in the upper left panel of Fig. 3.1.

To set a benchmark for the error on the relative gain measurement, a simulation of uncorrected calibration drift was done in the MacTavish simulations [62]. This simulation found that an uncorrected out-of-phase calibration drift of 0.5% had residuals of less than 5% on a $r = 0.1$ B-mode spectrum. (By out-of-phase, we mean that the calibration drift is not the same for every detector.) An uncorrected drift in the relative gain can be thought of as an uncertainty on the relative gain. So from this simulation, we set our benchmark for relative gain uncertainty at $\Delta(g_1/g_2)/(g_1/g_2) = 0.5\%$. A calibration drift of 0.5% causes a 5% residual on an $r = 0.1$ spectrum, which is equivalent to a $0.05 * 0.1/0.03 \approx 17\%$ residual on a $r = 0.03$ spectrum.

Measuring relative gain has been approached in several ways in previous experiments. A previous balloon experiment, BOOMERanG, used a calibration lamp in flight that measured the drifts in gain with brief pulses of mm-wave light. The final accuracy on the relative gain measurement was $\sim$0.4% [52]. The BICEP2 experiment, which uses the same style

of detector as SPIDER, measured relative gain by regressing the detector response against the change in atmospheric loading from a small step in elevation ("el nods"). El nods track variations in the detector responsivity in relation to the spectrum of the atmosphere. In theory, changes in the atmospheric spectrum over time can affect the fidelity of this measurement, though this has not been seen in practice. This option is not available to SPIDER, as the sub-orbital ballooning platform means that we will be above most of the atmosphere. Additionally, BICEP2 has shown that it is possible to remove relative gain differences via deprojection [5]. Briefly, deprojection is the process of generating a template for a specific source of polarization contamination, regressing that template against the data, and then subtracting it away. A fuller description of deprojection is covered nicely in [9].

The current plan for SPIDER is to derive relative gains from small steps in the detector bias, which have been shown to be a good proxy for small steps in the optical power. The bias steps will track changes in the detector responsivity without reference to an external source (unlike an el nod) and so will affect all sources (CMB, dust, atmosphere) equally. The TESs in a detector pair share the same bias line, which eliminates the need to precisely measure the stability of the bias step amplitude. The precision of this measurement for the current-to-current gain is estimated to be less than 0.1%. A simulation indicates that the drifts in estimated optical gain will stay within the 0.5% benchmark for fairly large changes in optical power, though this breaks down for detectors that are biased near their normal regions [33]. Long term drifts in the detector gain can be measured in the analysis of the data by calibrating against the known temperature spectrum of the CMB.

### 3.2.1 Spectral Differences

A difference in the spectral response of the two detectors in an A/B pair effectively becomes a relative gain difference, although it differs from the relative gain uncertainty mentioned in the previous section in that it is frequency-dependent. It will, therefore, affect sources of different spectra differently (i.e., the relative gain will be different if the detectors are looking at the atmosphere than if they are looking at the CMB). We would like to verify that the spectra between the two detectors are well-matched. The BICEP1 experiment was able to set an upper limit on the relative gain errors due to spectral mismatch of 1% rms over the array [84]. This was done using a Fourier Transform Spectrometer (FTS), which

is the same technique SPIDER uses to measure the detector spectra.

The spectrum for each detector has been measured in the test cryostat or the flight cryostat (see §4.5). An archival version of this measurement will also be done in the flight cryostat prior to flight. Between these measurements and the deprojection technique developed by BICEP2 mentioned above, we do not expect spectral differences to be a significant source of polarization contamination.

## 3.3 Beam Systematics

In a perfect CMB polarimeter, every detector beam would be exactly the same. For SPIDER, we model this beam as a (azimuthally symmetric) Gaussian with a full width at half-maximum (FWHM) of 30 arcminutes at 150GHz. The 30 arcminute beam is small enough to capture the approximately 1 degree peak of the BB spectrum, but large enough that it can be created with relatively small aperture telescopes. In practice, every detector will not have the same beam due to variations in the fabrication process, the location of the pixel on the focal plane, and imperfections in the optics. The lowest-order beam differences can be described as differences in centroid, width, and ellipticity. Differential errors in a pair of beams can cause very large false polarization signals from the unpolarized temperature anisotropies or mixing between E- and B-modes. Examples of these differential beam parameters can be seen in Fig. 3.1. The following section describes how these differential errors contaminate the polarization measurement and the simulation efforts to set benchmark values for these errors.

The O'Dea simulations use a differential pointing error of 1.5 arcminutes, a differential ellipticity of 0.012 and a differential beam width of 0.5%. These values were chosen to match the actual measurements of these parameters from BICEP2 beams. They start by doing a baseline simulation with ideal instrumental beams — each bolometer has the same perfect Gaussian beam. Using an azimuthally symmetric Gaussian kernel also improves the efficiency of the simulation since the computationally intensive convolution of the beam kernel with the map only needs to be performed once. For a non-azimuthally symmetric kernel this is not the case because the convolution will be a function of the instrument orientation, which changes constantly throughout the scan. In order to investigate the beam mismatches mentioned above, each non-ideality is modeled as the sum of a small

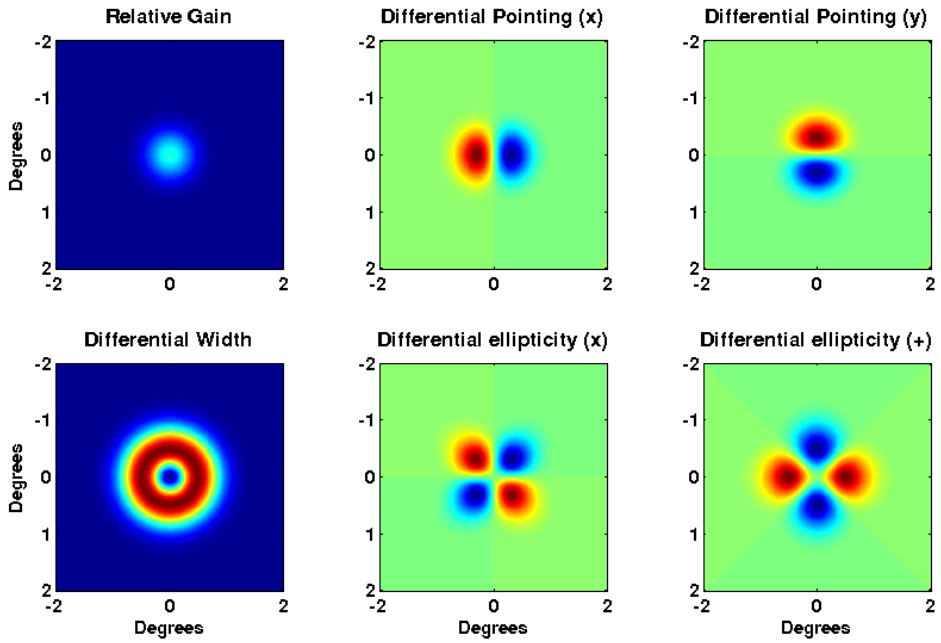


Figure 3.1: Differential beam modes. Monopole components come from differential beam width and relative gain mismatches (upper and lower left). Dipole components come from differential pointing (upper middle and right). Quadrupole components come from differential ellipticity (lower middle and right).

number of Gaussian beams, with a combination of offsets to the nominal pointing, different widths, and different amplitudes from the ideal beam:

$$B(x) = \sum_{n=1}^{N} a_n G(x; x_n, \sigma_n). \tag{3.1}$$

Here $B(x)$ is the beam as a function of position on the sky when the instrument is in some pre-determined orientation, $G(x; x_0, \sigma)$ is a unit-normalized Gaussian centered on $x_0$ with width $\sigma$, and the amplitudes $a_n$ sum to unity. It is convenient that the amplitudes sum to unity when reconstructing the beam function $B_\ell$, as this property ensures that $B_{\ell=0} = 1$. The pointing generator tracks both the nominal pointing direction on the sky as well as the location of the sub-beams so that the full beam can be reconstructed at all points in the timestream at the correct location and orientation.

The O'Dea simulations of differential beam parameters were easily done by using different parameter values for the two beams. Additionally, these simulations accounted for beams that vary across the focal plane by using different beam models for different pixel

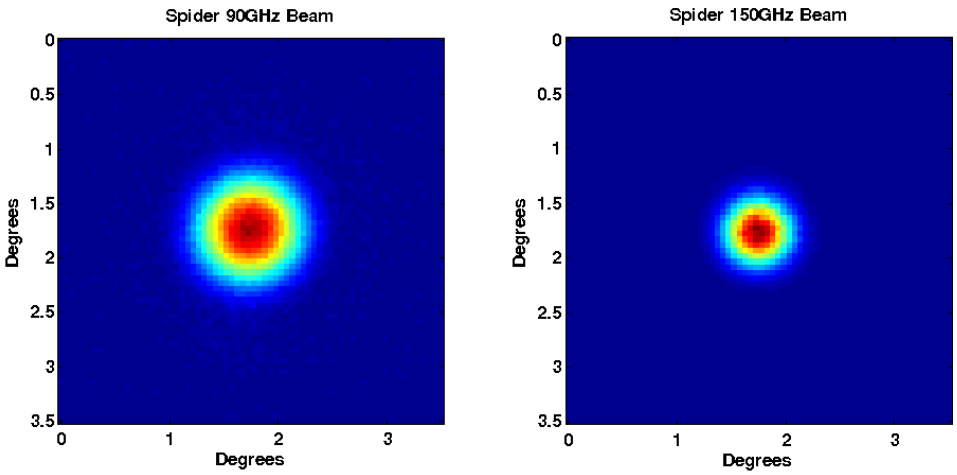


Figure 3.2: Examples of SPIDER beams at 90GHz (left) and 150GHz (right). The 90GHz beam has a full-width at half-maximum (FWHM) of 45 arcminutes, while the FWHM of the 150GHz beam is 30 arcminutes.

locations.

While the beam systematics simulations determined the benchmarks for the differential errors on the SPIDER beams, measuring and characterizing the true beams of the instrument was done through far field beam maps. During a beam map, we use either the test cryostat or the flight cryostat to scan the detectors over a bright thermal or microwave chopped source in the far field of the telescope. A full description of these measurements is given is §5.1. A typical example of our measured beams, at both 150GHz and 90GHz, can be found in Fig. 3.2.

### 3.3.1 Differential Beam Width

Differential beam errors (assuming nearly Gaussian beams) can be decomposed into monopole, dipole, and quadrupole components. (Non-Gaussian beams will have higher-order components. As they are not thought to be leading order contributors to the false B-mode residuals, we do not consider them here.) The monopole component describes mismatches in beam width, known as differential beam width: $(\sigma_1 - \sigma_2)/\sigma$, where $\sigma_1, \sigma_2$ are the Gaussian

beam widths of the detectors in a pair and $\sigma$ is the average beam width. Differentials in beam size are sensitive to the second spatial derivative of the temperature field, which means that they distort the E- and B-mode maps.

The simulation of errors in differential width is a relatively easy simulation to set up: use one sub-beam for each detector and use the appropriate width for that beam. Here the simulation was done for a typical value of differential beam width, 0.5%, which is also our benchmark value. From Fig. 3.3, we can see that this has a negligible effect on the residuals. In practice, we have used far-field beam maps of the SPIDER detectors to determine that a typical value of the differential beam width is $\approx 0.3\% - 0.4\%$.

### 3.3.2 Differential Pointing

The dipole component of the decomposition of differential beam errors describes mismatches in beam pointing, known as differential pointing: $(\vec{r}_1 - \vec{r}_2)/\sigma$, where $(\vec{r}_1, \vec{r}_2)$ are the $(x, y)$ coordinates of the beam centroid and $\sigma$ is the beam standard deviation. In early papers on CMB polarization systematics, this has also been described as "beam squint." Differential pointing is sensitive to the temperature gradient, which means that it can potentially leak the very large temperature signal into polarization. These pointing errors must be very small if they are not to affect the science result (or they have to be deprojected during the data analysis, as was done for the BICEP1 and BICEP2 analyses.) However, differential pointing reverses under a 180-degree rotation (i.e. it is a spin-1 operator). As polarization is a spin-2 operator, the differential pointing will transform differently under the rotation of the sky or instrument than the true polarization signal and thus can be removed during analysis. By the same reasoning, even very large errors in differential pointing will be averaged out of the data by the rotation of the HWP. (One simulation by Sean Bryan found that an ideal wave plate will offset differential pointing errors as large as FWHM of the beam!)

The differential pointing simulation in O'Dea et. al. used an independent beam for each TES in a spatial pixel with an offset of 1.5 arcminutes between them. The pointing errors are assumed to be time-invariant. The low residuals seen in Fig. 3.3 indicate that the HWP is doing a sufficient job of removing the effects of the differential beam parameters even without accounting for them in the data analysis. (Remember that the HWP is turned once per day for these simulations.) The residuals are small at the angular scales

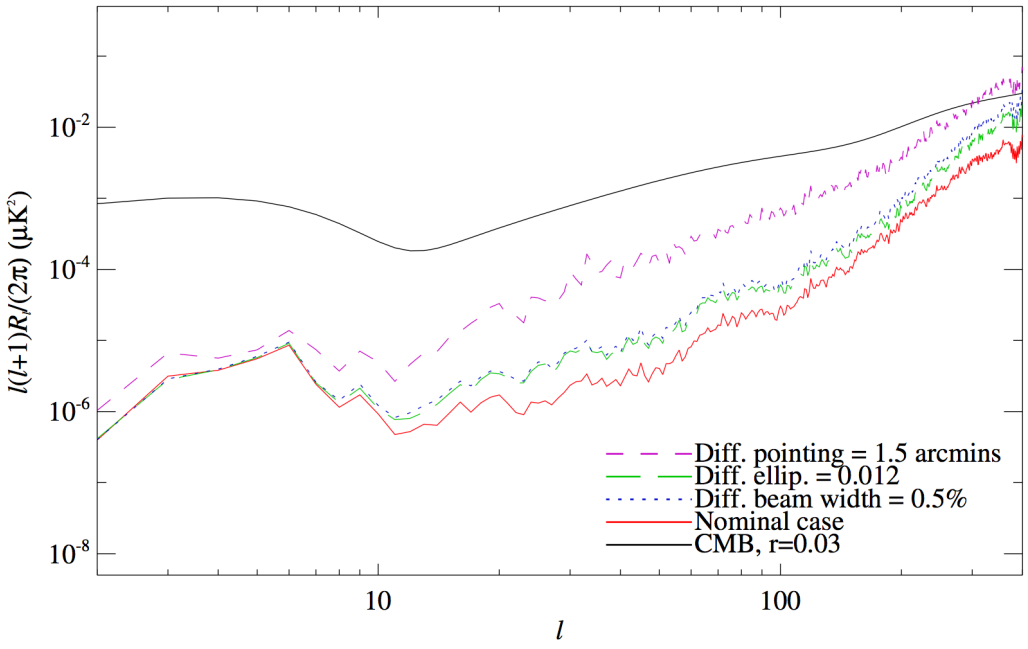


Figure 3.3: Residual BB spectra for simulations of differential beam errors. Figure from [68].

of interest to SPIDER (low multipole, where the B-modes from primordial gravitational waves reside) and become comparable to the CMB signal at smaller angular scales (high multipoles). However, since SPIDER is expected to be dominated by instrument noise at those multipoles, this is not of concern. Additionally, at high multipoles the inflationary B-mode spectrum becomes sub-dominant to the lensing B-mode spectrum. The simulations also show that the residuals do not depend strongly on the orientation of the pointing offset with respect to the focal plane.

In some of the early batches of SPIDER detectors we measured a differential pointing large enough that we estimated it would have caused a residual B-mode signal larger than 20% of a real B-mode signal for $r = 0.03$. This was a major problem that prompted several additional rounds of research and development in our detector technology. It was eventually found to be caused by a problem in the quality of the films forming the detector wiring (more on this can be found in §5.1.1. Detectors with reduced dipoles have been fabricated and deployed by the Keck array. A typical value of the SPIDER differential pointing (as measured in far-field beam maps) is $\approx 2.3\%$, which is less than an arcminute on a beam with a FWHM of 30 arcminutes. Our benchmark value for differential pointing is 1.5 arc

minutes, or 10%, which we easily meet.

### 3.3.3 Differential Ellipticity

The quadrupole component of the decomposition of differential beam errors describes mismatches in beam ellipticity, known as differential ellipticity: $(e_1 - e_2/2)$, where $(e_1, e_2)$ are the values of the ellipticity of the detectors in a pixel pair. We define ellipticity as $e = (\sigma_{maj} - \sigma_{min})/(\sigma_{maj} + \sigma_{min})$ where $\sigma_{maj,min}$ are the widths of the semimajor and semiminor axes, respectively. Differential ellipticity couples the second derivative of the temperature anisotropy into linear polarization. Differential ellipticity is symmetric under a 180-degree rotation (i.e., it is a spin-2 operator). As we have seen in §1.4.2.1, polarization is also a spin-2 operator. This means that differential ellipticity cannot be separated from the polarization signal via sky or instrument rotation. Without a HWP, the differential ellipticity poses a much harder problem, since its effect is indistinguishable from a true polarization signal.

The simulation for differential ellipticity used a typical value for this parameter of $e_1 - e_2 = 0.012$. (Note that this is different definition of the differential ellipticity than the one used for the systematics table, which divides by two.) Each elliptical beam is modeled as two sub-beams with identical widths, $\sigma = 30$ arcminutes, and centers that are displaced from the nominal pointing center by $\delta/2 = 1$ arcminute in opposite directions along the major axis. Since the polarizations are orthogonal, this results in a beam with ellipticity $e = 0.006$. Differential ellipticity is produced by aligning the major axes of the elliptical beams with the polarization directions of their antennas. The simulation found that the residuals for this value of the differential ellipticity were negligible in the angular scales that SPIDER cares about.

Furthermore, the orientation of the differential ellipticity is important. If the major axes of the beams are at 45 degrees with respect to the antenna polarization signals (as opposed to being parallel to it, as in the previous paragraph), then the differential ellipticity produces a false B-mode signal in the maps. A simulation was also done with the major axes of the elliptical beams rotated by various amounts to the polarization direction. This, too, was found to have a negligible effect, which means that the HWP is doing its job and removing this effect [68]. The detectors that are nominally slated for deployment in SPIDER have differential ellipticities less than the benchmark in Table 3.1.

### 3.3.4 Measuring the Beam Function

SPIDER's beams are well-fit by a Gaussian model. Despite beam problems in early detectors, especially with differential pointing, the detectors deployed to the field were well within all systematic requirements. The measured values for the beam systematics can also be found in Table 3.1.

It is possible to attempt to measure the beam function $B_\ell$ (and therefore the width) of the SPIDER detectors without mapping the beams directly. This is done by comparing maps of the CMB as observed by SPIDER with maps of the CMB as observed by an independent instrument with comparable noise and higher resolution (likely, maps from the Planck satellite).

I simulated the reconstruction of $B_\ell$ in the following way.

- Simulate the full CMB sky using the `synfast` function of the `HEALpy` software package.
- Smooth the map by a Gaussian of FWHM=30 arcminutes (the SPIDER beam).
- Create a noise map where

$$\textbf{noise map} = \frac{NET}{\sqrt{N_{hits} * t_{hit}}} \tag{3.2}$$

  with reasonable assumptions for noise equivalent temperature (NET $\approx 130 \mu \mathrm{K}_{\mathrm{CMB}}/\sqrt{\mathrm{Hz}}$), $t_{hit}$, and $N_{hits}$.
- Multiply the noise map by a map of Gaussian random numbers (mean=0 and variance=1) to get a map of the random noise we might expect for the SPIDER detectors.
- Add the random noise map to the observed CMB map to get the CMB sky as observed by one detector.
- Mask out unobserved portions of the sky in all maps.
- Apodize the maps with a 3-degree apodization at the edges.
- Create power spectra from the simulated (ideal) map, the smoothed map, the smoothed map with noise, and the noise-only map. (Using the anafast function of HEALpy.)
- Repeat the above steps 200 times.

- Take the mean of all the noise spectra: $< C_{\ell,noise} >$.
- Calculate the beam function (squared) for each of the 200 simulations:

$$B_\ell^2 = \frac{C_{\ell,observed} - < C_{\ell,noise} >}{C_{\ell,ideal}}. \tag{3.3}$$

- Fit each beam function individually to get a reconstructed beam width.

The map is constructed using a HealPy map with 256 sides. This works out to approximately 0.05 sq. degrees per map pixel. The integration time per hit is calculated by taking the width of the pixel and dividing by the scan speed of the instrument (6 degrees per second). The number of hits per pixel is found via simulations of the scan strategy. For this simulation, I used a pre-made `.fits` file that was output from the scan strategy simulations.

The reconstructed beam functions for each of the 200 simulations are shown in Fig. 3.4a. I fit a one-dimensional Gaussian to each of the beam functions. The fitted widths are shown in Fig. 3.4b This simulation showed that it is possible to reconstruct the beam width to less than 1% of the FWHM. Our benchmark goal for the differential beam width is 0.5%, which means that we will need to measure the beams at least that well. This rudimentary simulation very nearly meets this benchmark, and an improved version could prove to be sufficient for our purposes.

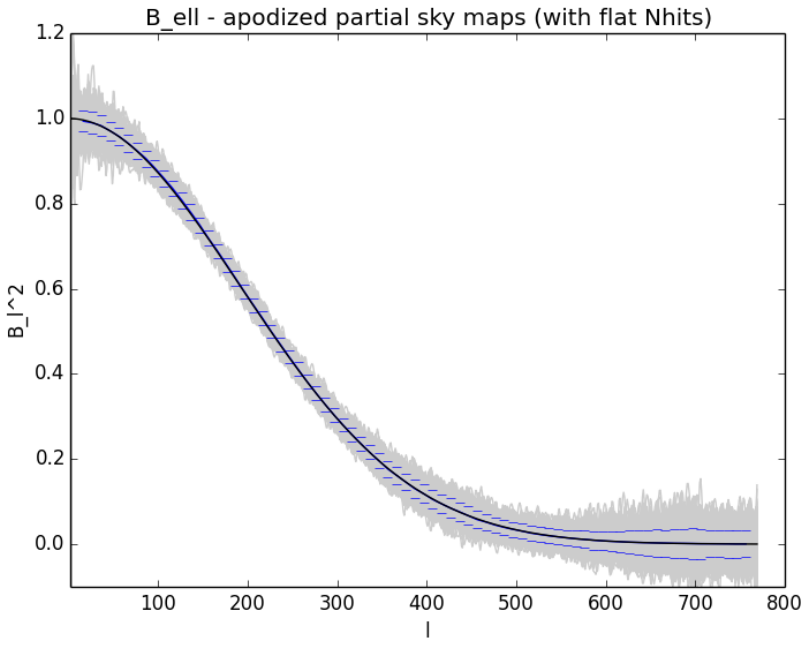


(a) The reconstructed beam functions for each of the 200 simulations is shown in grey. The mean of all the beam functions and one sigma error bar are shown in blue. The input beam function is shown in black.

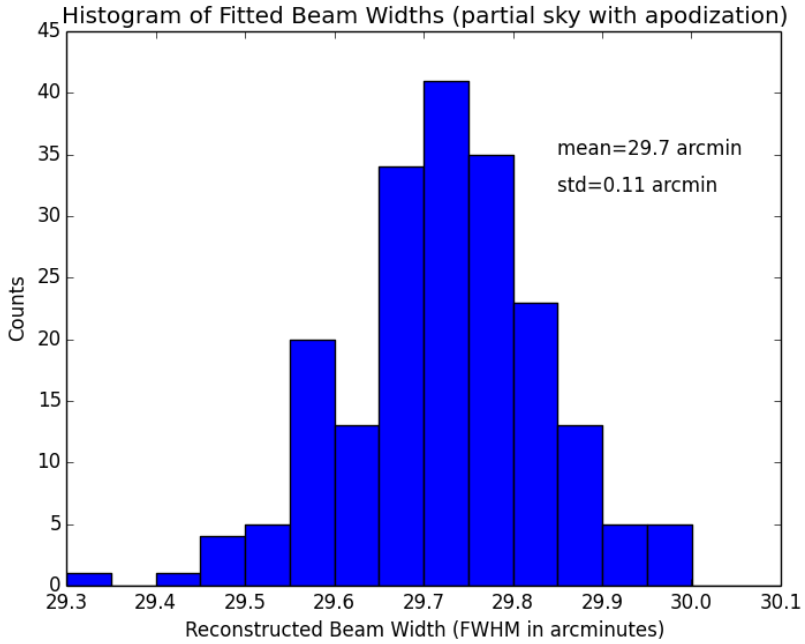


(b) The fitted widths from fitting a one-dimensional Gaussian to the reconstructed beam functions.

Figure 3.4: Results from a simulated reconstruction of the beam function, $B_\ell$.

## 3.4 HWP Non-Idealities

SPIDER's half-wave plates (HWPs) are critical in our mission to tightly control our systematics. However, the HWP itself is susceptible to non-idealities that could affect the fidelity of our data analysis. This section describes how these non-idealities come about and efforts to include realistic descriptions of the HWPs in our simulation efforts.

SPIDER uses plates of single-crystal, birefringent sapphire as half-wave plates to rotate polarization. Each HWP is tuned such that its thickness corresponds to an optical path difference of exactly half a wavelength at the center of the appropriate frequency band. Each telescope in SPIDER is monochromatic, so there are two sets of HWPs: one set for 90GHz telescopes and another set for 150GHz telescopes. The 90GHz HWPs are, naturally, thicker — 4.930mm rather than 3.160mm for the 150GHz sapphire plates. These HWPs are also anti-reflection coated with either quartz (90GHz) or Cirlex (150GHz).

A HWP of this design will act as a perfect HWP for the central frequency and will become non-ideal for all frequencies other than this one, including the frequencies at the edges of our frequency bands. The modulation efficiency will decrease at the edges of the band because the optical path difference for these frequencies is no longer exactly a half wavelength. As the anti-reflection (AR) coating on the HWPs is also tuned to the central frequency, reflections off the HWP will increase for frequencies at the edges of the band because the AR coating is not optimal at those frequencies. These non-idealities remain even when averaged over the frequency band (this is true even for an idealized "top hat" passband). The band-averaged non-idealities will also depend on the spectrum of light incident on them from the combination of the CMB and foregrounds, which we do not have the advantage of knowing prior to the flight.

Using the analytic formula derived in Bryan et. al. [23], O'Dea et. al. [68] calculates the band-averaged Muller matrix that describes the SPIDER HWP for both the CMB and dust-emission spectra. These simulations use the refractive index measurements of sapphire from Bryan et. al. and assume an index for quartz. This simulation was done before the decision to use Cirlex was made, so Cirlex is not included. FDS model 8 is used for the dust emission spectra. (Details of that model can be found in [34].) O'Dea also incorporates the SPIDER detector response spectrum as measured in the lab with a Fourier transform spectrometer.

Table 3.2: HWP Parameters used for simulations.

| | $T$ | $p$ | $c$ | $s$ |
|---|---|---|---|---|
| Ideal | 1 | 0 | -1 | 0 |
| CMB | 0.97127 | 0.00673 | -0.94157 | 0.03126 |
| Dust | 0.96952 | 0.00628 | -0.94067 | -0.01190 |

HWP parameters for simulations of the HWP response to the CMB and dust. Parameters for a perfect HWP are also shown. [68]

The parameters used for these simulations can be found in Table 3.2. $T$ is the overall transmission, $p$ characterizes differences between the transmission spectra for radiation polarized along the crystal axes, $s$ is the coupling to circular polarization, and the extent to which $-c$ is equal to $T$ is the modulation efficiency. The expectation is that the total intensity seen by the bolometer will be reduced by the transmission loss caused by the HWP. Additionally, the modulation efficiency is reduced to $(T-c)/2$. These two effects are degenerate with other systematic errors within the experiment (namely, gain and detector angle calibration).

However, there are other effects of HWP non-ideality that are not degenerate with the instrument calibration. These effects can be independent of $\theta$, go as $\theta$, or as $2\theta$ and thus transform differently under the effects of HWP rotation than the ideal bolometer outputs, which go as $4\theta$. This is good, because these effects will be suppressed in the maps by the HWP modulation.

This simulation was increased to eight days (from the standard four) to capture the full effects of stepped HWP rotation. Two simulations were done, one for the CMB and one for galactic dust. The dust only simulation showed that the residuals from a non-ideal HWP are not negligible, with residuals rising to 40% of the expected B-mode spectrum for $r = 0.03$ at low multipoles. The CMB simulation is similar, though somewhat better, with the residuals rising to only 20%. A further dust-only simulation with $T, c, s = 0$ on an unpolarized sky indicates that the residuals are dominated by the leakage of the dust intensity into polarization. The residuals from these simulations can be seen in Fig. 3.5.

These effects, which would otherwise affect SPIDER's science reach, can be accounted for in the analysis of the SPIDER data by upgrading the map-making algorithm to include the the calibrated values of $T$, $\rho$, and $c$ determined in Bryan et. al. Currently, no correction

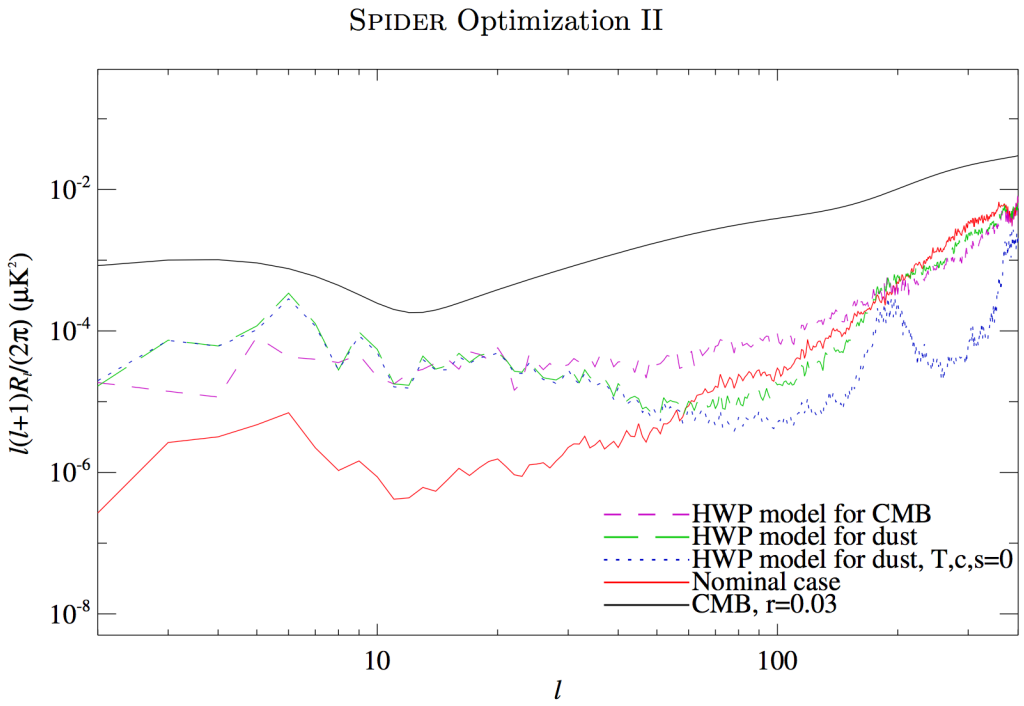


Figure 3.5: Residual BB spectra for simulations of non-ideal HWPs. Figure from [68].

is made for the non-ideality of the HWP. According to O'Dea et. al. [68], adding these values to the pointing matrix is expected to reduce the map-level residuals by at least an order of magnitude, which will make them completely acceptable for the SPIDER design sensitivity of $r = 0.03$. One area for suggested work is to run further simulations exploring these proposed upgrades.

### 3.4.1 Ghosting

Internal reflections off the SPIDER optics (and off the HWP in particular), cause a faint secondary beam for each detector, also known as its "ghost" beam. The ghost beams are in a known position — due to geometric optics, they are reflected across the focal plane from the main beam. There are two mechanisms by which ghost beams could distort the polarization maps. The first is that each detector will essentially be viewing two uncorrelated points of the sky simultaneously. A highly reflective HWP can cause ghost beams that have amplitudes as high as 10% of the amplitude of the main beam, which could cause a large contamination of the timestream of each detector. Another way in which the ghost beams affect polarization is when the A and B detectors within a pair see a ghost at the same

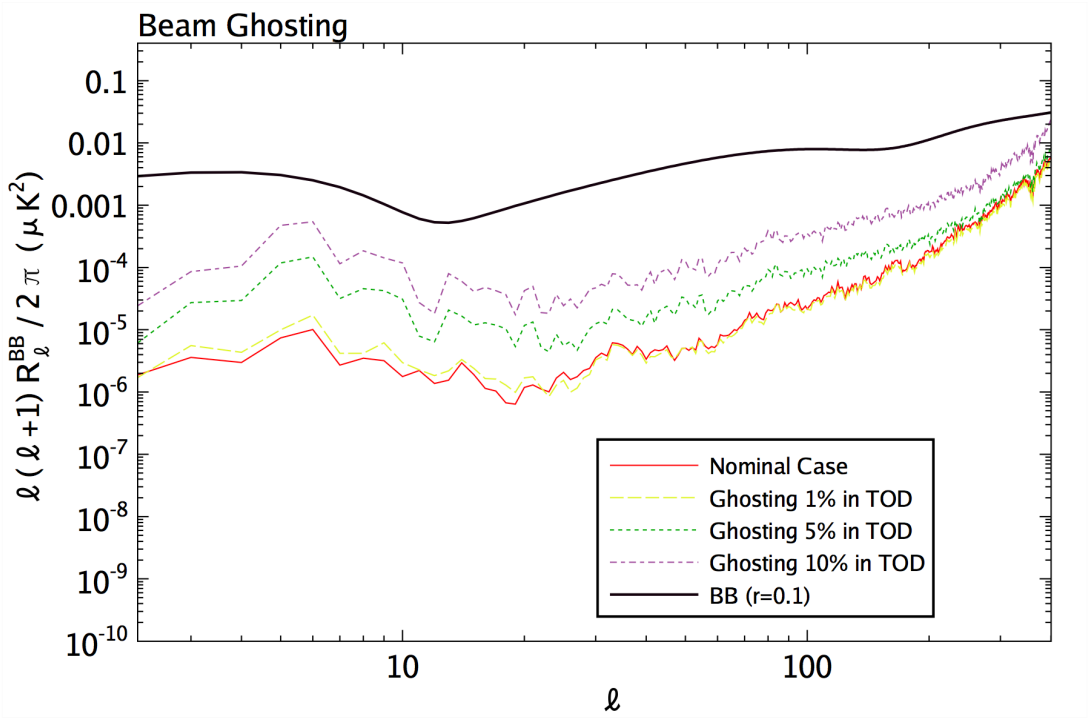


Figure 3.6: Residual BB spectra for simulations of ghost beams of varying amplitude in the time-ordered data (TOD). Figure from [62].

location but with different amplitudes. This produces a false polarization signal.

Two simulations of the effect of the ghost beams were done. The first, as seen in MacTavish et. al., was simulated by generating a time stream for a particular detector and then generating a time stream for its ghost beam by adjusting the instrument coordinates so that it was mirrored across the focal plane. (The first mechanism described above.) The two time streams are then summed with various weights, depending on the level of ghost contamination simulated. That is, a ghost contamination of 1% indicates that the ghost beam has an amplitude of 1% of the main detector time stream. This simulation assumes that the A and B detector see the same ghost (i.e. that there is no "polarized" ghost), which means that the ghost contamination here does not produce leakage from the temperature spectrum into the polarization spectra.

The results of this simulation can be seen in Fig. 3.6. The results from this simulation indicate that ghost contamination (by amplitude) of 1% is negligible for $r = 0.1$ [62]. Our typical ghost amplitudes for good HWPs, as measured during integration in Palestine, were less than 2%.

Another simulation of ghosting using the entire focal plane (not just a single row of detectors, as in the MacTavish simulations) was done for the SPIDER collaboration by Tom Montroy. In this simulation, the ghost beams were modeled as coming from a detector whose position is mirrored across the focal plane from the detector of interest. The B detectors were assumed to have no ghost, and the A detector's ghost was varied in amplitude. (The second mechanism described above.)

This simulation uses two full telescopes, with a half-wave plate that does not rotate, no time domain filtering, and one day of observations from an Antarctic flight. Additionally, the maps from which the power spectra are calculated are apodized with a six-degree mask (meaning that the map is rolled off starting six degrees from the edges). This is done because the edges of the map are problematic for E/B mixing.

The result of this simulation can be seen in Fig. 3.7. The conclusion from this simulation was that a "polarized" ghost (ghost beam amplitude difference between the A and B pixels) of 1% would be safe for $r = 0.01$, but that anything higher might start to be problematic. Measurements of the amplitude difference between A and B ghosts were measured in Run 8.0 to be $< 0.5\%$, which is well within the benchmark set by this simulation.

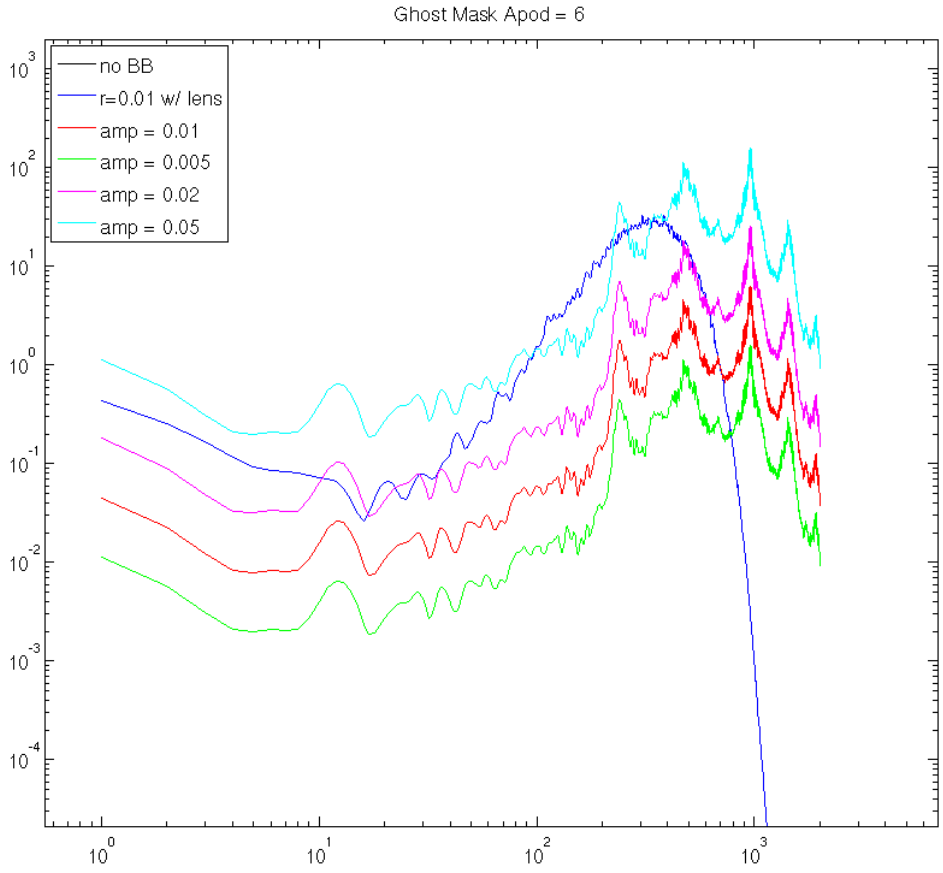


Figure 3.7: A comparison of recovered BB power spectra for various levels of contamination from ghost beams. Figure courtesy of Tom Montroy.

## 3.5 Telescope and Detector Pointing

The need for pointing reconstruction is a major difference between balloon-based and ground-based instruments. Balloon-based telescopes have extremely limited bandwidth for commanding, and so an automated in-flight pointing solution keeps the telescope pointing in roughly the right direction. After the flight, a detailed pointing reconstruction requires the integration of data from many different sources: gyroscopes, GPS, star-cameras, etc. This reconstruction can be a major (and limiting) source of systematic error. The SPIDER payload makes use of the BOOMERanG and BLAST legacies by using many of the same pointing sensors and reconstruction pipeline. BOOMERanG achieved 1.5-arcminute resolution in pointing [63] and BLAST achieved a resolution down to a few arcseconds [72]. Luckily for SPIDER, our pointing reconstruction needs are much less stringent than that due to the low resolution of our telescopes. Still, since we are using this previous architecture, our goal is to have sub-arcminute pointing reconstruction.

A simulation was done in MacTavish et. al. to determine how precise our pointing reconstruction really needs to be. In the first set of simulations, random pointing jitter was added to the pointing solution generated by the flight simulator (measured in right ascension and declination). Each offset is held constant for six seconds, and then a different random value is added to the solution. The six-second interval was chosen to mimic the pointing systematics that occur within the time scale of one gondola scan. Under the current flight and scan strategy, our scans will actually be somewhat slower than that. Two simulations were run: one with a nominal pointing jitter of one arcminute RMS and a worst-case scenario with a pointing jitter of 10 arcminutes RMS. Even for the worst case scenario, the residual on a $r = 0.1$ B-mode spectrum was found to be less than 1%.

A third pointing simulation was done to include the effects of pendulation of the gondola. In the simulation, this took the form of a sinusoidal oscillation with amplitude of six arcminutes and a 20 minute period. A one-arcminute RMS pointing jitter was also added to this simulation to reproduce typical in-flight conditions. This simulation also showed that pointing errors of this form are a negligible contribution to the systematic error. The residuals from all of these simulations can be found in Fig. 3.9.

It should be noted that these simulations assumed a gondola spin speed of 36 degrees per second (dos), which is no longer our nominal scan strategy. Instead, we expect to make

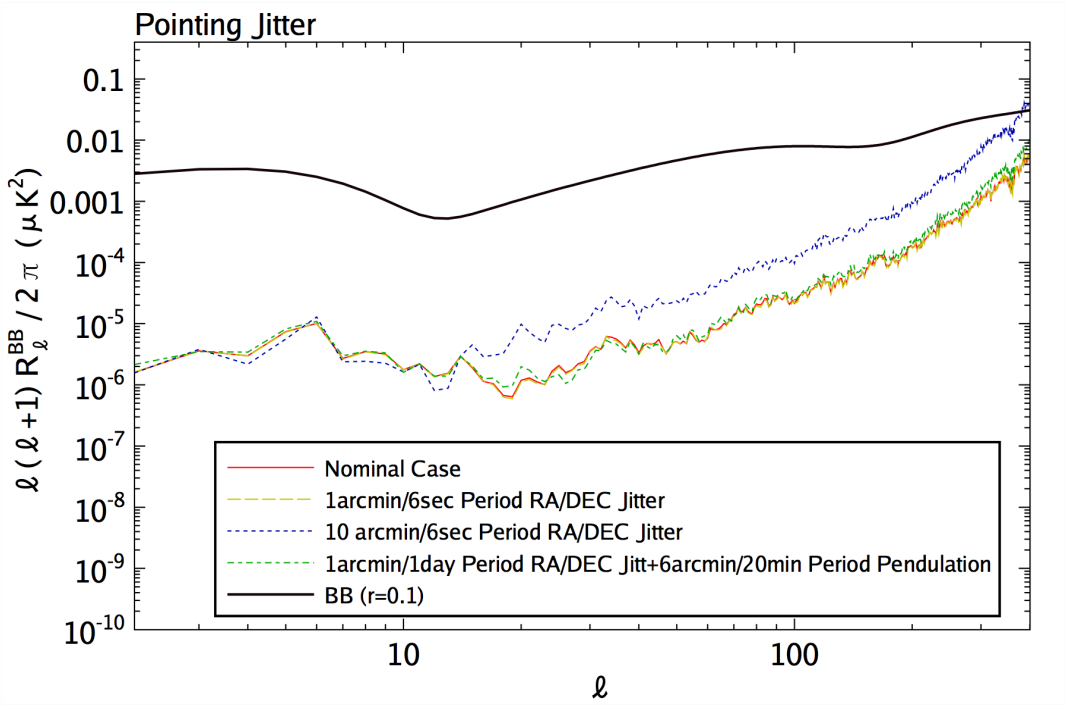


Figure 3.8: Residual BB spectra for simulations of pointing jitter. Figure from [62].

sinusoidal scans of 6 dps. In Palestine, TX, during the pre-flight integration of SPIDER, we tested the fully integrated pointing system and we expect to reconstruct the pointing to within our benchmark. Additionally, a SPIDER star camera was flown on the BLASTPol 2012 flight. The pointing solution from that camera is accurate to less than an arcminute, which meets our benchmark goal.

## 3.6 Polarization Rotation Systematics

One potentially damaging systematic error that mixes E and B polarization modes is the inaccurate characterization of the absolute and relative polarization orientation angles ($\Psi_{abs}$ and $\Psi_{del}$, respectively) of the various detectors. The absolute polarization angle is the angle that each bolometer antenna makes with respect to the fixed Q and U frame of reference on the sky. This is measured through the intermediate referencing of the antenna to the gondola and then from the referencing of the gondola (through pointing information) to the sky. Any miscalibration of the absolute polarization angle will show up as an error in $\psi$ and can lead to rotation of E-modes into B-modes. A truly uniform error in the absolute polarization

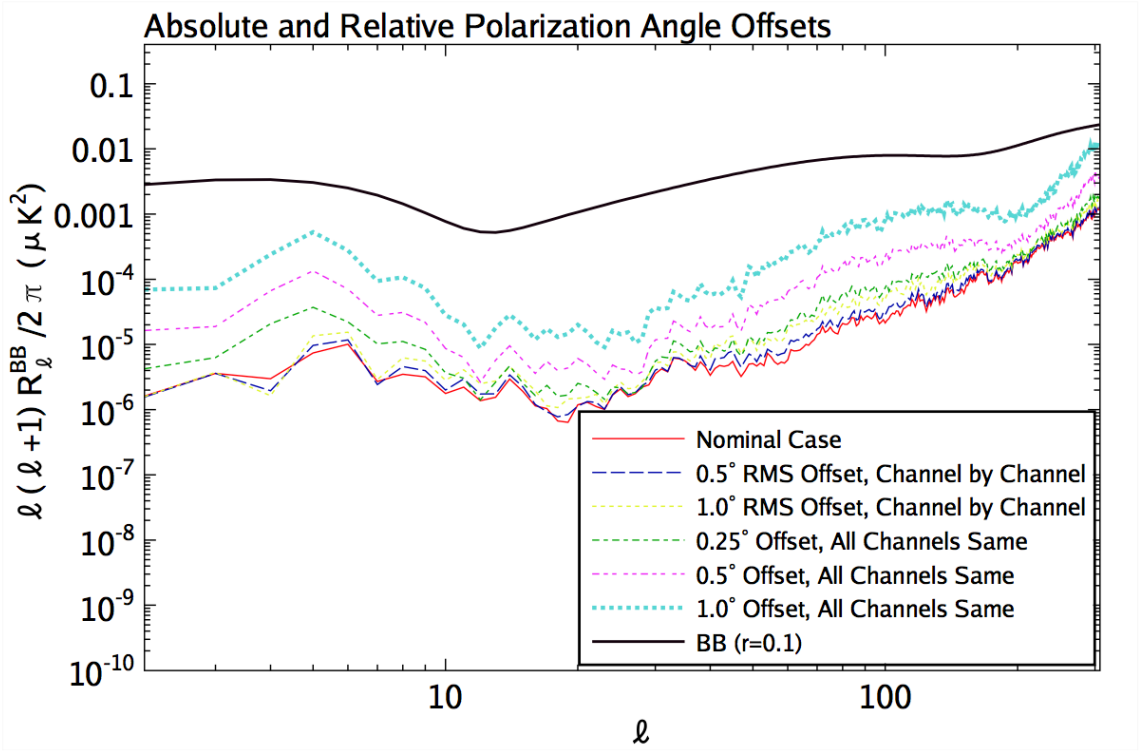


Figure 3.9: Residual BB spectra for simulations of absolute and relative polarization angle offsets. Figure from [62].

angle across the focal plane can be estimated in the analysis by forcing the TB and EB spectra to zero. This is completely degenerate with the detection of vacuum birefringence, which is generally assumed to be zero (though there are some theories in which it is not). The BICEP1 experiment used this technique to refine their physical measurements of the absolute polarization angle [56].

The relative polarization angle (which determines cross-polar response, $\epsilon$) is the angle between the two detectors in a pair. In a perfect polarimeter, this angle would be exactly 90°. The cross-polarization response determines the polarization efficiency, $\gamma = (1-\epsilon)/(1+\epsilon)$, which does not affect the separation of E- and B-modes, but does affect the overall scaling of the power spectra.

Systematic errors in both the absolute and relative polarization rotation were simulated by MacTavish et. al. In the first set of simulations, random 0.5- and 1-degree RMS errors in $\Psi_{rel}$ were added to each detector. This approximates having fixed (but random) offsets in the relative angle between the detectors. The residuals from these simulations are fairly

small, having approximately the same contribution to the residuals as the nominal case. Intuitively, this is because the random errors will average out over the focal plane as different detectors observe the same pixels on the sky.

A second set of simulations was done that applies the same offset (0.25, 0.5, and 1 degree) to all the detectors at the same time. (This is essentially the same systematic error as an overall calibration error in the HWP angle.) This absolute angle miscalibration turns out to be much worse than the relative angle miscalibration. For a 1-degree absolute error, the effect is as high as 20% of the BB spectrum for $r = 0.1$. To keep this systematic effect to only a few percent, the calibration goal for the accuracy of the absolute polarization angle is set to to $< 1^\circ$ [62].

Our current measurements of absolute and relative polarization angle can be found in §5.5. These measurements are quite difficult, and so far we have not constrained the polarization angle calibration to better than a few degrees. However, we have a strong prior from the BICEP2 experiment that the absolute polarization rotation is less than a degree and that the detectors are orthogonal to better than 0.3 degrees [9] .

## 3.7 Polarized Sidelobes

We define the polarized sidelobes of the SPIDER experiment as the difference in the sidelobes of an orthogonally polarized pair of detectors (not the absolute magnitude of each individual detector's sidelobe). Polarized far sidelobes can potentially sweep past bright sources such as the galactic plane, the Sun, the ground, and parts of the balloon, which could result in spurious polarization being picked up by the detectors. That is, the detector with the larger sidelobe will detect more radiation from an unpolarized source than its orthogonal mate. Depending on the amplitude of the far sidelobes and the brightness of the source, this could potentially be a major source of contamination in our polarization maps. Since we can't control the brightness of the sources, our only option to is reduce the far sidelobes as much as possible.

Fraisse et. al. [36] establishes benchmark goals for the SPIDER sidelobes. SPIDER's main beam and near ($2^\circ - 12^\circ$) sidelobes are well measured by thermal and microwave source beam maps in the Caltech test cryostat. They are in excellent agreement with the physical optics model of the internal optical chain, which includes both lenses and the half-

wave plate. Since the sunshields, baffles, and gondola have not yet been added to that model, we have no accurate model of SPIDER's far sidelobes. Instead, we model it as a power law out to 50 degrees, after which is it truncated. This model is consistent with the shape of BICEP's measurement of their polarized sidelobes [84], though our target is an order of magnitude smaller. The models of the BICEP and SPIDER sidelobes can be seen in Fig. 3.10a.

We then convolve this polarized sidelobe profile with a temperature map of the galactic emission that is based on the sky model developed in [68] and derive a B-mode spectrum from that map. The result is shown in Fig. 3.10b. The BB spectrum derived from the BICEP sidelobe model shows high contamination at low multipoles. The BB spectrum derived from the SPIDER sidelobe model is much fainter at low multipoles and essentially negligible at $l \sim 80$, which is the angular scale of the inflationary peak.

We note that the BICEP baffling scheme was designed for an overall instrument sensitivity of $r = 0.1$. Its less restrictive baffles are not sufficient for the rejection of galactic emission at the large angular scales that are of interest to SPIDER. In contrast, the SPIDER baffles were designed to reduce as much pick-up from large angles as possible. They are conical baffles with the base located inside the cryostat. They extend out of the cryostat by approximately 0.5m. In order for contamination from the galaxy to be subdominant to the CMB at $l \sim 30$ and negligible at the $l \sim 80$ peak, we will need an additional 10dB of attenuation at the far sidelobes as compared to BICEP. Our benchmark for the polarized far sidelobes is that they should have an amplitude of $\approx$ -70dB at 30° away from the bore site (assuming a peak beam height of 0 dB). We have measured SPIDER's sidelobes with these baffles down to $\approx$ -60dB, but our very stringent sidelobe requirements will require a measurement with even better signal to noise.

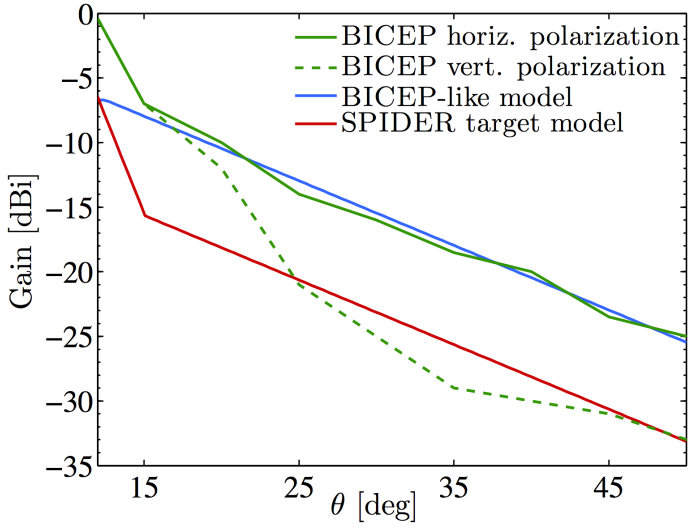


(a) Polarized sidelobe profiles from BICEP1 and SPIDER. Figure from [36].

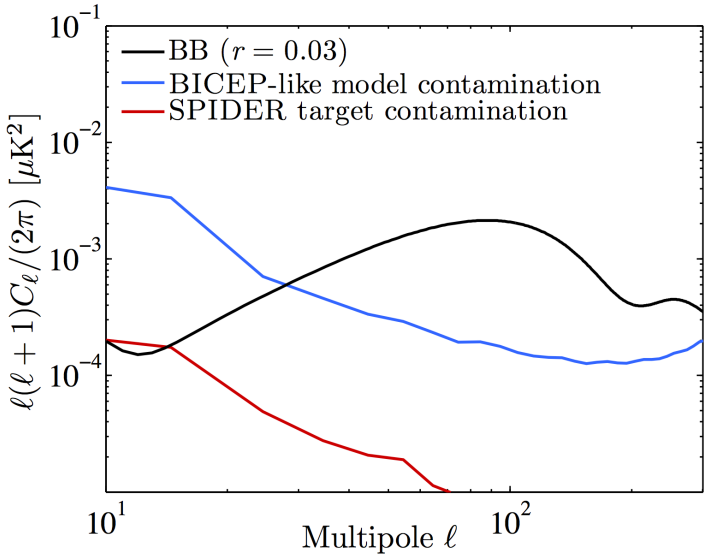


(b) B-mode power spectra of the sidelobe pickup from the sidelobe profiles shown in Fig. 3.10a. Figure from [36].

Figure 3.10: Sidelobe profiles and the resulting B-mode power spectra from sidelobe contamination for BICEP1 and SPIDER.

## 3.8 Cross-Talk

The SQUID readout system (see §2.7) is one of the main sources of cross-talk in the SPIDER system. There are several possible mechanisms at play. One of these is that the first-stage SQUIDs can inductively couple to the second-stage SQUIDs in the same column. Another is that each first-stage SQUID can inductively couple to its nearest-neighbor first-stage SQUIDs. These inductive sources of cross-talk are symmetric between the channels and independent of the readout order of the detectors. The symmetry of these mechanisms means that the A and B detectors in a pair will cross-talk to each other in equal amounts, which will appear as a reduction in polarization efficiency. Cross-talk between adjacent pixels that are not part of the same A/B pair creates a compact polarized sidelobe that would need to be accounted for in the analysis.

A simulation of detector cross-talk was done by Tom Montroy for the SPIDER collaboration. In this simulation, he assumes cross-talk between the A and B pixels in a pixel pair, as well as with the detector that is the nearest neighbor in a column (both are inductive mechanisms). As in §3.4.1, this simulation uses two full telescopes, a non-rotating HWP, no time domain filtering, and one day of observations from an Antarctic flight. The map is anodized with a six-degree mask.

The results of this simulation are shown in Fig. 3.11. The residual spectra show that cross-talk greater than 0.5% starts to become problematic for $r = 0.01$. Our typical measured cross-talk levels are around 0.5%, so this should be acceptable for our science goal of measuring the BB spectrum at the level of $r = 0.03$.

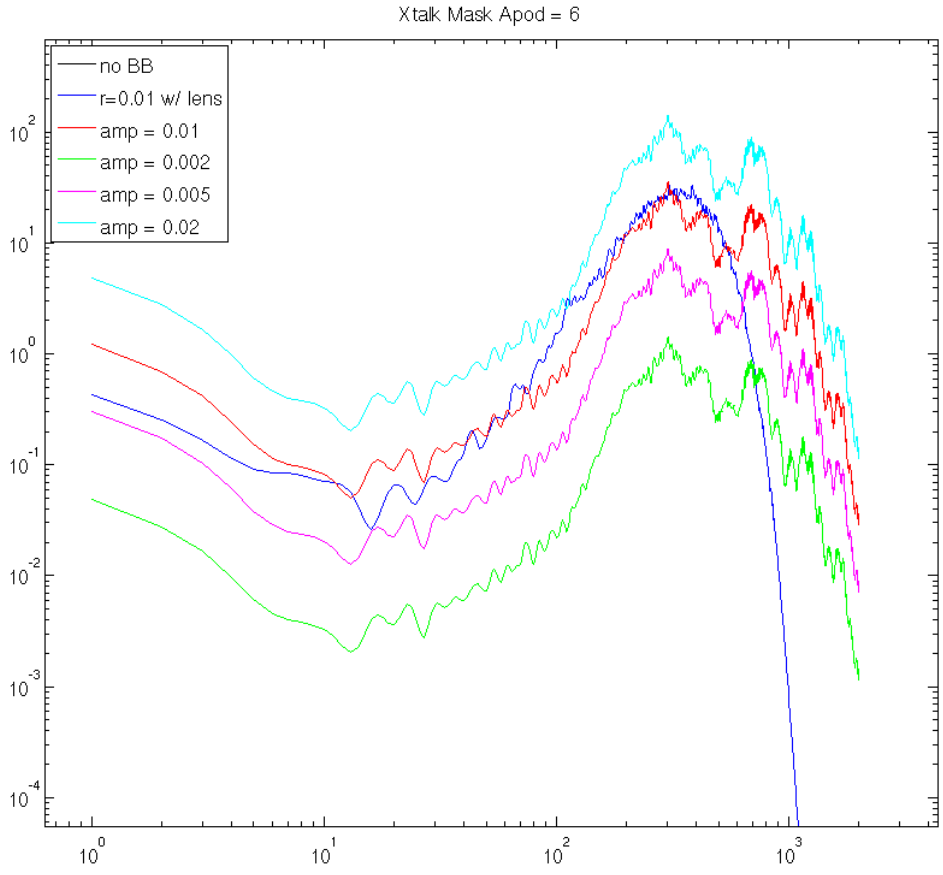


Figure 3.11: A comparison of recovered BB spectra for varying levels of crosstalk contamination in the maps. Figure courtesy of Tom Montroy.

## 3.9 Noise

The noise in the SPIDER system is a combination of noise from the TES detectors, noise from the SQUID readout system, and photon noise from the sky and instrument. It is important that the noise be low at science frequencies and well understood elsewhere, since the noise is inversely related to the overall sensitivity of the experiment and, therefore, to the science result.

### 3.9.1 Noise Model

We can think of noise as a random variable added to our true signal. Here we are using the variable $i$ to indicate that this is a current noise:

$$i_{meas}(t) = i(t) + n_i(t) \tag{3.4}$$

$$\langle n_i \rangle = 0, \langle n_i^2 \rangle = \sigma_{n_i}^2, \tag{3.5}$$

where $\sigma_{n_i}$ is the variance. The following equation describes the power spectral density (PSD) of the noise:

$$\sigma_{n_i}^2 = \int_0^\infty i_n^2(f) df. \tag{3.6}$$

The variance for Gaussian noise is uncorrelated as a function of frequency. Variances from uncorrelated noise sources add in quadrature. So for each component of the noise model, we will estimate a value and add the contributions in quadrature.

In order to understand the SPIDER noise, a noise model was developed to describe each component of the noise. The noise components include photon, phonon (thermal fluctuation), Johnson, excess and amplifier noise. This section is based on work done by Jeff Filippini. The noise model for TES bolometers is described in full detail in [51].

#### 3.9.1.1 Photon Noise

Shot noise in electronic systems originates from the fact that current actually consists of a flow of independent quanta (electrons). Shot noise is typically both temperature- and frequency-independent. Photon noise is the same phenomenon as shot noise, only it originates from the (quantized) particle nature of light. We expect photon noise to be the largest contribution to the unaliased noise in the science band of the SPIDER detectors.

Photons with Bose correlations in arrival times will add to the usual shot noise. The noise equivalent power (NEP) due to photon noise is

$$\mathrm{NEP}^2_{\mathrm{photon}} = 2h\langle\nu\rangle P_{\mathrm{opt}} + \frac{P^2_{\mathrm{opt}}}{2\Delta\nu}, \tag{3.7}$$

where $P_{\mathrm{opt}}$ is the optical power on the detectors, $\langle\nu\rangle$ is the band center, $\Delta\nu$ is the bandwidth, and $h$ is the Planck constant. Here the first term is considered the "shot" noise term and the second term is the "Bose" noise term. If the system is under flight-like loading, we are typically dominated by the shot noise term. If we are open to the room and on the aluminum transition, it turns out that the Bose noise term dominates.

For flight-like loading we can estimate a value for the contribution to the overall noise from photon noise by using the following typical values: $P_{\mathrm{opt}} = 0.9$ pW, $\nu = 150$GHz, and $\Delta\nu = 37.5$ GHz. Then,

$$\mathrm{NEP}_{\mathrm{photon}} \approx 14 \text{ aW}/\sqrt{\mathrm{Hz}}. \tag{3.8}$$

#### 3.9.1.2 Johnson Noise

Johnson noise (sometimes called Johnson-Nyquist noise) is a voltage noise from the Brownian motion of charge carriers inside an electrical conductor at equilibrium (i.e., regardless of applied voltage). It is a specific result of the Fluctation-Dissipation Theorem, which states that any dissipative element experiences temperature-dependent fluctuations due to coupling to thermal degrees of freedom.

The voltage noise due to Johnson noise is

$$v_n^2 = \langle (V - \langle V\rangle)^2\rangle = 4kTR, \tag{3.9}$$

where $k$ is Boltzmann's constant, $T$ is the resistor's temperature, and $R$ is the resistance of the resistive element.

There are two sources of Johnson noise in the TES circuit: the shunt resistor ($R_{\mathrm{sh}}$) and the TES resistance ($R_{TES}$) [51, 20]:

$$\begin{aligned}\mathrm{NEP}^2_{\mathrm{Johnson}} &= \mathrm{NEP}^2_{\mathrm{sh}} + \mathrm{NEP}^2_{\mathrm{TES}} \\ &= 4kT_{\mathrm{sh}}R_{\mathrm{sh}}I^2_{\mathrm{TES}}\frac{(\mathcal{L}_1 - 1)^2}{\mathcal{L}_1^2} + 4kTR_{\mathrm{TES}}I^2_{\mathrm{TES}}\frac{1}{\mathcal{L}_1^2},\end{aligned} \tag{3.10}$$

where $\mathcal{L}_1$ is the loop gain. Note that the Johnson noise of the TES resistor goes as the inverse of the square of the loop gain, which makes the DC contribution from this component several orders of magnitude smaller than that from the shunt resistor. This is due to the fact that the Johnson noise on the TES resistor is coupled to both the electrical and thermal circuits, and their correlated contributions cancel below the electrothermal feedback frequency.

We use the following typical values for the parameters in Eqn. 3.10 to get an estimate of the NEP contribution from Johnson noise: $R_{\rm sh} = 0.3\text{m}\Omega$, $R_{\rm TES} \approx 20\text{m}\Omega$, $I_{\rm sh} \approx 8\mu\text{A}$, $T_{\rm sh} = 350\text{mK}$, and $\mathcal{L}_1 \approx 20$.

We find

$$NEP_{\rm Johnson} \approx 2\text{aW}/\sqrt{\text{Hz}}. \tag{3.11}$$

#### 3.9.1.3 Thermal Fluctuation Noise

Thermal fluctuation noise is also known as phonon noise. Phonon noise arises from the random exchange of phonons between a thermal mass and its environment.

In analogy with Johnson noise, a thermal conductance has an equivalent power noise:

$$\text{NEP}^2_{\rm TFN} = 4kT^2G\gamma(T, T_b). \tag{3.12}$$

where $\gamma$ is a correction factor, k is the Boltzmann constant, $G$ is the thermal conductance of the link, $T$ is the temperature of the detector, and $T_b$ is the temperature of the bath. The correction factor $\gamma$ depends on the exponent of thermal conductance and on whether the phonon reflection from boundaries is specular or diffuse. It is a function of the temperature of the TES and typically takes a value between 0.5 and 1. It can be thought of as accounting for non-equilibrium temperature differences across the thermal link.

A rough number for this contribution to the noise for a SPIDER detector can be found using the following values: G = 15pW/K, $\gamma \approx 0.5$, and T $\approx$ 500mK.

So,

$$\text{NEP}_{\rm TFN} \approx 10\ \text{aW}/\sqrt{\text{Hz}}. \tag{3.13}$$

Excess noise at frequencies above our science band (see §3.9.1.5) indicate that that the above equation is describing an oversimplified model of the SPIDER TESs. The model should include internal thermal fluctuations across internal island conductances that look like excess Johnson noise. Additional complications to the model may include supercon-

ducting percolation effects or some other finite, temperature-dependent coupling.

#### 3.9.1.4 Amplifier Noise

Amplifier noise is a significant source of noise in the SPIDER system, especially while dark. It is approximately white to 2MHz and has a 1/f component. Both the warm and cold electronics contribute to amplifier noise. Much of the amplifier noise in the SPIDER system is aliased as a result of an avoidable property of the time-domain multiplexing used to read out the detectors. Although the detectors are only read out at 15kHz, the system must have the bandwidth to switch between detector rows every $\sim 2\mu$s and wait for the SQUIDs to settle before taking data. The upper limit of the bandwidth of the system is set by the readout card of the MCE, which has has analog-to-digital converters (ADCs) that operate at 50MHz.

If we sample at frequency $f_s$, all noise at $f > f_s/2$ is aliased back to $f \to |f - f_s/2|$ and the total noise variance is unchanged. The increase in current noise due to aliasing is proportional to the square root of the ratio of the bandwidth (BW) to the sampling frequency:

$$i_n(f) \to i_n(f)\sqrt{\frac{\mathrm{BW}}{f_s/2}}. \tag{3.14}$$

For SPIDER, $f_s = 15.15$ kHz and thus aliasing boosts SQUID noise by approximately 12 times. While this is not the leading contribution to the overall noise of the SPIDER detectors, it leads to a total NEI for the amplifier noise of approximately 45 pA/$\sqrt{\mathrm{Hz}}$. We can multiply this by a typical value for the responsivity of a detector dP/dI = 0.13 $\mu$V to get

$$NEP_{\mathrm{amp}} \approx 4\mathrm{aW}/\sqrt{\mathrm{Hz}}. \tag{3.15}$$

A fair amount of work was done by NIST (who create the SQUIDs used in the SPIDER system) to decrease aliasing by changing the SQUID design. This included reducing the SQUID noise current by adding input coil turns, reducing the SQUID bandwidth, and reducing the detector normal resistance. These changes improved the uniformity of the noise of on the detectors at science frequencies, although they did not improve the total noise of the lowest noise detectors.

Table 3.3: Noise Budget for 90GHz and 150GHz detectors

| | Photon | Johnson | Phonon | Amplifier | Total |
|---|---|---|---|---|---|
| 90GHz | 11 | 2 | 10 | 4 | 16 |
| 150GHz | 14 | 2 | 10 | 4 | 18 |

All values have units of aW/$\sqrt{\text{Hz}}$.

#### 3.9.1.5 Excess Noise

Our measured noise somewhat exceeds the noise predicted by the model, especially at kilohertz frequencies where we see an "excess noise bump" in our noise spectra (see the grey spectrum in Fig. 3.12). Excess noise is a known feature of TES systems and is not fully understood. There are several plausible explanations for it: internal thermal fluctuations, phase transition effects, and nonlinear or non-equilibrium behavior. The main concern of excess noise is that it will be aliased back into the science band, since a significant amount of power from the excess noise extends beyond the Nyquist frequency of our readout system. As described in the previous section, several changes were made to the readout system to reduce the aliasing from this noise.

### 3.9.2 Total Noise

We can add the contributions from each noise component to get an estimate for the total NEP:

$$\text{NEP}_{\text{tot}}^2 = \text{NEP}_{\text{photon}}^2 + \text{NEP}_{\text{Johnson}}^2 + \text{NEP}_{\text{TFN}}^2 + \text{NEP}_{\text{amp}}^2 \tag{3.16}$$

$$\text{NEP}_{\text{tot}} \approx 18 \text{ aW}/\sqrt{\text{Hz}}. \tag{3.17}$$

Estimated values for each noise component can be found in Tab. 3.3.

A fuller description of the noise components mentioned above can be used to get a frequency dependent model for the SPIDER noise that can be seen in Fig. 3.12. This formalism is worked through in detail in [51]. Note that the actual measured noise ($20 - 30$ aW/$\sqrt{\text{Hz}}$) is higher than the noise predicted by the model (18 aW/$\sqrt{\text{Hz}}$).

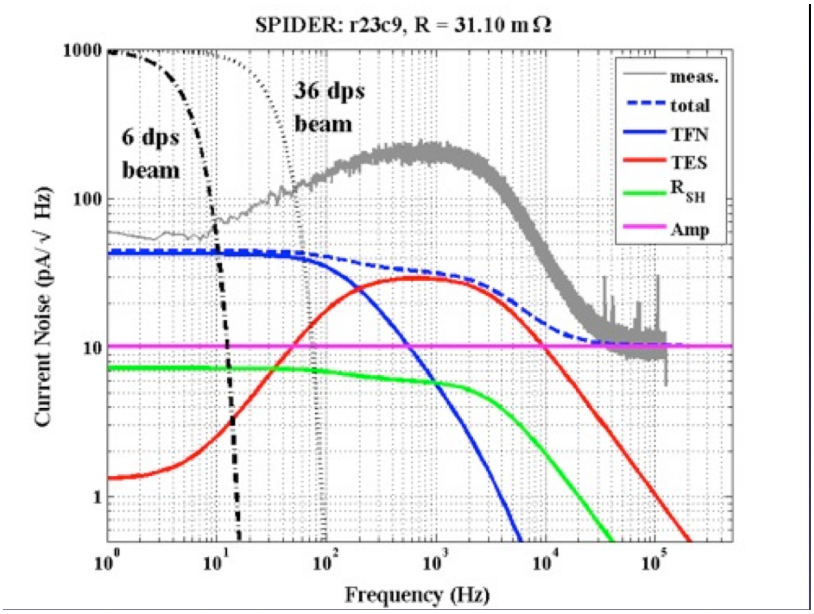


Figure 3.12: SPIDER noise model with a comparison to an actual noise spectrum. The blue dotted line is the total predicted noise from each of the components in the model, including the thermal fluctuation noise (blue), Johnson noise (red and green) and amplifier noise (purple). Figure courtesy of Jeff Filippini.

### 3.9.3 Expected Performance

The noise equivalent power (NEP) can be turned into a noise equivalent temperature (NET) by dividing the NEP for each detector by its optical responsivity (dP/dT). The per-detector NET is approximately 120 $\mu K_{CMB}\sqrt{s}$. The NET for the entire experiment is inversely proportional to the number of detectors. The final NET for the 96GHz detectors is expected to be $\approx 5.2\ \mu K_{CMB}\sqrt{s}$, and the final NET for the 150GHz detectors is expected to be $\approx 3.8\ \mu K_{CMB}\sqrt{s}$, for a combined instrument NET of $\approx 3.1\ \mu K_{CMB}\sqrt{s}$.

From the NET we can get an estimate for the map depth of a SPIDER flight using the following:

$$\text{map depth} = \frac{\text{NET}}{\sqrt{\text{flight time} \times \text{duty cycle/map area}}} \tag{3.18}$$

$$\text{map depth (96GHz)} \approx 0.25 \mu K_{CMB} \cdot \text{deg}$$

$$\text{map depth (150GHz)} \approx 0.18 \mu K_{CMB} \cdot \text{deg}.$$

The per detector NETs for the Planck satellite for their 100GHz and 143GHz channels are 50 $\mu K_{CMB}\sqrt{s}$ and 62 $\mu K_{CMB}\sqrt{s}$, respectively [85]. That translates to a map depth

(using the same order-of-magnitude calculation as above) of 0.5 $\mu K_{CMB}$ sq. deg for the 143GHz map and of 0.4 $\mu K_{CMB}$ sq. deg for the 100 GHz map. So while an individual Planck detector has lower noise than an individual SPIDER detector, SPIDER has so many more detectors on the sky (thousands, to Planck's eight) that the final map depth for SPIDER is expected to be lower. Unlike SPIDER, Planck has two additional frequency bands with polarized detectors (which will aid with foreground rejection) and covers essentially the entire sky.

Another relevant comparison might be to the BICEP2 map depth, which is quoted as 87.8 $nK_{CMB} \cdot$ deg in [6]. While the BICEP2 map depth is roughly twice the expected SPIDER map depth, SPIDER's data set will cover roughly five times the sky area as BICEP2. SPIDER will also have the advantage of an additional frequency band to help constrain the power spectrum.

While the noise is an important component of how sensitive SPIDER will be, our final estimated error bars are also a function of sky coverage, frequency bands, and integration time. Fig. 3.13 shows the estimated errors bars on the B-mode spectrum for SPIDER in comparison to BICEP2 and Planck. SPIDER is expected to have smaller error bars than both BICEP2 and Planck at multipoles corresponding to the peak of the gravitational wave spectrum.

## 3.10 Conclusion

SPIDER's tight control of systematics is necessary to achieve the sensitivity to measure the B-mode spectrum to an equivalent sensitivity of $r = 0.03$. Although many of the potential systematic errors have been simulated to set measurement benchmarks, they could be improved by being re-simulated with updated flight parameters, scan strategies, and telescope frequencies. All of the simulations in MacTavish et. al. and O'Dea et. al. would benefit from being redone using parameters for a 20 day McMurdo flight, rather than a four-day Alice Springs flight. Additionally, a simulation using an improved pipeline that accounts for the non-idealities of the HWP would be extremely helpful for data analysis. The next two chapters will describe how we measure the instrument systematics detailed here.

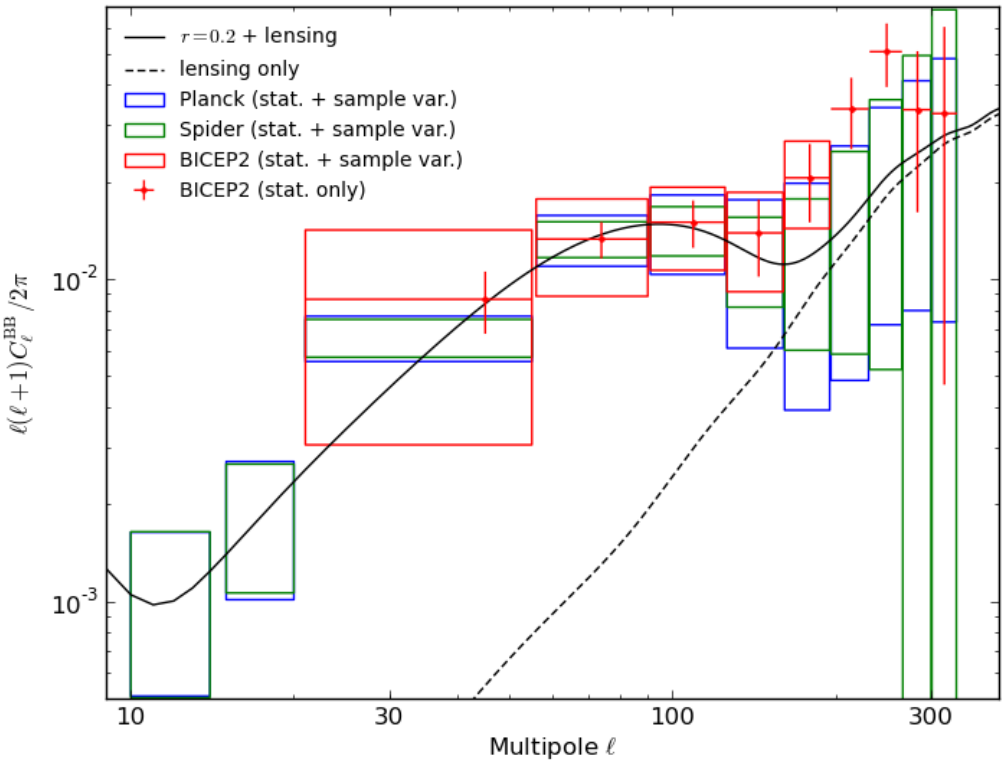


Figure 3.13: A forecast of the SPIDER statistical error bars on the B-mode spectrum in comparison to the current BICEP2 measurements and published Planck sensitivities. These error bars include contributions from sample variance. This figure does not account for foregrounds or instrument systematics. Figure courtesy of Lorenzo Moncelsi.

# Chapter 4

# Instrument Characterization: Efficiency, Spectra, and Noise

## 4.1 Introduction

The characterization of the SPIDER instrument consists of measurements of the optical efficiency, detector device parameters, mm-wave spectral bands, noise, and beams. These measurements demonstrate that the instrument is both sensitive enough in the appropriate mm-wave spectral bands and has sufficient control of systematic uncertainties that it will be able to achieve the science goal of measuring the B-mode spectrum to the sensitivity required. We use our measurements of the SPIDER detectors to help select good detectors for deployment and to feed information back to the fabrication team that will help improve the detectors. This section describes the techniques we use to make these measurements as well as the results for each focal plane.

Characterization of the SPIDER instrument is guided by the systematic error goals determined by the simulations. To make these measurements of sufficient accuracy and precision, the SPIDER team designed and built a number of calibration apparatuses and developed new techniques for these measurements. The following chapters describe our measurements of relative gain, beam characteristics, absolute and relative polarization angles, telescope pointing, far sidelobes, spectra, and noise, and compares them to the benchmark values. SPIDER currently meets most of the benchmark values, and will be further tested before flight.

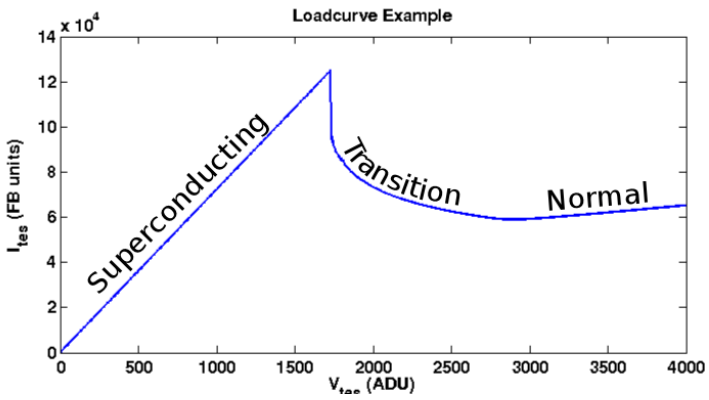


Figure 4.1: An example load curve for the titanium transition. There is a $\phi_0$ slip that occurs around 1700 ADU.

## 4.2 The Loadcurve

A "loadcurve" is one of most fundamental tools used in the characterization of the SPIDER TES bolometers. To take a loadcurve, we use a high bias voltage and a quick thermal pulse to get all of the TES detectors into the normal regime. The voltage bias is then ramped down, generally by steps of 100 ADU (analog to digital converter units) if we want to look at the aluminum transition, or by steps of 5-10 ADU if we want to look at the titanium transition. As the bias ramps down, the TES goes through its transition region and then eventually goes superconducting. An example loadcurve is shown in Fig. 4.1.

A simplified version of the circuit diagram for the detectors (Fig. 4.2) may be helpful in understanding what a loadcurve does and why it is helpful. From the data taken during the loadcurve, we can easily get the resistance of the TES, both when it is normal and during its transition. From there, we can calculate the amount of Joule power it takes to keep the TES in its transition region.

In equilibrium, the power flowing through the TES is described by

$$Q + P_{Joule} - \int_{T_{bath}}^{T} G(T)dT = 0 \tag{4.1}$$

$$P_{Joule} = I_{TES}^2 R_{TES} = \frac{V_{TES}^2}{R_{TES}}, \tag{4.2}$$

where $Q$ is the antenna power (heats the island), $\int_{T_{bath}}^{T} G(T)dT$ describes the cooling through the legs of the island, and $P_{Joule}$ is the power dissipated by the TES. Voltage-biasing the

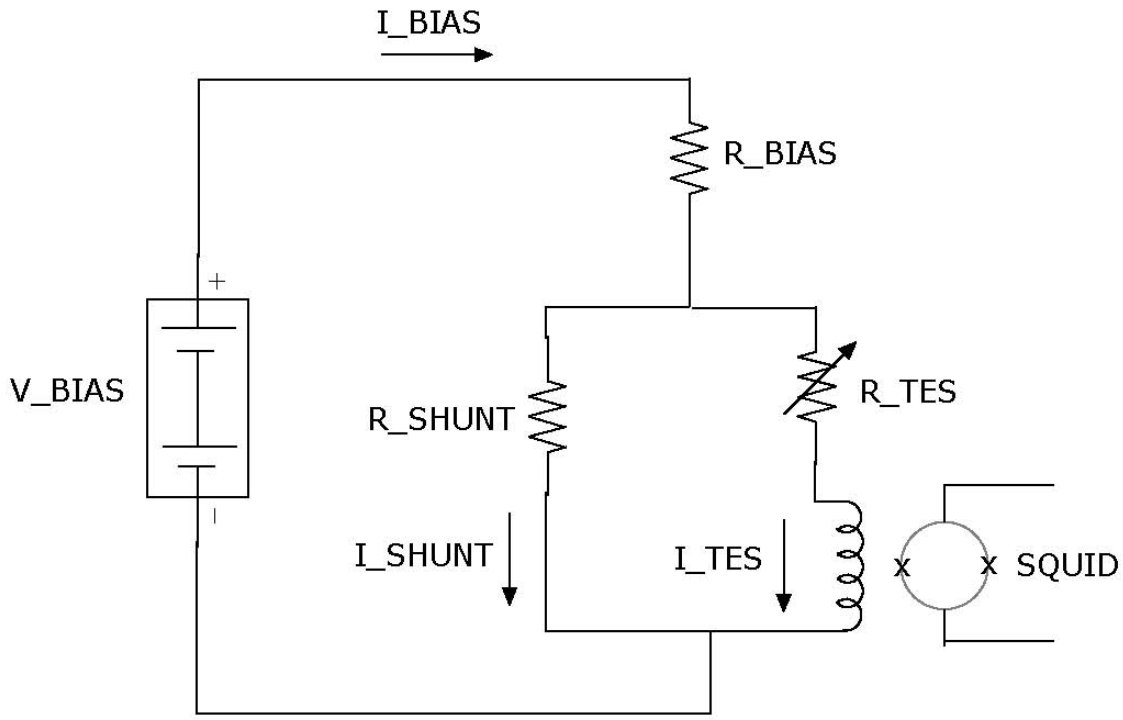


Figure 4.2: A simplified version of the detector circuit diagram. The voltage $V_{BIAS}$ is what we can control via the MCE. The shunt resistors voltage bias the TESs and are typically around $3m\Omega$. The shunt resistors are much lower than the resistance of the TESs, unless the detectors have gone superconducting or are very low in their transitions. This means that most of the current flowing through the two branches goes through the shunt branch, which has the effect of keeping a steady voltage across the TES. Figure courtesy of Amy Trangsrud.

TESs puts them in the regime of negative electrothermal feedback (ETF), which helps keep them in their transition regions. If the temperature on the island rises, the resistance of the TES will also rise, and the Joule power will decrease, thus cooling the island. If the temperature on the island falls, the resistance of the TES will fall and the Joule power will increase, thus warming the island. Negative ETF keeps the island temperature, and therefore the temperature of the TES, stable.

We can calculate $V_{TES}$ and $R_{TES}$ (and therefore $P_{Joule}$) in the following way:

$$\begin{aligned} V_{shunt} &= V_{TES} \\ I_{shunt} &= I_{bias} - I_{TES} \\ I_{shunt} * R_{shunt} &= I_{TES} * R_{TES} \\ R_{TES} &= \frac{I_{shunt}}{I_{TES}} R_{shunt} \\ R_{TES} &= \frac{I_{bias} - I_{TES}}{I_{TES}} R_{shunt} \\ R_{TES} &= (\frac{I_{bias}}{I_{TES}} - 1) R_{shunt}. \end{aligned} \tag{4.3}$$

Once we have calculated the Joule power necessary to keep a particular detector on transition, we can begin to vary the other terms in Eqn. 4.1, such as the amount of optical power incident on the detectors ($Q$) or the temperature of the focal plane unit ($T_{substrate}$). Varying these parameters in systematic ways allows us to use the loadcurve as the foundation of other measurements.

## 4.3 Measuring Device Parameters

The TES devices are parameterized by their thermal conductances ($G_0$), the temperature dependence of the conductance (characterized by a power law index, $\beta$), and critical temperatures ($T_c$). The critical temperature is the temperature at which the device goes normal. The best way to measure these parameters is by taking a series of loadcurves, all at differing substrate temperatures. In practice, we change the substrate temperature by heating the focal plane with a small high current heater mounted at the edge.

If the optical power $Q$ in Eqn. 4.1 is kept constant (which is easy during a dark run or

on dark detectors), then in equilibrium, the power flowing through the TES is described by

$$\Delta P_{Joule} = \Delta P_{legs}. \tag{4.4}$$

Recall from §2.6.2 that the power through the thermal link of the island legs is fully described by the following equation:

$$P_{legs} = \frac{G_0 T_0}{1+\beta}\left[\left(\frac{T_{TES}}{T_0}\right)^{1+\beta} - \left(\frac{T_{bath}}{T_0}\right)^{1+\beta}\right], \tag{4.5}$$

and that the temperature dependence of the thermal conductance goes as a power law:

$$G(T) = G_0\left(\frac{T}{T_0}\right)^{\beta}. \tag{4.6}$$

Thus, $G_0$ is equivalent to the value of the thermal conductance at the temperature $T_0$: $G_0 = G(T_0)$

By taking load curves at several values of the substrate (FPU) temperature, we can use the above equation to fit for $G_0$, $\beta$, and $T_c$. The parameter $G_0$ will mostly affect the slope of the fit, while $\beta$ will affect the curvature. Taking these loadcurves at as broad a temperature range as possible will improve the uncertainty on $\beta$. An example of this measurement and a fit to Eqn. 4.5 can be seen in Fig. 4.3.

A measurement of the device parameters is only possible during dark runs (when the focal plane is covered by a 300mK plate) or on the (always) dark TES detectors. In an ideal world, each focal plane would be run dark to get this measurement in addition to the light runs to get some of the other measurements (e.g., optical efficiencies and spectra). Most of the measurements of the device parameters for the SPIDER focal planes were done using the dark TES data, since we are rarely able to run a dark focal plane. Besides the fact that this leaves us with extremely small statistics (four pixels/eight TESs per focal plane), the measurement is also difficult because the fit to $T_c$ is degenerate with stray loading and tile heating. A table of device parameters for each focal plane can be found in Table 5.2.

Table 4.1: Device Parameters for all FPUs.

| Focal Plane | Tile ID | $G_0$ (pW/K) | $T_c$ (K) | $\beta$ | $P_{sat}$ (pW) |
|---|---|---|---|---|---|
| X1 | T130204.3 | 16.2 | 0.481 | 1.8 | 2.04 |
| X1 | T130204.4 | 16.2 | 0.454 | 1.8 | 1.58 |
| X1 | M130130 | 16.8 | 0.484 | 2.5 | 2.06 |
| X1 | T130204.2 | 13.4 | 0.496 | 1.7 | 1.94 |
| X2 | T110609.3 | 11.0 | 0.486 | 2.3 | 1.39 |
| X2 | T110609.2 | 11.0 | 0.506 | 2.2 | 1.68 |
| X2 | T110609.4 | 13.6 | 0.509 | 2.2 | 2.13 |
| X2 | T110606.1 | 13.8 | 0.481 | 2.1 | 1.70 |
| X3 | W130311.2 | 23.8 | 0.482 | 2.5 | 2.86 |
| X3 | M130319 | 13.4 | 0.529 | 2.5 | 2.45 |
| X3 | W130311.3 | 15.7 | 0.508 | 2.5 | 2.40 |
| X3 | W130311.1 | 16.8 | 0.509 | 2.5 | 2.59 |
| X4 | T120823.4 | 15.0 | 0.515 | 2.0 | 2.49 |
| X4 | M120916 | 18.6 | 0.412 | 1.7 | 1.10 |
| X4 | T121127.1 | 14.2 | 0.501 | 2.6 | 2.03 |
| X4 | T120823.3 | 16.6 | 0.505 | 2.0 | 2.54 |
| X5 | JAB120109.1 | 19.1 | 0.454 | 2.0 | 1.81 |
| X5 | M130521 | 19.1 | 0.515 | 2.2 | 3.14 |
| X5 | W130508.3 | 18.3 | 0.457 | 2.0 | 1.79 |
| X5 | W130508.1 | 21.6 | 0.508 | 1.9 | 3.40 |
| X6 | M121206 | 13.8 | 0.534 | 2.0 | 2.64 |
| X6 | W130709.1 | 20.0 | 0.526 | 1.9 | 3.62 |
| X6 | T130508.1 | 14.0 | 0.536 | 1.7 | 2.73 |
| X6 | T121127.2 | 11.8 | 0.529 | 1.6 | 2.20 |

Saturation powers are calculated assuming no optical loading on the detectors.

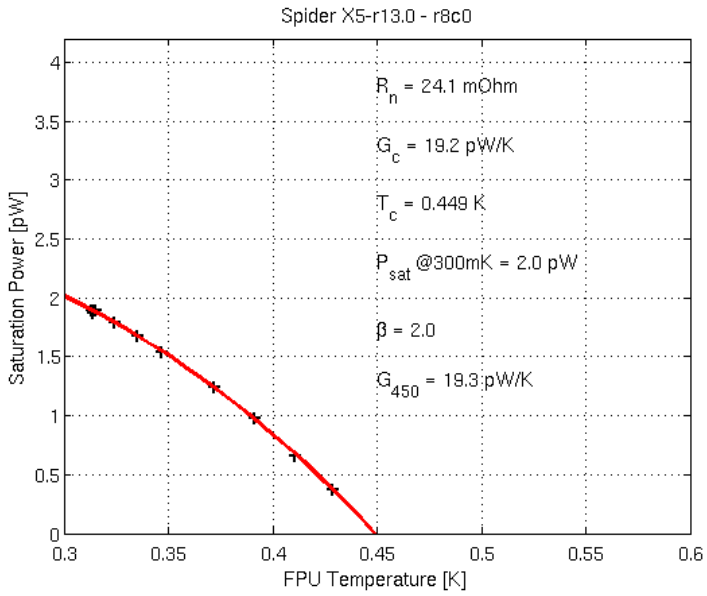


Figure 4.3: An example of the data and fit for device parameters from X5. Figure courtesy of Lorenzo Moncelsi.

## 4.4 Optical Efficiency

Optical efficiency ($\eta(\nu)$) is the unitless ratio of how much power the detectors absorb to how much power is incident upon them. Recall from §3.9 that the NET is inversely proportional to the optical response of the detectors. So a higher optical efficiency means that the detectors will be more sensitive (i.e., have a lower NET). We measure optical efficiency by taking sets of loadcurves at differing levels of incident power and fixed tile temperature (in contrast to the measurement of the device parameters). One loadcurve is taken while the aperture is covered with a black sheet of Eccosorb at room temperature (300K). A second loadcurve is taken while the aperture is covered with a tray of liquid nitrogen (77K), which also contains sheets of Eccosorb. (The Eccosorb is there to assure that we are looking at a blackbody spectrum.) From these loadcurves, we can get a measure of how much power it takes to get the detectors into their transition regions in each case. The difference in the (Joule) power necessary between the loadcurves at the two different temperatures, along with some calibration factors, is the optical efficiency of our detectors. If $P_R$ is the power necessary to get a detector onto transition while looking at a room temperature load (300K) and $P_N$ is the power necessary to get the detector onto transition while looking at a liquid

nitrogen load (77K), then the optical response $dP/dT$ is

$$dP/dT = \frac{P_N - P_R}{300K - 77K}. \tag{4.7}$$

These powers are the Joule powers discussed in Section 4.2. It should be noted that the linearity of the TES response (created by negative electrothermal feedback) allows us to assume this relation between the large-scale and small-scale signal.

To calculate $\eta$, we need to know how much power was incident on the bolometers. The spectral radiance of an unpolarized blackbody (per unit area, frequency, and solid angle) at temperature T, as observed by a diffraction-limited, single-moded detector is

$$dP = \frac{2h\nu^3}{c^2}\frac{1}{e^{h\nu/kT} - 1}\, d\nu\, dA\, d\Omega. \tag{4.8}$$

Each polarization mode contributes half of this amount, so we divide by two when dealing with polarized optics. For a diffraction limited, single-mode receiver, $\int dA d\Omega = \lambda^2 = \frac{c^2}{\nu^2}$, so the incident power is

$$P = \int_0^\infty \frac{h\nu}{e^{h\nu/kT} - 1}\, d\nu. \tag{4.9}$$

The optical efficiency, $\eta(\nu)$, is then defined such that the power absorbed by the device when viewing a beam filling blackbody is

$$Q = \int_0^\infty \eta(\nu)\frac{h\nu}{e^{h\nu/kT} - 1}\, d\nu. \tag{4.10}$$

If the focal plane temperature is kept constant, then a change in power flowing through the island legs between the two loadcurves is negligible and Eqn. 4.1 reduces to

$$\Delta Q \approx \Delta P_{Joule}. \tag{4.11}$$

A full description of the optical efficiency as a function of frequency requires the spectral passband, $F(\nu)$, of the detector. Then the optical efficiency becomes

$$\eta(\nu) = \frac{dP_{Joule}}{d\left(\int_0^\infty F(\nu)\frac{h\nu}{e^{h\nu/kT}-1}d\nu\right)}F(\nu) \tag{4.12}$$

For ease of comparison between detectors, we typically assume each detector has a 25%

bandwidth around the band center $\nu_0$ (90GHz or 150GHz): $\eta(\nu) = \eta_0$ for $(0.875\nu_0 < \nu < 1.125\nu_0)$ and $\eta(\nu) = 0$ otherwise. Then, the optical efficiency becomes

$$\eta_0 = \frac{dP_{Joule}}{d(\int_{\nu_1}^{\nu_2} \frac{h\nu}{e^{h\nu/kT}-1}\, d\nu)}, \tag{4.13}$$

where $\nu_1 = 0.875\nu_0$ and $\nu_2 = 1.125\nu_0$. In the limit of high temperatures or low frequencies, $h\nu << kT$, (the Rayleigh-Jeans limit) the integral in the denominator can be simplified to $kT\Delta\nu$, where $\Delta\nu$ is the bandwidth, $0.25\nu_0$.

The expression for optical efficiency finally becomes

$$\eta_0 = \frac{|dP/dT_{RJ}|}{0.25k\nu_0}. \tag{4.14}$$

where $dT_{RJ}$ indicates that we are using an expression for optical efficiency that was derived in the Rayleigh-Jeans limit.

The typical SPIDER detector has an end-to-end optical efficiency of 30%-40%. This includes absorption, scattering and reflections from all the elements in the optical chain.

A table of optical efficiencies can be found in Table 4.2. Plots of the optical responses and efficiencies of each detector can be found in Figs. 4.4-4.7. Plots of the normal resistance of each detector, which is frequently calculated in conjunction with this measurement, can be found in Figs. 4.8-4.9. In these figures, blank pixels indicate detectors for which we do not have data. Entire columns of missing figures are typically due to failures in the SQUID Series Arrays, which can be replaced or repaired prior to flight. Individual blank pixels could be due to failures in the detectors themselves (overetching or other problems during the fabrication process) or to failures in the first stage SQUIDs used to read them out. The typical yield for working detectors on SPIDER tiles is 80%-90%.

Table 4.2: Optical Efficiencies for all FPUs

| Focal Plane | Tile ID | Optical Efficiency |
|---|---|---|
| X1 | T130204.3 | 45% |
| X1 | T130204.4 | 41% |
| X1 | M130130 | 49% |
| X1 | T130204.2 | 45% |
| X2 | T110609.3 | 29% |
| X2 | T110609.2 | 29% |
| X2 | T110609.4 | 30% |
| X2 | T110606.1 | 29% |
| X3 | W130311.2 | 35% |
| X3 | M130319 | 35% |
| X3 | W130311.3 | 38% |
| X3 | W130311.1 | 35% |
| X4 | T120823.4 | 40% |
| X4 | M120916 | 33% |
| X4 | T121127.1 | 39% |
| X4 | T120823.3 | 38% |
| X5 | JAB120109.1 | 31% |
| X5 | M130521 | 32% |
| X5 | W130508.3 | 28% |
| X5 | W130508.1 | 31% |
| X6 | M121206 | 43% |
| X6 | W130709.1 | 35% |
| X6 | T130508.1 | 41% |
| X6 | T121127.2 | 46% |

These values for the optical efficiencies in this table are based on the assumption of 25% top hat band.

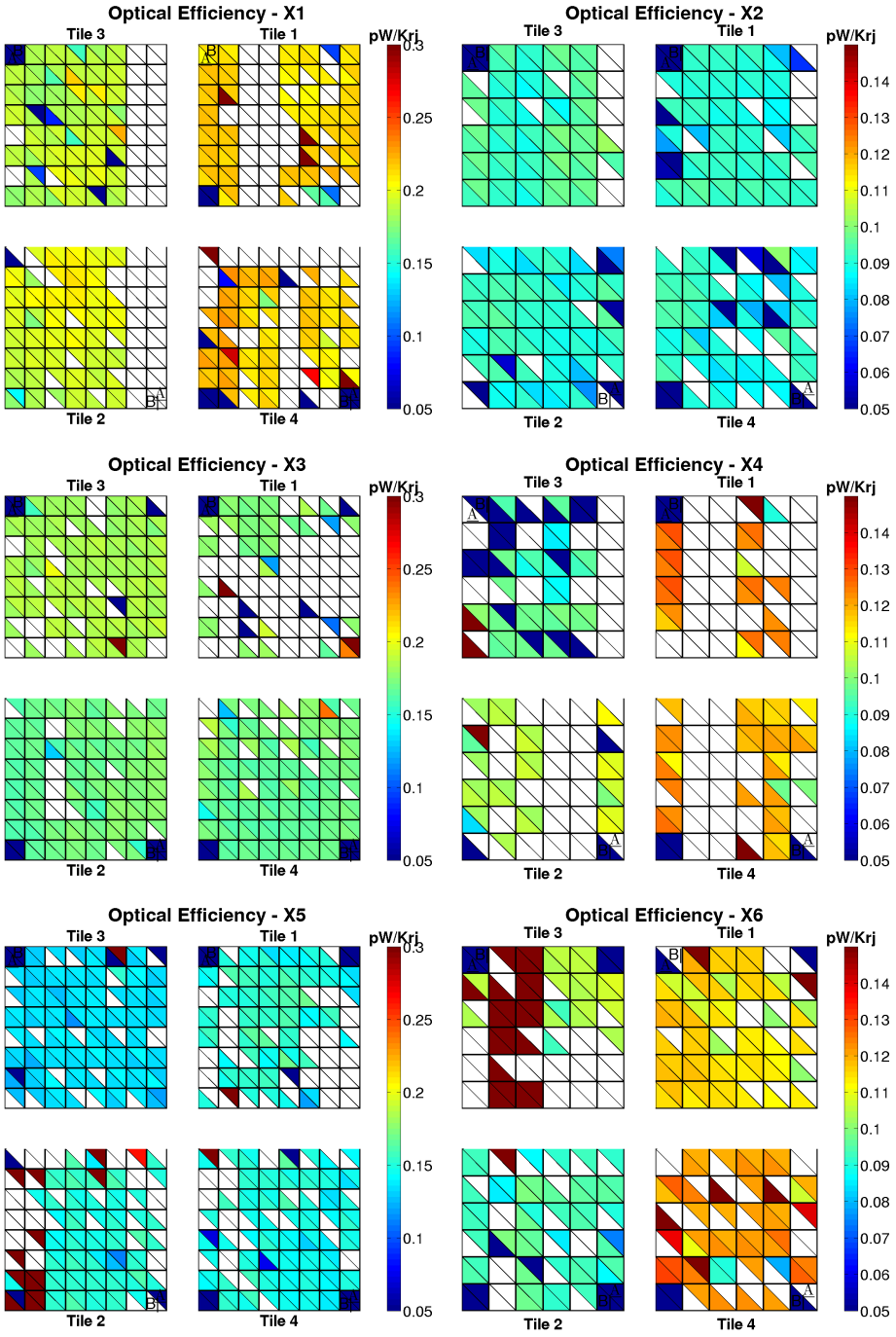


Figure 4.4: Optical Efficiency in $pW/K_{RJ}$ for all FPUs (test cryostat).

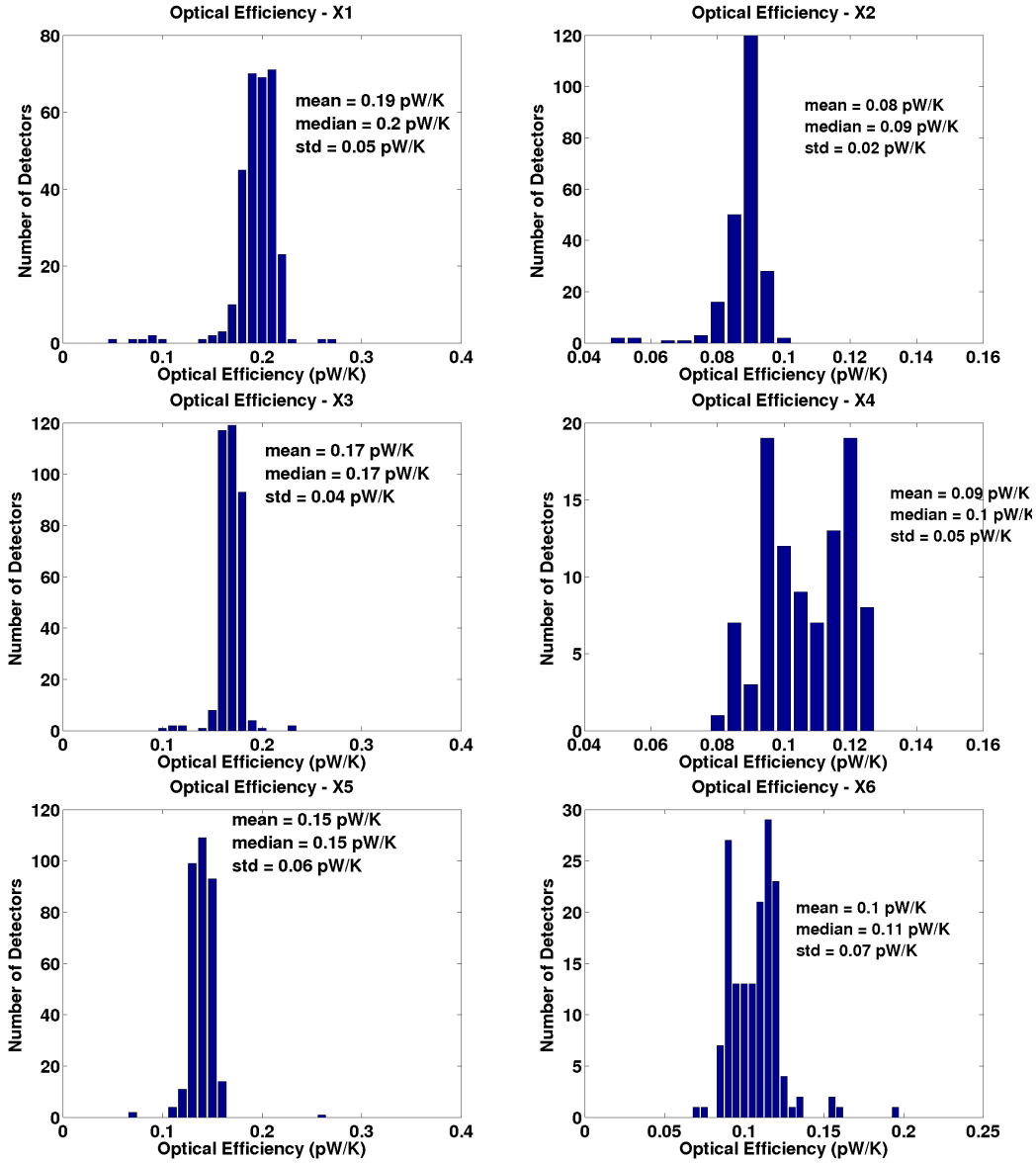


Figure 4.5: Histograms of optical efficiency in $pW/K_{RJ}$ for all FPUs (test cryostat).

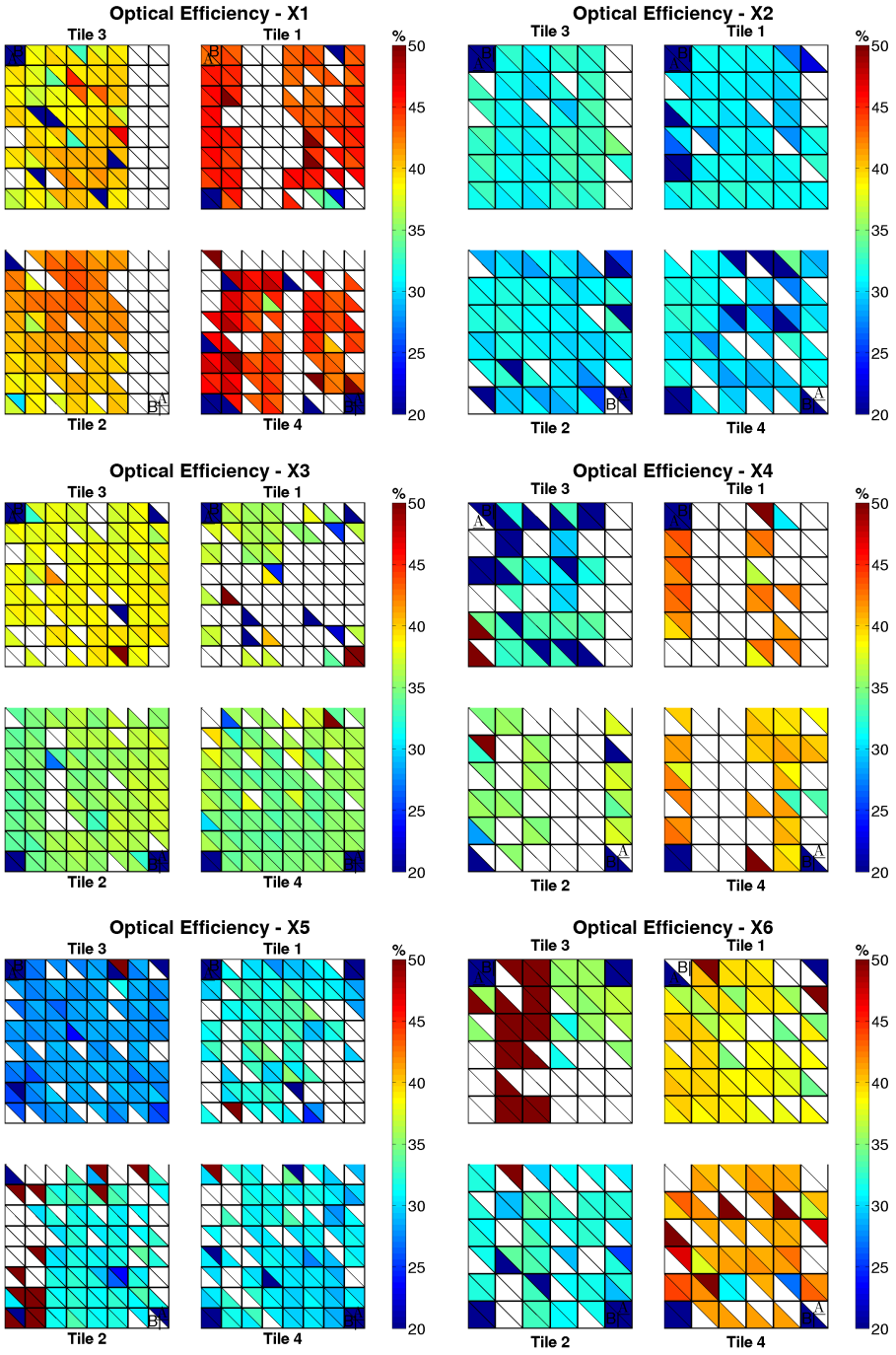


Figure 4.6: Optical Efficiency in % for all FPUs (test cryostat).

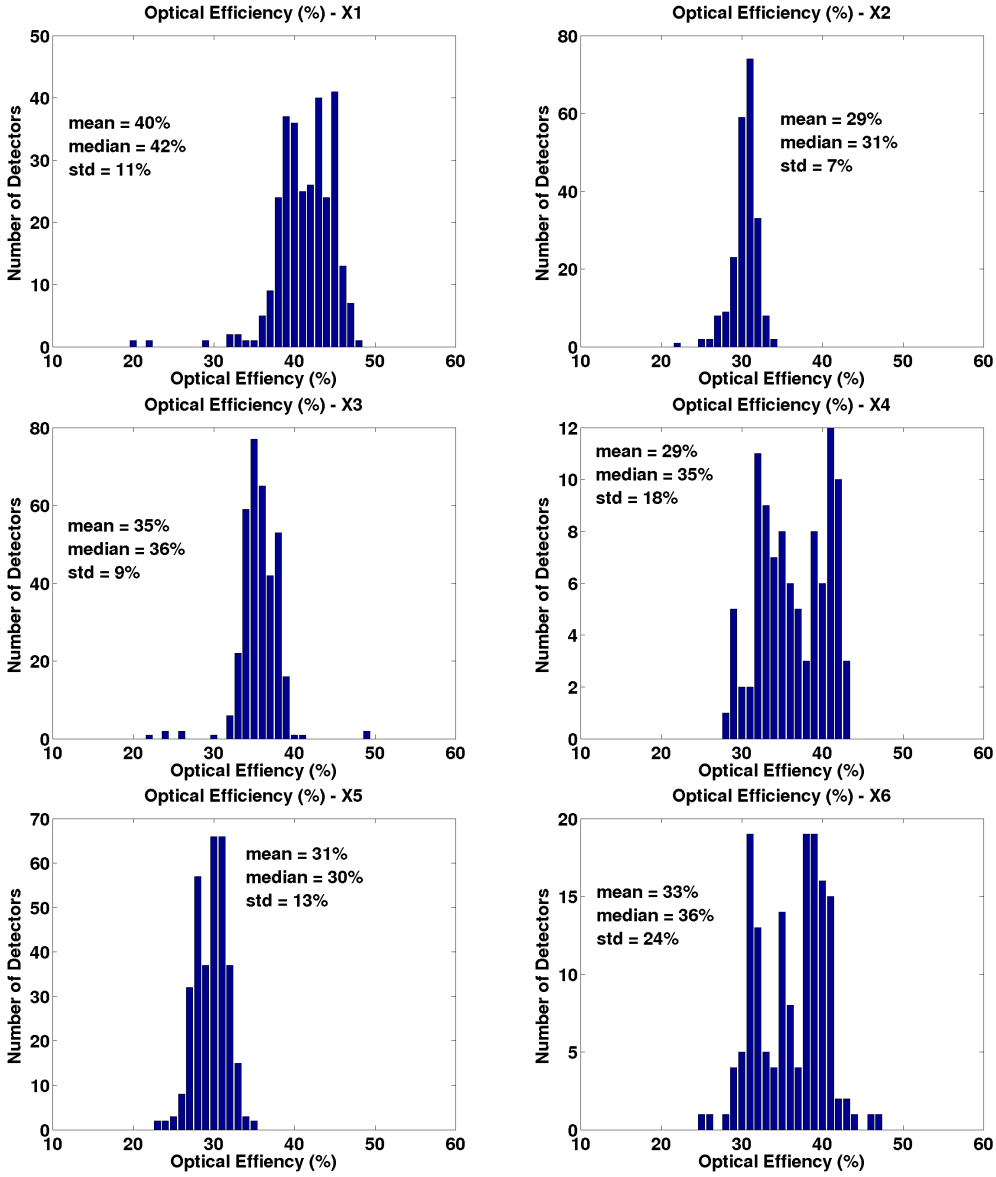


Figure 4.7: Histogram of optical efficiency in % for all FPUs (test cryostat).

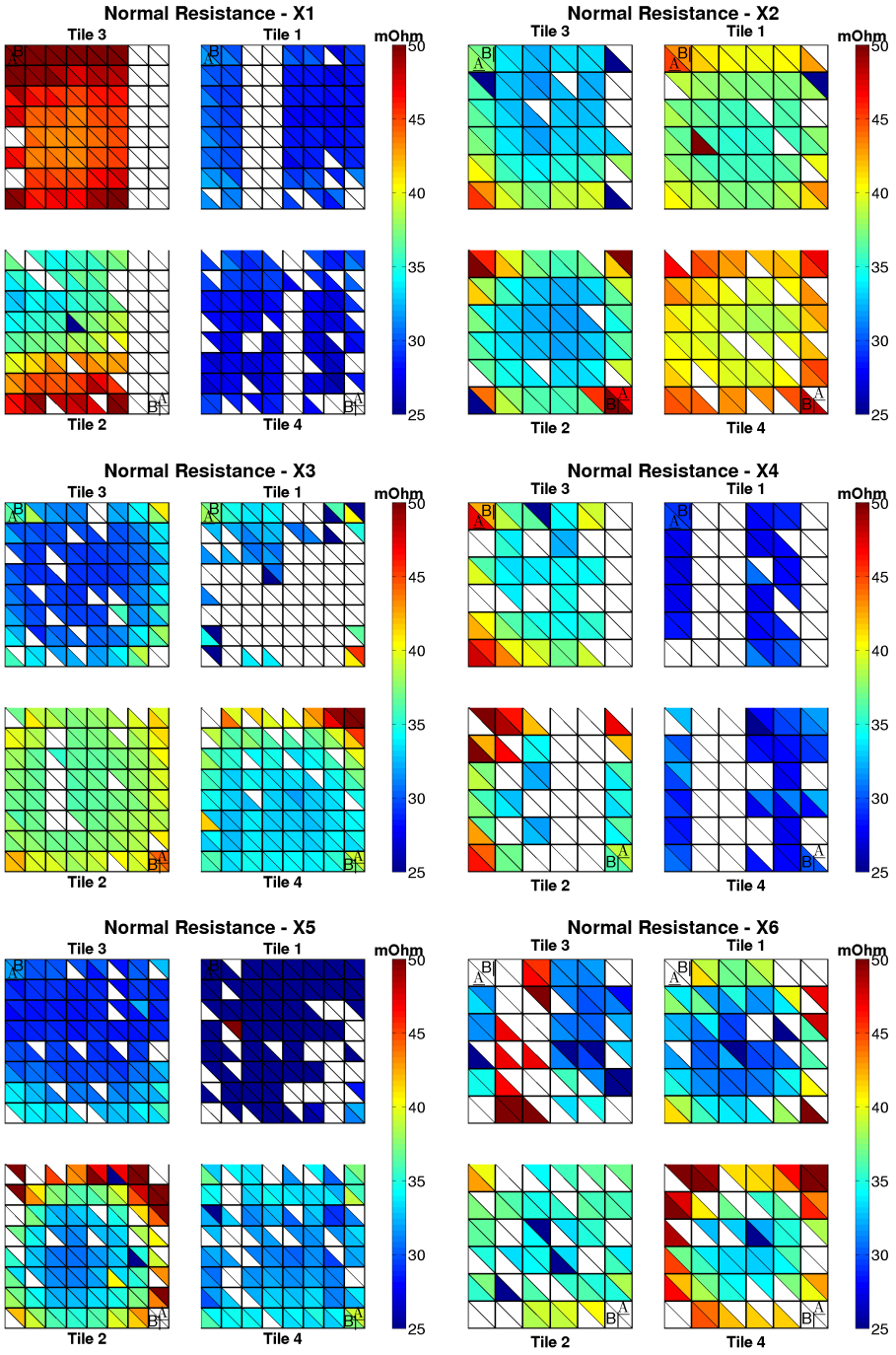


Figure 4.8: Normal resistance in $m\Omega$ for all FPUs (test cryostat).

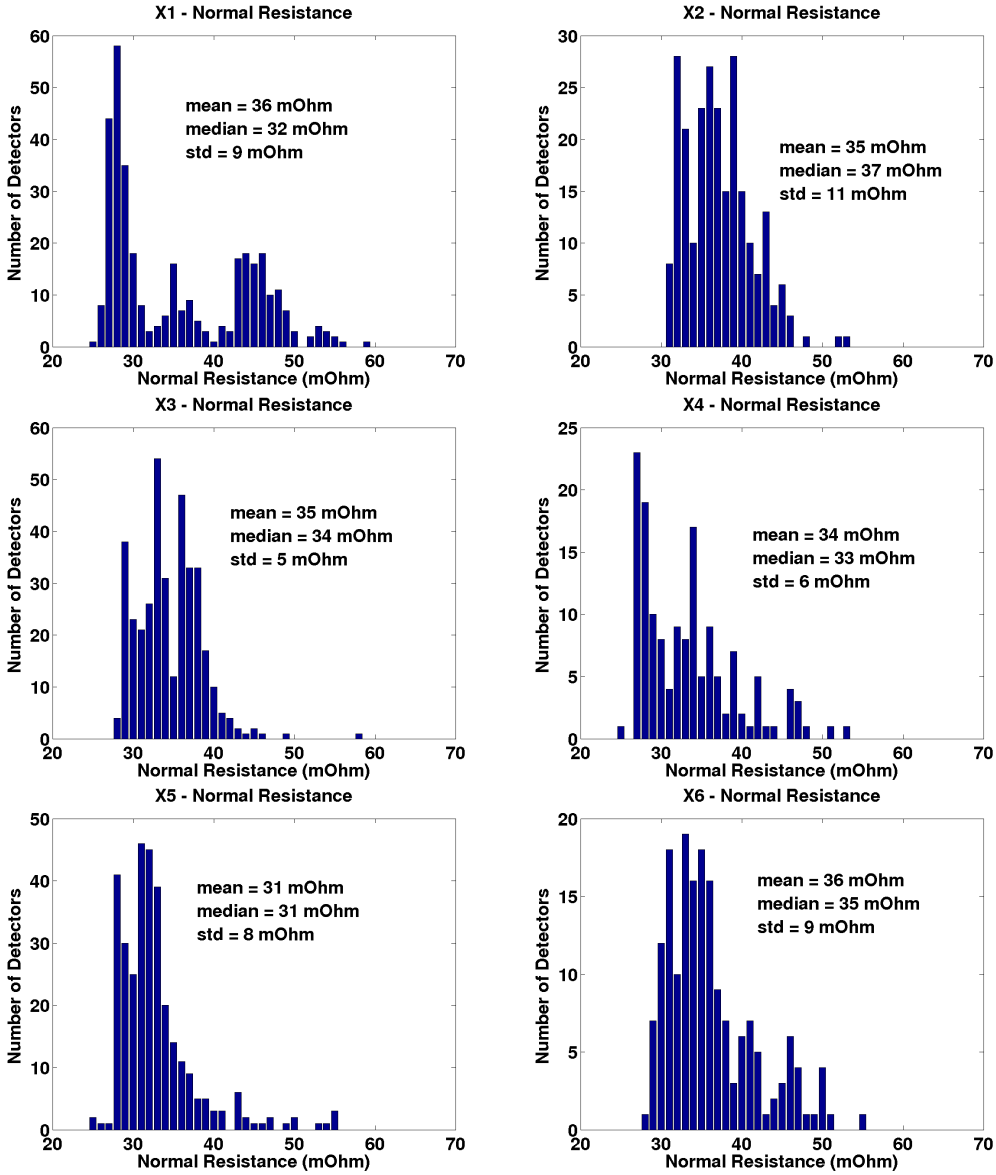


Figure 4.9: Histograms of normal resistance in $m\Omega$ for all FPUs (test cryostat).

## 4.5 Bandpass Spectra

The spectral response of the SPIDER detectors is chosen to maximize sensitivity to the CMB and minimize contamination from atmospheric lines (e.g., oxygen at 118GHz and water at 183GHz) and other foregrounds (e.g., galactic CO, which has lines at 115GHz and 230GHz). The bandwidth and bandcenter of each detector are set by the antenna design and the LC filters in the chips. Fourier transform spectroscopy is the primary method by which we determine the full bandpass spectra of the SPIDER detectors.

### 4.5.1 The FTS

A Fourier Transform Spectrometer (FTS) was built for SPIDER by Jon Gudmundsson while he was a graduate student at Princeton University. It is essentially a polarized Michelson interferometer with a moving mirror (Fig. 4.10a), also known as a Martin-Puplett interferometer [57]. Light from a source is collimated with a parabolic mirror and then split into two beams by a wire grid beam splitter. One beam travels down the fixed leg and the other down the leg with the scanning mirror. Each leg is terminated by a rooftop mirror (an orthogonal assembly of two plane mirrors attached to each other along one "roof" edge). Rooftop mirrors are often used in Fourier Transform spectroscopy because they are relatively insensitive to misalignment. The light travels down each leg, reflects off this mirror, and recombines at the beam splitter. The resultant beam is then detected by the SPIDER bolometers. The mirror is scanned back and forth at a fixed velocity. As it scans, the light from the two legs interferes with itself, producing a pattern of constructive and destructive interference at the detector, known as an interferogram. The interferogram is the Fourier transform of the bandpass spectrum. The SPIDER FTS has a resolution of 1GHz, which is set by the moving mirror scan length, and is calibrated to approximately 1% in frequency (which is related to the calibration of the scanning linear stage).

The SPIDER FTS accommodates both liquid nitrogen and hot thermal sources. The mirror was scanned back and forth at 2mm/s along a length of 300mm. Although we typically took both forward and backward scans, there were no differences in the resulting spectra. The SPIDER FTS also incorporated an internal goniometer that allowed us to direct the recombined beam to different parts of the focal plane. One of the challenges of working with this FTS was that this pointing was not especially effective or repeatable.

The central parts of each focal plane were much easier to illuminate than the edges, leading to occasionally sparse results. The difficulty of controlling the pointing of the FTS is why there are a few tiles in Figs. 4.12-4.14 that do not have any spectra.

### 4.5.2 Interferograms and Spectra

The interferogram is the pattern of constructive and destructive interference actually seen by the SPIDER detectors as the FTS mirror is scanned back and forth. A typical interferogram can be seen in Fig. 4.11. The calculation of the signal seen by the detectors for a monochromatic source follows. Note that in reality, SPIDER does not use a monochromatic source.

Assuming a coordinate system set up as in Fig. 4.10b, we have

$$\hat{a} = \frac{1}{\sqrt{2}}(\hat{x} + \hat{y}) \tag{4.15}$$

$$\hat{b} = \frac{1}{\sqrt{2}}(\hat{y} - \hat{x}). \tag{4.16}$$

The light from the souce is split into two beams by the wire grid beamsplitter, one polarized in the $\hat{a}$ direction (reflected) and one in the $\hat{b}$ direction (transmitted). These beams travel down the legs of the FTS, where they are reflected by the rooftop mirrors. When the two beams recombine at the beamsplitter, the total electric field becomes

$$\begin{aligned}
\vec{E}_{final} &= \frac{E_0}{\sqrt{2}}\left(\cos(\omega t - kx_m)\hat{b} + \cos(\omega t - kx_s)\hat{a}\right) \\
&= \frac{E_0}{2}\left(\cos(\omega t - kx_m)(\hat{y} - \hat{x}) + \cos(\omega t - kx_s)(\hat{x} + \hat{y})\right) \\
&= \frac{E_0}{2}\left[\cos(\omega t - kx_m) + \cos(\omega t - kx_s)\right]\hat{x} \\
&+ \frac{E_0}{2}\left[\cos(\omega t - kx_m) - \cos(\omega t - kx_s)\right]\hat{y},
\end{aligned} \tag{4.17}$$

where $k = 2\pi/\lambda$ is the wave number of the monochromatic source, $x_s$ refers to the stationary arm of the FTS, and $x_m$ refers to the moving arm of the FTS. An additional wire grid mirror that reflects this recombined beam into the cryostat will select a polarization parallel to $\hat{x}$ or $\hat{y}$. The SPIDER FTS is typically used with a flat mirror instead of a wire grid mirror, and so the following calculations do not assume that a particular polarization has been selected.

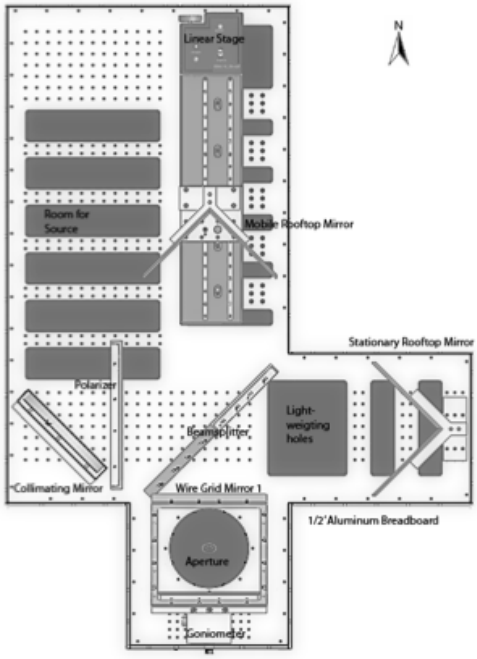


(a) A schematic of the SPIDER FTS. Image courtesy of Jon Gudmundsson.

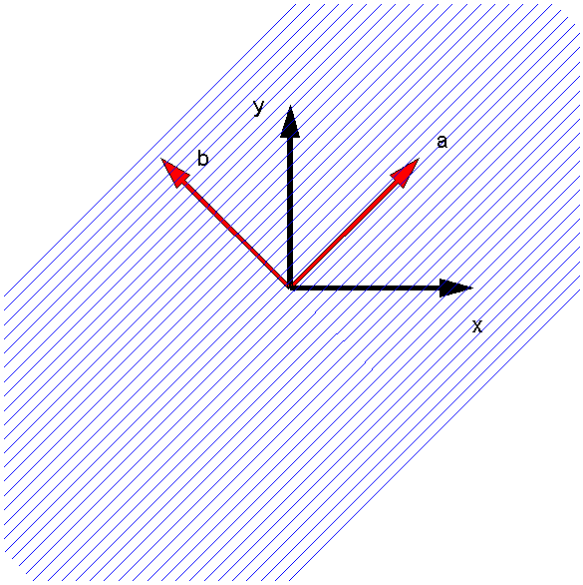


(b) If the blue lines are the wires of the wire grid, $\hat{a}$ points along the wires, $\hat{b}$ points perpendicular to the wires, $\hat{x}$ points east in Fig. 4.10a and $\hat{y}$ is perpendicular to $\hat{x}$ in the plane of the grid. Here $\hat{x}$ is referencing the cardinal coordinate system used in the figure above (which means that $\hat{y}$ would point out of the page in Fig. 4.10a). Image courtesy of Jon Gudmundsson.

Figure 4.10: Diagrams of the FTS and the wire grid beam splitter.

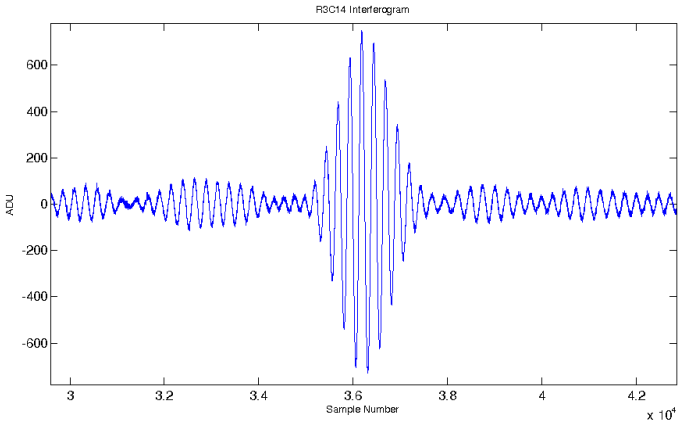


Figure 4.11: A typical interferogram for a SPIDER detector taken with the FTS. The central or white light fringe (where the two light waves have traveled the same distance from the source) is at sample number $\approx 3.65 * 10^4$.

The SPIDER detectors are polarized at some angle $\theta$ relative to this beam of light. The polarization direction, $\vec{e}$, of the detector can be represented in the following way:

$$\begin{aligned} \vec{e} &= \cos\theta\hat{x} + \sin\theta\hat{y} \\ &= e_1\hat{x} + e_2\hat{y} \\ &= \frac{1}{\sqrt{2}}((e_1+e_2)\hat{a} + (e_2-e_1)\hat{b}). \end{aligned} \tag{4.18}$$

The signal that the SPIDER detectors will measure is proportional to the inner product of this polarization vector with the electric field:

$$I \propto (\vec{E}_{final} \cdot \hat{e})^2. \tag{4.19}$$

The full algebra for this calculation has been worked out in [40]. I will only state the result here:

$$I_{\{a,b\}} \propto \frac{E_0^2}{4}\left(\frac{(e_2-e_1)^2}{2} + \frac{(e_2+e_1)^2}{2} + (e_2^2-e_1^2)\cos(kx_m - kx_s)\right). \tag{4.20}$$

If the detector is polarized parallel to the wires of the beamsplitter, then $\hat{e} = \hat{a}$ or $e_1 = e_2 = 1/\sqrt{2}$. The first and third terms in Eqn. 4.20 cancel out and the detector sees

$$I \propto \frac{E_0^2}{4}. \tag{4.21}$$

If the detector is polarized perpendicular to the wires of the beamsplitter, then $\hat{e} = \hat{b}$ or $e_1 = -e_2 = -1/\sqrt{2}$. The second and third terms in Eqn. 4.20 cancel out and again the detector sees

$$I \propto \frac{E_0^2}{4}. \tag{4.22}$$

Finally, if the detector is polarized along $\hat{x}$ or $\hat{y}$ then, the detector sees

$$I \propto \frac{E_0^2}{4}\left(\frac{1}{2} \pm \cos(kx_m - kx_s)\right). \tag{4.23}$$

The above equations show that it matters how you align the detectors with respect to the FTS. The modulation signal is maximized if the detector polarization is aligned parallel to $\hat{x}$ or $\hat{y}$, and there is no modulation signal at all if the detector polarization is aligned 45 degrees away from these axes.

For a white light source, the interferogram becomes a sum of cosines of different wavenumber, weighted by $\eta(\nu)$ and $B(\nu)$ where $B(\nu)$ is the source brightness. Multiplication in real space corresponds to convolution in Fourier space, so the Fourier transform of this is the convolution of $\eta(\nu)$ and $B(\nu)$ with a delta function at $\nu_0$, which thus gives the bandpass spectrum multiplied by $B(\nu)$. We calculate the spectra from the interferograms by fitting to the white light fringe in order to center on it and get the phase correct for a Fourier Transform. A miscentered white light fringe creates unnecessary complex phase in the resulting spectra. Additionally, we divide the spectra by $\nu^2$ to correct for the blackbody emission of the source. In practice, baseline drifts and gain variations in the detector timestreams require that we also clean up the interferograms by subtracting a third or fourth order polynomial and applying a Hanning window. Plots of the band centers, bandwidths, and spectra from data taken during our integration campaign in Palestine, TX can be seen in Figs. 4.12-4.14. (Note that the X5 focal plane is not included in these figures, as X5 was not completed prior to the integration campaign.) These data will need to be retaken on the ice prior to flight for an archival measurement, though we do not expect them to change significantly.

Table 4.3: Bandcenters and Bandwidths for all FPUs

| Focal Plane | Tile ID | $\nu_0$ (GHz) | Bandwidth (fractional) |
|---|---|---|---|
| X1 | T130204.3 | 148 | 0.31 |
| X1 | T130204.4 | 146 | 0.32 |
| X1 | M130130 | 148 | 0.27 |
| X1 | T130204.2 | 148 | 0.29 |
| X2 | T110609.3 | 93 | 0.23 |
| X2 | T110609.2 | 93 | 0.26 |
| X2 | T110609.4 | 93 | 0.28 |
| X2 | T110606.1 | 93 | 0.26 |
| X3 | W130311.2 | 147 | 0.34 |
| X3 | M130319 | 147 | 0.24 |
| X3 | W130311.3 | 115 | – |
| X3 | W130311.1 | 147 | 0.31 |
| X4 | T120823.4 | 93 | 0.23 |
| X4 | M120916 | 93 | 0.31 |
| X4 | T121127.1 | 95 | 0.21 |
| X4 | T120823.3 | 94 | 0.27 |
| X5* | JAB120109.1 | 144 | 0.22 |
| X5* | M130521 | 147 | 0.21 |
| X5* | W130508.3 | 146 | 0.22 |
| X5* | W130508.1 | 147 | 0.22 |
| X6 | M121206 | 94 | 0.24 |
| X6 | W130709.1 | 94 | 0.23 |
| X6 | T130508.1 | – | – |
| X6 | T121127.2 | 94 | 0.28 |

*X5 spectra numbers are from a test cryostat run, since X5 was not finished before the Palestine integration campaign.

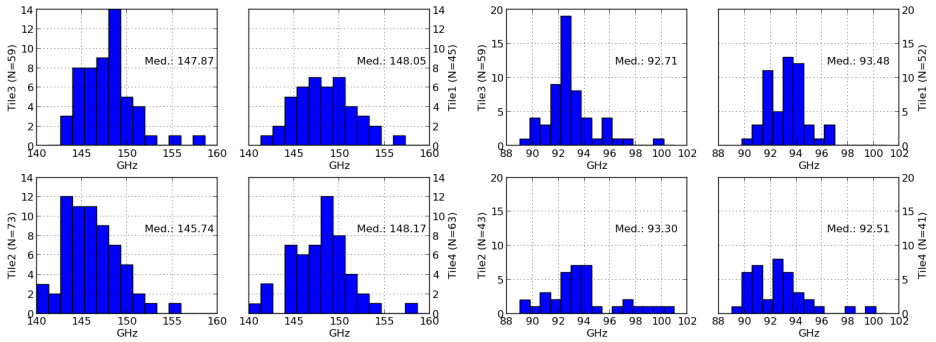


(a) X1.




(b) X2.

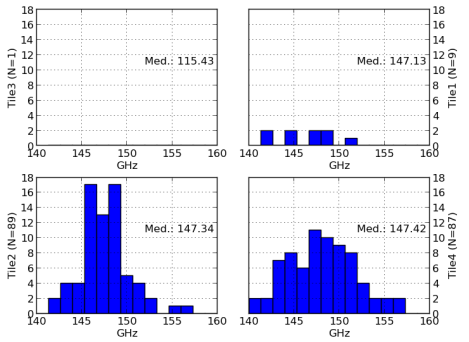


(c) X3.

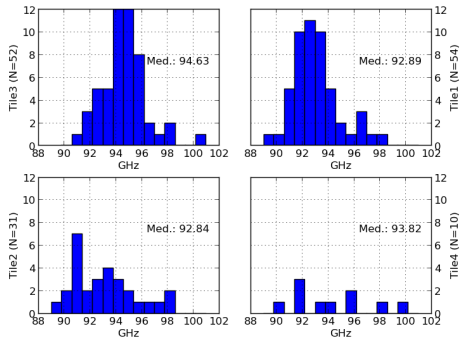


(d) X4.

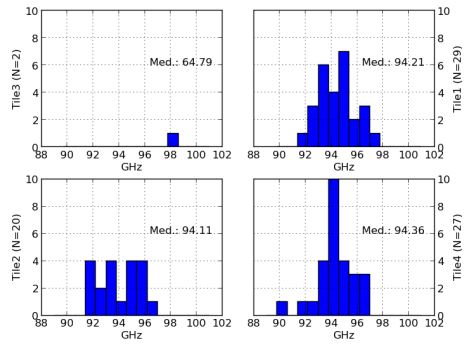


(e) X6.

Figure 4.12: Histograms of bandcenter in $GHz$ for all FPUs (flight cryostat). Figures courtesy of Anne Gambrel.

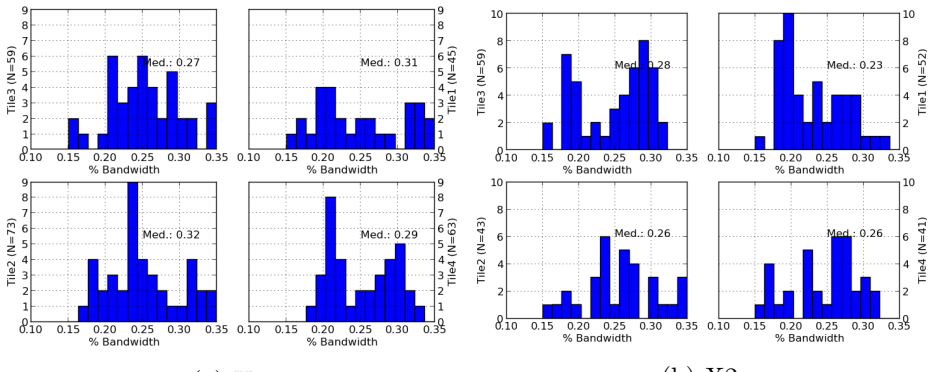


(a) X1.

(b) X2.

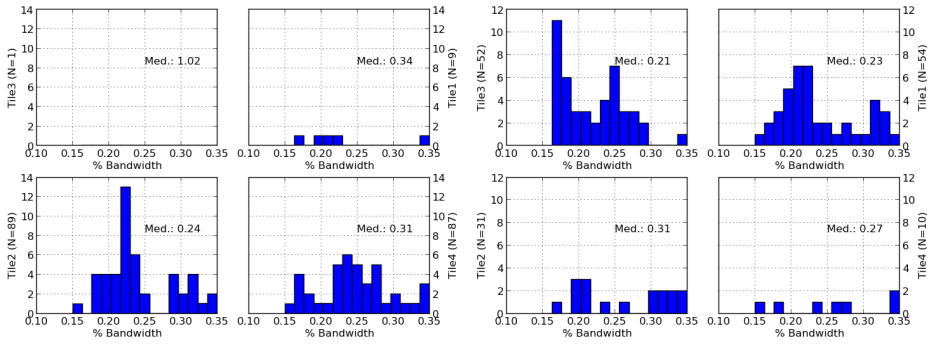


(c) X3.

(d) X4.

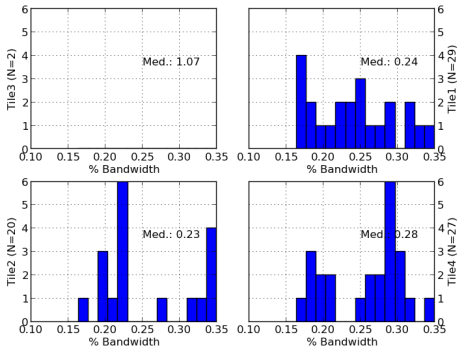


(e) X6.

Figure 4.13: Estimated spectral bandwidths (fractional) for all FPUs (flight cryostat). Figures courtesy of Anne Gambrel.

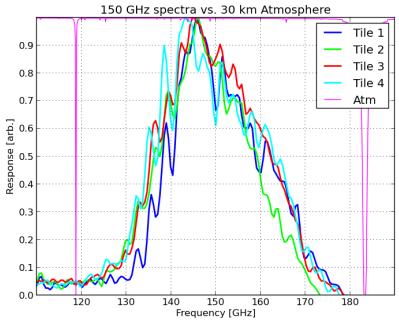


(a) X1.

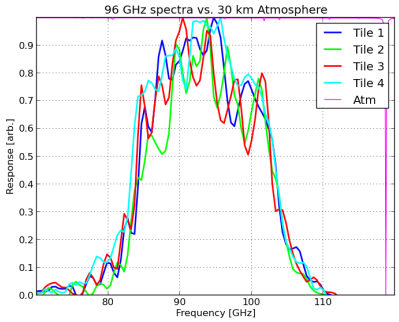


(b) X2.

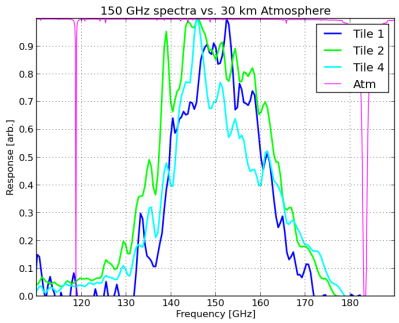


(c) X3.

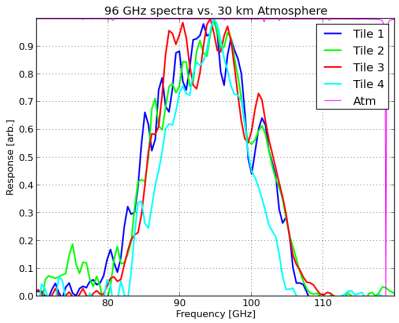


(d) X4.

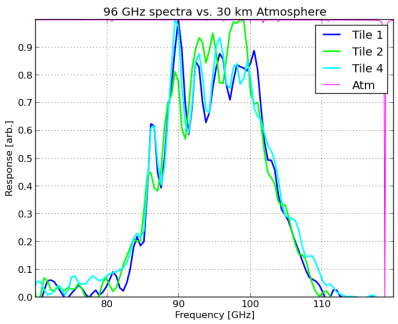


(e) X6.

Figure 4.14: Detector bandpass spectra vs. atmosphere at 30km for all FPUs (flight cryostat). Figures courtesy of Anne Gambrel. Atmospheric spectra calculated from [71].

## 4.6 Noise

The noise inherent in the SPIDER detectors and readout system is full of rich and interesting phenomena. We are typically interested in the noise while the detectors are "dark" — otherwise we are limited by the photon noise of the incoming radiation, and not the inherent noise in the system. That is, a dark run allows us to characterize the noise of the detectors and readout. Of course, in the end we are most interested in the total noise of the detectors under flight-like conditions. In science operation, SPIDER will take data at approximately 120Hz.

One way to find the bias point that minimizes the detector noise is to take noise at our science frequency (data mode=10, 100-400 Hz) and see how the mean noise in the science band varies with detector bias. The noise traces are converted from DAC (readout) units to units of equivalent current at the TES. We then take the power spectral density of the time trace, which is the noise spectrum as a function of frequency (Figs. 4.15a-4.15b). We then compute mean noise in the band corresponding to our science frequencies (2-8Hz). This is the noise-equivalent current (NEI), which is measured in units of pA/$\sqrt{Hz}$. We can also approximate the noise-equivalent power (NEP) as the NEI multiplied by voltage of the TES. More accurately, the noise-equivalent power is the square root of the power-spectral density of the power referred noise. This is approximately equal to NEI $\times$ $V_{bias}$, with corrections for the fact that the voltage source is non-ideal.

Examples of these measurements as a function of $R/R_n$ are shown in Figs. 4.16a-4.16b. Ideally, the noise should be flat as a function of TES bias (which is functionally equivalent to $R/R_n$). In practice, we do not typically see this — the noise goes up at points that are either very low or very high in the transition. SPIDER detectors typically have NEPs around 20-30 aW/$\sqrt{Hz}$, which is in agreement with the noise model described in §3.9.

If we have both dark noise and optical efficiencies for a detector (which turns out to be rare, since these measurements require two separate runs of each focal plane), we can convert the noise-equivalent power to a noise-equivalent temperature (NET) by dividing by the optical response $dP/dT$. SPIDER's per detector NET is typically between 110-150 $\mu K_{CMB}\sqrt{s}$, which gives per tile NETs of 10-20 $\mu K_{CMB}\sqrt{s}$ and per focal plane NETs of 5-10 $\mu K_{CMB}\sqrt{s}$. The combined NET for the entire SPIDER experiment is roughly estimated to be around 3 $\mu K_{CMB}\sqrt{s}$.

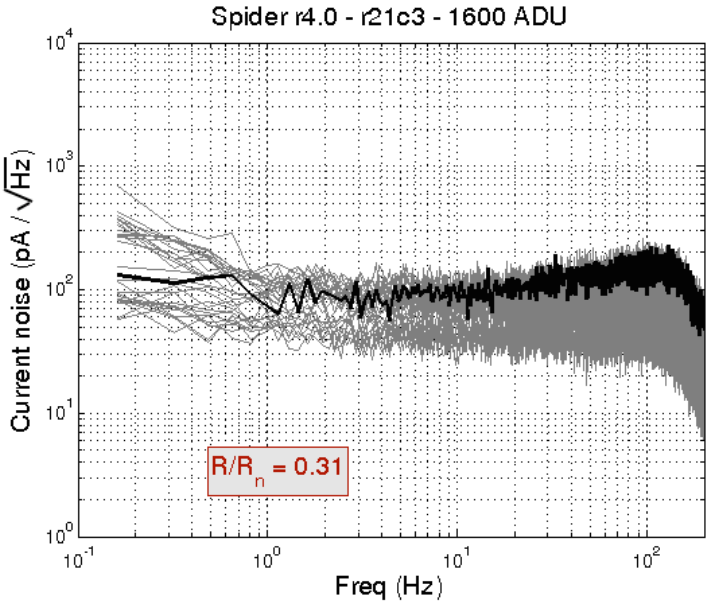


(a) The noise spectrum with TES bias = 1600 ADU, which is equivalent to $R/R_n = 0.31$, is highlighted.

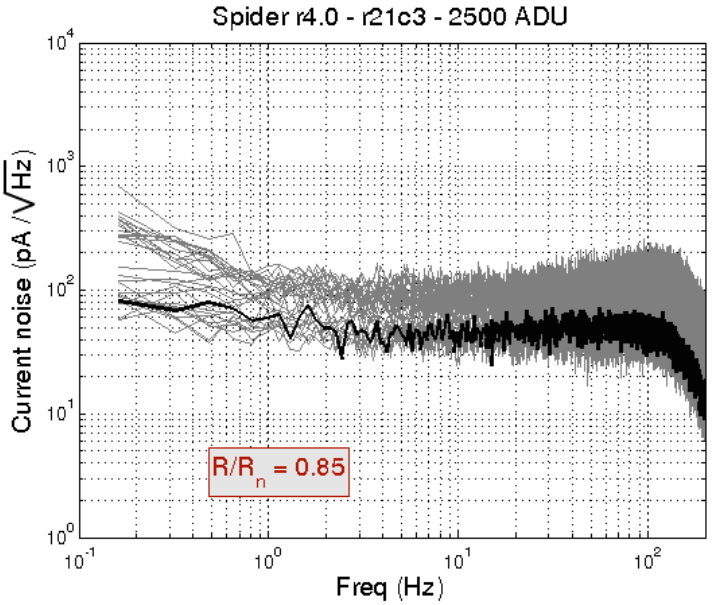


(b) The noise spectrum with TES bias = 2500 ADU, which is equivalent to $R/R_n = 0.85$, is highlighted.

Figure 4.15: Example noise spectra at two different biases.

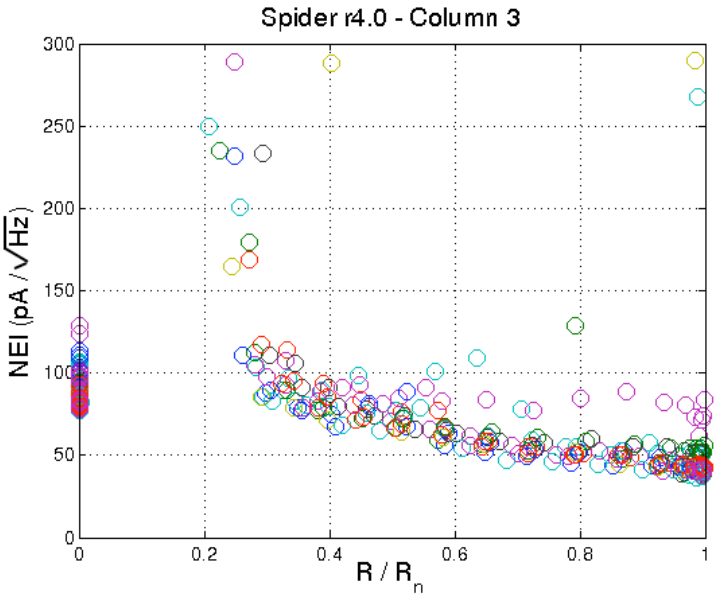


(a) NEI vs. $R/R_n$ (X1)

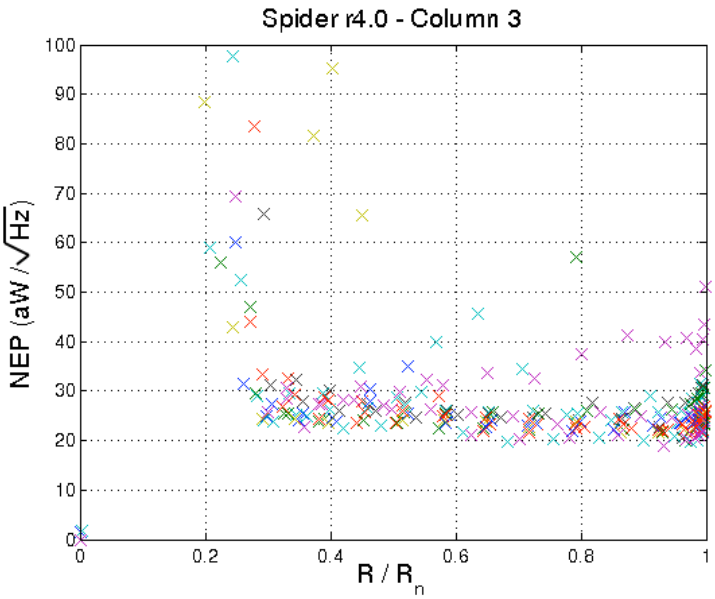


(b) NEP vs. $R/R_n$(X1)

Figure 4.16: Noise equivalent current and noise equivalent power versus TES resistance.

## 4.7 Optical and Electrical Gain

To measure the optical gain, we use a separate LHe cryostat with a temperature controlled plate that can be put on the front of the test cryostat in order to have controlled, flight-light loading. We added a stainless steel light pipe to the plate inside this cryostat. A broadband source can be put on the room side of the light pipe in order to apply an optical step to the detectors at any frequency.

To measure the electrical gain, we apply electrical bias steps using the MCE's internal ramp generator. We can choose the amplitude and frequency of the bias square wave. Using these two mechanisms, we can apply simultaneous optical and electric steps to the detectors and thus measure the fractional optical and electrical gains. As shown in Fig. 4.17, the fractional optical and electrical gains have a nearly linear relationship with each other. Unfortunately, during this measurement we did not monitor the brightness of the optical source, so we cannot differentiate whether the non-linearities shown in that figure are due to real variations in gain or slow drifts in the brightness of the source. Recall from §3.2 that our benchmark for (optical) relative/fractional gain uncertainty is 0.5% and that the electrical fractional gain uncertainty can be measured to less than 0.1%. To the extent that the electrical gain of the entire readout chain is stable, the linearity of the relationship shown in Fig. 4.17 gives us confidence that SPIDER will be able to meet this benchmark.

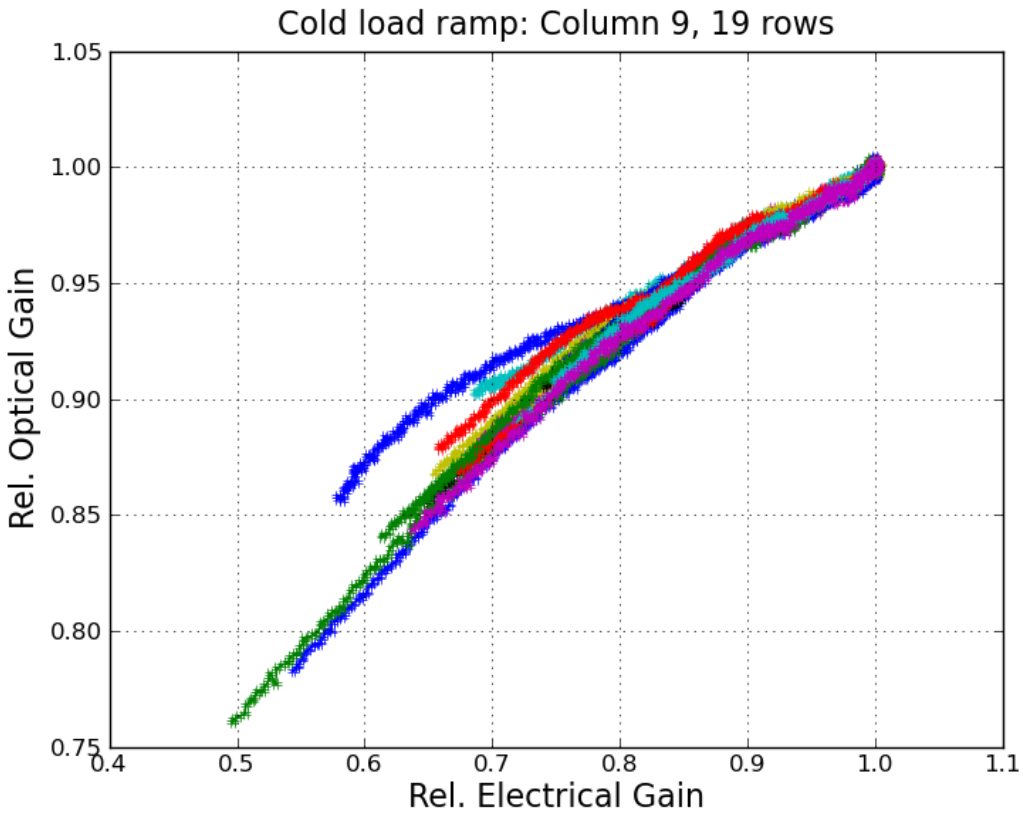


Figure 4.17: The relative optical and relative electrical gains plotted against each other. A clear correlation is visible with a slope of $\sim 2$. The different line colors represent different detectors in the column. Figure courtesy of Jeff Filippini.

# Chapter 5

# Instrument Characterization: Optical Systematics

The optical characterization of the SPIDER telescope is primarily a study of the beams of the instrument and how they are affected by various elements in the optical stack, such as lenses, HWPs, filters, and windows. A thorough understanding of the instrument's optical properties is necessary for the tight control of systematics that will be critical to SPIDER's success. This chapter describes the testing and optical characterization of the beams of the SPIDER detectors and, in particular, the non-idealities in the beams that can cause systematic effects in the final data.

As explained in §4.4, blank pixels in the four tile plots in this chapter indicate detectors for which we do not have data, due to failures in the detectors or in the SQUIDs used to read them out.

## 5.1 Beams

As mentioned in §3.3, it is crucial that the beams of the SPIDER detectors meet the systematic requirements in differential pointing, differential ellipticity, and differential width if we are to avoid contamination of our polarization maps. Determining these characteristics of the SPIDER beams was done primarily through beam mapping in the Caltech high bay. A mount (the"az-el gadget") was built by the University of Toronto that allowed us to scan the test cryostat systematically and repeatably in azimuth and elevation over a millimeter-wave source located in a balcony about 30m away from the cryostat. This puts the source just in the far-field of the SPIDER telescopes, as $D^2/\lambda \approx 30m$. We did beam maps with a variety of sources and techniques, depending on what particular feature of the beams we

were trying to see.

While these maps are easily made in the Caltech high bay with the test cryostat, it turned out to be much harder to do them in the flight cryostat, mainly due to the limited range of motion provided by the gondola and the difficulty of reconstructing the telescope pointing on the ground. Pointing reconstruction is significantly harder when using the gondola on the ground, since a simple integration of the gyroscopes does not account for drifts or sudden movements in the telescope motion. In flight we will be able to use the star cameras to achieve sub-arcminute pointing resolution, but on the gondola on the ground this option was not available to us.

Our most common beam map was done using a chopped thermal source ($T_{\rm source} \approx 800K$) with a four-inch diameter. This source was made by the SPIDER team (myself, Marc Runyan, and Amy Trangsrud) for this purpose. The sources we had available prior to this were not bright enough to make this measurement with high signal-to-noise. The az-el gadget scanned the cryostat over the hot source, which was being chopped mechanically with a rotating blade between 10-15 Hz. Each full map took approximately 12 hours. The source chop and the az-el pointing information were acquired by the housekeeping system to allow us to synchronize the chop cycles with the data for demodulation. This style of beam map typically had a SNR of approximately 35dB.

Typical beams at both 90GHz and 150GHz are shown in Fig. 5.1. These maps were taken with the thermal source. A typical 90GHz beam has a full-width at half-max (FWHM) of 45 arcminutes. A typical 150GHz beam has a FWHM of 30 arcminutes.

Large scans allowed us to map the beam for each detector in the focal plane. I fitted two-dimensional Gaussians to each map in order to estimate the pointing center, width (FWHM), and ellipticity of each detector beam. The beams are fit with a two-dimensional Gaussian of the following form:

$$z = A * e^{\left[a(x-x_0)^2+2b(x-x_0)(y-y_0)+c(y-y_0)^2\right]} + C. \tag{5.1}$$

We fit for $A$, $C$, $a$, $b$, $c$, $x_0$, and $y_0$. The values for $x$ and $y$ are given by the pointing solution from the az-el gadget. The $z$ values are given by the detector response. From this

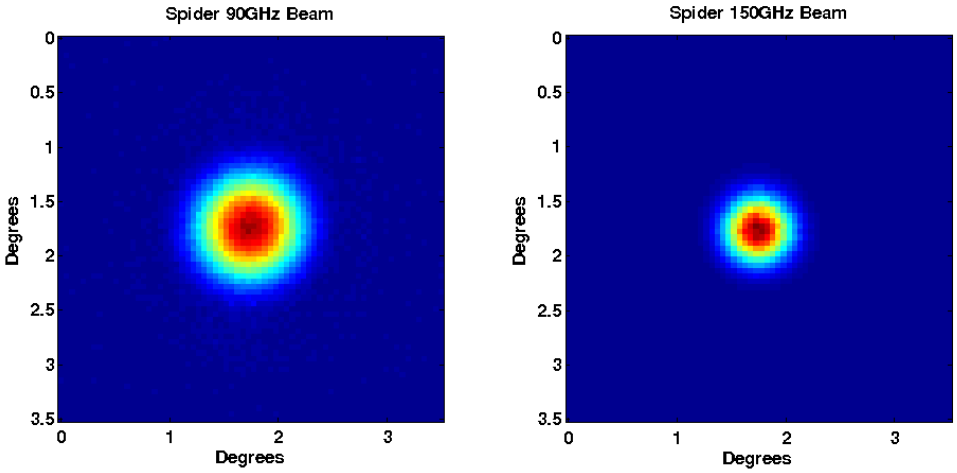


Figure 5.1: Typical SPIDER beams for a 90GHz detector (left) and a 150GHz detector (right). The expected beam widths (FWHM) are 45 arcminutes and 30arc minutes, respectively.

fit, we can construct a matrix of the Gaussian fit parameters:

$$M = \begin{bmatrix} a & b \\ b & c \end{bmatrix}. \tag{5.2}$$

The eigenvalues of $M$ are related to the width of the Gaussian along the semimajor and semiminor axes in the following way. If $a_1$ and $a_2$ are the eigenvalues of $M$, then the widths of the beam are

$$\sigma_1 = \frac{1}{\sqrt{2a_1}} \tag{5.3}$$

$$\sigma_2 = \frac{1}{\sqrt{2a_2}}. \tag{5.4}$$

The full-width at half-max (FWHM) is

$$FWHM = \sqrt{\sigma_1^2 + \sigma_2^2} * 2.35/\sqrt{2}, \tag{5.5}$$

Table 5.1: Beam Parameters for all FPUs.

| Focal Plane | FWHM (arcmin) | ellipticity |
|---|---|---|
| X1 | 30.1 ± 1.7 | 0.018 ± 0.013 |
| X2 | 46.8 ± 0.5 | 0.014 ± 0.006 |
| X3 | 29.1 ± 1.1 | 0.016 ± 0.010 |
| X4 | 41.7 ± 0.7 | 0.014 ± 0.010 |
| X5 | 29.7 ± 0.6 | 0.015 ± 0.009 |
| X6 | 42.1 ± 0.6 | 0.014 ± 0.008 |

These parameters are determined by averaging the parameters derived from individual beam maps for each focal plane. The errors describe the spread over the pixels (one standard deviation).

and the ellipticity is

$$e = \frac{\sigma_1 - \sigma_2}{\sigma_1 + \sigma_2}. \tag{5.6}$$

Beam width and ellipticity statistics for each of the focal planes are given in Figs. 5.2 - 5.5. The beam widths for the X2 focal plane are roughly five arcminutes larger than those of the other 90GHz focal planes (X4 and X6). This is due to a difference in stop diameter size of the cooled optics sleeve when the beam maps were taken. The X2 focal plane was among the earliest to be tested and at that time the stop diameter was roughly three cm smaller than it was in later iterations of the telescopes. For flight, X2 will have the same expanded stop diameter as the other telescopes.

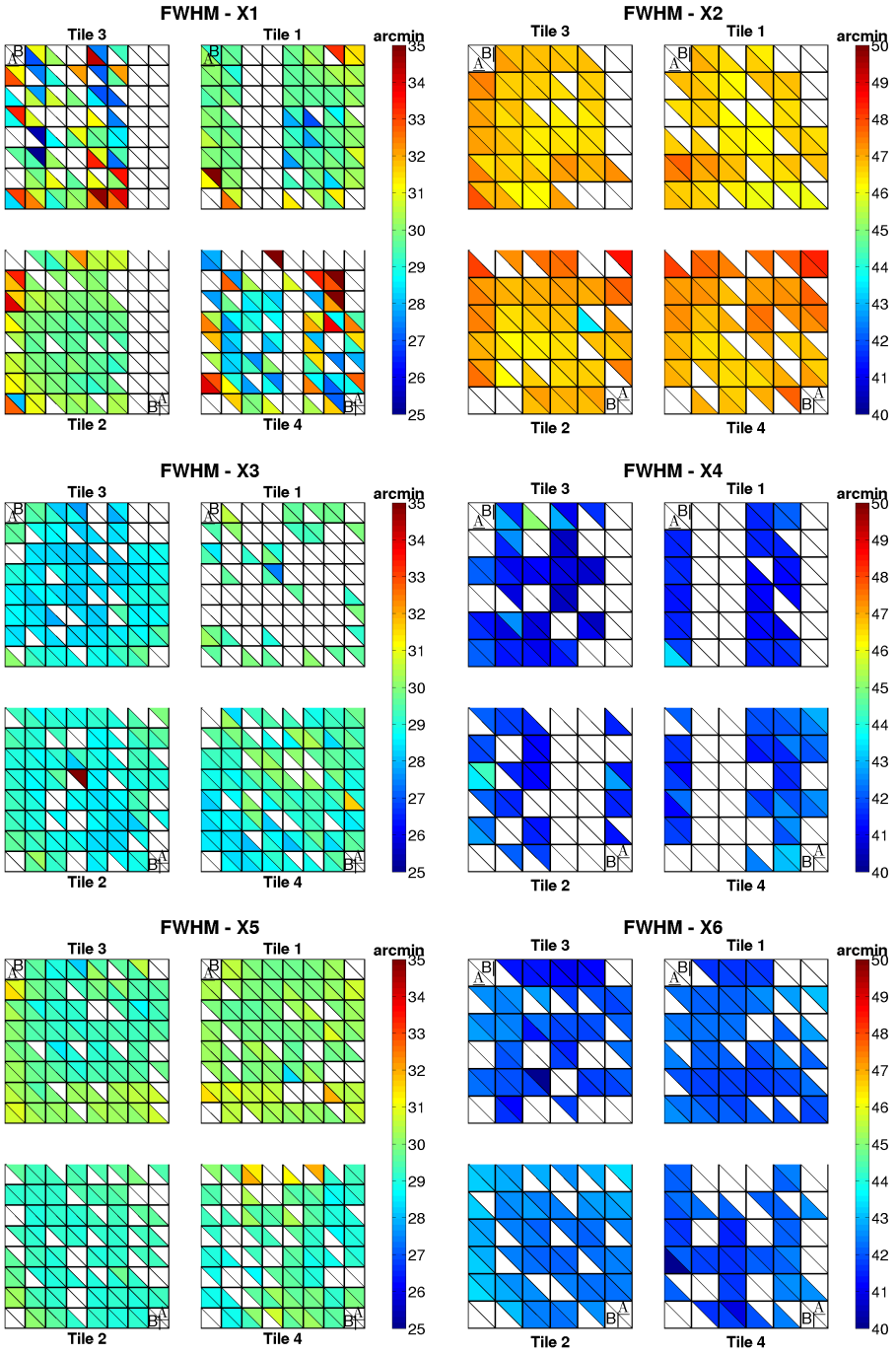


Figure 5.2: Beam widths for all FPUs.

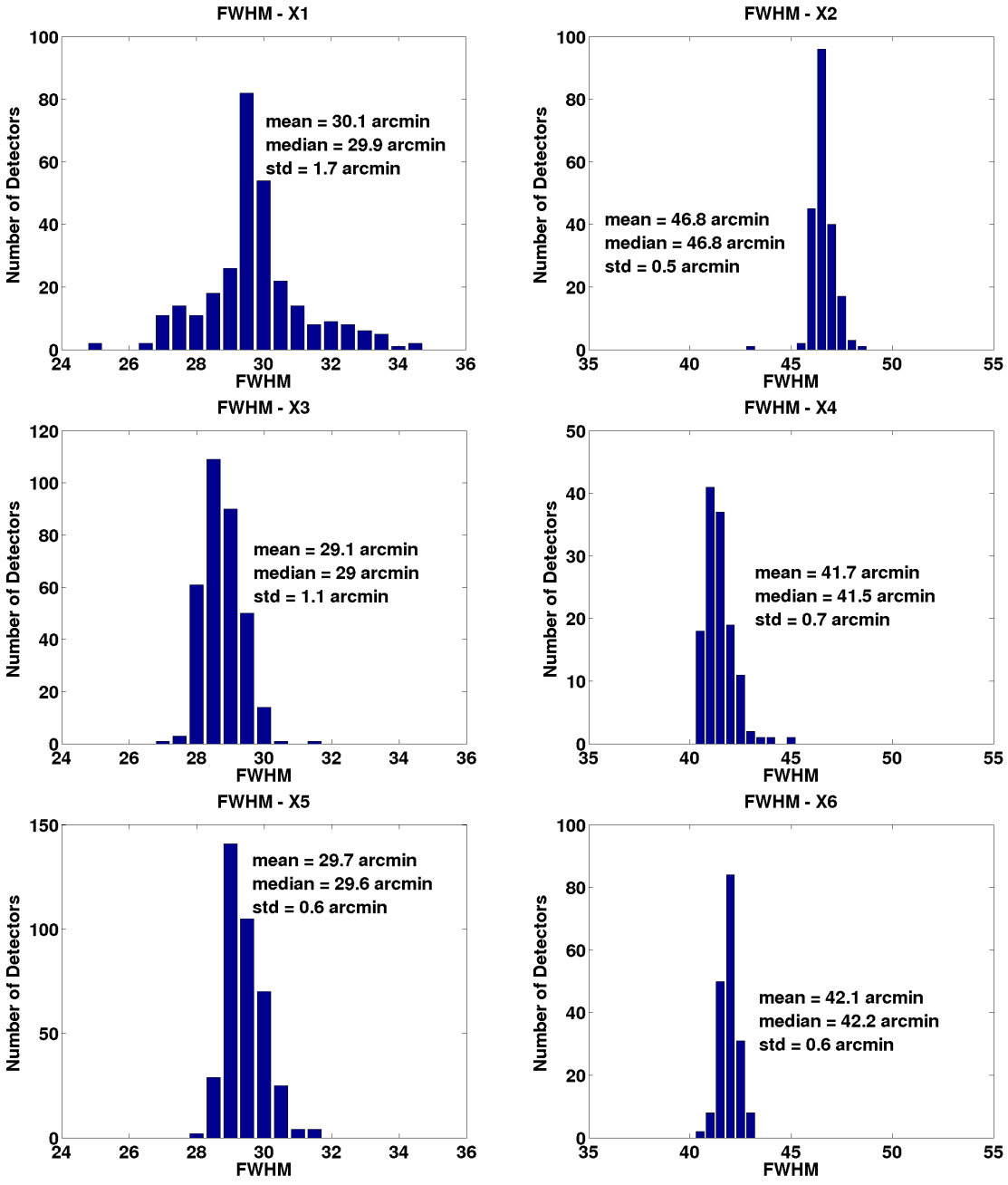


Figure 5.3: Histogram of beam widths (FWHM) for all FPUs.

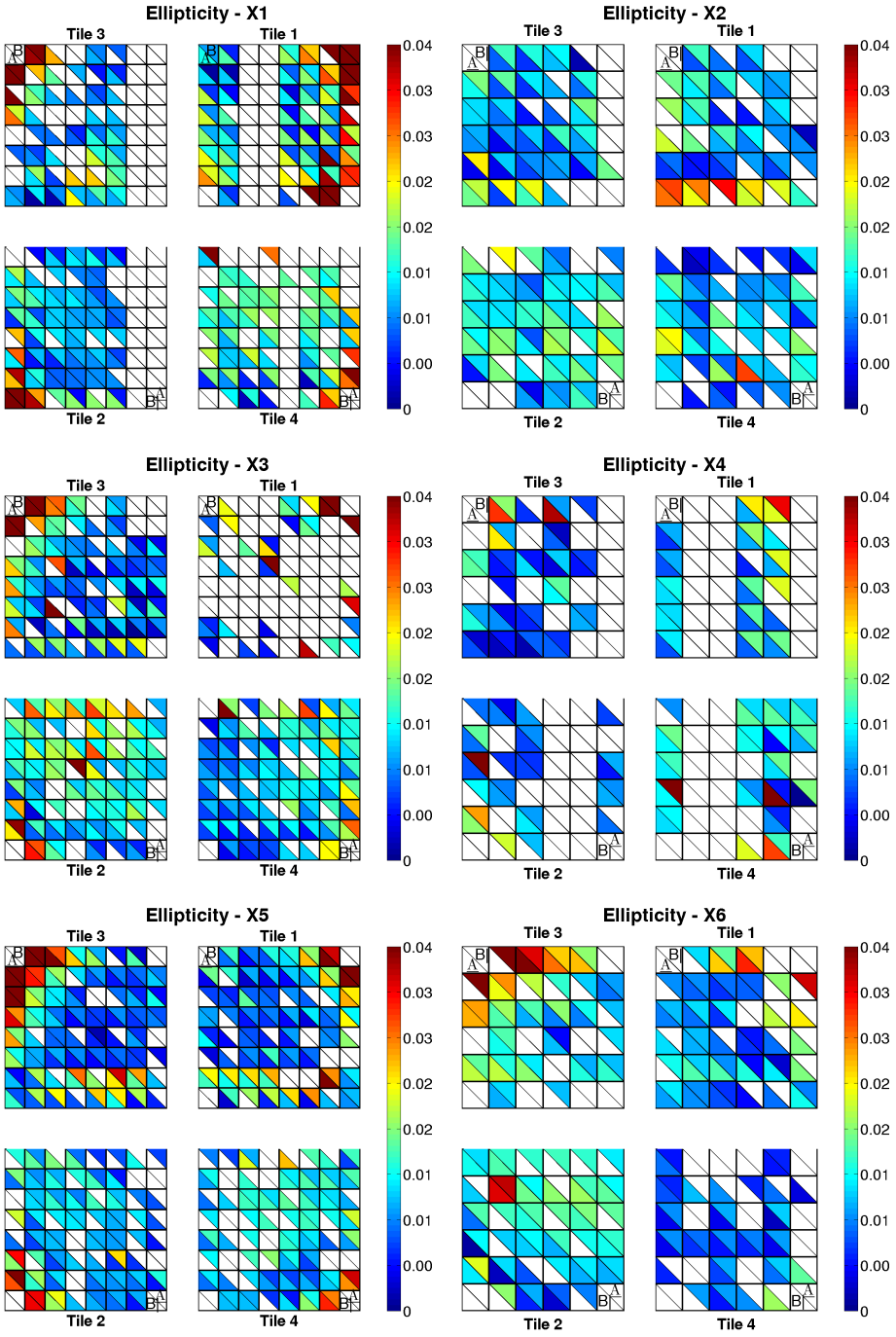


Figure 5.4: Beam ellipticity for all FPUs.

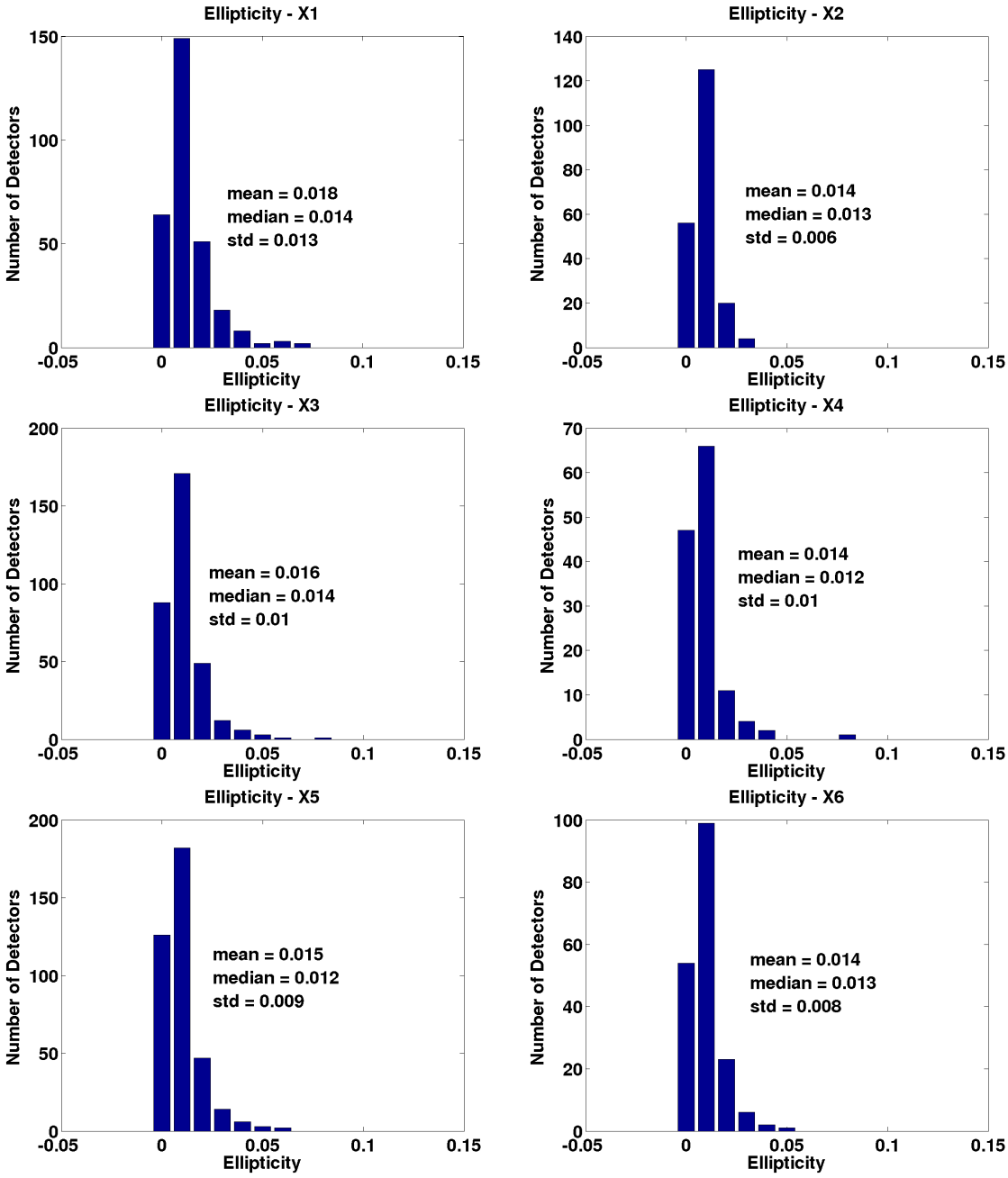


Figure 5.5: Histograms of beam ellipticity for all FPUs.

### 5.1.1 Differential Pointing

We get differential beam parameters by differencing the individual fitted beam parameters from the previous section between A/B pairs. The differences in the fitted beam centroids, $(x_0, y_0)_A - (x_0, y_0)_B$ are also known as differential pointing. We typically show this as a normalized quantity

$$\textbf{differential pointing} = (\vec{r}_A - \vec{r}_B)/\sigma, \tag{5.7}$$

where $\vec{r}_A, \vec{r}_B$ are the centroids of the beams and $\sigma$ is the standard deviation. (Note that this is different than the beam width, which we typically quote as a full-width at half-maximum.)

If the beams of the A and B detectors (corresponding to the perpendicular polarizations of light) in a pixel pair are truly coincident, this difference will be zero. If this difference is non-zero and is not removed before the final data analysis, either physically or by analysis techniques, it can transform the spatial derivatives of the CMB temperature anisotropies into a false polarization signal (see §3.3).

In some of the early batches of SPIDER detectors, we measured large values of differential pointing which caused a residual dipole structure when the beams were differenced. An example of what large differential pointing looks like is shown in Fig. 5.6a. The differential beam pointing in the x-direction was eventually traced to asymmetries in the summing trees that sum the power from the antennas. On one side of the summing tree were two lines from different polarizations that were very close together. The coupling between these lines changed the wave speed in the transmission line, so the same physical path length resulted in the taps experiencing a phase shift that was different for the A and B detector. This was solved by redesigning the summing tree to space out these lines as much as possible, which brought the horizontal dipole to zero. The differential pointing in the vertical (y) direction was thought to be caused by gradients in the films used to make the detectors. These gradients can be caused by "dirty" materials (which may be intrinsically impure or contaminated via other steps in the fabrication process). The gradients can be caused by a varying normal state resistivity, which affects the superconducting penetration depth and thus the kinetic inductance contribution to the inductance per unit length. This affects the wave speed ($v = 1/\sqrt{LC}$) where $L$ and $C$ are inductance and capacitance per unit length. After noticing impurities in the niobium used to make the detectors, the fabrication team switched from a lift-off technique to a cleaner etching technique. After these changes were

made, the value of differential pointing decreased dramatically, and the characteristic dipole structure in the differences maps was greatly reduced for the vast majority of the detectors. An example of the beams after these changes is shown in Fig. 5.6b.

Our benchmark value for the differential pointing is 10% (as discussed in §3.3.2). As shown in the statistics for differential pointing (Figs. 5.7-5.9), our flight detectors have typical values of differential pointing of 2-3% and are well within our benchmark values.

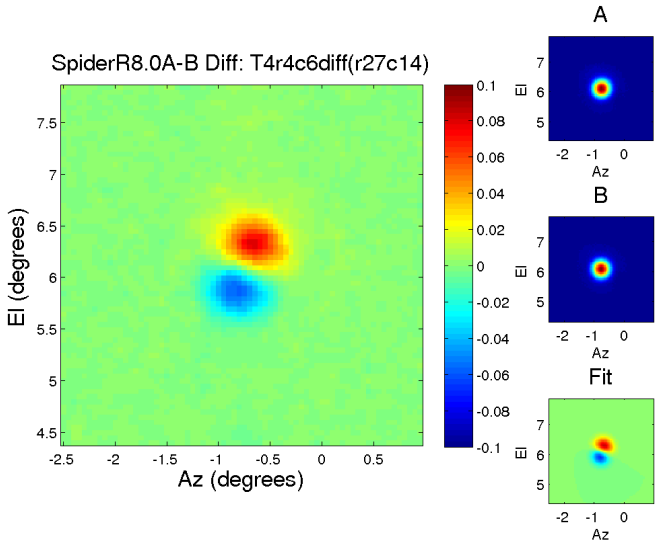


(a) An example of the beams from an A/B pair and their difference beam from SPIDER Run 8.0 (an early test of X3) in the Caltech test cryostat. The strong dipole structure is the result of large differences in the pointing between the A and B pixel.

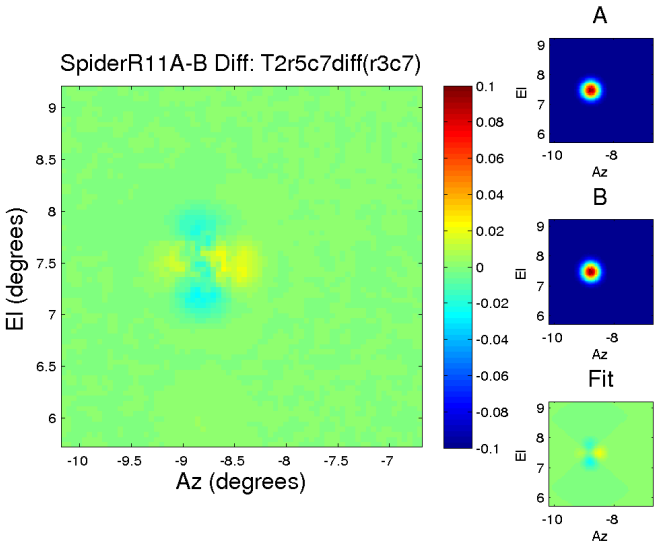


(b) An example of the beams from an A/B pair and their difference beam from SPIDER Run 11.0 (X1) in the Caltech test cryostat. This map was taken after material and antenna design changes to the detectors, which solved the problem with large values of differential pointing.

Figure 5.6: Differenced beam maps showing the change in differential pointing between early and late iterations of the SPIDER detectors.

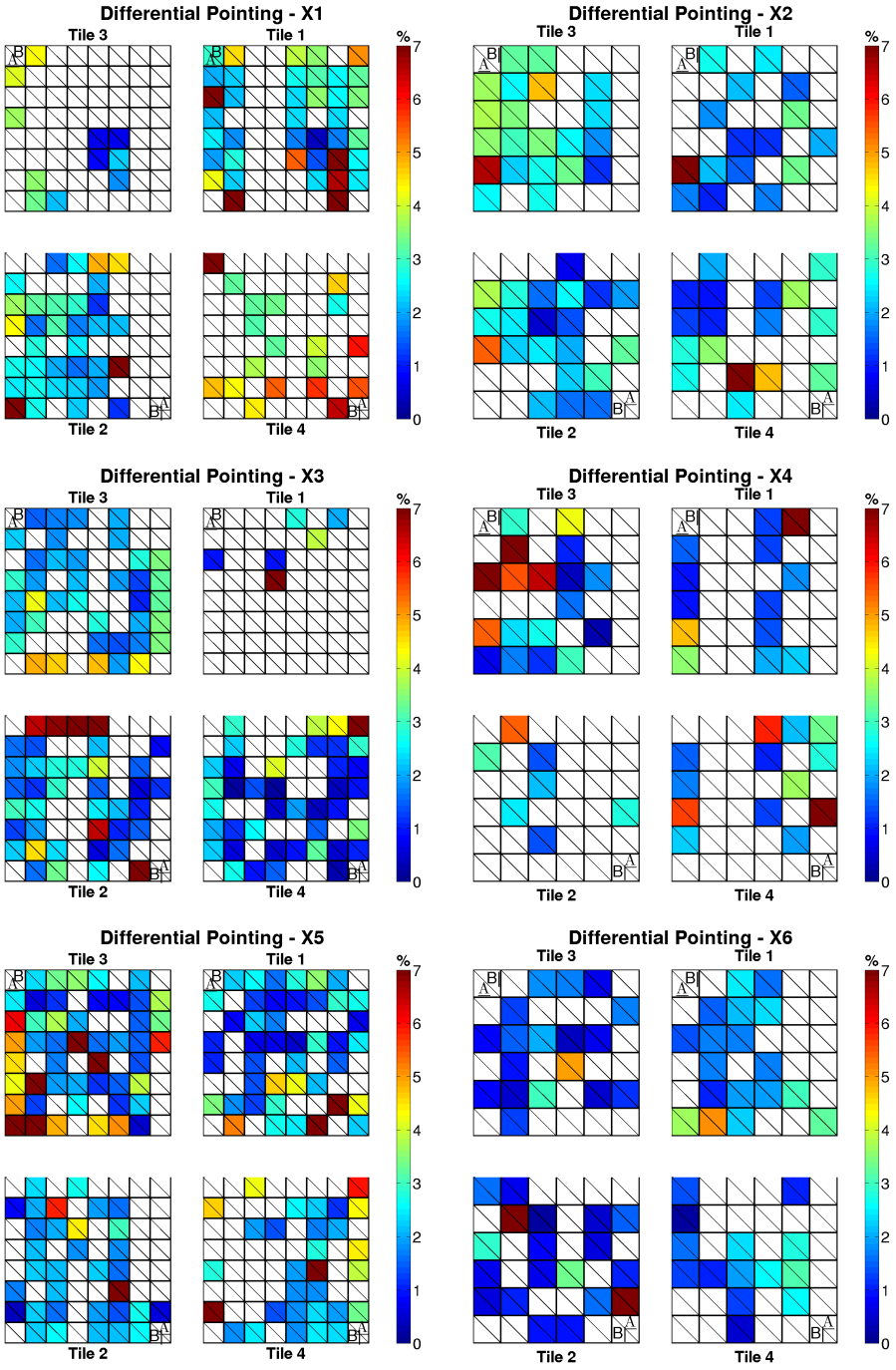


Figure 5.7: Differential pointing for all FPUs.

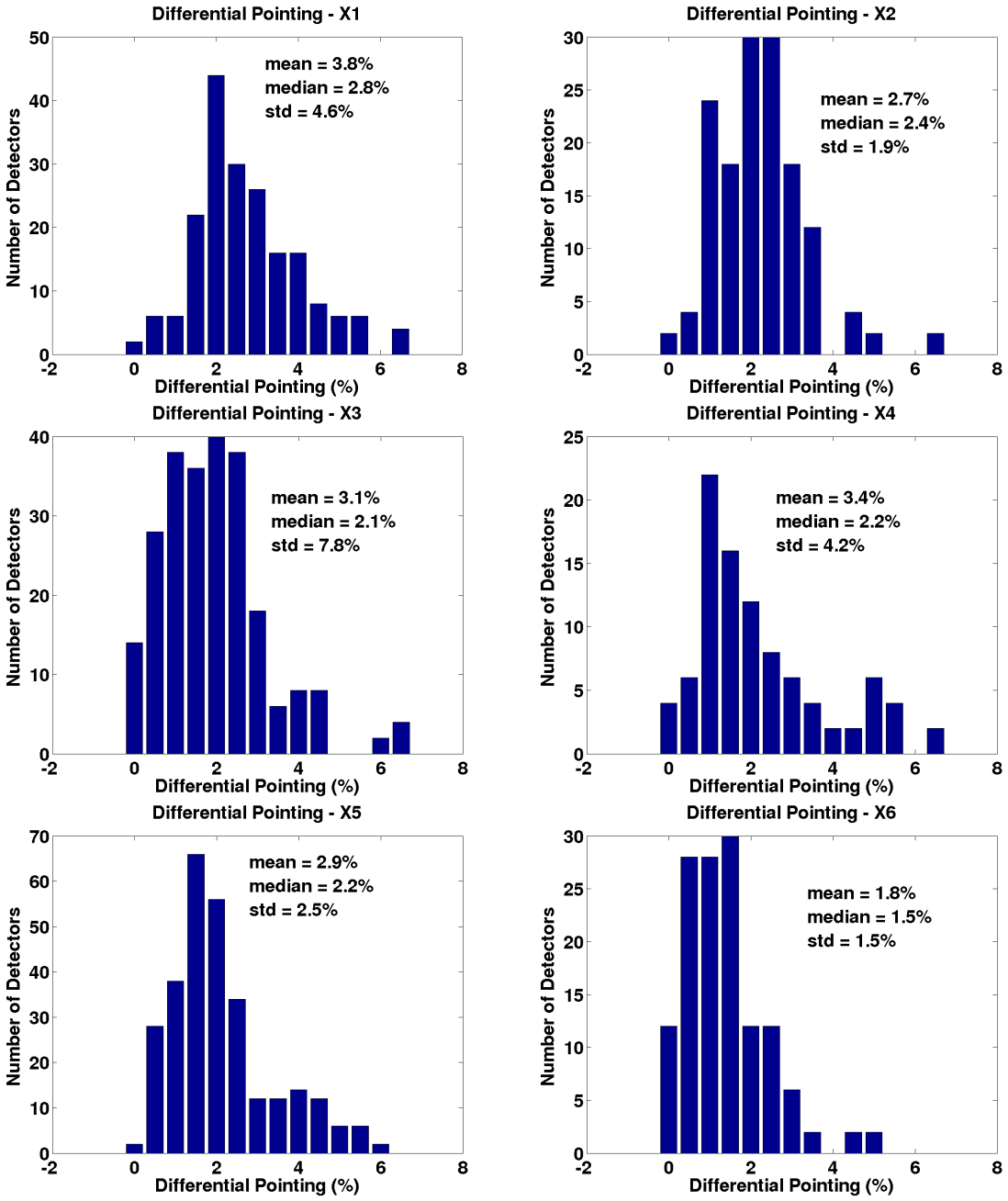


Figure 5.8: Histograms of differential beam ellipticity for all FPUs.

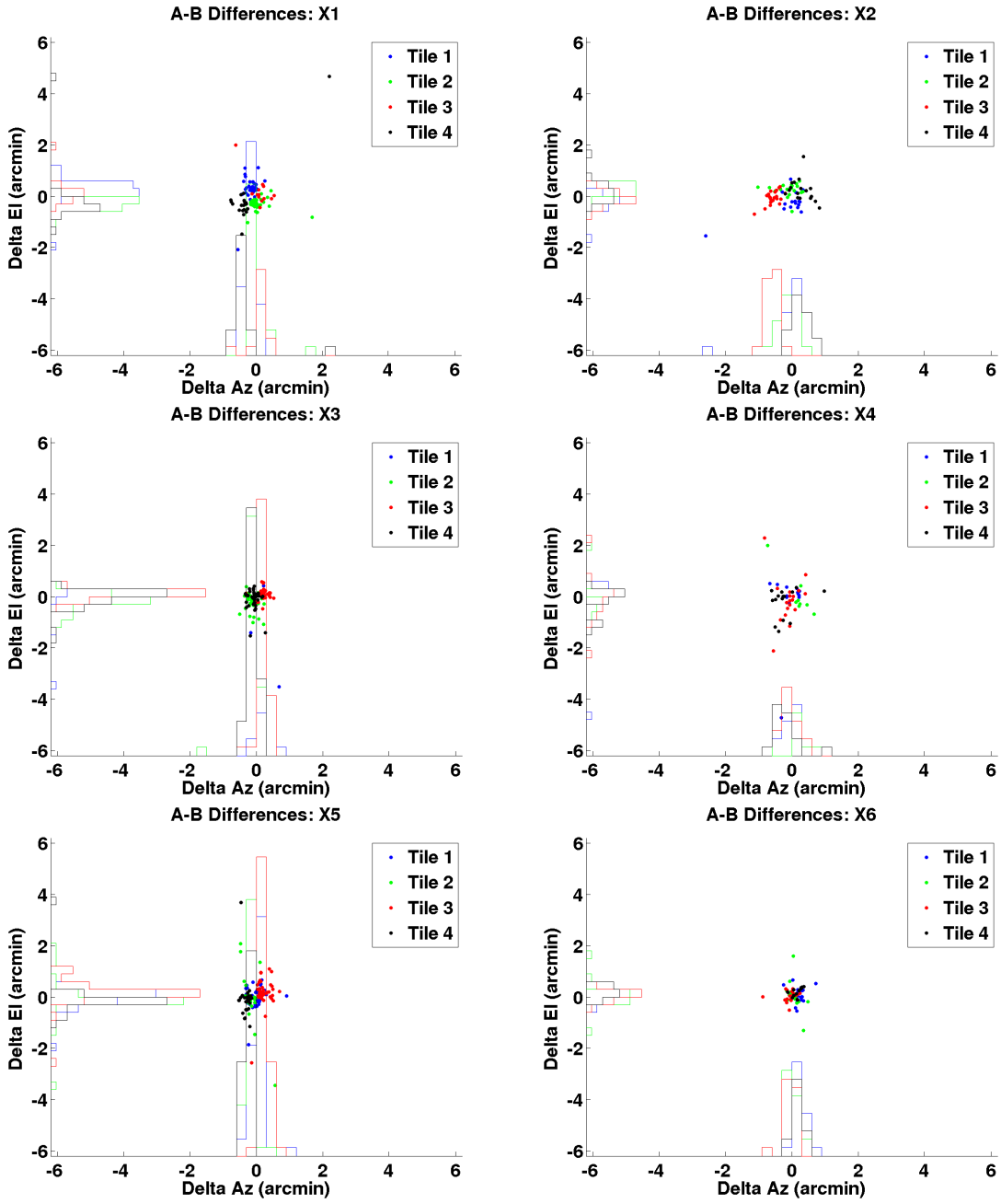


Figure 5.9: A-B pointing differences for all FPUs.

### 5.1.2 Differential Width

Much like differential pointing, large differences in the widths of the beams in a A/B pair have the potential to contaminate the polarization spectra. Differential width leaks the azimuthally symmetric component of a second derivative of the CMB temperature anisotropies into polarization. We define differential width as the difference in the beam standard deviation:

$$\textbf{differential width} = (\sigma_A - \sigma_B)/\sigma. \tag{5.8}$$

Our benchmark value for the differential beam width is 0.5% (as discussed in §3.3.1). As shown in the statistics for differential beam width (Figs. 5.10-5.11), our flight detectors have typical median values of differential beam width of 0.3%-1.2% with large standard deviations. The large standard deviations are due to the relative insensitivity to width of the Gaussian fits used to determine these values. Examining the residuals of the difference maps between A and B beams shows no residual "monopole" structure (actually differential beam width is the $m = 0$ component of the $\ell = 2$ mode) that would indicate errors in differential beam width. So even though not all the values for differential beam width meet our benchmark specifications, we are not concerned about this as a limiting source of systematic error.

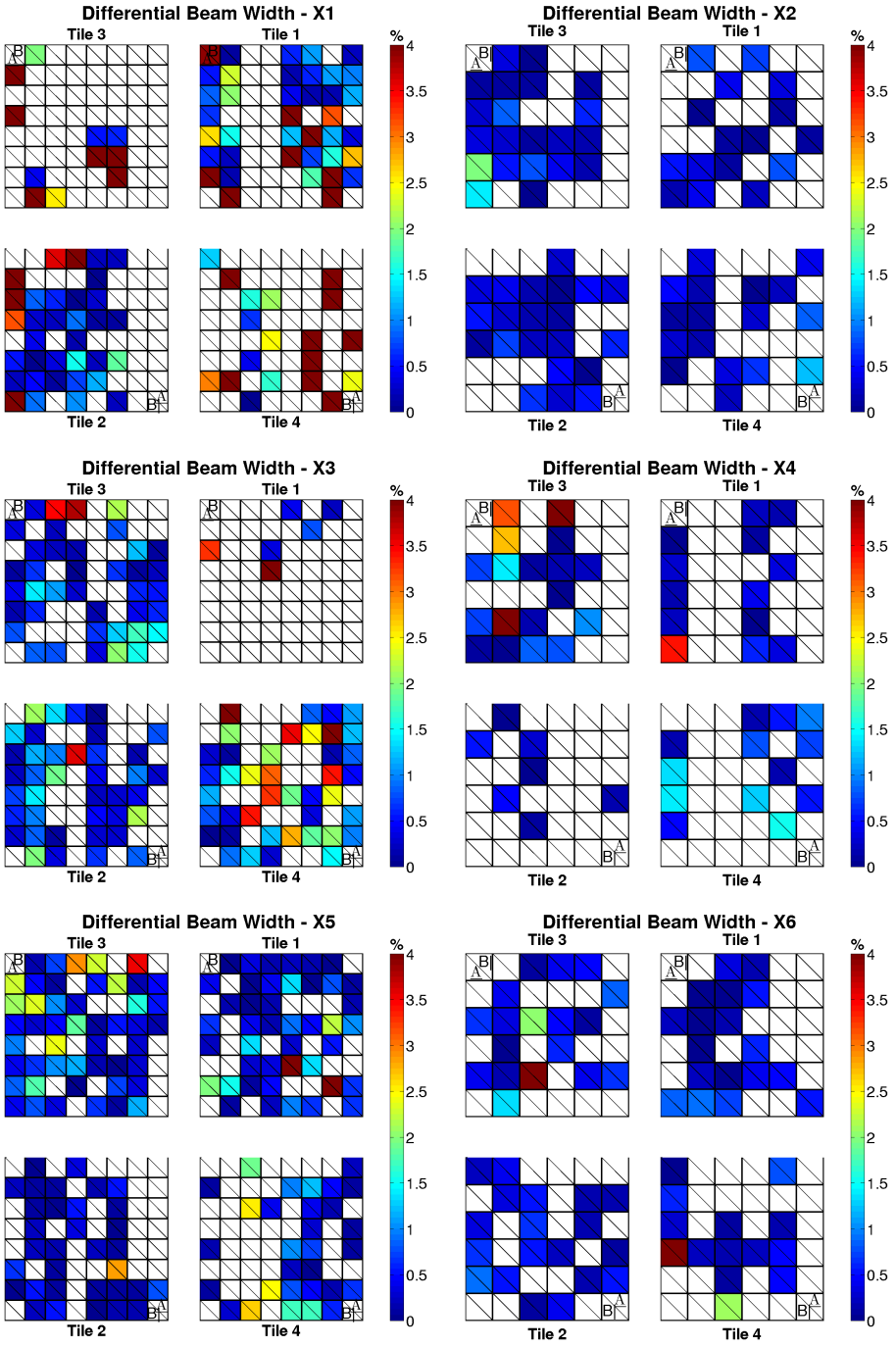


Figure 5.10: Differential beam width for all FPUs.

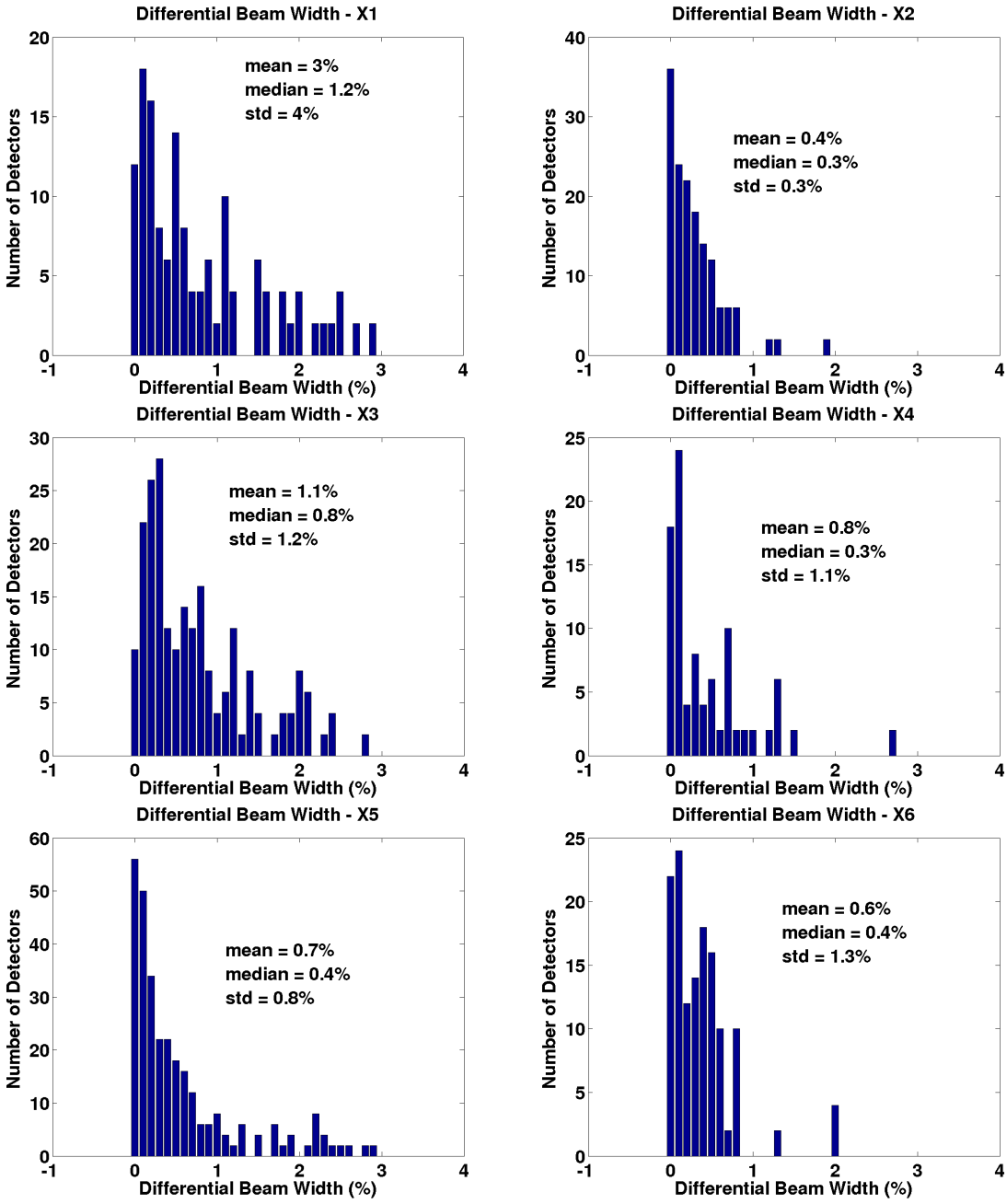


Figure 5.11: Histograms of differential beam width for all FPUs.

### 5.1.3 Differential Ellipticity

Differential ellipticity couples to the second derivative of the temperature of the CMB, and so, like the other differential beam parameters, it has the potential to contaminate the polarization spectrum. We define differential ellipticity in the following way:

$$\textbf{differential ellipticity} = (e_A - e_B)/2. \tag{5.9}$$

The BICEP2 experiment found that they had to subtract their measured differential ellipticity from their maps rather than deprojecting it in their analysis, as was done with some of the other beam systematics [5]. This is due to the fact that the differential ellipticity creates false polarization by coupling to quadrupoles in the temperature anisotropy. This is also how E-mode polarization is created, which means that deprojection of differential ellipticity corrupts the TE spectrum.

SPIDER will likely also need to measure the differential ellipticity well enough to subtract it from the analysis unless another way of evaluating the contamination from this systematic is found. Ideally, the differential ellipticity should be small enough that the rotation of the HWP is enough to make it completely negligible in the final data analysis, and thus, able to be ignored. This is the case described by our benchmark value. One possible method of getting an upper limit on the effect of beam systematics in the data (without using a beam map) may be to co-add the maps from different HWP angles in such a way that, rather than canceling out any systematics, maximizes their effect. These maps may be useful to estimate the leakage.

Our benchmark for differential ellipticity is 0.6%, which was shown to have negligible residuals for an $r = 0.03$ B-mode spectrum (§3.3.3). Typical values for the differential ellipticity, as shown in the statistics for differential ellipticity for all of the SPIDER focal planes (Figs. 5.12-5.13), are 0.3%-0.4%. Most of the pixels in the instrument meet our benchmark value. The contamination from pixels that do not can be handled in the data analysis via subtraction of the measured differential ellipticity or cut from the analysis completely (in highly elliptical cases).

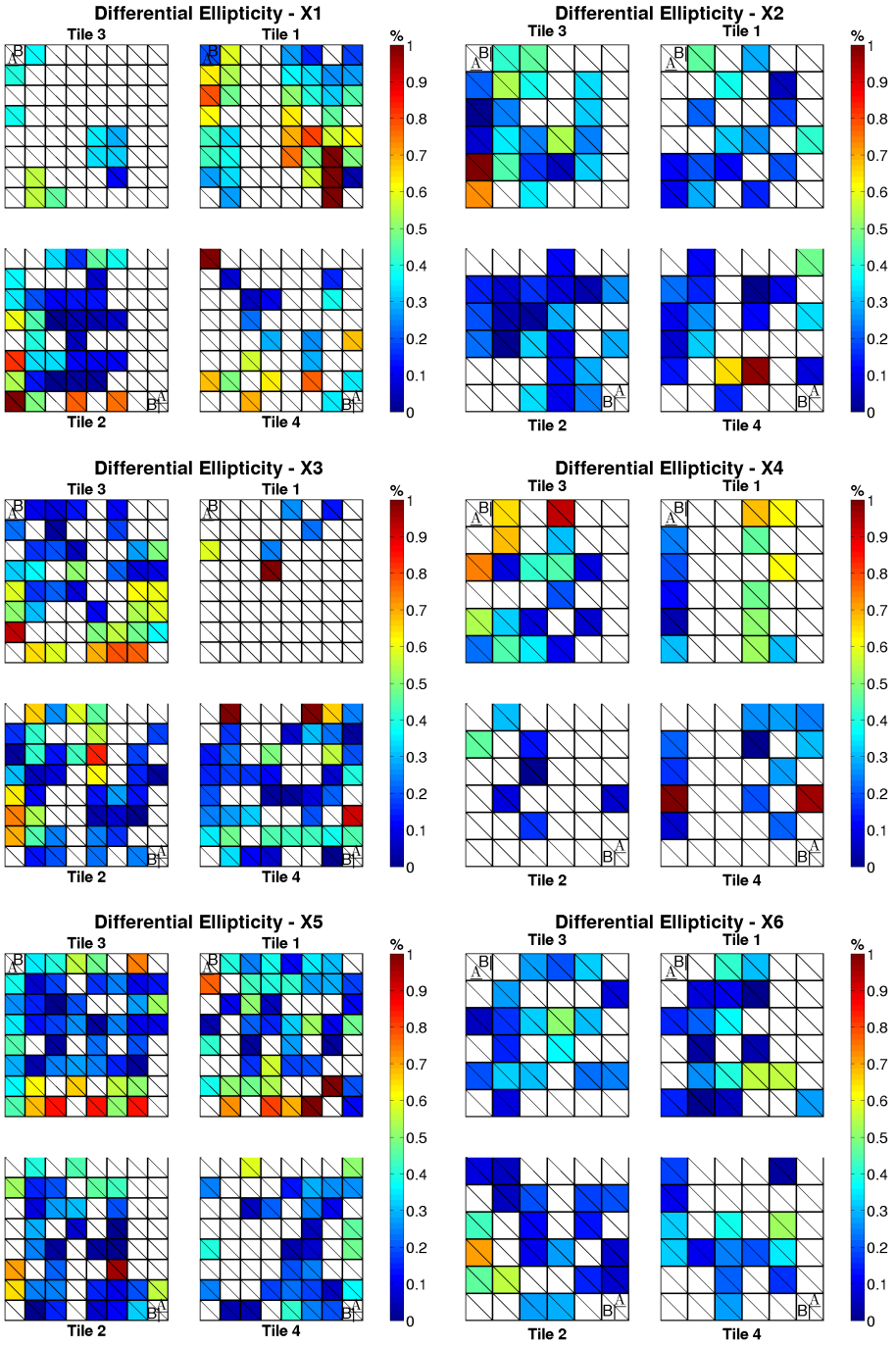


Figure 5.12: Differential beam ellipticity for all FPUs.

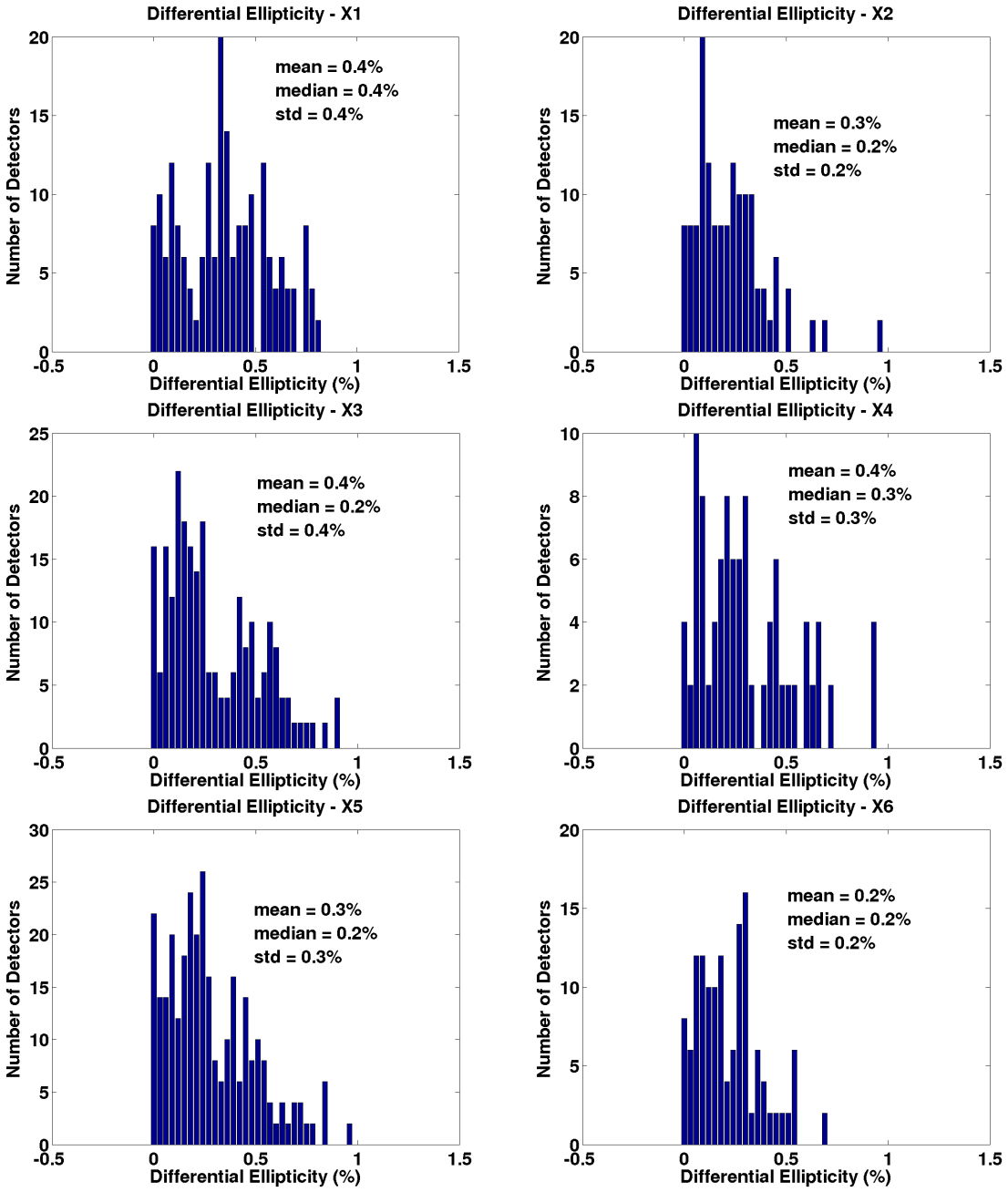


Figure 5.13: Histograms of differential beam ellipticity for all FPUs.

Table 5.2: Differential Beam Parameters for all FPUs

| | differential pointing (%) | differential width (%) | differential ellipticity (%) |
|---|---|---|---|
| Benchmark | 10% | 0.5 % | 0.6 % |
| X1 | 3.8 ± 4.6 | 3.0 ± 4.0 | 0.4 ± 0.4 |
| X2 | 2.7 ± 1.9 | 0.4 ± 0.3 | 0.3 ± 0.2 |
| X3 | 3.1 ± 7.8 | 1.1 ± 1.2 | 0.4 ± 0.4 |
| X4 | 3.4 ± 4.2 | 0.8 ± 1.1 | 0.4 ± 0.3 |
| X5 | 2.9 ± 2.5 | 0.7 ± 0.8 | 0.3 ± 0.3 |
| X6 | 1.8 ± 1.5 | 0.6 ± 1.3 | 0.2 ± 0.2 |

These parameters are determined by averaging the parameters derived from individual beam maps for each focal plane. The errors describe the spread over the pixels (one standard deviation).

### 5.1.4 Beam Steer

The maps used in the previous section were all done in the far field of the telescope. Taking maps of the detectors in the near field of the telescope is useful to examine the alignment of the SPIDER beams. Occasionally, we have found detectors in which the beam axes were misaligned with the optical axis. The result is a beam that has been "steered" into the walls of the telescope. An extreme example of this phenomenon is shown in Fig. 5.14a. When this happens, much of the beam's power terminates on the interior of the telescope, causing a decrease in optical efficiency.

We can calculate the magnitude and direction of the beam steer. The expected locations of the beam are given by

$$x = h \tan r \cos\theta \tag{5.10}$$

$$y = h \tan r \cos\theta, \tag{5.11}$$

where $h$ is the height of the near-field beam mapper above the aperture and $(r, \theta)$ are the coordinates of each pixel (given in degrees).

I fit a Gaussian to the measured beams to get $(x_{\rm fit}, y_{\rm fit})$. The beam steer in the $x$ and $y$ directions is then given by

$$\text{Beam Steer}_x = x_{\rm fit} - x \tag{5.12}$$

$$\text{Beam Steer}_y = y_{\rm fit} - y. \tag{5.13}$$

See Fig. 5.14b for an arrow plot showing the magnitude and direction of the beam steer for an early iteration of the X3 focal plane. The beams are steered in different directions at the top and bottom of each tile. From this, we concluded that the beam steer is a problem in the tile fabrication and is unrelated to the optical elements in the SPIDER telescope. Furthermore, we see that the effect does not propagate to the far field of the telescopes, as seen in the far field maps mentioned previously.

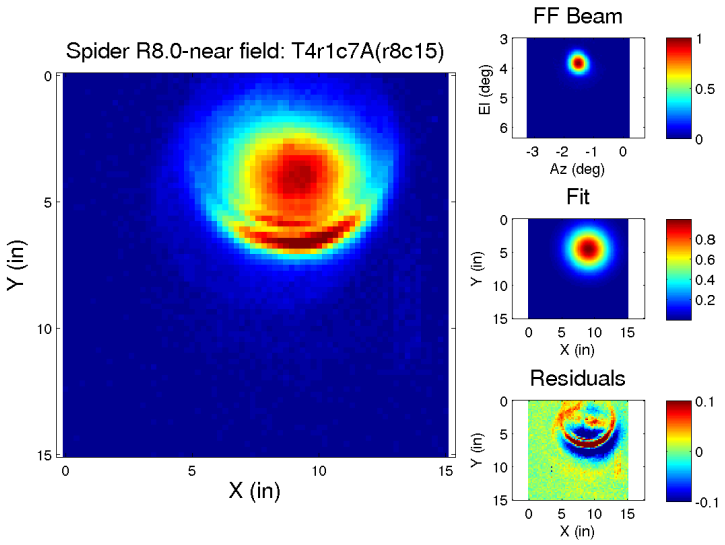


(a) An example of a near field beam map where the beam shows significant misalignment. The far field beam of the same detector is shown in the upper right. It is clear that the effect does not propagate into the far-field. The fit and residuals (middle and lower right) are to the near field beam.

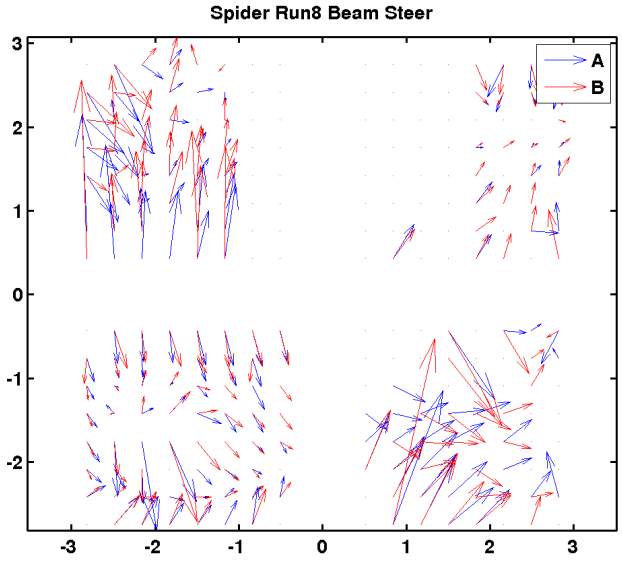


(b) Arrow plot of beam steer for SPIDER Run 8.0 (X3). The origin of each vector indicates the ideal centroid of the beam. The length of the arrow corresponds to the magnitude of the beam steer. The direction of the arrow corresponds to the angle of the beam steer. The axes and arrows are both measured in inches.

Figure 5.14: Beam steer measurements.

### 5.1.5 Other Beam Effects

The maps for the characterization of the beam parameters were done with a chopped thermal source. We additionally took maps with a number of coherent microwave sources. These maps were problematic in the high bay, since they were generally so bright as to saturate the detectors on the main beam and cause reflections off the ceilings and walls in the maps.

Fig. 5.15 contains an example of a map taken with a polarized microwave source. There are many features in this map, and it's tricky to understand them all. The main beam is the brightest feature in the map. The map has been normalized to the height of the main beam, though, since the main beam saturates because of the brightness of the source, this normalization is not physically accurate. (For example, the amplitude of the ghost may appear to be -10dB based on the color scale of the map, but the true amplitude is much lower than that.) The near sidelobe structure of the main beam (covered in more detail in the next section) is clearly visible.

The ghost is recognizable as the feature reflected across the center of the focal plane from the main beam. (The main beam and ghost stay in the same relative position to each other in other detector maps.) The features directly above the main beam and the ghost are reflections off the ceiling of the highbay. This was determined by comparing detector maps, which show that these features have a fixed position relative to the main beam/ghost. The three faint features in the lower left of the map are cross-talk beams. We know this because their positions are the same as the beams of the detectors causing the cross-talk. These three features all stay within the same detector row. The other, unlabeled features in the map may be due to additional cross-talk beams or reflections off the walls and other structures in the high bay. There are so many features in these maps that it becomes difficult to accurately identify the cause of each one.

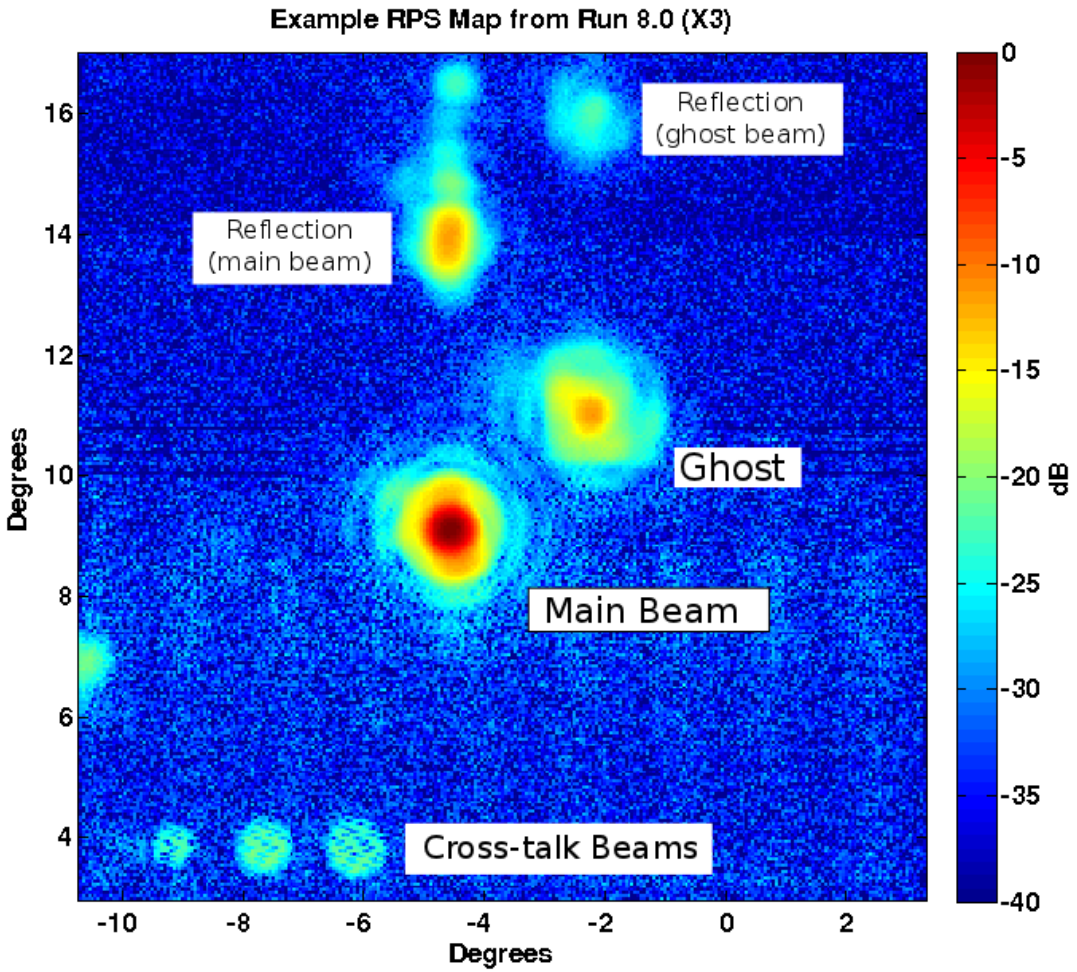


Figure 5.15: A beam map taken with a bright amplified noise source. Various features and reflections of the beam are labeled.

## 5.2 Sidelobes

### 5.2.1 Near Sidelobes

A study of the near sidelobes of the 150GHz beams was done by taking two beam maps: a thermal map and a map with a polarized microwave source [19]. The microwave source was aligned with the horizontal polarization axis of the detectors.

Beam profiles for individual detectors were obtained by taking annular averages of the beam maps. The beam profiles were then averaged over all detectors to obtain high signal-to-noise and to obtain average profiles. The profiles for the map taken with the thermal source turn out to be different than the profiles for the map taken with the microwave source — the first sidelobe is higher and the profile is much smoother for the map taken with the thermal source(see Fig. 5.16). We believe the smoother profile is due to the fact that the thermal source has a much larger bandwidth than the microwave source, and the detectors have broad bandwidths around their band centers. So the thermal source will cause the detectors to respond at a broader range of frequencies than the microwave source, broadening the beam and smoothing the profile. The increased the height of the first sidelobe of the thermal profile relative to the microwave profile is not well understood. The height of the first sidelobe is -14dB to -18dB from the amplitude of the main beam.

The sidelobes of the beams vary as a function of the distance from the center of the focal plane. The sidelobes are higher in the center of the focal plane and drop off radially at the edges. This can be seen in a four-tile plot, Fig. 5.17.

This was a surprising result — we had no reason to expect the height of the sidelobes to vary across the focal plane. We speculate that pixels near the edge of the focal plane terminate more of their power onto the cooled optics sleeve, which we see as a reduced sidelobe in comparison to detectors in the middle of the focal plane. A Zemax model created by Sean Bryan confirms the radial dependence of the sidelobes. I used it to plot the sidelobes for pixels in various locations across the focal plane. The sidelobes from the Zemax model, seen in Fig. 5.18, are in agreement with our measured results, at least at the first sidelobe. This would be a good topic to explore in more detail in future simulations.

Another systematic to check for is polarized sidelobes (as in §3.7), which is a difference in the sidelobes for the A and B detectors of a pair. If, for example, the A detectors had uniformly higher sidelobes than the B detectors, this would cause a polarization signal,

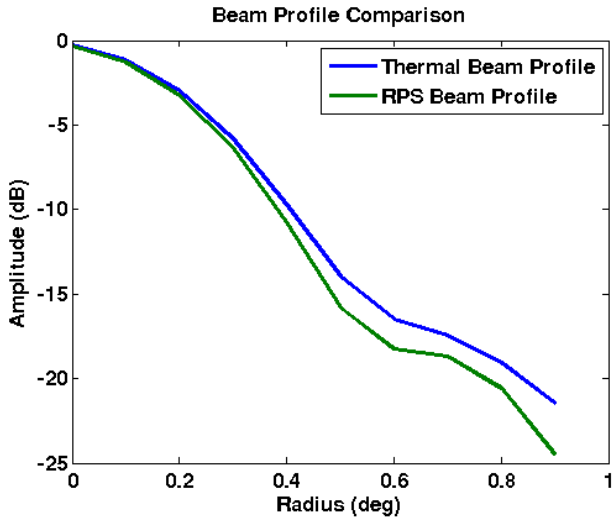


(a) A comparison of the mean beam profiles out to 1 degree for maps taken with the thermal source and the rotating polarized source (RPS). The sidelobes are not as visible in the thermal map because we have hit the noise floor of the map.

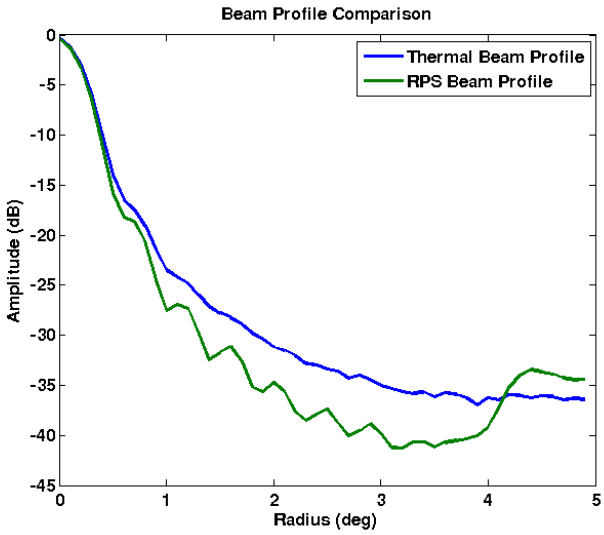


(b) A comparison of the mean beam profiles out to 5 degrees for maps taken with the thermal source and the rotating polarized source (RPS). The large bump at large radii for the RPS map is due to ghosting reflections of the HWP. It is not part of the sidelobe structure.

Figure 5.16: Mean beam profiles for 150GHz detectors.

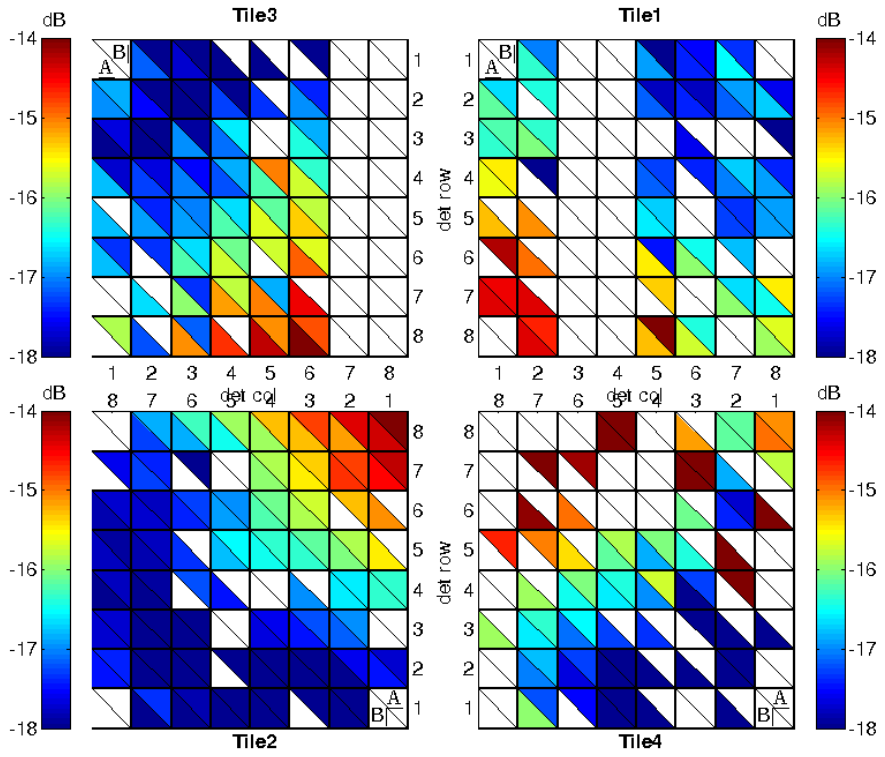


Figure 5.17: A four-tile plot showing the radial distribution of the amplitude of the first side lobe across the focal plane. The side lobes are higher in the center of the focal plane and drop off radially. This data was taken from the thermal beam map. The same pattern is also seen in the RPS maps.

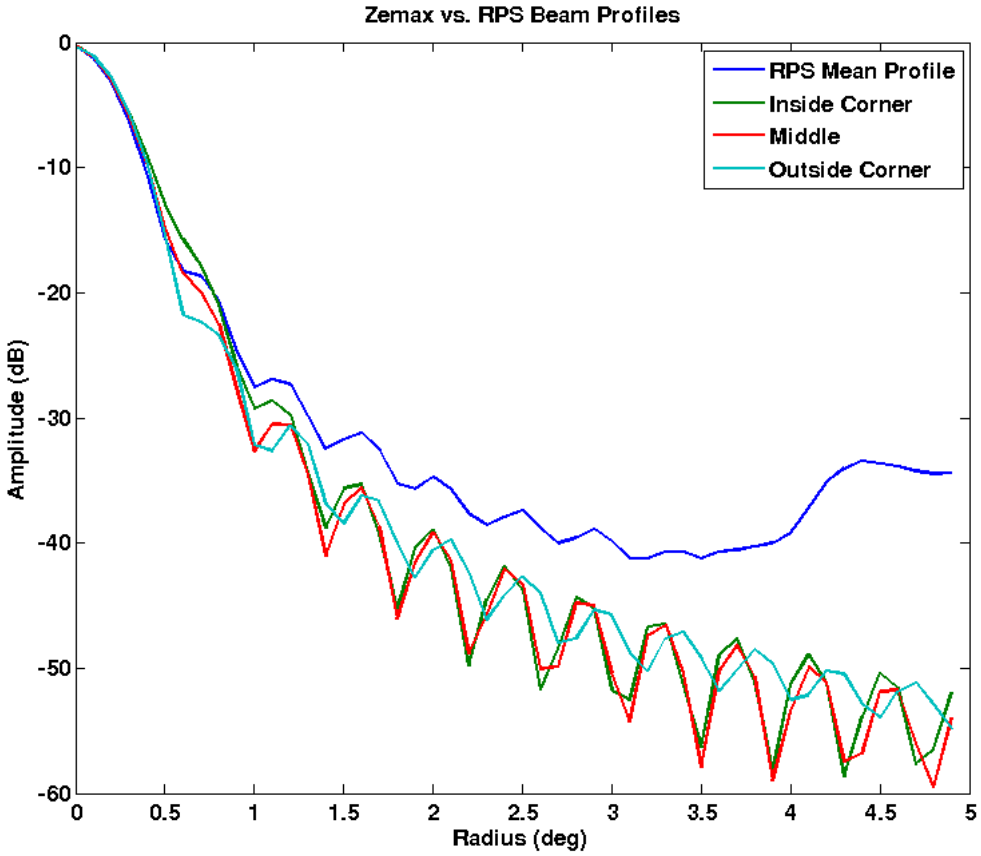


Figure 5.18: Beam profiles showing the sidelobes from maps created by a Zemax calculation (done by Sean Bryan). Beam profiles from pixels at varying locations across the focal plane are shown, along with the mean beam profile from the RPS map, for comparison. "Inside corner" refers to pixels near the center of the focal plane (at the inside corner of a tile), "middle" refers to pixels in the middle of a tile, and "outer corner refers" to pixels at the edge of the focal plane (at the outside corner of a tile). At the first side lobe, we again see the pattern that the pixels near the center of the focal plane have higher side lobes than those at the edges.

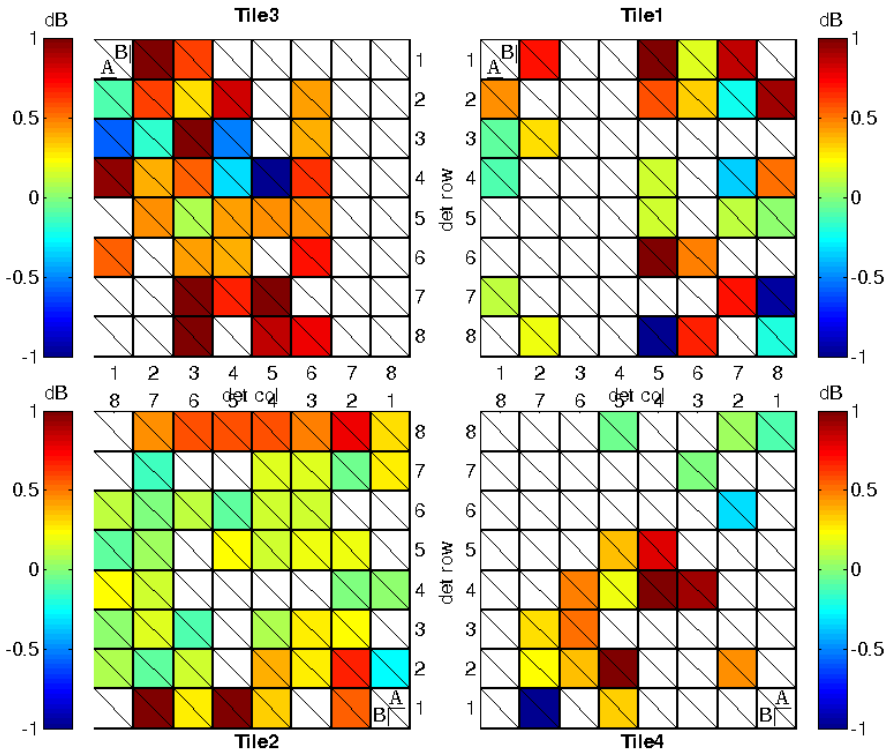


Figure 5.19: A four tile plot of the difference of the height of the first side lobe for A/B pixel pairs. The differences are small and random across the focal plane.

even for an unpolarized source. We find that the sidelobes do not systematically vary with detector polarization. This can be seen by eye in Fig. 5.17. This can be measured more systematically by differencing the amplitude of the first sidelobe for each working A/B pixel pair (Fig. 5.19). The difference in sidelobe amplitude between A/B pairs is small ($\leq 1dB$) and random across the focal plane.

### 5.2.2 Far Sidelobes

Our systematic requirements for the far sidelobes are set by the need to reduce the B-mode power spectrum contamination that can result from pickup of polarized emission from the galaxy. Futhermore, these sidelobes can potentially sweep past the galactic plane, the Sun, the ground, and parts of the balloon, which could result in spurious polarization being picked up by the detectors. The galaxy is both complex and proximate to the SPIDER scanning region, and is expected to comprise the largest fraction of polarized contamination at the angular scales we are interested in.

During our deployment to Palestine, Texas, we attempted to get a rough measurement of the far sidelobes by scanning the cryostat across an amplified noise source. This was done while SPIDER was outside the high bay, hanging on "Tiny Tim" during the compatibility tests. ("Tiny Tim" is an extremely large vehicle used to transport flight payloads from the high bay to the launch pad at the Columbia Scientific Ballooning Facility.) The 90GHz IMPATT source was mounted on the roof of the high bay and pointed down at SPIDER. The distance between the source and the aperture was approximately 20-30m. These scans were done by hand. (That is, our fearless leader was physically scanning the cryostat back and forth, rather than relying on the gondola motors to provide motion.) Photos of the experimental set up can be found in Figs. 5.20a and 5.20b.

This measurement was complicated by the fact that the beams saturated when SPIDER was pointed directly at the source. We attenuated the source with layers of Eccosorb HR-10 in order to measure the main beam (and therefore get a normalization of the sidelobes) and then did a separate pass with the source unattenuated for the far sidelobes. The analysis of this data required us to match the two passes and stitch them together to create a continuous beam profile. Nonetheless, we were able to measure the far sidelobes down to approximately -60dB, which is near our systematic requirement of -67dB. Here we are assuming a peak beam height of 0dB.

The results of this measurement are shown in Fig. 5.20c. This plot shows the beam slices in both polarizations of a detector in the X3 focal plane. The large bump in the beam profile at -8 degrees is due to the "ghost" beam (a secondary beam caused by internal reflections off of the half-wave plate). The noise floor kicks in around -50dB for the "A" detector and around -60dB for the "B" detector. (We do not expect the noise floor to be the same for both polarizations because the source is fully polarized, so the two detectors are not seeing the same source intensity.) The beam profiles hit the noise floor about 20 degrees off of the main beam. There should be a significant reduction in signal amplitude around 15 degrees due to the forebaffles.

This measurement will need to be improved to achieve the -70dB signal-to-noise ratio necessary for the systematic requirements of the experiment. This will likely be achieved by a combination of using a brighter source or putting the existing source closer to the cryostat and finding a systematic way to sweep the beams through the source (rather than doing it by hand).

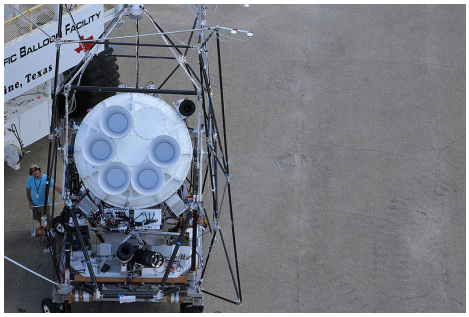

(a) Bill Jones, scanning SPIDER across the telescope. Photo courtesy of Jon Gudmundsson.

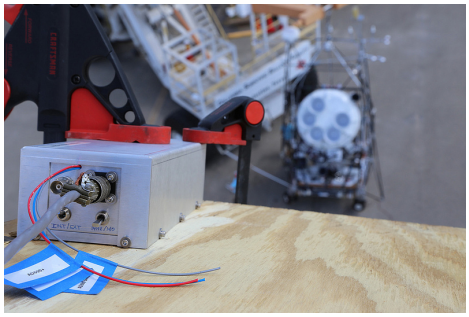

(b) The amplified noise source, clamped to the railing on the roof. Photo courtesy of Jon Gudmundsson.

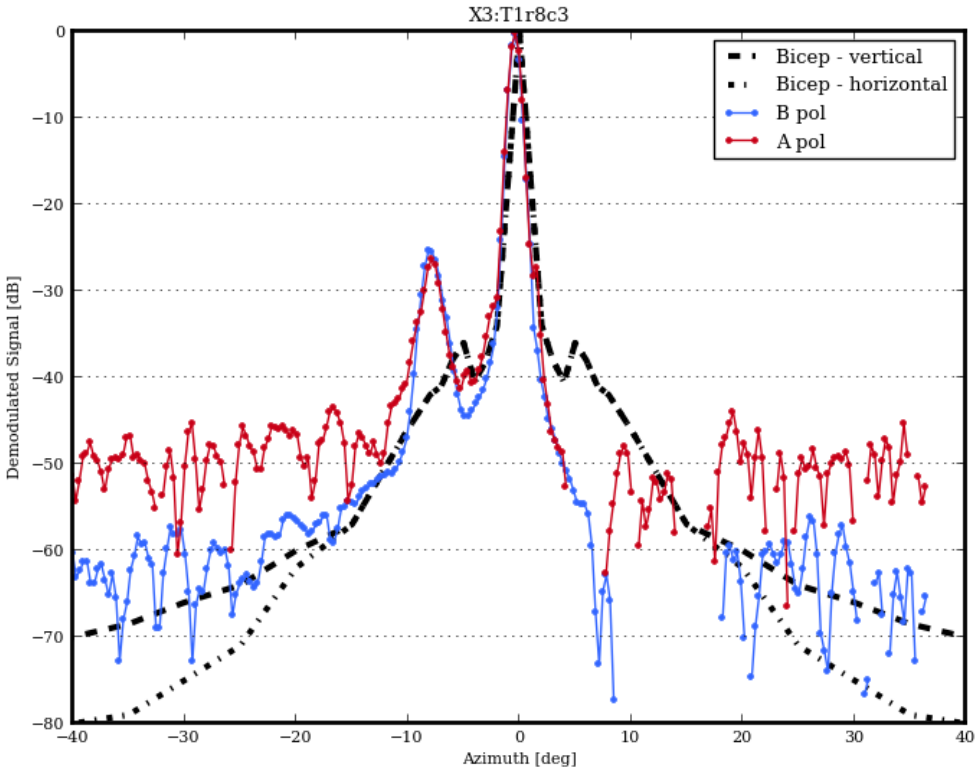


(c) A slice through the far sidelobes of both polarizations of a SPIDER pixel (red and blue lines). Also shown are the same beam profiles for the BICEP1 experiment [84], which have been used in SPIDER simulations. Figure courtesy of Jon Gudmundsson.

Figure 5.20: Experimental setup and measurement of the far sidelobes.

## 5.3 Using Beam Maps to Test Half-Wave Plates

The HWP is a tremendous advantage of the SPIDER experiment. By rotating the polarization on the sky without rotating the beam, the HWP will ameliorate many beam systematics. In order for this to work, it is important that the HWP does not change the beam shape or cause other undesirable effects. Beam maps turned out to be an effective way to test many of the characteristics of the HWPs, in particular their effects on beam pointing and their reflectivity.

### 5.3.1 Beam Effects

It is important that the HWP not cause the beams to shift or change shape as it rotates, or else its usefulness in canceling out systematic effects will be largely negated. One of the ways I explored this was by taking beam maps at several relative angles of the HWP and then comparing the beams from each of those maps to see if they had changed.

This measurement turned out to be relatively difficult due to the necessity of keeping the az-el gadget pointing exactly the same between beam maps. The pointing, which is precise during a map, is frequently reset for other measurements and can be difficult to reproduce to better than a degree. However, the measurement of differential pointing depends only on the relative pointing between detectors and not the absolute pointing of the cryostat, so it can be easily compared for maps taken at different HWP angles.

Fig. 5.21a shows the differential pointing for the X3 focal plane from maps taken with different relative angles between the HWP and the detectors. It shows that the differential pointing does not shift or rotate as a function of the HWP angle. This is further shown in Fig. 5.21b, which takes the differences of the differential pointing measured for each A/B pair for maps taken at different HWP angles. The histograms in that figure center around zero in both dimensions, showing that the angle of the HWP does not affect the relative pointing of the detectors.

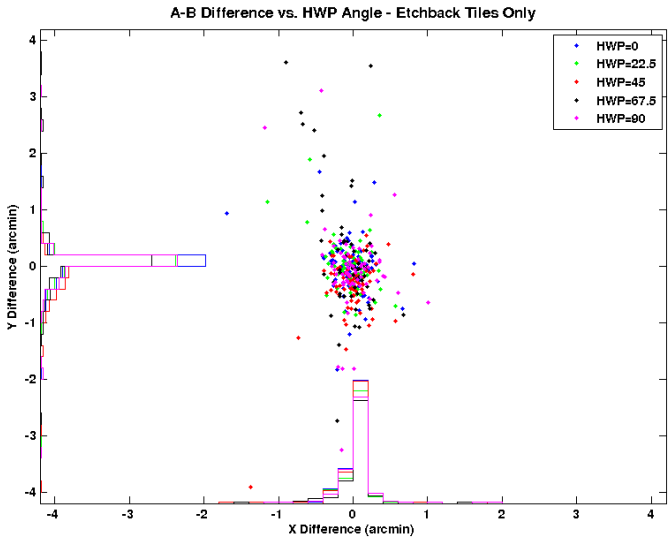


(a) Pointing difference between detectors (A-B difference) for maps taken at varying HWP angles. SPIDER Run 8.0 (X3)

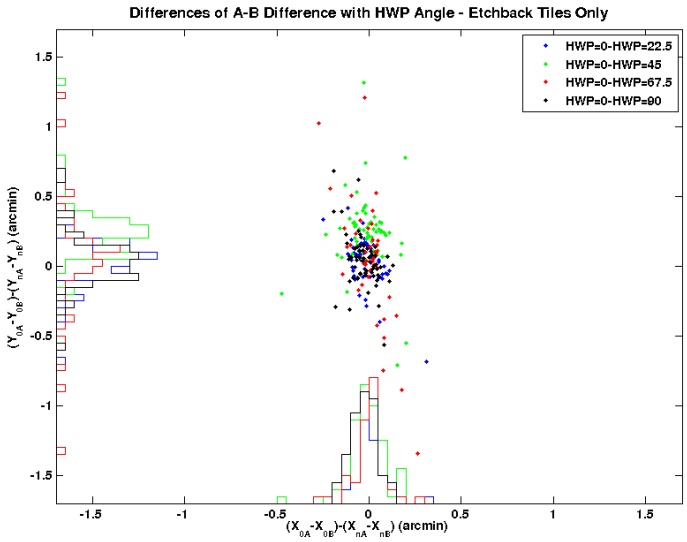


(b) Differences of A-B differences for maps taken at varying HWP angles. The points for HWP=0-HWP=45 (green) show some slight deviation away from zero in the vertical direction. Since the other map differences are well-centered around zero, we do not interpret this as a problem with the half-wave plate. It is likely due pointing calibration errors in the beam maps. SPIDER Run 8.0 (X3)

Figure 5.21: A-B pointing difference histograms and scatter plots for combinations of maps taken at various HWP angles.

### 5.3.2 Ghosts

Early on in the creation of the SPIDER HWPs, there were some issues with the anti-reflection coatings, such that the HWPs ended up being much more reflective than was desirable. This was hard to catch, since the reflectivity was often very low when the HWP was tested warm, but quite high when tested in a cryogenic environment. These very reflective wave plates caused internal reflections within the cryostat that resulted in large "ghost" beams in the beam maps. (i.e., faint secondary beams caused by internal reflections off the HWP.) A geometric ray trace of this phenomenon can be seen in Fig. 5.22.

An example of a ghost beam in a map from Run 9.0 can be seen in Fig. 5.23a. If we zoom in on the portion of the map that contains the ghost beam, we can fit a Gaussian profile to it and compare the heights of the fitted ghost beams to the heights of the main beam. The ghost beam in Fig. 5.23a can be seen in more detail in Fig. 5.23b. The ghost beams show radial differences in amplitude, width, and ellipticity across the focal plane. These can be seen in Figs. 5.24-5.26. One theory for how these radial patterns come about is that they are due to small aberrations in the optics that get magnified by the ghost beam, since it passes through the optics three times before being seen by the detectors (in comparison to the main beam, which only passes through the optics once).

During Run 9.0, I found that ghost beams had approximately 10% of the power of the the main beams, indicating that the HWPs had a reflectivity of $> 20\%$ (the exact value depends on the focal plane reflectivity assumed, which we estimate to be somewhere between 1/4 and 1/2). Since our target reflectivity for the HWPs was less than 2%, this prompted us to use new techniques for applying anti-reflection coatings that ultimately got all of the HWPs to within the goal. Prior to this, the anti-reflection coatings were mechanically attached to the sapphire plates through small clips around the perimeter of the plate. AR coatings attached with this technique were found to sag in the middle of the plate. The eventual solution was to bond the AR coatings to the sapphire plates with either adhesives or a hot-pressed bonding process (see §2.4). When we repeated this measurement with beam maps taken in the flight cryostat in Palestine with improved HWP anti-reflection coatings, we found that the ghosting was $<2\%$, which meets our benchmark for this systematic (see §3.4.1).

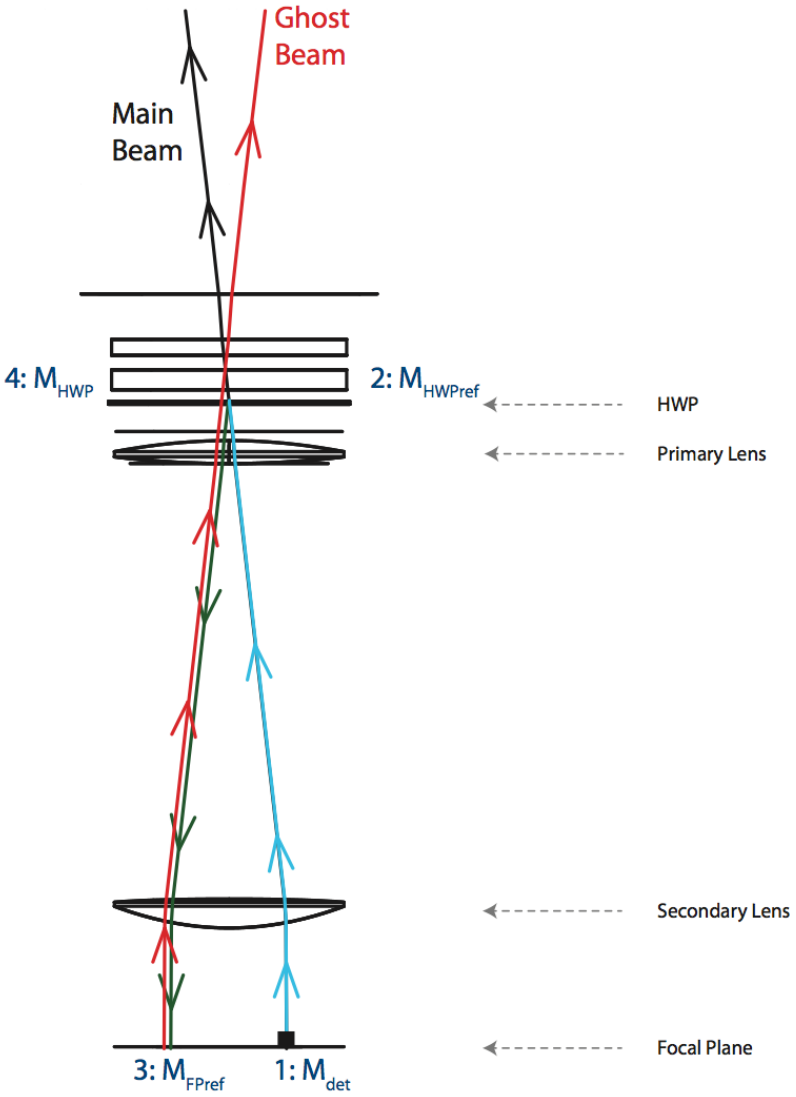


Figure 5.22: A ray trace of how ghost beams are formed. In the time-reversed picture, the main detector beam leaves the focal plane (cyan). The majority of it is transmitted through the HWP as the main beam (black), but a small fraction of it is reflected back through the optics (green) and then reflects off the FPU and exits the optical stack as the ghost beam (red). Figure from [22].

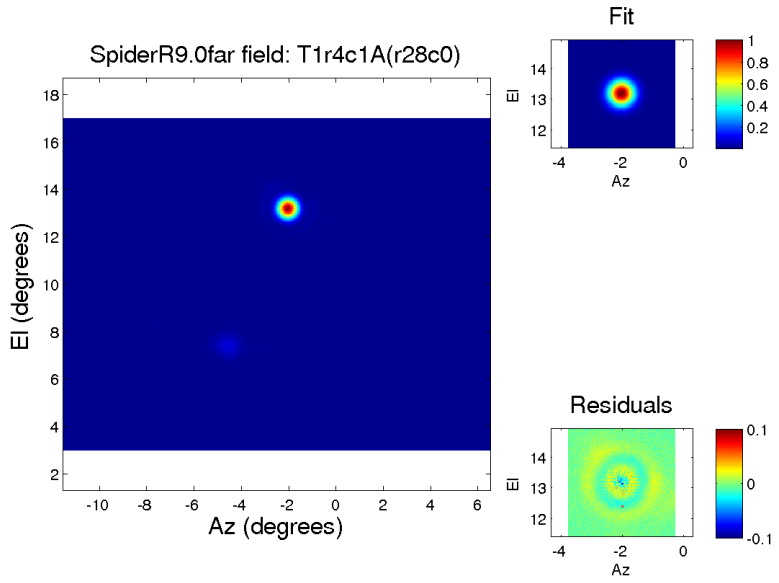


(a) An example of a beam map with a visible ghost beam from SPIDER Run 9.0 (X4). The faint secondary beam at az $= -5^o$ and el $= 7^o$ is caused by internal reflections, primarily off the HWP.

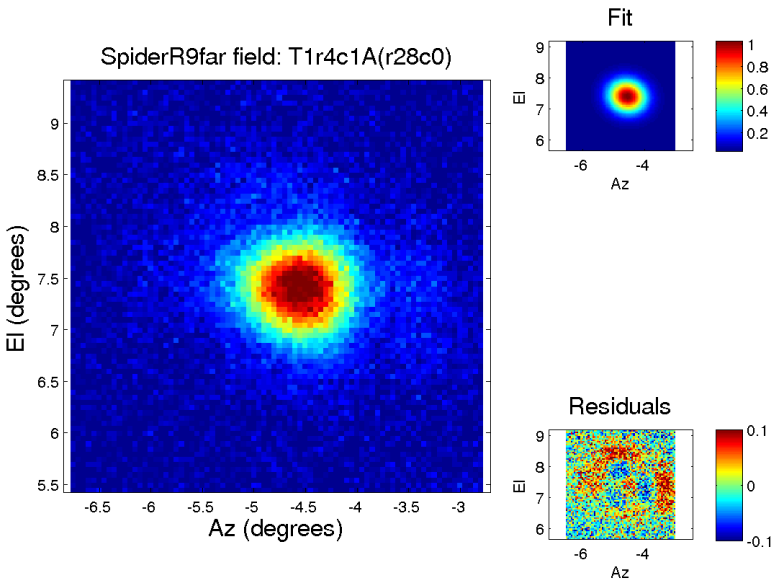


(b) A zoomed-in map of the ghost beam in Fig. 5.23a. The map has been renormalized such that the height of the ghost beam is equal to one.

Figure 5.23: Maps of the main and ghost beams.

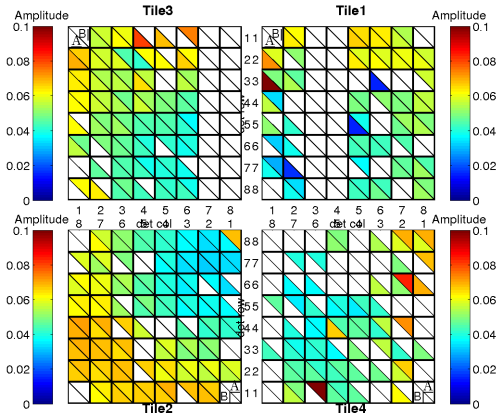


Figure 5.24: Ghost amplitude (as a percentage of the height of the main beam). The amplitude varies radially across the focal plane, with the amplitude lowest in the center of the focal plane.

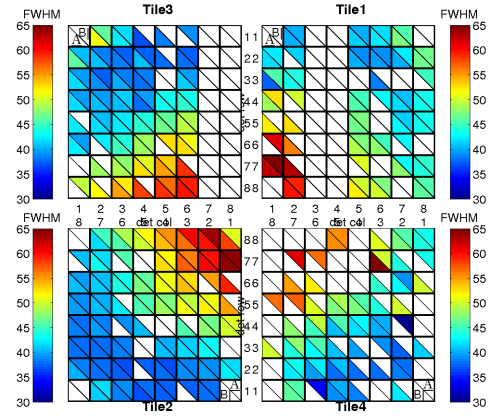


Figure 5.25: Ghost beam width (arc minutes). The width varies radially across the focal plane, with the largest widths in the center of the focal plane.

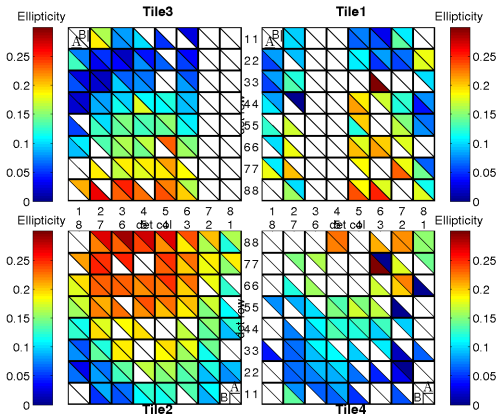


Figure 5.26: Ghost beam ellipticity. The ellipticity also shows a radial pattern across the focal plane with most ellipticitical beams in the center of the focal plane.

## 5.4 Diffuse Scattering

Another way to use the SPIDER beam maps is to look for diffuse scattering (power outside the main beam). It is possible for elements in the optical chain to scatter incident light in such a way that it doesn't create a coherent feature, but rather is diffusely spread outside the main beam. By calculating the power in the beam map outside of a given radial angle of the main beam, we can constrain the amount of diffuse scattering.

We add the power in annuli around the main beam and then take the cumulative sum of the power, starting from the edges of the map. The result is normalized by the total power in the map. Because the maps are small and square, a correction for the "missing" area in the ring is included. We also want to exclude the ghost from the upper limit since it is not really "diffuse" scattering. Lastly, because these maps are taken in the high bay, there are reflections of the main beam off the walls and ceiling. These features, since they are not intrinsic to the optics, are also masked out. Fig. 5.27a shows what a masked map looks like.

For a a figure of merit, I take the upper limit of diffuse scattering as the percentage of power in the maps outside of three degrees. This number was chosen to distinguish truly diffuse scattering from the power in the near sidelobes.

This measurement was done with two sources — an amplified noise source and a thermal source. For the maps taken with the noise source, I am able to give an upper limit on diffuse scattering of $\sim$3%. For the maps taken with the thermal source, the upper limit on diffuse scattering is $\sim$5%. The difference between the upper limits for the maps taken with different sources is not entirely understood.

We do not have a simulation benchmark for diffuse scattering, but it is essentially degenerate with the measurement of the far sidelobes. Ideally, we would take beam maps with extremely large scans in azimuth ($> 90^\circ$) to directly measure both the far sidelobes and the coupling to power at large angles. This measurement is difficult due to the gondola's limited range of motion when inside the high bay and the amount of time (more than 12 hours) it takes to complete the map. Our cryogenic difficulties (§6.1) prevented us from taking this measurement during the integration campaign in Palestine, TX.

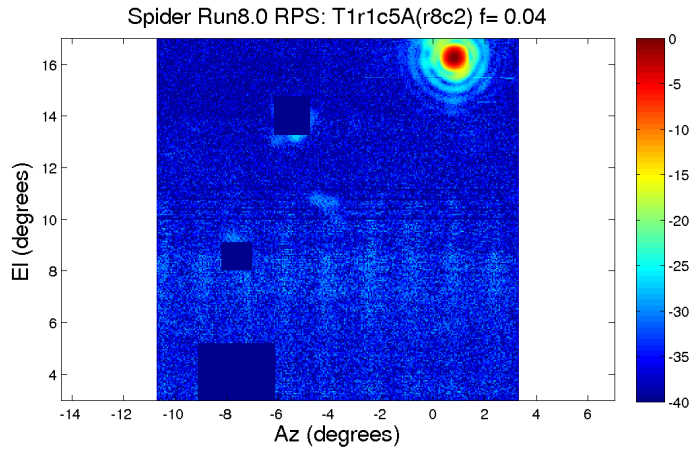


(a) An example beam map with the ghost and reflections masked out. There are some faint vertical stripes in this map that we were originally concerned about biasing the measurement. However, they were measured to contain less than 0.2% of the power outside the main beam. SPIDER Run 8.0 (X3)

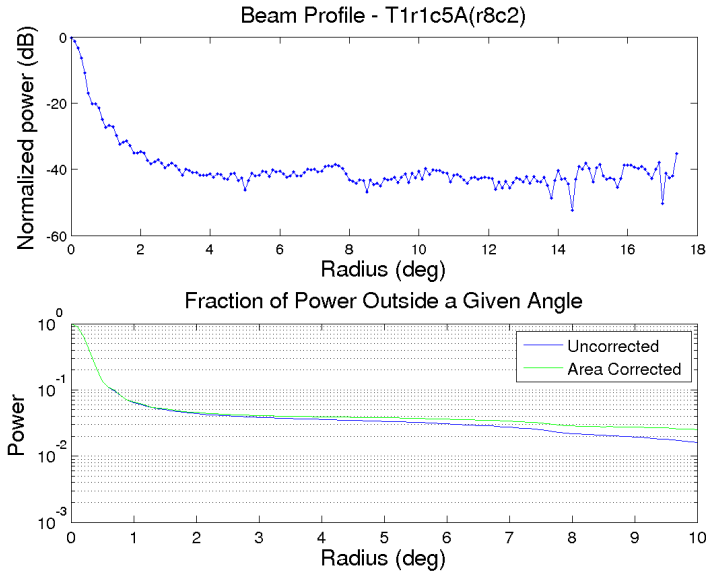


(b) Beam profile and fraction of power outside a given angle. The "uncorrected area" refers to the correction to the area in the rings due to the map size mentioned in the text. SPIDER Run 8.0 (X3).

Figure 5.27: An example beam map and beam profile from measurements of diffuse scattering.

## 5.5 Polarization Efficiency and Rotation

As discussed in §3.6, the ideal SPIDER detector would have a relative polarization angle ($\Psi_{rel}$) of 90° and a perfectly known absolute orientation angle ($\Psi_{abs}$). The relative polarization angle determines the cross-polarization response, which is ideally zero. Cross-polarization response determines the polarization efficiency, $\gamma = (1-\epsilon)/(1+\epsilon)$. The amplitudes of the polarization power spectra are proportional to the square of the polarization efficiency, $\gamma^2$ [84]. Errors on the calibration of the absolute orientation angle (the angle that references the antennas to the sky) will lead to E-B mixing. Accurate determinations of these angles must be made to prevent rotation of E-mode signals into false B-mode signals. We developed several techniques and built specialized calibration equipment in order to make these measurements.

### 5.5.1 Caltech Measurement

We attempted to measure $\epsilon$, $\Psi_{rel}$, and $\Psi_{abs}$ for the X3 focal plane by observing polarized radiation at many different angles with respect to the detectors. We put a rotating polarized noise source in the Caltech high bay balcony (which is in the far-field) and made small beam maps with the polarizing grid at each of the following angles: 0, 5, 10, 25, 40, 45, 65, 80, 85, 90, 95, 100, 125, 150, 170, 180, 185, and 190 degrees. We then used a Gaussian fit to determine the amplitude of the beam for each map. Many maps are required for this measurement, so we were not able to do this measurement for every pixel in the focal plane. We used a small subset of the detectors. A plot of the beam amplitude of each working detector pixel pair as a function of wire grid angle can be found in Fig. 5.28.

There are some rather obvious imperfections in the data from this measurement: the A and B detectors have different amplitudes, and the minimum of the B polarization is slightly offset from the maximum of the A polarization. Both of these problems are likely due to the physical alignment of the source with respect to the aperture. The source was not well-aligned with the telescope mount. It was pointed above the cryostat and at a skewed angle. The fits in the plot are of the form $y = A\sin^2(bx+\phi)+c$.

Using this data, I compute the cross-polar leakage for each pixel by taking the minimum of the fit for the B polarization and dividing by the maximum of the corresponding A

Table 5.3: Polarization Efficiency and Rotation Measurement I.

| Pair Number | 1 | 2 | 3 | 4 | 5 | 6 | mean |
|---|---|---|---|---|---|---|---|
| Cross-pol Response | 0.21% | 0.29% | 0.39% | 0.33% | 0.21% | 0.27% | 0.28% |
| $\phi_A - \phi_B$ | 5.7° | 9.8° | 10.3° | 10.3° | 7.5° | 12.4° | 9.3° |

polarization:

$$\epsilon = \frac{B_{min}}{A_{max}}. \tag{5.14}$$

From Table 5.3, I calculate the cross-polarization response at around 0.3%, which indicates a polarization efficiency of $> 94\%$. This is, coincidentally, very close to the magnitude of inductive cross-talk, which appears exactly as reduced polarization efficiency. (For symmetric cross-talk mechanisms, the A detector cross-talks into the B detector and vice-versa.) From this we conclude that the cross-polarization response is dominated by cross-talk, and that the true cross-polar beam is likely to be $\leq 0.1\%$.

I can also look for a rotation of the polarization angles about the expected orientation. We expect the phase offset, $\phi$, to be the same for both detectors. The polarization rotation offset is

$$\textbf{offset} = \phi_A - \phi_B. \tag{5.15}$$

From Table 5.3, I calculate that the A polarization detectors are offset from the B polarization detectors by $> 5$ degrees — a significant non-orthogonality. However, measurements of similar detectors in the BICEP2 experiment find that the detectors are orthogonal to $< 0.3$ degrees [9]. Thus, we have prior empirical evidence that the detectors should be highly orthogonal. Additionally, BICEP2 also finds an uncertainty on the absolute polarization angle of 0.04 degrees ($1\sigma$) [9] when using a dielectric sheet calibrator. Our benchmark for the uncertainty on $\Psi_{rel}$ and $\Psi_{abs}$ is $< 1$ degree, which our measurement does not meet. This measurement was done in the test cryostat with a non-ideal setup and so should be interpreted as an upper limit, rather than a true measurement.

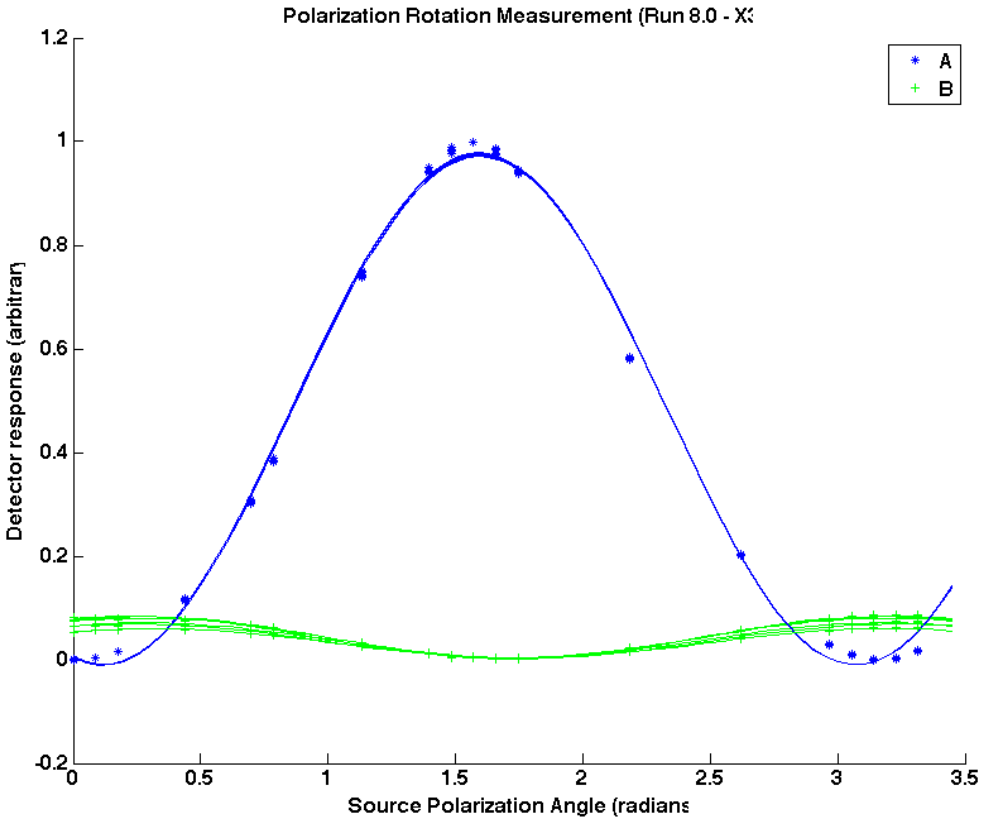


Figure 5.28: Data for all the working detector pixel pairs in the minimaps in arbitrary units. The A polarization detectors are plotted in blue, and the B polarization detectors are plotted in green. The lines are fits for each individual detector to $y = A*\sin^2(bx+\phi)+c$.

#### 5.5.1.1 Polarization Dependence of Beam Centers

Using the same dataset as in the previous section, I did a further analysis of whether the beam centroids move in a systematic way as the polarization of the incident light changes. In Figs. 5.29a and 5.29b one can see the offsets of the beam centers in azimuth and elevation as a function of the polarizing grid angle. Here, the offset has been calculated as the beam center for a single detector at a particular grid angle subtracted from the median of the beam centers for that detector at all grid angles. The black and green lines are medians over the A and B detectors.

These plots are directly comparable to those from a BICEP2 measurement (Fig.5.30a-5.30b). It's easier to see the variation in the BICEP2 plots, since their data was taken over the entire focal plane (rather than on just 6 pixels). We see that there is no displacement of the beam center for a co-polar source polarization, but a very large displacement when the source polarization is cross-polar. The same pattern is emerging in the SPIDER data and we, too, see evidence for the polarization dependence of beam centers. The effect is well-modeled by a tangent curve.

We speculate that this effect is due to coherent interference between the summing trees of the A and B detectors in a pair. Simulations from the BICEP2 collaboration suggest that the effect of this phenomenon will be negligible in the final data analysis.

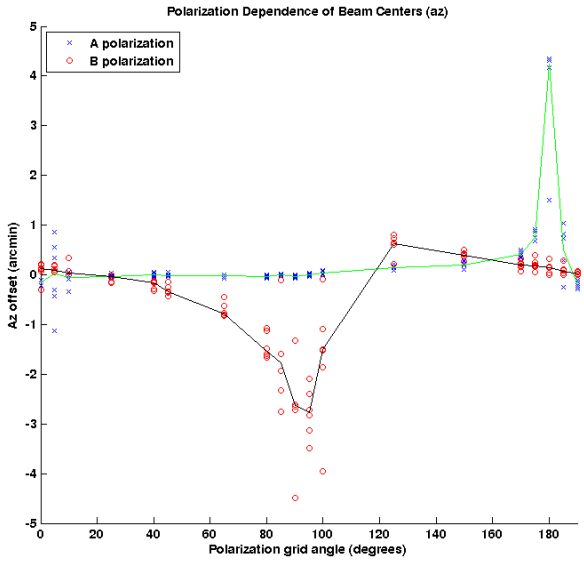


(a) Offset of the beam centers in azimuth as a function of the polarizing grid angle. The black and green lines are medians over the A and B detectors

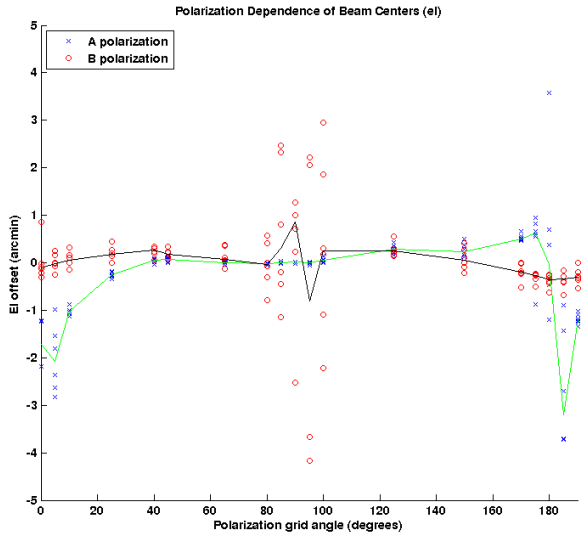


(b) Offset of the beam centers in elevation as a function of the polarizing grid angle. The black and green lines are medians over the A and B detectors

Figure 5.29: Polarization dependence of beam centroid in both azimuth and elevation for SPIDER.

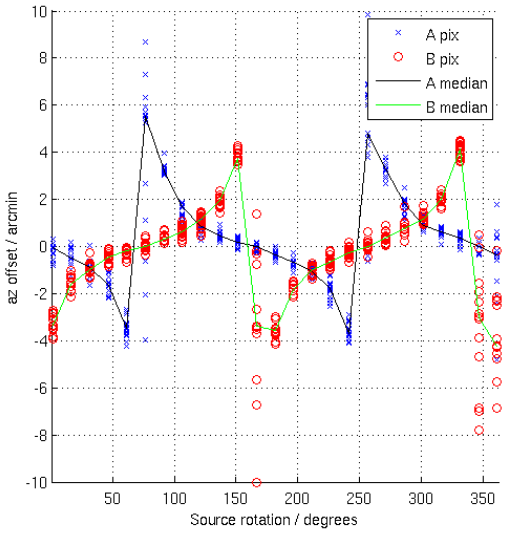


(a) Offset of the beam centers in azimuth as a function of the polarizing grid angle for the BICEP2 experiment. Figure courtesy of Walt Ogburn.

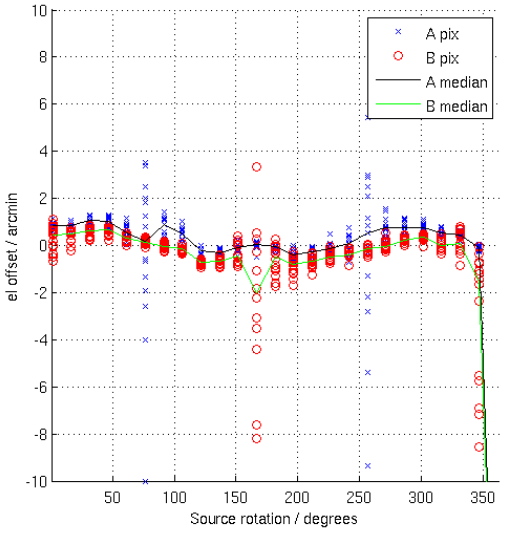


(b) Offset of the beam centers in elevation as a function of the polarizing grid angle for the BICEP2 experiment. Figure courtesy of Walt Ogburn.

Figure 5.30: Polarization dependence of beam centroid in both azimuth and elevation for BICEP2.

### 5.5.2 Palestine Measurement

A second attempt at the measurement of the relative polarization angle of the SPIDER detectors was made in a slightly different way during our deployment to Palestine. For this measurement, we used a different rotating polarized thermal source (RPS) (based on the design for the previous RPS made by Keck) at a distance that was in the mid-field of the telescopes. The thermal source was chopped at 13Hz. A detector was centered on the source and then the RPS wire grid was rotated by 720 degrees at a speed of 2 degrees per second. Much like the previous measurement in the test cryostat, this measurement was too difficult to perform over an entire focal plane, so a subset of detectors was selected.

Each detector time stream was demodulated, and then a fit to $y = A\sin^2(bx + \phi) + c$ was used to get the offset angles for each detector (as in §5.5.1). An example of one of these datasets is shown in Fig. 5.31.

This measurement was thought to improve upon the previous test cryostat measurement in several ways. Practically, it's a much faster measurement since we are not taking beam maps for each angle. Additionally, since it is a thermal source (rather than a microwave source), a misalignment of the source with the cryostat should affect the fidelity of the measurement less. Lastly, since it utilizes a continuously rotating wire grid, we have data at a much finer set of angles.

A table of the results is shown in Table. 5.4. I once again find that the relative angles between pixel pairs are non-orthogonal, typically between 2° and 4°. While this could be seen as evidence of true non-orthogonality of our detectors, I suspect that this measurement is subject to projection effects due to the source being in the mid-field of the telescopes instead of the far-field. This measurement was done with the source clamped to a board on a cherry-picker (see §6.1), which could not have been aligned to better than a few degrees. Retaking this measurement with the source in the true far field of the telescopes would be a much more convincing measurement. This is another measurement that will be need to improved and retaken prior to flight.

Table 5.4: Polarization Efficiency and Rotation Measurement II.

| Pixel Pair | Cross-pol Response | $\phi_A - \phi_B$ |
|---|---|---|
| X1r03/04c00 | 0.46% | 2.4° |
| X1r09/10c12 | 0.11% | 1.4° |
| X1r11/12c03 | 0.21% | 3.9° |
| X1r17/18c14 | 0.48% | 2.3° |
| mean | 0.31% | 2.5° |

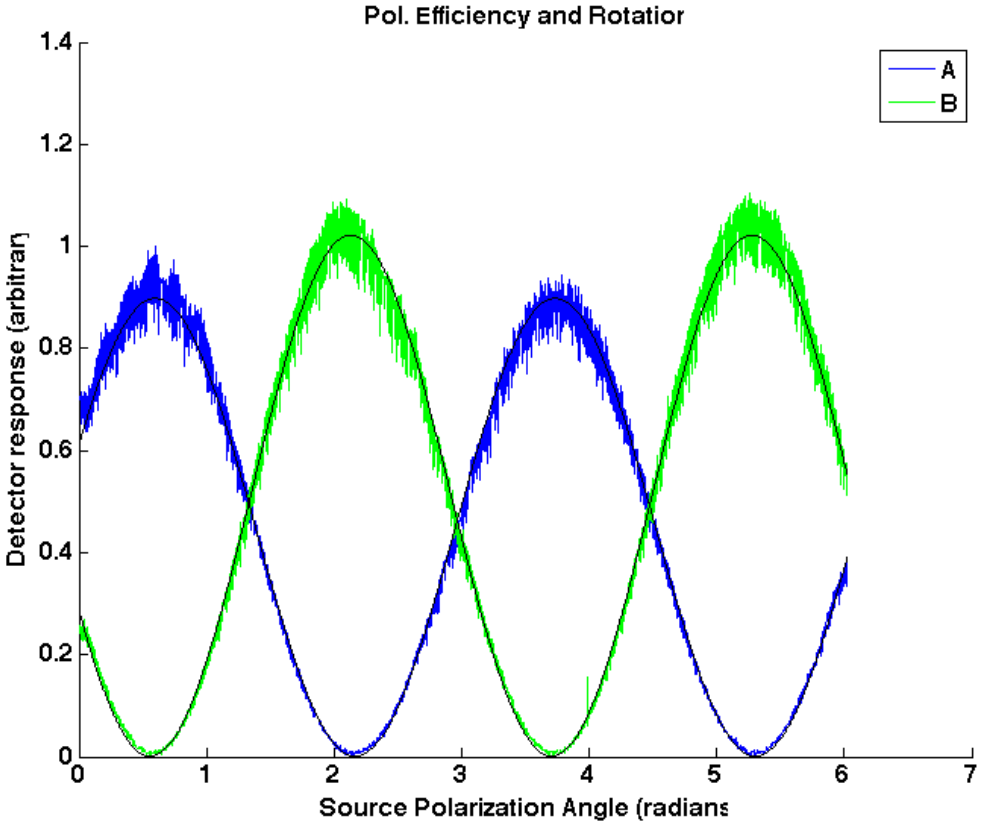


Figure 5.31: Example time stream for a working detector pixel pair. The A polarization detector is plotted in blue, and the B polarization detector is plotted in green. The lines are fits for each detector time stream to $y = A\sin^2(bx + \phi) + c$.

# Chapter 6

# The Path to Deployment

This thesis has described the characterization and calibration of the SPIDER detectors, including our ability to tightly control sources of the systematic error through simulations and measurements. I conclude with a brief description of the work that remains to get SPIDER ready for deployment in the austral summer of 2014. I start with a summary of our pre-flight integration campaign at the Columbia Scientific Ballooning Facility in Palestine, TX and the current status of the instrument, which leads to a discussion of the remaining hardware and software challenges.

## 6.1 Integration in Palestine

Our pre-flight integration campaign took place in summer 2013 at the Columbia Scientific Ballooning Facility in Palestine, TX. This campaign was the first time that all of the Spider subsystems were integrated. Our goal was to confirm that the fully integrated instrument worked in a simulated flight-like environment. At that time, we were preparing for deployment in the austral summer (December) of 2013. Five of the six SPIDER telescopes, the flight cryostat, the gondola, and the contents of an entire lab were shipped to CSBF for this campaign. The tiles for the sixth SPIDER telescope were still in fabrication in early June, which meant it could not be shipped in time for the campaign.

At the beginning of the campaign, I worked as part of the insert team to integrate the FPUs into the SPIDER telescopes and close up the cryostat. This part of integration went exactly as scheduled. We started the process of cooling down the flight cryostat (a process that takes approximately two weeks, due to the size and complexity of the system) in mid-June. An ice-plug and some other cryogenic difficulties meant that we did not actually have

cooled and working detectors until the first week of July.

Shortly after the focal planes reached sub-Kelvin temperatures, we found that the helium environment inside the flight cryostat was substantially worse than it was during previous runs of the flight cryostat at Princeton University, due to a probable helium leak between the main tank and the vacuum space. This helium leak was originally found in the very early days of testing the cryostat, and many attempts have been made over the years to fix it (with varying levels of success). The run immediately prior to shipping the flight cryostat to Palestine had cryogenic performance that achieved our benchmark goals. Unfortunately, the process of shipping the cryostat appears to have caused the leak to reappear.

Our evidence for this helium leak took the form of a degradation in the performance of the detectors, which would typically work for only a few hours before their thermal properties would begin to change. In the hours after cycling the $^3$He sorption fridges, progressively higher voltage biases were necessary to get the detectors into their transition regions. At some point, no amount of voltage bias could get them into transition and the detectors would be locked superconducting. At this point the only way to recover the detectors was to reset the system by heating the SFT such that all the helium boiled away. This process also made it necessary to recycle the fridges.

We believe this behavior was due to superfluid helium films. During the initial phases of condensation we see pulses of heat on the tiles, which could be due to the condensation of the gas. As helium accumulates on the detectors, it causes the thermal conductance of the TES island legs to go up (which is why the TESs require a higher voltage bias to be brought into transition). At some point, so much helium accumulates that the legs are completely thermally shorted to the substrate, which is when the detectors lock superconducting. Heating the SFT and the focal planes cause this accumulated helium to evaporate, which allows the detectors to resume normal operations for a short period of time.

The helium leak vastly complicated our work during the summer. The detectors would typically only be useable (or partially useable) for 10-12 hours at a time and the process of recovering them also took approximately 12 hours. This cut the number of available hours to do tests to less than half of what we anticipated. Additionally, a great deal of time and manpower was spent trying to figure out the cryogenic problems and how to solve them (or work around them) rather than using that same time and manpower to test detectors and calibrate the instrument. The shortened detector span between fridge cycles

also hindered our ability to take long measurements, such as long scans and full beam maps (which typically take at least 12 hours).

Beam mapping was a unique challenge in Palestine due to the elevation constraints of the gondola. The gondola's elevation is restricted to $15^\circ - 40^\circ$, which means that the source for the beam mapper needed to be visible from within these bounds. This $25^\circ$ elevation range is not much larger than our $20^\circ$ field of view. (In comparison, in the test cryostat we have access to the full range of elevation from $0^\circ - 90^\circ$.) The tilted orientations of the focal plane and parallax effects make the situation even less favorable for beam mapping. The balance of keeping the source visible while also in the far field turned out to be a challenge due to the geography of the Palestine high bay. We decided to put the calibration sources on a cherry picker (Fig. 6.1a), whose maximum elevation turned out to be insufficiently high to map the entire focal plane.

The pointing reconstruction for the beam maps turned out to be difficult as well. The original plan was to use a false star field attached to the source and use the star cameras to get a pointing solution. This didn't work, as the star camera was not able to reference the false star field. The best pointing solutions eventually came from beam maps taken at night, when the star cameras could see the hot glow of the thermal source.The cherry picker also had the unfortunate side effect of swaying in the wind. This caused the source to translate by a few inches during the maps, which makes the beams in a beam map blurry and less accurate. A stable structure would be a much better choice for mounting the source. The water tower at CSBF has been used for this purpose before, but we didn't have the time to attempt it during the campaign.

My work prior to the integration campaign included building the calibration sources for these measurements. The first was a rotating polarized source (RPS) that was based on the design for a similar source built for the Keck Array. I designed, built, and deployed this source in the field. A diagram of this source can be seen in Fig. 6.2. It was intended to use a microwave source behind a finely controlled, rotating wire grid so that the polarization of the light from the source could be rotated as necessary. A tiltmeter ensures the alignment of the grid to less than $0.1^\circ$. We calibrated the angle of the wire grid using the diffraction pattern from a laser pointer. Though the RPS could be used for making polarized beam maps, it was also intended to be a way to measure relative polarization angles (§5.5.2). Due to restrictions on elevation, this measurement had to be done in the mid field of the


(a) (b)

Figure 6.1: *Left:* The beam-mapping set-up at CSBF. The source and a false star field have been attached to the cabin of the cherry picker, which is extended to its full height for mapping. Photo courtesy of Steve Benton. *Right:* A mechanically chopped thermal source. The box is a field modification made to shield the photodiode from the sun.

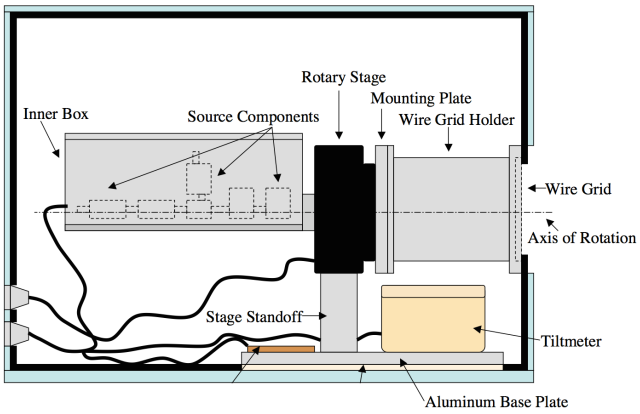


Figure 6.2: A diagram of the RPS with labeled components. Figure adapted from [19].

detectors. It should be noted that the microwave source was replaced with a thermal source for this measurement. For these measurements, the source had to be aligned remotely, since the source was clamped to the (elevated) cherry picker. This made the alignment of our polarized measurements impossible to better than a few degrees, as the process of extending the cherry picker vibrated and shifted the source around.

The second source I built was a mechanically chopped thermal source. This source was built rather quickly during the campaign, using the Princeton thermal source and a chopper wheel I designed and had made. This mechanical chopper relied on a photodiode in order to regulate and read out the chop frequency. It turned out that if we tried to beam map during the day, the sun saturated the photodiode. A field improvisation was made to shield the photodiode (Fig. 6.1b).

We eventually figured out how to optimize our detector performance and calculated that we would be able achieve a useful map depth on the CMB, even with a reduced duty cycle. We also hoped that the helium environment inside the vacuum space could be improved with more charcoal to absorb helium and a helium tight shield around the telescopes. (These suggestions were implemented in a follow-up run, which does in fact show improved cryogenic performance.) We passed our compatibility tests with NASA (Fig. 6.3), so we decided to proceed with the plan to fly SPIDER in December 2013. The SPIDER team packed most of the inserts and FPUs, the flight cryostat, the gondola, tools and other equipment into the three shipping containers. These containers were put on a ship to New Zealand (and eventually McMurdo Station). A few of the telescopes were sent back to Caltech for minor refits and they (and the sixth insert) were delivered to Port

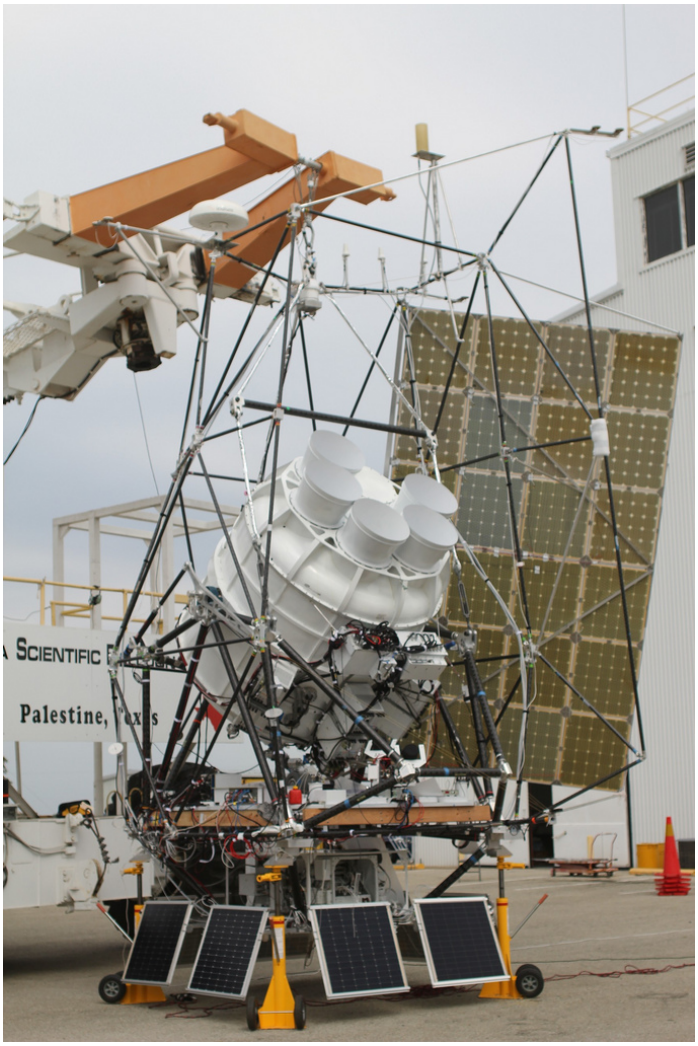


Figure 6.3: SPIDER, fully integrated and hanging on "Tiny Tim" during the NASA compatibility tests. Photo courtesy of Steve Benton.

Hueneme in October to be shipped to the ice by air.

Unfortunately, the government shutdown in October of 2013 wreaked havoc on polar operations. The Office of Polar Programs ran out of funding during the shutdown and all Antarctic operations were suspended. By the time Congress refunded the government, it was too late for the Antarctic ballooning campaign for that year. The entire campaign was canceled (which also affected two other balloon experiments scheduled to deploy that year). Some of ground-based instruments were able to get people and equipment out to Antarctica later in the season, but the ballooning window was too narrow to be recovered.

## 6.2 Current Status

The flight cryostat and shipping containers were returned to the collaboration in December 2013. The shipping crate for the flight cryostat had standing water, which caused corrosion and mold on the flight cryostat. The team at Princeton repaired the cryostat and prepared for another run in Spring 2014.

At the time of this writing, six telescopes in the flight cryostat have been cold for several weeks. The system is showing improved cryogenic performance. The rest of the SPIDER instrument (gondola, telescopes, and electronics) seems to have survived its world tour without incident. The current plan is to deploy to Antarctica in December 2014.

## 6.3 Suggestions for future work

### 6.3.1 Simulations

**Systematics** Many of the simulations discussed in Chapter 3 could be easily improved and updated for our current understanding of the SPIDER instrument. Most of them were done with the assumption of a four-day flight from Alice Springs, Australia, rather than a 20 day flight from Antarctica. Additionally, they could benefit from updated calibrations of the detectors and the scan strategy. There are also a few potential sources of systematic error that have never been simulated, particularly non-differential beam asymmetries and spectral mismatch.

**Foregrounds** With the release of the BICEP2 results, there has been renewed interest in polarized foregrounds and particularly in synchrotron radiation, which was not included in our previous simulations. A simulation of contamination from polarized synchrotron radiation would be informative for SPIDER and give confidence to any detection of primordial B-modes. Additionally, a simulation of the instrument's ability to separate emission from dust from the CMB with an additional frequency band (280GHz has been proposed for the second flight of SPIDER) would be informative for future hardware work, especially in light of the detections made by the BICEP2 experiment.

**On-Sky Calibration** In an ideal world, the pre-flight calibration of the SPIDER detectors will include archival measurements of the optical efficiencies, spectra, noise, beams,

sidelobes, and polarization rotation angles. However, many of these measurements are complicated and time-consuming. SPIDER is a difficult instrument to integrate and cool down, and our time on the ice prior to launch will be extremely limited. It is unlikely that we will have time to complete all of these measurements. We are actively researching whether some of these measurements can be calibrated or deprojected from the data after the flight, so that they can be eliminated from the calibration plan. Several experiments (notably BICEP2) have had good luck using deprojection to remove the effects of certain systematic errors from their data [9].

### 6.3.2 Preparation for flight

**Hardware** In addition to simulation work, there is still plenty of work on both the SPIDER hardware and SPIDER software to get ready for flight. We are still actively researching how to improve the blackening of the cooled optics sleeves to reduce internal loading and large-angle coupling to the sky. Additionally, the collaboration is still exploring schemes for better control of the helium environment inside the flight cryostat: changing the location and amount of charcoal for helium absorption inside the vacuum space and creating a helium-tight bag around each insert to prevent helium from getting to the detectors.

A second flight of SPIDER in 2016 will feature a third frequency band at 220GHz or 280GHz to help with the rejection of polarized foregrounds. The detectors for this band are relatively untested, and there is still plenty of development to be done on optics that are optimized for this frequency. We expect anti-reflection coatings to be somewhat challenging for these bands.

**Software** The flight software is rapidly being developed, tested and debugged, with particular emphasis on the automated tuning and in-flight stability of the TES detectors. The analysis pipeline is still in its early stages, and will need large improvements and additions for the science analysis of our data.

**Calibration and Characterization** The calibration campaign in McMurdo prior to flight will include several measurements that need to be refined — specifically the measurement of the absolute and relative polarization angles and taking beam maps from the ground with the flight cryostat.

One place to start is with the calibration sources. The RPS needs a better interface for commanding the wire grid (and recording the tiltmeter data). The chopped thermal source needs a more reliable method for shielding the photodiode. Additionally, both of these sources had to be read out with extremely long BNC cables, which was inconvenient and may prove impossible on the ice. A better system for reading out the chop frequency when the sources are far away from the cryostat would allows us to make these measurements in the true far field of the telescopes, which we suspect as a source of error in previous attempts. Both of these measurements would benefit from having the calibration source mounted on a stable structure (e.g., the top of a building).

## 6.4 The Future of CMB Polarimetry

The field of CMB and CMB polarimetry measurements has long been competitive, with many experiments and many approaches. On the ground, we can expect further measurements of the B-mode lensing spectrum from experiments like SPTPol [66], Polarbear [55], and ACT [83]. These high-resolution experiments also hope to measure the number of neutrino-like species and search for an offset in the neutrino mass scale. ABS [32], BICEP3 (scheduled for deployment in the austral summer of 2014) and the Keck Array [81] will continue to refine the measurement of the primordial B-mode spectrum.

The recent and exciting results from the BICEP2 experiment have renewed interest in next-generation CMB polarization experiments. Next-generation experiments, such as SPT-3G and Advanced ACTpol [67], hope to be the first instruments to characterize the B-mode lensing map well enough to subtract its contamination from the primordial B-mode map. (A process known as "de-lensing" the B-mode spectrum.) There have also been proposals of a fourth-generation ground-based experiment utilizing half a million pixels on the sky to make the definitive de-lensing and neutrino measurements. Finally, there has also been renewed interest in a satellite (such as EPIC [18] or CMBpol [16]) to make a definitive measurement of CMB polarization.

## 6.5 Conclusion

While there is much work to be done prior to deployment, SPIDER has the potential to uniquely contribute to the field of cosmology with a highly sensitive measurement of the

polarization of the CMB at two frequencies. Its balloon-borne platform will allow it to measure the B-mode spectrum at larger angular scales and with less sample variance than its ground-based competitors. This thesis has described the testing and characterization of the SPIDER detectors and telescopes, with a focus on controlling sources of systematic error. SPIDER hopes to confirm the detection of the primordial B-mode spectrum in order to set new and tighter constraints on the tensor-to-scalar ratio, $r$, and the energy scale of inflation.

# Bibliography

[1] P. A. R. Ade et al., *Planck 2013 results. I. Overview of products and scientific results*, (2013), arXiv: 1303.5062.

[2] ———, *Planck 2013 results. XXIII. Isotropy and statistics of the CMB*, (2013), arXiv: 1303.5083.

[3] ———, *Planck 2013 Results. XXIV. Constraints on primordial non-Gaussianity*, (2013), arXiv: 1303.5084.

[4] ———, *A Measurement of the Cosmic Microwave Background B-Mode Polarization Power Spectrum at Sub-Degree Scales with POLARBEAR*, (2014), arXiv: 1403.2369.

[5] ———, *BICEP2 I: Detection Of B-mode Polarization at Degree Angular Scales*, (2014), (preprint), arXiv: 1403.3985.

[6] ———, *BICEP2 II: Experiment and Three-Year Data Set*, (2014), (preprint), arXiv: 1403.4302.

[7] Peter A. R. Ade, Giampaolo Pisano, Carole Tucker, and Samuel Weaver, *A review of metal mesh filters*, Proceedings of the Society of Photo-Optical Instrumentation Engineers (SPIE) **6275** (2006), 62750U–62750U–15.

[8] R. W. Aikin, P. A. Ade, S. Benton, J. J. Bock, J. A. Bonetti, J. A. Brevik, C. D. Dowell, L. Duband, J. P. Filippini, S. R. Golwala, M. Halpern, V. V. Hristov, K. Irwin, J. P. Kaufman, B. G. Keating, J. M. Kovac, C. L. Kuo, A. E. Lange, C. B. Netterfield, H. T. Nguyen, R. W. Ogburn, IV, A. Orlando, C. Pryke, S. Richter, J. E. Ruhl, M. C. Runyan, C. Sheehy, S. A. Stokes, R. Sudiwala, G. P. Teply, J. E. Tolan, A. D. Turner, P. Wilson, and C. L. Wong, *Optical performance of the BICEP2 Telescope at the South Pole*, Proceedings of the Society of Photo-Optical Instrumentation Engineers (SPIE) **7741** (2010), http://adsabs.harvard.edu/abs/2010SPIE.7741E..23A.

[9] Randol W. Aikin, *Testing Inflationary Cosmology with the BICEP1 and BICEP2 Experiments*, Ph.D. thesis, California Institute of Technology, 1200 E. California Blvd, Pasadena, CA 91125, May 2013.

[10] A. Albrecht and P. J. Steinhardt, *Cosmology for grand unified theories with radiatively induced symmetry breaking*, Physical Review Letters **48** (1982), 1220–1223, http://adsabs.harvard.edu/abs/1982PhRvL..48.1220A.

[11] D. H. Andrews, W. F. Brucksch, W. T. Ziegler, and E. R. Blanchard, *Attenuated Superconductors I. For Measuring Infrared Radiation*, Review of Scientific Instruments **13** (1942), no. 7, 281–292.

[12] J. Bardeen, L. N. Cooper, and J. R. Schrieffer, *Microscopic Theory of Superconductivity*, Physical Review **106** (1957), 162–164, http://adsabs.harvard.edu/abs/1957PhRv..106..162B.

[13] D. Barkats, R. Aikin, C. Bischoff, I. Buder, J. P. Kaufman, B. G. Keating, J. M. Kovac, M. Su, P. A. R. Ade, J. O. Battle, E. M. Bierman, J. J. Bock, H. C. Chiang, C. D. Dowell, L. Duband, J. Filippini, E. F. Hivon, W. L. Holzapfel, V. V. Hristov, W. C. Jones, C. L. Kuo, E. M. Leitch, P. V. Mason, T. Matsumura, H. T. Nguyen, N. Ponthieu, C. Pryke, S. Richter, G. Rocha, C. Sheehy, S. S. Kernasovskiy, Y. D. Takahashi, J. E. Tolan, and K. W. Yoon, *Degree-Scale CMB Polarization Measurements from Three Years of BICEP1 Data*, The Astrophysical Journal **783** (2014), no. 2, 67, arXiv: 1310.1422.

[14] E. S. Battistelli, M. Amiri, B. Burger, M. Halpern, S. Knotek, M. Ellis, X. Gao, D. Kelly, M. MacIntosh, K. Irwin, and C. Reintsema, *Functional Description of Read-out Electronics forTime-Domain Multiplexed Bolometers forMillimeter and Submillimeter Astronomy*, Journal of Low Temperature Physics **151** (2008), no. 3-4, 908–914 (English).

[15] Daniel Baumann, *The physics of inflation - a course for graduate students in particle physics and cosmology*, http://www.damtp.cam.ac.uk/user/db275/TEACHING/INFLATION/Lectures.pdf, 2011.

[16] Daniel Baumann et al., *CMBPol Mission Concept Study: Probing Inflation with CMB Polarization*, American Institute of Physics Conference Proceedings **1141** (2009), 10–120, arXiv: 0811.3919.

[17] C. L. Bennett et al., *Nine-Year Wilkinson Microwave Anisotropy Probe (WMAP) Observations: Final Maps and Results*, The Astrophysical Journal Supplement **208** (2013), 20, arXiv: 1212.5225.

[18] James Bock et al., *Study of the Experimental Probe of Inflationary Cosmology (EPIC)-Intemediate Mission for NASA's Einstein Inflation Probe*, (2009), arXiv: 0906.1188.

[19] Kristi J. Bradford, *A Rotating Polarized Source: Instrument Development for Precision Calibration of the Cosmic Microwave Background Polarimeters at the South Pole*, Harvard Undergraduate Thesis, 2012.

[20] J. A. Brevik, R. W. Aikin, M. Amiri, S. J. Benton, J. J. Bock, et al., *Initial performance of the BICEP2 antenna-coupled superconducting bolometers at the South Pole*, Proceedings of the Society of Photo-Optical Instrumentation Engineers (SPIE) **7741** (2010), 7411H–1.

[21] Justus A. Brevik, *Searching for Primordial Gravitational Waves at Degree Scales from the South Pole*, Ph.D. thesis, California Institute of Technology, 1200 E. California Blvd, Pasadena, CA 91125, May 2012.

[22] Sean Bryan, *Half-wave Plates for the Spider Cosmic Microwave Background Polarimeter*, (2014), arXiv: 1402.2591.

[23] Sean A. Bryan, Peter A. R. Ade, Mandana Amiri, Steve Benton, Richard Bihary, et al., *Modeling and characterization of the SPIDER half-wave plate*, Proceedings of the Society of Photo-Optical Instrumentation Engineers (SPIE) **7741** (2010), arXiv: 1006.3874.

[24] Jungyeon Cho and A. Lazarian, *Galactic foregrounds: Spatial fluctuations and a procedure of removal*, The Astrophysical Journal **720** (2010), 1181–1201, arXiv: 1007.3740.

[25] Sudeep Das, Thibaut Louis, Michael R. Nolta, Graeme E. Addison, Elia S. Battistelli, et al., *The Atacama Cosmology Telescope: Temperature and Gravitational Lensing Power Spectrum Measurements from Three Seasons of Data*, (2013), arXiv: 1301.1037.

[26] L. Davis, Jr. and J. L. Greenstein, *The Polarization of Starlight by Aligned Dust Grains*, The Astrophysical Journal **114** (1951), 206, http://adsabs.harvard.edu/abs/1951ApJ...114..206D.

[27] P. de Bernardis, P. A. R. Ade, R. Artusa, J. J. Bock, A. Boscaleri, B. P. Crill, G. De Troia, P. C. Farese, M. Giacometti, V. V. Hristov, A. Iacoangeli, A. E. Lange, A. T. Lee, S. Masi, L. Martinis, P. V. Mason, P. D. Mauskopf, F. Melchiorri, L. Miglio, T. Montroy, C. B. Netterfield, E. Pascale, F. Piacentini, P. L. Richards, J. E. Ruhl, and F. Scaramuzzi, *Mapping the CMB sky: THE BOOMERanG experiment*, New Astronomy Review **43** (1999), 289–296, arXiv: astro-ph/9911461.

[28] P. de Bernardis et al., *A Flat universe from high resolution maps of the cosmic microwave background radiation*, Nature **404** (2000), 955–959, arXiv: astro-ph/0004404.

[29] Piet A. J. de Korte, Joern Beyer, Steve Deiker, Gene C. Hilton, Kent D. Irwin, Mike MacIntosh, Sae Woo Nam, Carl D. Reintsema, Leila R. Vale, and Martin E. Huber, *Time-division superconducting quantum interference device multiplexer for transition-edge sensors*, Review of Scientific Instruments **74** (2003), no. 8, 3807–3815.

[30] R. H. Dicke, P. J. E. Peebles, P. G. Roll, and D. T. Wilkinson, *Cosmic Black-Body Radiation.*, The Astrophysical Journal **142** (1965), 414–419, http://adsabs.harvard.edu/abs/1965ApJ...142..414D.

[31] Albert Einstein, *Cosmological Considerations in the General Theory of Relativity*, Sitzungsberichte der Preussischen Akademie der Wissenschaften, Physikalisch-Mathematische Klasse **1917** (1917), 142–152.

[32] T. Essinger-Hileman, J. W. Appel, J. A. Beall, H. M. Cho, J. Fowler, et al., *The Atacama B-Mode Search: CMB Polarimetry with Transition-Edge-Sensor Bolometers*, (2010), arXiv: 1008.3915.

[33] J. P. Filippini, *In-flight electrical calibrations for spider*, internal Spider document, June 2011.

[34] Douglas P. Finkbeiner, Marc Davis, and David J. Schlegel, *Extrapolation of galactic dust emission at 100 microns to CMBR frequencies using FIRAS*, The Astrophysical Journal **524** (1999), 867–886, arXiv: astro-ph/9905128.

[35] L.M. Fissel, P. A. R. Ade, F. E. Angilè, S. J. Benton, E. L. Chapin, M. J. Devlin, N. N. Gandilo, J. O. Gundersen, P. C. Hargrave, D. H. Hughes, J. Klein, A. L. Korotkov, G. Marsden, T. G. Matthews, L. Moncelsi, T. K. Mroczkowski, C. B. Netterfield, G. Novak, L. Olmi, E. Pascale, G. Savini, D. Scott, J. A. Shariff, J. D. Soler, N. E. Thomas, M. D. P. Truch, C. E. Tucker, G. S. Tucker, D. Ward-Thompson, and D. V. Wiebe, *The balloon-borne large-aperture submillimeter telescope for polarimetry: BLAST-Pol*, Proceedings of the Society of Photo-Optical Instrumentation Engineers (SPIE) **7741** (2010), arXiv: 1007.1390.

[36] A .A. Fraisse, P. A. R. Ade, M. Amiri, S. J. Benton, J. J. Bock, et al., *SPIDER: Probing the Early Universe with a Suborbital Polarimeter*, Journal of Cosmology and Astroparticle Physics **1304** (2013), 047, arXiv: 1106.3087.

[37] A. Friedmann, *Über die Krümmung des Raumes*, Zeitschrift fur Physik **10** (1922), 377–386, http://adsabs.harvard.edu/abs/1922ZPhy...10..377F.

[38] ———, *Über die Möglichkeit einer Welt mit konstanter negativer Krümmung des Raumes*, Zeitschrift fur Physik **21** (1924), 326–332, http://adsabs.harvard.edu/abs/1924ZPhy...21..326F.

[39] Matthew J. Griffin, James J. Bock, and Walter K. Gear, *Relative Performance of Filled and Feedhorn-Coupled Focal-Plane Architectures*, Applied Optics **41** (2002), no. 31, 6543–6554.

[40] J. E. Gudmunddson, *Spider Experiment - FTS Manual - Rev A*, internal Spider document, 2010.

[41] J. E. Gudmundsson, P. A. R. Ade, M. Amiri, S. J. Benton, R. Bihary, et al., *Thermal architecture for the SPIDER flight cryostat*, Proceedings of the Society of Photo-Optical Instrumentation Engineers (SPIE) **7741** (2010), 77411M, arXiv: 1106.2507.

[42] Alan H. Guth, *Inflationary universe: A possible solution to the horizon and flatness problems*, Physical Review D **23** (1981), 347–356.

[43] John S. Hall, *Observations of the Polarized Light From Stars*, Science **109** (1949), no. 2825, 166–167, http://www.sciencemag.org/content/109/2825/166.full.pdf.

[44] S. Hanany, P. Ade, A. Balbi, J. Bock, J. Borrill, et al., *MAXIMA-1: A Measurement of the cosmic microwave background anisotropy on angular scales of 10 arcminutes to 5 degrees*, The Astrophysical Journal **545** (2000), L5, arXiv: astro-ph/0005123.

[45] D. Hanson et al., *Detection of B-mode Polarization in the Cosmic Microwave Background with Data from the South Pole Telescope*, Physical Review Letters **111** (2013), 141301, arXiv: 1307.5830.

[46] W. A. Hiltner, *Polarization of Light From Distant Stars by Interstellar Medium*, Science **109** (1949), no. 2825, 165, http://www.sciencemag.org/content/109/2825/165.full.pdf.

[47] Wayne Hu and Scott Dodelson, *Cosmic microwave background anisotropies*, The Annual Review of Astronomy and Astrophysics **40** (2002), 171–216, arXiv: astro-ph/0110414.

[48] Edwin Hubble, *A relation between distance and radial velocity among extra-galactic nebulae*, Proceedings of the National Academy of Sciences **15** (1929), no. 3, 168–173, http://www.pnas.org/content/15/3/168.full.pdf+html.

[49] E. M. L. Humphreys, Mark J. Reid, Jim M. Moran, Lincoln J. Greenhill, and Alice L. Argon, *Toward a New Geometric Distance to the Active Galaxy NGC 4258. III. Final Results and the Hubble Constant*, The Astrophysical Journal **775** (2013), 13, arXiv: 1307.6031.

[50] K. D. Irwin, *An application of electrothermal feedback for high resolution cryogenic particle detection*, Applied Physics Letters **66** (1995), no. 15, 1998–2000.

[51] K. D. Irwin and G. C. Hilton, *Transition-edge sensors*, Cryogenic Particle Detection (Christian Enss, ed.), Topics in Applied Physics, vol. 99, Springer Berlin Heidelberg, 2005, pp. 63–150.

[52] William C. Jones, P. Ade, J. Bock, J. Bond, J. Borrill, et al., *A Measurement of the angular power spectrum of the CMB temperature anisotropy from the 2003 flight of BOOMERANG*, The Astrophysical Journal **647** (2006), 823–832, arXiv: astro-ph/0507494.

[53] William C. Jones, T. E. Montroy, B. P. Crill, C. R. Contaldi, T. S. Kisner, et al., *Instrumental and Analytic Methods for Bolometric Polarimetry*, Astronomy and Astrophysics (2006), arXiv: astro-ph/0606606.

[54] Marc Kamionkowski, Arthur Kosowsky, and Albert Stebbins, *Statistics of cosmic microwave background polarization*, Physical Review **D55** (1997), 7368–7388, arXiv: astro-ph/9611125.

[55] Zigmund D. Kermish, Peter Ade, Aubra Anthony, Kam Arnold, Darcy Barron, David Boettger, Julian Borrill, Scott Chapman, Yuji Chinone, Matt A. Dobbs, Josquin Errard, Giulio Fabbian, Daniel Flanigan, George Fuller, Adnan Ghribi, Will Grainger, Nils Halverson, Masaya Hasegawa, Kaori Hattori, Masashi Hazumi, William L. Holzapfel, Jacob Howard, Peter Hyland, Andrew Jaffe, Brian Keating, Theodore Kisner, Adrian T. Lee, Maude Le Jeune, Eric Linder, Marius Lungu, Frederick Matsuda, Tomotake Matsumura, Xiaofan Meng, Nathan J. Miller, Hideki Morii, Stephanie Moyerman, Mike J. Myers, Haruki Nishino, Hans Paar, Erin Quealy, Christian L. Reichardt, Paul L. Richards, Colin Ross, Akie Shimizu, Meir Shimon, Chase Shimmin, Mike Sholl, Praween Siritanasak, Helmuth Spieler, Nathan Stebor, Bryan Steinbach, Radek Stompor, Aritoki Suzuki, Takayuki Tomaru, Carole Tucker, and Oliver Zahn, *The POLARBEAR experiment*, Proceedings of the Society of Photo-Optical Instrumentation Engineers (SPIE) **8452** (2012), 84521C–84521C–15.

[56] John Kovac, E.M. Leitch, C Pryke, J.E. Carlstrom, N.W. Halverson, et al., *Detection of polarization in the cosmic microwave background using DASI*, Nature **420** (2002), 772–787, arXiv: astro-ph/0209478.

[57] D. K. Lambert and P. L. Richards, *Martin-Puplett interferometer: an analysis*, Applied Optics **17** (1978), no. 10, 1595–1602.

[58] A. Lazarian and D. Finkbeiner, *Microwave emission from aligned dust*, New Astronomy Reviews **47** (2003), 1107–1116, arXiv: astro-ph/0307012.

[59] G. Lemaître, *Un Univers homogène de masse constante et de rayon croissant rendant compte de la vitesse radiale des nébuleuses extra-galactiques*, Annales de la Societe Scietifique de Bruxelles **47** (1927), 49–59, http://adsabs.harvard.edu/abs/1927ASSB...47...49L.

[60] ———, *Expansion of the universe, A homogeneous universe of constant mass and increasing radius accounting for the radial velocity of extra-galactic nebulae*, Monthly Notices of the Royal Astronomical Society **91** (1931), 483–490, http://adsabs.harvard.edu/abs/1931MNRAS..91..483L.

[61] A. D. Linde, *A new inflationary universe scenario: A possible solution of the horizon, flatness, homogeneity, isotropy and primordial monopole problems*, Physics Letters B **108** (1982), 389–393, http://adsabs.harvard.edu/abs/1982PhLB..108..389L.

[62] C. J. MacTavish, P. A. R. Ade, E. S. Battistelli, S. Benton, R. Bihary, et al., *Spider Optimization: Probing the Systematics of a Large Scale B-Mode Experiment*, (2007), arXiv: 0710.0375.

[63] Silvia Masi, P. Ade, J. Bock, J. Bond, J. Borrill, et al., *Instrument, method, brightness and polarization maps from the 2003 flight of BOOMERANG*, (2005), arXiv: astro-ph/0507509.

[64] J. C. Mather, E. S. Cheng, D. A. Cottingham, R. E. Eplee, Jr., D. J. Fixsen, T. Hewagama, R. B. Isaacman, K. A. Jensen, S. S. Meyer, P. D. Noerdlinger, S. M. Read, L. P. Rosen, R. A. Shafer, E. L. Wright, C. L. Bennett, N. W. Boggess, M. G. Hauser, T. Kelsall, S. H. Moseley, Jr., R. F. Silverberg, G. F. Smoot, R. Weiss, and D. T. Wilkinson, *Measurement of the cosmic microwave background spectrum by the COBE FIRAS instrument*, The Astrophysical Journal **420** (1994), 439–444, http://adsabs.harvard.edu/abs/1994ApJ...420..439M.

[65] J. C. Mather, D. J. Fixsen, R. A. Shafer, C. Mosier, and D. T. Wilkinson, *Calibrator Design for the COBE Far Infrared Absolute Spectrophotometer (FIRAS)*, The Astrophysical Journal **512** (1999), no. 2, 511.

[66] J. J. McMahon, K. A. Aird, B. A. Benson, L. E. Bleem, J. Britton, J. E. Carlstrom, C. L. Chang, H. S. Cho, T. de Haan, T. M. Crawford, A. T. Crites, A. Datesman, M. A. Dobbs, W. Everett, N. W. Halverson, G. P. Holder, W. L. Holzapfel, D. Hrubes, K. D. Irwin, M. Joy, R. Keisler, T. M. Lanting, A. T. Lee, E. M. Leitch, A. Loehr, M. Lueker, J. Mehl, S. S. Meyer, J. J. Mohr, T. E. Montroy, M. D. Niemack, C. C. Ngeow, V. Novosad, S. Padin, T. Plagge, C. Pryke, C. Reichardt, J. E. Ruhl, K. K. Schaffer, L. Shaw, E. Shirokoff, H. G. Spieler, B. Stadler, A. A. Stark, Z. Staniszewski,

K. Vanderlinde, J. D. Vieira, G. Wang, R. Williamson, V. Yefremenko, K. W. Yoon, O. Zhan, and A. Zenteno, *SPTpol: an instrument for CMB polarization*, American Institute of Physics Conference Proceedings **1185** (2009), no. 1, 511–514.

[67] M. D. Niemack, P. A. R. Ade, J. Aguirre, F. Barrientos, J. A. Beall, et al., *ACTPol: A polarization-sensitive receiver for the Atacama Cosmology Telescope*, Proceedings of the Society of Photo-Optical Instrumentation Engineers (SPIE) **7741** (2010), 77411S, arXiv: 1006.5049.

[68] D. T. O'Dea, P. A. R. Ade, M. Amiri, S. J. Benton, J. J. Bock, et al., *Spider Optimization II: Optical, Magnetic and Foreground Effects*, The Astrophysical Journal **738** (2011), 63, arXiv: 1102.0559.

[69] R. W. Ogburn, IV, P. A. R. Ade, R. W. Aikin, M. Amiri, S. J. Benton, J. J. Bock, J. A. Bonetti, J. A. Brevik, B. Burger, C. D. Dowell, L. Duband, J. P. Filippini, S. R. Golwala, M. Halpern, M. Hasselfield, G. Hilton, V. V. Hristov, K. Irwin, J. P. Kaufman, B. G. Keating, J. M. Kovac, C. L. Kuo, A. E. Lange, E. M. Leitch, C. B. Netterfield, H. T. Nguyen, A. Orlando, C. L. Pryke, C. Reintsema, S. Richter, J. E. Ruhl, M. C. Runyan, C. D. Sheehy, Z. K. Staniszewski, S. A. Stokes, R. V. Sudiwala, G. P. Teply, J. E. Tolan, A. D. Turner, P. Wilson, and C. L. Wong, *The BICEP2 CMB polarization experiment*, Proceedings of the Society of Photo-Optical Instrumentation Engineers (SPIE) **7741** (2010).

[70] L. Page et al., *Three year Wilkinson Microwave Anisotropy Probe (WMAP) observations: polarization analysis*, The Astrophysical Journal Supplement **170** (2007), 335, arXiv: astro-ph/0603450.

[71] J.R. Pardo, J. Cernicharo, and E. Serabyn, *Atmospheric transmission at microwaves (atm): an improved model for millimeter/submillimeter applications*, Antennas and Propagation, IEEE Transactions on **49** (2001), no. 12, 1683–1694.

[72] E. Pascale, P. A. R. Ade, J. J. Bock, E. L. Chapin, J. Chung, M. J. Devlin, S Dicker, M. Griffin, J. O. Gundersen, M. Halpern, P. C. Hargrave, D. H. Hughes, J. Klein, C. J. MacTavish, G. Marsden, P. G. Martin, T. G. Martin, P. Mauskopf, C. B. Netterfield, L. Olmi, G. Patanchon, M. Rex, D. Scott, C. Semisch, N. Thomas, M. D. P. Truch,

C. Tucker, G. S. Tucker, M. P. Viero, and D. V. Wiebe, *The balloon-borne large aperture submillimeter telescope: Blast*, The Astrophysical Journal **681** (2008), no. 1, 400.

[73] A. A. Penzias and R. W. Wilson, *A Measurement of Excess Antenna Temperature at 4080 Mc/s.*, The Astrophysical Journal **142** (1965), 419–421, http://adsabs.harvard.edu/abs/1965ApJ...142..419P.

[74] J. P. Preskill, *Cosmological production of superheavy magnetic monopoles*, Physical Review Letters **43** (1979), 1365–1368, http://adsabs.harvard.edu/abs/1979PhRvL..43.1365P.

[75] Paul L. Richards, *Superconducting bolometers: high-tc and low-tc*, Proceedings of the Society of Photo-Optical Instrumentation Engineers (SPIE) **1477** (1991), 2–6.

[76] Adam G. Riess et al., *Observational evidence from supernovae for an accelerating universe and a cosmological constant*, The Astronomical Journal **116** (1998), 1009–1038, arXiv: astro-ph/9805201.

[77] H. P. Robertson, *Kinematics and World-Structure*, The Astrophysical Journal **82** (1935), 284, http://adsabs.harvard.edu/abs/1935ApJ....82..284R.

[78] M. C. Runyan, P. A. R. Ade, M. Amiri, S. Benton, R. Bihary, et al., *Design and performance of the Spider instrument*, Proceedings of the Society of Photo-Optical Instrumentation Engineers (SPIE) **7741** (2010), 774110, arXiv: 1106.2173.

[79] M. C. Runyan and W. C. Jones, *Thermal Conductivity of Thermally-Isolating Polymeric and Composite Structural Support Materials Between 0.3 and 4 K*, Cryogenics **48** (2008), 448–454, arXiv: 0806.1921.

[80] Uros Seljak and Matias Zaldarriaga, *Signature of gravity waves in polarization of the microwave background*, Physical Review Letters **78** (1997), 2054–2057, arXiv: astro-ph/9609169.

[81] Z. Staniszewski, R. W. Aikin, M. Amiri, S. J. Benton, C. Bischoff, J. J. Bock, J. A. Bonetti, J. A. Brevik, B. Burger, C. D. Dowell, L. Duband, J. P. Filippini, S. R. Golwala, M. Halpern, M. Hasselfield, G. Hilton, V. V. Hristov, K. Irwin, J. M. Kovac, C. L. Kuo, M. Lueker, T. Montroy, H. T. Nguyen, R. W. Ogburn, R. O'Brient,

A. Orlando, C. Pryke, C. Reintsema, J. E. Ruhl, R. Schwarz, C. Sheehy, S. Stokes, K. L. Thompson, G. Teply, J. E. Tolan, A. D. Turner, A. G. Vieregg, P. Wilson, D. Wiebe, and C. L. Wong, *The Keck Array: A Multi Camera CMB Polarimeter at the South Pole*, Journal of Low Temperature Physics **167** (2012), 827–833, http://adsabs.harvard.edu/abs/2012JLTP..167..827S.

[82] K. T. Story, C. L. Reichardt, Z. Hou, R. Keisler, K. A. Aird, et al., *A Measurement of the Cosmic Microwave Background Damping Tail from the 2500-square-degree SPT-SZ survey*, The Astrophysical Journal **779** (2013), 86, arXiv: 1210.7231.

[83] D. S. Swetz, P. A. R. Ade, M. Amiri, J. W. Appel, E. S. Battistelli, et al., *Overview of the Atacama Cosmology Telescope: Receiver, instrumentation, and telescope systems*, The Astrophysical Journal Supplement **194** (2011), 41, arXiv: 1007.0290.

[84] Y. D. Takahashi, P. A. R. Ade, D. Barkats, J. O. Battle, E. M. Bierman, et al., *Characterization of the BICEP Telescope for High-Precision Cosmic Microwave Background Polarimetry*, The Astrophysical Journal **711** (2010), 1141–1156, arXiv: 0906.4069.

[85] J. Tauber et al., *The Scientific Programme of Planck*, (2006), arXiv: astro-ph/0604069.

[86] Amy R. Trangsrud, *The Spider CMB Polarimeter*, Ph.D. thesis, California Institute of Technology, 1200 E. California Blvd, Pasadena, CA 91125, July 2011.

[87] Mark Trodden and Sean M. Carroll, *TASI lectures: Introduction to cosmology*, (2004), 703–793, arXiv: astro-ph/0401547.

[88] Carole E. Tucker and Peter A. R. Ade, *Thermal filtering for large aperture cryogenic detector arrays*, Proceedings of the Society of Photo-Optical Instrumentation Engineers (SPIE) **6275** (2006), 62750T–62750T–9.

[89] A. G. Walker, *On Milne's Theory of World-Structure*, Proceedings of the London Mathematical Society **s2-42** (1937), no. 1, 90–127.

[90] E. L. Wright, C. L. Bennett, K. Grski, G. Hinshaw, and G. F. Smoot, *Angular Power Spectrum of the Cosmic Microwave Background Anisotropy Seen by the COBE DMR*, The Astrophysical Journal Letters **464** (1996), no. 1, L21.

[91] K. W. Yoon, P. A. R. Ade, D. Barkats, J. O. Battle, E. M. Bierman, J. J. Bock, J. A. Brevik, H. C. Chiang, A. Crites, C. D. Dowell, L. Duband, G. S. Griffin, E. F. Hivon, W. L. Holzapfel, V. V. Hristov, B. G. Keating, J. M. Kovac, C. L. Kuo, A. E. Lange, E. M. Leitch, P. V. Mason, H. T. Nguyen, N. Ponthieu, Y. D. Takahashi, T. Renbarger, L. C. Weintraub, and D. Woolsey, *The Robinson Gravitational Wave Background Telescope (BICEP): a bolometric large angular scale CMB polarimeter*, Proceedings of the Society of Photo-Optical Instrumentation Engineers (SPIE) **6275** (2006), 62751K, arXiv: astro-ph/0606278.

[92] Y. B. Zeldovich and M. Y. Khlopov, *On the concentration of relic magnetic monopoles in the universe*, Physics Letters B **79** (1978), 239–241, http://adsabs.harvard.edu/abs/1978PhLB...79..239Z.